Chaos in Many-Body Quantum Systems

Christoph Sünderhauf

München 2021

Chaos in Many-Body Quantum Systems

Christoph Sünderhauf

Dissertation
der Fakultät für Physik
der Ludwig-Maximilians-Universität
München

vorgelegt von
Christoph Sünderhauf
aus Darmstadt

München, den 22. Februar 2021

Erstgutachter: Dr. Christian Schilling
Zweitgutachter: Prof. Dr. J. Ignacio Cirac
Tag der mündlichen Prüfung: 21. April 2021

Abstract

Chaos in many-body quantum systems is of great importance to both many-body physics as well as black hole physics. In the field of many-body physics, interactions and disorder in the system can lead to various dynamic phenomena, be it thermalisation, many-body localisation, chaotic behavior and scrambling of quantum information. In the field of high energy physics, the holographic principle connects chaos and scrambling in many-body quantum systems with the information-theoretic properties of black holes. Theoretical quantum physics provides the framework for the models, methods, and results in this thesis, while black hole physics partly provides some motivation and inspiration.

First, we introduce a new model for a many-body quantum system based on random quantum circuits. These are a popular framework for theoretic study of disordered spin chains. By drawing the random unitaries in the circuit from different ensembles, we can adjust the disorder strength in the interactions, which in turn leads to a thermal/many-body localisation phase transition.

Next, we study the Brownian SYK model, a disordered model of Majorana fermions with all-to-all interactions, motivated by its link to the holographic principle. We develop a new numerical method based on an effective permutational symmetry to reduce computational cost from exponential to linear or quadratic in system size N. As a consequence, we can compute scrambling quantifiers in detail, and find a $\log N$ scrambling time, as conjectured in the context of fast scrambling for black holes.

Finally, we develop a model based on the continuous-time limit of a random quantum circuit. It serves as a microscopic toy model for the evaporation of a black hole. With a similar method as developed for the Brownian SYK model, we can analyse its information theoretic properties. In particular, we follow established protocols for information retrieval from the Hawking radiation. We find a separation of time scales for entanglement growth and information retrieval, related to the intrinsic black hole dynamics ($\propto \log N$) and the coupling to the environment ($\propto N$).

Zusammenfassung

Chaos in Quantenvielteilchensystemen ist sowohl für Vielteilchenphysik als auch die Physik schwarzer Löcher von großer Bedeutung. Im Bereich der Vielteilchenphysik können Wechselwirkungen und Unordnung im System zu allerlei dynamischen Phänomenen führen, sei es Thermalisierung, Vielteilchenlokalisierung, sowie chaotisches Verhalten. Im Bereich der Hochenergiephysik verbindet das holographische Prinzip Chaos in Quantenvielteilchensystemen mit den informationstheoretischen Eigenschaften schwarzer Löcher. Theoretische Quantenphysik bildet den Rahmen für die Modelle, Methoden und Ergebnisse dieser Dissertation, derweil die Physik schwarzer Löcher teils etwas Motivation und Inspiration bietet.

Zunächst führen wir, basierend auf zufälligen Quantenschaltungen, ein neues Modell für Quantenvielteilchensysteme ein. Zufällige Quantenschaltungen sind ein beliebtes Rahmenkonzept für die theoretische Erforschung von ungeordneten Spinketten. Indem die zufälligen unitären Abbildungen aus der Schaltung aus verschiedenen Ensembles gezogen werden, können wir die Unordnungsstärke der Wechselwirkungen anpassen. Das wiederum führt zu einem Phasenübergang zwischen thermischer und vielteilchenlokalisierter Phase.

Als nächstes untersuchen wir, motiviert von seiner Verbindung zum holographischen Prinzip, das Brown'sche SYK Modell, ein Modell ungeordneter Majoranafermionen mit Wechselwirkungen aller Teilchen. Wir entwickeln ein neues numerisches Verfahren, das auf einer effektiven Permutationsinvarianz beruht, um den Berechnungsaufwand von exponentiell auf linear oder quadratisch in der Teilchenzahl N zu verringern. Dadurch können wir Chaosindikatoren im Detail berechnen und finden eine Zeitabhängigkeit $\log N$ des Chaos, wie von der *fast scrambling conjecture* für schwarze Löcher vorausgesagt.

Schließlich schlagen wir ein Modell beruhend auf zufälligen Quantenschaltungen im kontinuierlichen zeitlichen Limit vor. Es dient als mikroskopisches Spielzeugmodell für die Verdampfung schwarzer Löcher. Mit einer Methode ähnlich zu der für das Brown'sche SYK Modell entwickelten können wir die informationstheoretischen Eigenschaften des verdampfenden schwarzen Lochs analysieren. Insbesondere folgen wir etablierten Protokollen für die Wiederherstellung von Information aus der Hawkingstrahlung. Wir finden eine Trennung der Zeitskalen für den Aufbau von Verschränkung und die Wiederherstellung von Information, verknüpft mit der intrinschen Dynamik des schwarzen Lochs ($\propto \log N$) und der Wechselwirkung mit der Umgebung ($\propto N$).

List of publications

Publications included in this thesis

[1] *Localization with random time-periodic quantum circuits*
Christoph Sünderhauf, David Pérez-García, David A. Huse, Norbert Schuch, and J. Ignacio Cirac
Physical Review B 98, 134204 (2018), arXiv: 1805.08487 (24 citations)
Editors' suggestion
Included in appendix A

[2] *Quantum chaos in the Brownian SYK model with large finite N: OTOCs and tripartite information*
Christoph Sünderhauf, Lorenzo Piroli, Xiao-Liang Qi, Norbert Schuch, J. Ignacio Cirac
Journal of High Energy Physics 2019 , 38 (2019), arXiv: 1908.00775 (11 citations)
Included in appendix B

[3] *A random unitary circuit model for black hole evaporation*
Lorenzo Piroli*, Christoph Sünderhauf*, Xiao-Liang Qi
Journal of High Energy Physics 2020, 63 (2020), arXiv: 2002.09236 (18 citations)
* contributed equally
Included in appendix C

Other publications

[4] *Classification of Matrix-Product Unitaries with Symmetries*
Zongping Gong, Christoph Sünderhauf, Norbert Schuch, J. Ignacio Cirac
Physical Review Letters 124, 100402 (2020), arXiv: 1812.09183 (10 citations)

[5] *Two-dimensional simulation of quantum reflection*
Emanuelle Galiffi, Christoph Sünderhauf, Maarten DeKieviet, Sandro Wimberger
Journal of Physics B 50, 095001 (2017), arXiv: 1712.09874 (2 citations)

[6] *Behavior of eigenvalues in a region of broken PT symmetry*
Carl M. Bender, Nima Hassanpour, Daniel W. Hook, Sandra P. Klevansky, Christoph Sünderhauf, Zichao Wen
Physical Review A 95, 052113 (2017), arXiv: 1702.03811 (5 citations)

Citation counts according to NASA/ADS database, February 2020.

Contents

Chapter 1

Introduction

In recent years, experimental progress allows unprecedented access to and control of interacting many-body quantum systems. For example, ultracold atoms in optical lattices allow the microscopic study of thermalisation or the absence thereof [7–9]. Within theoretical quantum physics, this greatly revived interest in genuine many-body phenomena mediated by interactions. Disorder in the system leads to phenomena such as thermalisation [10–13], many-body localisation [9, 14, 15], and related concepts of chaos and scrambling [16–18]. These dynamical properties are vital to anybody wishing to understand the behaviour of generic condensed matter systems.

Chaos in many-body quantum systems also received a strong and perhaps unexpected impulse from the study of black holes. As the holographic principle relating black holes to a dual quantum theory was was fleshed out [19–21], it became increasingly clear that chaotic properties of many-body quantum systems play a fundamental role for black holes. In fact, high energy physicists contribute to the study of quantum chaos to better their understanding of the black hole information paradox and other information theoretic properties of black holes [22–25]. It is exciting that quantum chaos in many-body systems is relevant to both many-body quantum physics as well as high-energy physics, and research activity is greatly enriched by this intersection of fields.

This thesis studies chaos in many-body quantum systems. While the systems, methods and results are quantum, for some of them the link to black hole physics is a source of inspiration and motivation. The first article [1] concerns many-body localisation in an interacting one-dimensional system. We study a new model based on random quantum circuits, a popular framework for disordered systems. By adjusting the strength of disorder, we can drive a phase transition between thermal and many-body localised phases. The next article [2] uses the OTOC and tripartite information as indicators of chaos and scrambling in many-body quantum systems. The quantum model whose chaotic properties are studied in detail (the Brownian SYK model) is motivated by the holographic principle, which links a gravitational space-time to a quantum system, and the fast scrambling conjecture for black holes. In this context, we learn valuable lessons about the dynamics and speed of scrambling. Our new numerical method allows access to vast numbers of particles up to $N = 10^6$, such that a $\log N$ dependence can be accurately extracted. Finally, in the

third article [3], we propose and study a model consisting of a continuous version of a random quantum circuit coupling a system to an environment. As it is supposed to be a microscopic toy model for black hole evaporation, we perform research on its information-theoretic properties. This includes information retrieval: After qubits were injected into the black hole, they can be recovered from Hawking radiation at some later time. In our model, we find a separation of time scales for entanglement growth and information retrieval, related to the intrinsic black hole dynamics $\propto \log N$ and the coupling to the environment $\propto N$.

A presentation of relevant background is in order. First, we focus on a topic of mathematical nature, namely random unitaries in chapter 2. Then, we move to physics. Core physical concepts are explained in chapter 3, ranging from rather general terms like entanglement entropies and thermalisation to introducing the the much more specialised OTOCs and tripartite information that appear when studying chaos and scrambling. Background on the study of disordered many-body quantum systems follows in chapter 4, covering many-body localisation as well as random circuits that are widely used to model disordered dynamics. Black hole physics contributes towards the motivation of two of the articles. A quantum physicist may not be familiar with these topics, yet it can be interesting to appreciate also these aspects. Therefore chapter 5 concludes the background chapters with an accessible conceptual introduction to information theoretic properties of black holes. Links to the more quantum topics of the thesis will be pointed out. Finally, the articles [1–3] are reproduced in appendices A, B, and C, along with a short summary each.

Original research

The physical background as well as mathematical tools presented in the chapters do not stand alone. Instead, they form the basis for the original research included in this thesis, which in turn contributes to the physical understanding presented. To make clear this connection, this box will occur in every section and highlight the link to different aspects of the articles [1–3].

Chapter 2

Random unitaries

Classical information can easily be drawn from a uniform random distribution, since the set of possible bitstrings of length n is finite. The same holds for classical operations, namely functions $f : \{0,1\}^n \to \{0,1\}^n$.

The notion of random quantum information is much more subtle. To define a uniform distribution over all quantum states of n qubits, we may try to invoke the classical analogy and randomly draw product states from the finite set $\{|0\ldots0\rangle, \ldots, |1\ldots1\rangle\}$. This procedure however misses out on important aspects of quantum information, never generating superpositions and entanglement. Quantum states form a continuum, and one must use a uniform continuous distribution that includes entangled states. The same complications arise for quantum operators, corresponding to unitary matrices, which form a continuous group. In this section, we define and study the *invariant Haar measure*, which provides an intuitive generalisation of the uniform distribution for the unitary group. Once the Haar measure is defined, the notion of random state can be made precise by applying a random unitary to a product state, $U|0\ldots0\rangle$.

Apart from the unitary Haar ensemble, there are further random matrix ensembles. In physics, random matrices were introduced in the 1950s to model neutron resonances [26]. Since a lot of very complicated interactions of many constituent particles appear in the nucleus of heavy elements, they can be viewed as a disordered system with a random Hamiltonian. Thus, nuclear physicists study the statistical properties of suitable random matrix ensembles. In fact, there is remarkable consistency between the spacing of experimentally determined energy levels and the eigenvalues of random matrices. Random matrix theory since evolved into an established branch of physics, see for example the standard book [26].

Recently, random unitary matrices are used to model disordered unitary dynamics of a quantum system. Haar random unitaries can either be used directly as the time evolution operator for the entire system [27], or they can be used as buildings blocks to build a random circuit stepping in as the time evolution operator [16, 17, 28], introducing some kind of local structure (see section 4.2 for details).

In the next section 2.1, the Haar measure will be defined. Then, methods to compute averages with respect to the Haar measure both analytically (section 2.2) and numerically (section 2.3) will be presented.

Original research

Haar-distributed random unitaries form the basis of different unitary ensembles used in [1] to couple two spins. Specifically, the random ensembles characterised by a coupling strength h are defined by

$$(u_1 \otimes u_2) e^{ia\,\sigma_x \otimes \sigma_x + ib\,\sigma_y \otimes \sigma_y + ic\,\sigma_z \otimes \sigma_z} (u_3 \otimes u_4), \tag{2.1}$$

where $u_1, u_2, u_3, u_4 \in U(2)$ are distributed according to the Haar measure, and $a, b, c \in [-h, h]$ uniform. Adjusting the parameter h unveils an MBL phase transition (see section 4.1).

Global Haar unitaries are maximally scrambling and provide a theoretical upper bound. The Haar measure thus serves as a benchmark for the scrambling power of the Brownian SYK model in [2].

Finally, in [3], unitary matrices are used for the intrinsic interaction within a system. They form a random circuit, whose continuous time limit is a toy model of an evaporating black hole for the purpose of information-theoretic study.

2.1 The invariant Haar measure

We are mostly interested in the unitary group, but the beautiful idea underlying the Haar measure is more widely applicable to groups in general. For ease of presentation, we focus on the integral rather than measuring subsets. Translational invariance is a basic feature of conventional integration

$$\int_{\mathbb{R}} f(x)dx = \int_{\mathbb{R}} f(x+a)dx \;\forall a \in \mathbb{R} \tag{2.2}$$

and encompasses the essence of uniformity: Each number $x \in \mathbb{R}$ is treated on equal footing to every other number $x + a \in \mathbb{R}$, there is no special origin. The Haar measure generalises this idea to *right-invariance* of locally compact groups G:

$$\int_G f(g)dg = \int_G f(ga)dg \;\forall a \in G. \tag{2.3}$$

The Haar theorem [29] shows that, up to global scaling and some regularity conditions, there exists a single unique measure satisfying this condition of right invariance. As the group operation (here written as a multiplication) need not be commutative, there is in general a second and distinct *left-invariant* Haar measure. For abelian or compact groups, the left and right invariant measures can be shown to coincide. The Haar theorem goes back to A. Haar in 1933 [30], and a version for Lie groups dates even earlier to A. Hurwitz in 1897 [31].

The unitary group $U(d)$ is compact, such that there is a single both left- and right-invariant Haar measure. Morever, it has finite total volume such that the Haar integral can be normalised, giving a probability density for the unitary group. The beautiful simplicity of the Haar measure's definition shows that this is indeed a "uniform" distribution, where any two unitaries U and $V = UA$ are treated the same by the Haar measure, for all $U, V \in U(d)$. Applied to random states, we see that any two states $|\psi\rangle = U|0\rangle$ and $|\phi\rangle = V|0\rangle$ are treated on equal footing. In random matrix theory [26], the invariant Haar measure on $U(d)$ is also called CUE (circular unitary ensemble), where circular refers to the uniform eigenvalue density on the unit circle.

To calculate the expectation value of a function $f(U)$ on the unitary group, we must perform the integration (2.3). The first method coming to mind may be a parametrisation of the unitary group with several angles, and subsequent transformation of the integral in terms of these angles. This can be done [31–33] and leads to myriads of trigonometric functions in the integrand and very hard integrals. An alternative approach solves the Haar integral algebraically for polynomials $f(U)$. In the next section 2.2, we will explain this algebraic method. In the age of computers, numerical sampling of Haar random unitaries is a viable method to approximate the distribution. We visit this in section 2.3.

Original research

Haar invariance underlies the twirling technique developed in [1]. It exploits that the distribution of random unitaries used in the model possesses single site Haar invariance, where a in (2.3) is a tensor product of identities at all but one site. The twirling technique allows us to make statements closely connecting the initial and final state of a time evolution. Thus, we can study localization rather directly (see section 4.1).

2.2 Computing integrals with Weingarten functions

An important result for Haar random unitaries is the integral [34–36]

$$\int_{U(d)} U_{i_1 j_1} \cdots U_{i_n j_n} U^*_{i'_1 j'_1} \cdots U^*_{i'_n j'_n} dU = \sum_{\sigma,\tau \in S_n} \mathrm{Wg}(d,\sigma,\tau)\, \delta_{i_1 i'_{\sigma(1)}} \cdots \delta_{i_n i'_{\sigma(n)}}\, \delta_{j_1 j'_{\tau(1)}} \cdots \delta_{j_n j'_{\tau(n)}}. \tag{2.4}$$

This allows to expand and compute the integral of any polynomial function $f(U)$. If the number of factors n of U and U^* were not the same, the integral would vanish, as can be seen by exploiting Haar invariance (2.3) with $a = e^{i\phi}\mathbb{1}$. The coefficients Wg are called Weingarten functions. They depend only on the conjugacy class of the permutation $\sigma\tau^{-1}$, and are the matrix inverse of the $d! \times d!$ matrix

$$\mathrm{Wg}(d,\sigma,\tau) = \left(d^{\#(\sigma\tau^{-1})}\right)^{-1}, \tag{2.5}$$

where # denotes the number of cycles in the permutation. The expansion (2.4) can be proved with tools from representation theory, including Schur-Weyl duality that relates irreducible representations of the symmetric and unitary groups. This procedure also yields a group-theoretic formula in terms of characters, partitions, and Schur polynomials for Wg, in addition to (2.5).

For practical usage of (2.4), the Weingarten functions can be looked up in tables (cf. [34]). Here we print the Weingarten functions for $n \leq 2$ factors, in terms of the cycle structure of $\sigma\tau^{-1}$:

$$n = 1: \ \mathrm{Wg}(d, (1)) = \frac{1}{d}, \qquad n = 2: \ \mathrm{Wg}(d, (2)) = \frac{1}{d^2 - 1}, \ \mathrm{Wg}(d, (1)(1)) = -\frac{1}{d(d^2 - 1)}. \tag{2.6}$$

To facilitate the application of (2.4), a graphical calculus [37, 38] was developed. It is very useful if the integrand is drawn as a tensor network containing the random matrix U.

A fundamental issue of the Weingarten calculus is the superexponentiality: The sum in (2.4) contains $(n!)^2$ terms. For small n and arbitrary matrix dimension d, it can still be performed explicitly. For large matrix size $d \gg 1$, asymptotic formulas for the Weingarten functions have been developed [34, 39]. These can lead to many terms in the sum (2.4) being subleading and negligible.

Original research

To study the random circuit model for an evaporating black hole developed in [3], Haar integrals of up to $n = 2$ have to be evaluated. Thanks to the Weingarten formalism, this is easily possible.

The random unitary circuit (see also section 4.2) used in [1] features random unitaries of fixed matrix size $d = 4$, that reappear at each timestep. Therefore n is large for late-time behaviour. Direct application of the Weingarten formalism is impossible since the integrals lie in the regime of superexponentiality. Instead, we develop a trick, the twirling technique, based directly on Haar invariance.

2.3 Sampling with the QR decomposition

In the age of computers, it is a very natural idea to sample random unitary matrices numerically. Expectation values can likewise be computed numerically.

A simple and standard way to sample a random Haar-distributed unitary matrix makes use of the QR-decomposition (see [40, 41]). The QR-decomposition is a standard matrix decomposition [42] and is available in many software packages such as Matlab and Scipy. It decomposes a (complex) matrix M into the product $M = QR$ of a unitary matrix Q and an upper triangular matrix R. Furthermore, if M is invertible, the decomposition is unique once the signs of the real diagonal entries of R have been chosen.

To generate a random Haar unitary, we start with a random matrix M with all real and imaginary parts of each matrix element independently normally distributed. Then, the Q from the unique QR decomposition is a Haar distributed unitary. This is because the joint probability density $p(M)$ of all of M's matrix elements is invariant under unitary multiplication:

$$p(M) \sim e^{\sum_{i,j} |M_{ij}|^2} = e^{\mathrm{tr}\, MM^\dagger} = e^{\mathrm{tr}(UM)(UM)^\dagger} \sim p(UM) \quad \forall U \in U(d) \tag{2.7}$$

Since the QR decomposition is unique, the invariance of $p(M)$ under unitary left-multiplication carries over to the generated Q. Invariance is the unique definition of the Haar measure, such that Q must be distributed accordingly.

When implementing the procedure outlined above, a possible caveat is that popular implementations of the QR decomposition do not perform it in a unique fashion, and the signs of the diagonal entries of R must be adjusted manually. For example, in Matlab, the following code can be used to create a Haar-distributed unitary Q:

```
d = 4;
M = randn(d) + j*randn(d);
[Q, R] = qr(M);
Q = Q*diag(sign(diag(R)));
```

Let us remark that in order to generate a Haar random state, it is not necessary to generate a full random unitary and take a column, or apply it to any other reference state. Instead, the real and imaginary parts of the random state's coefficients may be independently drawn from a normal distribution, and the state subsequently normalised [43]. This results in the same random state distribution.

Original research

The above code to generate a Haar random matrix is employed in [1]. After applying the twirling technique based on single-site Haar invariance, one parameter determining the time evolution remains. It must be found numerically. For this, the problem is simplified, shedding a factor exponential in time from the total Hilbert space dimension necessary for the circuit. Then random unitary matrices are sampled with the help of the QR decomposition. In order to improve the sampling and reduce the variance, a Monte-Carlo Metropolis method is used.

Chapter 3

Core concepts in many-body quantum physics

This chapter introduces a number of core concepts in many-body quantum physics related to topics of chaos and scrambling. We start with rather general introductions to entanglement (section 3.1) and thermalisation (section 3.2). Then, we move to more specialised topics, and present two main quantifiers of chaos and scrambling, namely out-of-time ordered correlation functions (OTOCs) in section 3.3, and the tripartite information in section 3.4.

3.1 Entanglement and entanglement entropies

Entanglement is perhaps the most quintessential quantum phenomenon. In the classical everyday world, it cannot be experienced directly. As such, it can seem very elusive and strange. Indeed, even for physicists: When Einstein, Podolsky, and Rosen published their famous thought experiment on entangled particles very far away from each other [44], even Einstein himself referred to entanglement's consequences as *spukhafte Fernwirkung* (spooky action at a distance) [45]. Later, Bell's theorem [46] paved the way to a number of experiments, most notably the recent loophole-free Big Bell test [47]. Bell test experiments probe for strong correlations obtainable with entanglement, yet impossible to achieve with local classical systems. The consequence is striking: Entanglement cannot be explained by any local hidden variable theory. Instead, entanglement is a physical concept here to stay and a pillarstone of quantum physics. It is relevant and important to understand nature and opens up new possibilities to process quantum information and for emerging technical applications such as quantum computers or quantum communication. For all of the concepts introduced in this thesis, entanglement is a crucial ingredient. Even mathematically, entanglement is a difficult concept. While there is a hierarchy for two-body entanglement, classification of multi-body entanglement between three or more parties is still an open question [48].

In the physics of many-body quantum systems, entanglement is the origin of the di-

mensionality curse. The state space needed to fully describe a system grows exponentially with the number of particles. The dimension of the Hilbert space of N particles with d-dimensional state space each is d^N, as the composite Hilbert space is the N-fold tensor product of $\mathbb{C}^d$. The dimensionality curse prohibits numerical investigations of many-body quantum systems for more than just a very small number of particles. For larger systems, numerical analysis relies on clever methods to handle this, for example density functional theory [49], quasiparticle pictures [49] or tensor network methods including DMRG [50]. All of these methods are approximate, restricting the amount of entanglement included in computations.

A particularly simple way to assess entanglement of a many-body system, described by a density matrix ρ, is to bipartition the system into two parts A and B, and consider only the two-body entanglement between these two parts. The subsystem A is described by the reduced state

$$\rho_A = \mathrm{tr}_B\, \rho, \tag{3.1}$$

tracing out the other degrees of freedom. If a pure state ρ is entangled, then the reduced state will be mixed. The eigenvalues of ρ_A, also called entanglement spectrum, determine the entanglement between A and B. Convenient measures for entanglement are the Rényi entanglement entropies

$$S_A^{(\alpha)} = \frac{1}{1-\alpha} \log \mathrm{tr}(\rho_A^\alpha). \tag{3.2}$$

The limit $\alpha \to 1$ gives the von Neumann entanglement entropy

$$S_A = -\,\mathrm{tr}(\rho_A \log \rho_A). \tag{3.3}$$

Numerically, it is often easier to deal with the exponentials of Rényi entropies with integer α (see section 4.2), due to the lack of logarithm. However, the von Neumann entanglement entropy mimics classical Shannon and thermodynamic entropy more closely and has a stronger information-theoretic meaning. For example, in quantum information theory, the von Neumann entropy often appears when characterising capacities of quantum channels [48].

Entanglement entropy is excellent for pure states. Pure states have $\mathrm{tr}\,\rho = \mathrm{tr}\,\rho^2 = 1$, and all correlations between the particles stems from entanglement. Two maximally entangled systems A and B each of dimension d will have entanglement entropy $S_A = S_B = \log d$. Conversely, for an unentangled product state, $S_A = S_B = 0$. When A and B are composite systems of qubits, it can be useful to use logarithms base 2, such that the entanglement entropy counts the number of maximally entangled qubit subsystems. In contrast, mixed states ($\mathrm{tr}\,\rho^2 < 1$) contain classical correlations, along with any entanglement. Then, mutual information

$$I(A:B) = S_A + S_B - S_{AB} \tag{3.4}$$

is a good measure to quantify the amount of information shared between the systems A and B, both classical and quantum correlations [51].

Original research

Entanglement plays a central role in all of the articles [1–3], and we compute entanglement entropies in all of them. In [1], we compute the entanglement entropy of eigenvectors of the time evolution operator. This is a diagnostic of a many-body localisation phase transition, see section 4.1. To characterise scrambling in the Brownian SYK model (see section 5.3 for an introduction to the SYK model), in [2] we compute entanglement entropies, mutual information, as well as tripartite information (see section 3.4). Finally, in [3], we calculate entanglement entropies and mutual information related to the action of the time evolution operator. With this, we can determine how information thrown into the system (a model for a black hole) can be later retrieved (see also section 5.2).

Since it is always multi-particle systems under investigation, the dimensionality curse of entanglement affects all of the work. Therefore, in [1], we can only compute the von Neumann entanglement entropy for a spin chain of 12 particles. (Further understanding beyond numerical calculation of entanglement entropy is gained by the Haar measure, see chapter 2.) In the other articles, we bypass the dimensionality curse by considering systems that become effectively permutation invariant after considering a disorder average (see chapter 4 for an introduction to disordered systems). The permutational invariance strongly restricts the possible states in the Hilbert space and allows us to work in an effectively polynomial rather than exponential space. Instead of the von Neumann entropy, we compute the Rényi-2 entropy, and Rényi-2 version of mutual information, which is better accessible with our approach.

3.2 Thermalisation of closed systems

At first sight, it may seem surprising that closed quantum systems can thermalise. After all, the Schrödinger equation always evolves an initially pure state into pure states, thus prohibiting the development of a thermal mixture. The idea behind thermalisation in closed systems is to consider reduced systems, i.e. observables that are local and act only on limited subsystems. Thermalisation is then closely linked to entanglement: As entanglement builds up, the reduced density matrix of each subsystem becomes mixed. Thus, subsystems can become thermal, and the rest of the system acts as a bath [11–13].

Progressive build-up of entanglement between the subsystem A and B (with B now acting as environment/bath) will typically lead to a mixed state of ρ_A, approaching the Gibbs ensemble

$$\rho_A \sim \mathrm{tr}_B(e^{\beta H}). \tag{3.5}$$

The Gibbs ensemble is the thermal mixed state of the system. It depends on the values

of conserved quantities, which cannot change upon evolution from the initial state and must therefore be present in any thermal state. In the above equation, this is the time-independent Hamiltonian H (energy conservation), which fixes inverse temperature $\beta = \frac{1}{k_B T}$. If the system has further conserved quantities, such as particle number or parity, the equilibrium ensemble reached is called generalised Gibbs ensemble with the further conserved quantities appearing in the exponent [10]. If there are no conserved quantities, not even energy, the notion of a finite temperature does not exist. Instead, the infinite-temperature thermal state is simply

$$\rho_A \approx \mathbb{1}_A / \dim(A), \tag{3.6}$$

the maximally mixed state, which is the only fixed point of the system.

Integrable systems (i.e. with an extensive number of local conserved quantities) are too constrained to thermalise, yet are still expected to reach the equilibrium state given by the generalised Gibbs ensemble [10, 12]. On the other hand, generic non-integrable systems will build up entanglement and thermalise. There is abundant evidence and explanation, for example the eigenstate thermalisation hypothesis [11, 52, 53]. Regardless, the system may still escape thermalisation. This (surprising) absence of thermalisation in interacting many-body systems is called many-body localisation, see section 4.1.

Original research

In [1], we study single site reduced density matrices, after evolution with a random unitary circuit (see also section 4.2). Since the circuit does not preserve energy, the corresponding thermal state is of infinite temperature. However, depending on the strength of interactions, we can show that single sites either become thermalised, or retain information about the initial state. This absence of thermalisation is an example of many-body localisation (see section 4.1).

For the Brownian SYK model in [2], we study OTOCs as identifiers of quantum chaos (see the next section 3.3). The system thermalises to an infinite temperature state, and when calculating OTOCs, we take correlation functions with respect to this infinite temperature state.

3.3 Chaos and out-of-time-ordered correlators (OTOCs)

OTOCs (out-of-time-ordered correlation functions) are an excellent quantifier for quantum chaos and operator spreading. While they were originally introduced in the study of disordered superconductors [54], they are now widely used in many-body physics [55]. For example, studies of random circuits often focus on OTOCs, see section 4.2.

In order to motivate the intimate link to quantum chaos, let us first consider classical chaos [18]. In classical physics, chaos is defined as exponential dependence of a system's

path on the initial condition. Only very slightly different setups will give rise to vastly different time evolutions, i.e. the system is chaotic. This is also termed the butterfly effect, as a small perturbation such as a butterfly flapping its wings will later lead to vast differences in the system. The Hamiltonian formulation of classical mechanics relies on the Poisson bracket. For a chaotic system with canonical coordinates q and p, this exponential dependence on the initial state $q(0)$ can be written as

$$\{q(t), p(0)\} = \frac{dq(t)}{dq(0)} \simeq e^{\lambda t} \tag{3.7}$$

with the Lyapunov exponent λ. A positive Lyapunov exponent is indicative of chaotic dynamics.

In the quantum-classical correspondence, Poisson brackets $i\{\cdot,\cdot\}$ are replaced with the commutator $[\cdot,\cdot]$. Rather than position and momentum operators, we consider the commutator of any observables O, O' in the Heisenberg picture:

$$C(t) = \frac{1}{2}\,\mathrm{tr}\left(\rho[O(t), O'(0)]^\dagger[O(t), O'(0)]\right). \tag{3.8}$$

As in the classical equation (3.7), one of the the operators is evolved in time while the other is fixed at time 0. The commutator $C(t)$ can be understood intuitively for local operators in a picture of operator growth, see Fig. 3.1. If we consider two local operators acting on different parts of the system, they will initially commute, $C(0) = 0$. Time evolution will grow the support of $O(t)$, such that the magnitude of the commutator increases $C(t) > 0$, indicative of operator spreading. If operators would not not follow chaotic evolution (but correspond to particles moving across the system ballistically, for example), then the commutator would not increase as the support does not spread. In contrast to the classical case, quantum observables are bounded operators such that $C(t)$ cannot grow indefinitely, although in chaotic systems they do have a time window of exponential growth.

The OTOC is defined as

$$\mathcal{F}_{O,O'}(t) = \mathrm{tr}\left\{\rho O(t)O'(0)O(t)O'(0)\right\}. \tag{3.9}$$

Its name out-of-time ordered correlator stems from the fact that in this correlation function, the operators do not appear ordered in time but rather $t \to 0 \to t \to 0$. To establish the connection between operator growth and the OTOC, the commutators in (3.8) can be expanded. Apart from usual time-ordered correlation functions, the OTOC is an important prominent part in $C(t)$.

Since the OTOC is a correlation function, it can depend on the choice of state ρ. Typically, a thermal Gibbs ensemble

$$\rho_\beta = \frac{e^{-\beta H}}{\mathrm{tr}(e^{-\beta H})} \tag{3.10}$$

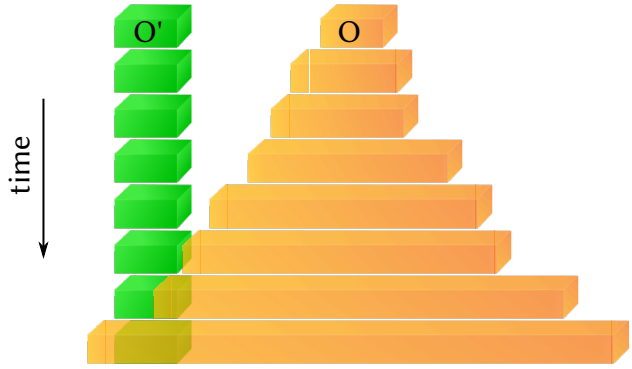

Figure 3.1: Illustration of operator growth. At time $t = 0$, the local operators act on different parts of the system and commute. As $O(t)$ is evolved in time, its support grows and it eventually stops commuting with O'. This behaviour is quantified with the OTOC commutator (3.8).

can be used, see section 3.2. In chaotic systems, the commutator $C(t)$ will exhibit initial exponential growth before it saturates. As in classical chaos, this exponential growth can be characterised by a Lyapunov exponent λ; at small times:

$$C(t) \simeq \epsilon e^{\lambda t}. \tag{3.11}$$

While ϵ depends on the system [55], there is an upper bound for the Lyapunov exponent, [18, 56, 57]

$$\lambda \leq \frac{2\pi}{\beta}, \tag{3.12}$$

which is expected to be saturated for black holes, part of the fast scrambling conjecture (see also section 5.1). In local systems, OTOCs typically spread (decay) ballistically (i.e. in a time proportional to t) with a speed called the butterfly velocity v_B. See section 4.2 for studies of quantum circuits and more discussion on the behaviour of OTOCs.

Original research

When working with fermionic systems and operators, $C(t)$ can analogously be defined with anti-commutators rather than commutators to motivate the OTOC. This is the situation in our work [2] on the Brownian SYK model, which is based on Majorana fermions (see section 5.3).

In this model, we develop a toolbox based on emergent permutational symmetry to study the OTOC numerically with very high efficiency. This allows us to access a very large number of particles N, up to one million Majorana fermions. Thanks to this, we can find the dependence of the scrambling time $t^* = 3/4 \log N$ needed for OTOCs to decay; the fast onset of chaotic behaviour is important in the context of holography and the fast scrambling conjecture, see chapter 5. With a scaling collapse for system size, we can

identify the Lyapunov exponent.

Since the model features all-to-all interactions, there is no spacial dependence of the OTOC, and it only depends on time and initial operator choice. Surprisingly we find, that its late time behaviour only depends on the length of operators.

3.4 Scrambling and the tripartite information

Scrambling refers to the scrambling of quantum information across the system. This means that it cannot not be recovered by means of any local measurements. The concept of scrambling is closely related to chaos (see the previous section). In 2016, Hosur et al suggested a new measure for quantum scrambling, the tripartite information [58]. It quantifies the scrambling power of a quantum channel. Here we consider a unitary operation, whose input is split into two regions A and B, and output split into two regions C and D, c.f. Fig. 3.2. The tripartite information is then defined as

$$I_3 = I(A:C) + I(A:D) - I(A:CD). \tag{3.13}$$

Mutual information $I(X:Y)$ (see section 3.1) is defined through the von Neumann entanglement entropies:

$$I(X:Y) = S_X + S_Y - S_{XY}, \;\; S_X = -\operatorname{tr}(\rho_X \log \rho_X). \tag{3.14}$$

The meaning of the tripartite information (3.13) is illustrated in Fig. 3.2.

Even from the defining formula (3.13), we see that the tripartite information is minus the information of A that can only be learnt by joint measurement of CD. The more negative the tripartite information is, the more the unitary scrambles any information, and it becomes hidden in nonlocal correlations (entanglement) in the output.

Oftentimes, it is simpler to use the Rényi-2 tripartite information, as the Rényi-2 entropy $S_X^{(2)} = -\log \operatorname{tr}(\rho_X^2)$ can be more amenable to analytic as well as numeric considerations than the more information theoretic von Neumann entropy. A maximally scrambling channel can be modelled by a Haar random unitary (see chapter 2). In this case, by virtue of the Weingarten calculus, the average and thereby typical Rényi-2 tripartite information can be computed exactly [58]. This can be seen as a lower bound for tripartite information, that will be approached if the system in question is an excellent scrambler.

As mentioned in the beginning of this section, scrambling is very intimately related to chaos. In fact, it was shown [58] that the butterfly effect (quantum chaos) implies scrambling. An expression involving the average of all OTOCs from a basis of observables is an upper bound for the tripartite information.

Finally, let us emphasise that scrambling as captured by the tripartite information and chaos as captured by OTOCs go above and beyond thermalisation and entanglement growth. A typical picture for entanglement growth in Gaussian models (free fermions) is that of quasiparticles [59, 60]. While they spread ballistically and generate entanglement

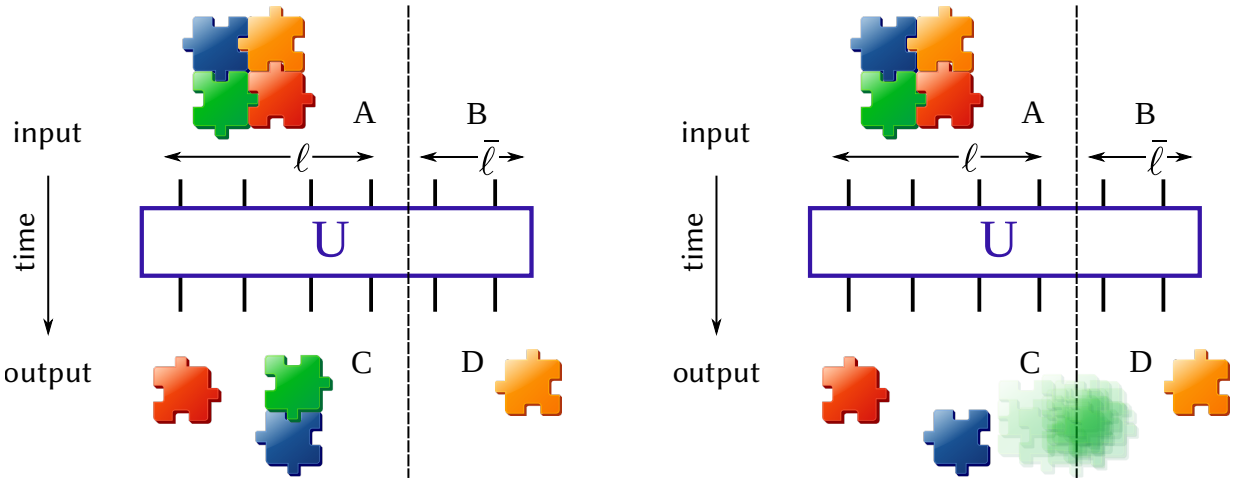

Figure 3.2: Scrambling of quantum information, as measured by the tripartite information. Left: classical situation. The unitary scrambles classical information. By separately measuring regions C and D, all initial information in A can be recovered. Right: quantum situation. The unitary can spread some information into the entanglement between regions C and D, such that this information cannot be recovered by separate independent measurements of C and D. The negativity of the tripartite information (3.13) quantifies how much information is hidden in the entanglement between C and D, i.e. the green jigsaw piece.

throughout the system, they do not scramble information. One need just measure the small subsystem of where the two quasiparticles are located to recover information about them.

Original research

A direct relation between the Rényi-2 tripartite information and averages of OTOCs of all operators was found for bosons in [58], while we extended this relation to fermions in [2].

With a similar technique used to calculate OTOCs, we can make use of an emergent permutational symmetry in the Brownian SYK model [2] to study various Rényi-2 entanglement entropies, and thereby, the Rényi-2 mutual information. While they undergo non-trivial dynamics at early times, we recover the maximally scrambling Haar values at late times. Thus we show that the Brownian SYK model indeed shows strong scrambling of quantum information. This is important in the context of SYK as a holographic model (see chapter 5).

The integrable Gaussian version of the Brownian SYK model (appendix A in [2]) contains disordered 2-body rather than 4-body interactions. While entanglement does grow, as an integrable system it does not display chaos

or scrambling dynamics; we check this by computing OTOCs and tripartite information. It is thus an example showing that chaos and scrambling goes beyond mere entanglement growth.

Chapter 4

Dynamics of disordered many-body quantum systems

Randomness is inherent to disordered many-body quantum systems: The Hamiltonian or the time evolution operator contains disorder and random components. In this chapter, we first present a possible dynamical property of disordered systems: Typically, disordered systems are expected to be chaotic and thermalise. Even for interacting systems, this can be avoided and is dubbed many-body localisation (MBL), which we introduce in section 4.1. Then, we present a method to create models for disordered systems. Random quantum circuits allow to construct many useful models to study the dynamics of disordered many-body quantum systems, these are covered in section 4.2.

4.1 Many-body localisation (MBL)

Localisation for single-particle systems has been known for a long time, since 1958, and is called Anderson localisation after its discoverer [61–64]. Anderson localisation relies on disorder in the system: A particle hops in a disordered potential (that is, constant in time but random in space). If the disorder is strong enough, eigenstates will be localised in space, with exponential tails. This means that the probability to find the particle at a position other than its initial placement is exponentially suppressed. In one dimension, the statement is even stronger—localisation holds for arbitrarily low disorder. A bizzare analogy displaying the power of this statement is the following: Apart from the necessary one-dimensionality, a quantum plane flying over Europe would get stuck in the Alps, even if it sours hundreds of kilometers above.

The analogous phenomenon for interacting many-body systems is called many-body localisation (MBL), see [9] for a recent review of this topic. It is a surprising phenomenon: Unless the Hamiltonian is integrable (i.e. has an extensive number of conserved quantities), it was found that thermalisation is quite ubiquitous. General explanations for thermalisation were developed, such as the eigenstate thermalisation hypothesis [52, 53]. See section 3.2 for details on thermalisation. Due to this preponderance supporting thermali-

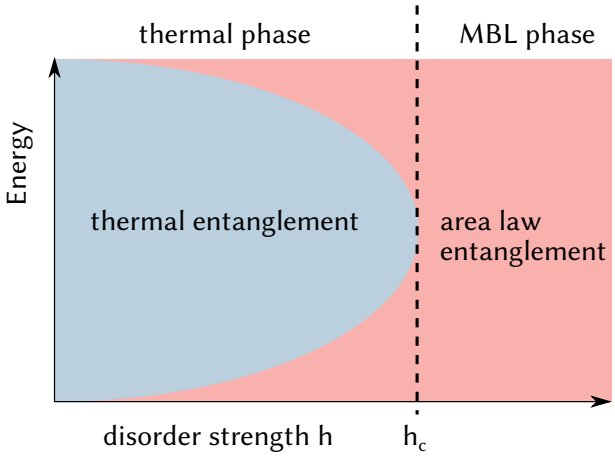

Figure 4.1: Schematic view of the MBL transition and MBL mobility edge. In the MBL phase, all eigenstates at every energy are localised and display low area law entanglement, independent of system size for 1D (red). As the disorder parameter h moves below the critical value h_c, eigenstates near the middle of the spectrum become thermal and highly volume-law entangled (blue). Deep in the thermal phase, all eigenstates are thermal, except for those at the very bottom and top of the spectrum.

sation very generally [11], one would not expect localisation in seemingly chaotic interacting systems. Yet, there exists experimental evidence of MBL [7, 8].

As in single-particle Anderson localisation, MBL is contingent on disorder, the stronger the better. By varying the disorder strength in a Hamiltonian, a thermal/MBL phase transition can be induced. The prototypical MBL Hamiltonian for one dimension is the XXX Heisenberg chain for a chain of spin 1/2 particles [14]

$$H = \sum_i J(S_i^x S_{i+1}^x + S_i^y S_{i+1}^y + S_i^z S_{i+1}^z) + h_i S_i^z. \tag{4.1}$$

In this model, the local magnetic fields h_i are disordered and drawn uniformly and independently from the interval $h_i \in [-h, h]$. Above the critical disorder strength $h > h_c \sim 3.5$ (for $J = 1$), the system ceases to be thermal and becomes many-body localised. Before we move on to general properties of MBL eigenstates, a quick note about the nomenclature of the XXX chain: The three X refer to the coupling constant J, which couples the x, y and z spins alike. Physicists also study models with coupling constants $J_x = J_y \neq J_z$, which is called XXZ chain. The case $J_x \neq J_y \neq J_z$ is accordingly referred to as XYZ chain.

The two dynamical phases in MBL systems have vastly different consequences for the entanglement of the Hamiltonian's eigenstates. This so-called MBL mobility edge [15] is summarised in Fig. 4.1. Deep in the thermal phase, all eigenstates are thermal states. In order for reduced density matrices to resemble the thermal Gibb's ensemble, they must have very high volume law entanglement, growing linearly with system size. In the MBL phase however, all eigenstates are lowly entangled. Entanglement does not grow with system size in 1D. This is because in the MBL phase, an extensive number of quasi-local

integrals of motions (conserved quantities) emerge. These correspond to local operators, with exponentially small tails. Thus, in an MBL system, all eigenstates have the same entanglement properties as the ground state. There is not enough entanglement for subsystems to look thermal; MBL thereby impedes thermalisation. See section 3.2 for more on thermal states and entanglement.

Even across the phase transition, lowly entangled eigenstates persist, as sketched in Fig. 4.1. In fact, the ground state of a gapped local Hamiltonian will have area law entanglement throughout. The entanglement properties along a cut through the system can be used as a diagnostic for the MBL transition point [65]. The average entanglement entropy across the spectrum is a first crude indicator, as it will rise as the system enters the thermal phase. As found in the letter cited above, the variance of the entanglement entropy across the spectrum is a better indicator. Near the transition point, it will have a distinct peak, because both thermal and area-law entangled eigenstates are present. Deep in either phase, the variance will vanish because (almost) all eigenstates display the same entanglement properties.

When studying MBL, Floquet systems proved useful [66, 67]. A Floquet system refers to a time-periodic Hamiltonian $H(t) = H(t+T)$. These types of systems can be bar of any conserved quantity, as even energy is not conserved. Prototypically, a Floquet system can be engineered by adding a periodic driving force to an otherwise time-independent Hamiltonian. Integrating the Hamiltonian over one period then gives the Floquet unitary

$$U_F = \int_0^T H(t)dt \tag{4.2}$$

that determines the stroboscopic evolution at times $nT, n \in \mathbb{N}$. The driving force can be thought to inject energy into the system, which is therefore expected to thermalise to the infinite temperature Gibb's ensemble. This is the relevant thermal ensemble for a system without any conservation laws. However it was found that adding driving to an MBL Hamiltonian can result in a Floquet system that stays MBL and avoids thermalisation. In fact, the thermal/MBL transition can be made more abrupt by adding a driving force [68].

A main open question concerns the microscopic details of the MBL transition. Another question concerns the role of disorder. It asks, whether spatial disorder is strictly necessary, or whether localisation can persist in translational invariant systems. It is thought that translational invariance will eventually lead to thermalisation [9].

Original research

In [1], we consider a unitary Floquet model, where the Floquet unitary U_F is made up of a random unitary circuit (see section 4.2 for more about unitary circuits). Rather than varying the disordered potential's strength, complementarily we vary the coupling strength. This is done by choosing different random ensembles for the random unitaries. Thereby, we can drive a thermal/MBL phase transition.

We can make rather direct statements about the evolved state and lo-

calisation in terms of reduced density matrices thanks to the Haar measure (see chapter 2 for more about the Haar measure). Specifically, we compute how close individual sites become to the maximally mixed infinite temperature state. The model is thereby a rare occurrence in MBL studies, which often rely on exact diagonalisation. Additionally, we apply the diagnostic of the MBL mobility edge, using the eigenvectors' entanglement, to further pin-point the critical coupling strength.

On top of unitary Floquet evolution, [1] also considers Floquet evolution with Gaussian operations. Then, both inhomogeneous and homogeneous (translational-invariant) evolutions can be considered. While inhomogeneous evolution displays localisation, a random homogeneous evolution operator delocalises the initial state. This gives further evidence that MBL cannot exist without spatial disorder.

4.2 Random unitary circuits—a formidable model for disordered dynamics

Unitary circuits (also called quantum circuits) are well known from the usual model of circuit-based quantum computation [48]. A set of unitary gates act on a number of qubits (or more generally, higher dimensional qudits). Graphically, a circuit can be conveniently represented as in Fig. 4.2. For random quantum circuits, the gates are drawn from an ensemble of unitaries, such as the Haar measure. There are several factors characterising random circuits. First is the spacial dimensionality. For simplicity, usually one-dimensional circuits acting on spin chains are considered. Dimensionality is only relevant for local circuits where gates act on adjacent qubits only. In non-local circuits, gates can act on arbitrary groups of (possibly far-away) spins. Second, is the geometric structure of the circuit. Many examples consider regular brickwork-pattern circuits (as in Fig. 4.2), but sometimes even the geometry and placement of gates are random. Third, the specific gate content in the circuit. The exact measure for the gates (for example, the Haar measure, see chapter 2), and any independence or interdependence of gates are important ingredients.

The Haar measure is intricately linked with random circuits. On the one hand, the unitary Haar measure is often employed as the defining element of the constituent gates. On the other hand, deep random circuits, viewed as a black box, resemble a single big random Haar unitary [69, 70]. This notion of convergence to the Haar measure can be made more precise with unitary t-designs. A unitary t-design is a unitary measure, whose first t moments are identical to the Haar measure. For polynomials up to degree t of random unitaries, a t-design is indistinguishable from the Haar measure. It was proven [69] that t-designs can be well approximated by random quantum circuits with sufficient depth dependent on t and the number of qubits. In line with this link, techniques from random matrix theory [26], such as the spectral form factor or eigenvalue spacing are sometimes also used in studies of unitary circuits.

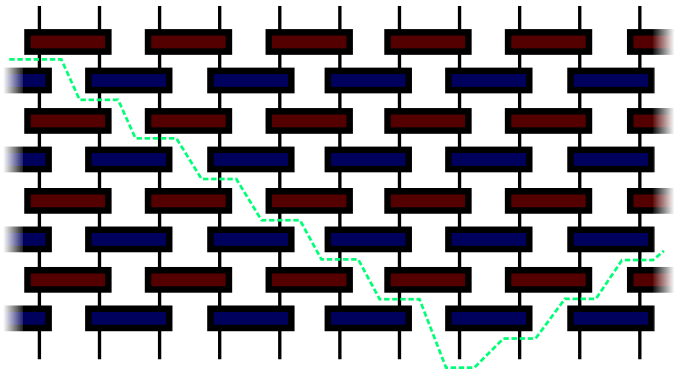

Figure 4.2: Sketch of a unitary circuit. Vertical lines represent qubits. Each box represents a unitary operator, in this case a gate acting on two qubits. Time flows from bottom to top in these types of sketches. In a random circuit, the gates would be chosen from a random ensemble. This one-dimensional unitary circuit is local, since gates only couple adjacent qubits. Further, this example possesses a regular brickwork structure. The green dashed line indicates the lightcone of one site, showing which qubits the site can affect.

In the study of interacting disordered many-body systems, random unitary circuits have proven as an ideal testbed for their dynamics. The average of physical quantities over the unitary ensembles of the individual gates can oftentimes be computed analytically by making use of the random ensemble's properties. By concentration of measure arguments, the average results will often be expected to resemble that of a single random circuit instance. This analytical access is in stark contrast to disordered interacting systems with random potentials in the Hamiltonian, where often numerical exact diagonalisation is necessary. Therefore, toy models based on random circuits are very important in studying and understanding physical concepts like chaos, scrambling and entanglement spreading.

In the last years, the field of random circuits has flourished and a number of studies have appeared, for example [16, 17, 28, 71–77]. In the following, these works will be discussed in more detail.

A regular brickwork circuit with all gates independently Haar random is studied in [16, 17, 77]. Since each subsequent timestep of the circuit is independent, each random unitary only appears a small number of times in quantities of interest. Therefore the Haar measure can be explicitly integrated with the help of Weingarten functions (see section 2.2). Again owing to the *Brownian* nature of the circuit (i.e. uncorrelated in time), [16, 17] can setup a hydrodynamic equation for the progression of time, and [77] a recursion relation. Among the objects of interest are the OTOCs (see section 3.3) and the entanglement entropy (see section 3.1). The spreading of OTOCs is related to the butterfly effect, how soon a local operation affects far away regions, defining the butterfly velocity v_B. It is found that operators spread ballistically (meaning $\propto t$) with v_B, and the wavefront of the propagating OTOC spreads diffusively (meaning $\propto \sqrt{t}$). Entanglement spreads with a separate velocity v_E, both of which are lower than the lightcone velocity v_{LC}: $v_E < v_B < v_{LC}$. The lightcone velocity corresponds to the maximal speed limit that information can be moved due to the

geometry of the circuit, see the green dashed example in Fig. 4.2.

A similar situation is studied in [71, 72]. The circuit again follows a regular brickwork pattern with all gates independent, but each obeying $U(1)$ charge conservation. For a qubit circuit, this means the individual gates coupling nearest-neighbours have the block form

$$U = \begin{pmatrix} U_{Q=0} & & \\ & U_{Q=1} & \\ & & U_{Q=2} \end{pmatrix}. \tag{4.3}$$

This is called charge-conserving because it preserves the charge sector of the number of spin down. Within each charge sector, the unitaries U_Q themselves are Haar random, $U_{Q=0}, U_{Q=2} \in U(1)$ and $U_{Q=1} \in U(2)$. Again, the OTOC spreads ballistically, but part of the OTOC is slower: It has a diffusively spreading tail.

The above articles made use of the Brownian nature of the quantum circuit. Instead, [73, 74], consider a brickwork Floquet circuit. The geometry is again as in Fig. 4.2, but the unitaries are not independently drawn from the Haar distribution. Instead, in the spirit of Floquet evolution (see also section 4.1), it is time-periodic: Each time step (two sublayers in the circuit) are repeated identically. Every random unitary then appears several times in physical expressions, and contrary to the Brownian case, the Weingarten method is unwieldy. Instead, as a major simplification the authors consider a local dimension $d \to \infty$ instead of spin 1/2 particles for each site. In this limit, expressions of random unitaries can be solved, because Weingarten functions have known asymptotic behaviour (see section 2.2). This allows the authors to compute the spectral form factor, OTOCs, and Rényi-2 entropies. The spectral form factor $K(t) = \operatorname{tr} U^t \operatorname{tr} U^{*t}$ is the Fourier transform of the eigenvalue spacing. In random matrix theory, its behaviour for Haar random unitaries is well known, saturating to the maximal value N (the matrix dimension) after $t = N$ timesteps. Using the one timestep of the random circuit as U, the authors find the same behaviour. OTOCs and Rényi-2 entropies display ballistic growth. They both have the same velocity as the light cone, which is attributed to the $d \to \infty$ limit.

In [75], a Floquet circuit with a different structure than the prototypical brickwork-pattern is considered. A timestep includes one layer of single-site Haar random unitaries, followed by a random coupling which is diagonal and depends on adjacent sites. The random coupling strength is tunable, and in $d = 3$ dimensions they can find a many-body localized (ML) phase transition (MBL is discussed in the previous section 4.1).

Finally, let us turn to models where the geometry of the circuit itself is random. In [28], a random circuit is considered, where Haar random unitaries are applied to two neighbouring spins at a random position each timestep. They are able to map the entanglement growth to the Kardar-Parisi-Zhang (KPZ) equation. The KPZ equation stems from classical surface growth problems. The result is in line with above models; entanglement grows ballistically, with a velocity $v_E < v_B$ slower than the butterfly velocity describing operator growth. In [76], the actual goal was to study disordered continuous dynamic Hamiltonian systems (related to holography, see section 5.3), and see when they approach random matrix behaviour. The main diagnostic for random matrix behaviour considered in this work is the spectral form factor. However, since disordered Hamiltonian dynamics are hard to

grasp analytically, they also consider Brownian random quantum circuits instead. They use both geometrically local 1D brickwork circuits, as well as k-local random geometry circuits. This common nomenclature is confusing: k-local circuits are not at all geometrically local, instead, each gate is added such that it randomly couples any set of k possibly very distant qubits. Since the Brownian quantum circuits don't have energy conservation, they also consider quantum circuits with a different conserved charge, with gates as in (4.3). In this situation, they find different timescales N^2 and $\log N$ until the local and k-local circuits reach random matrix theory behaviour.

The recent experimental advances in building quantum computers have moved random circuits into the spotlight from a yet another perspective [78]. In order to show quantum supremacy, output bitstrings of random quantum circuits can be sampled. Sampling from random quantum circuits classically with a high fidelity is a very hard computational task, but execution on a quantum processor is straightforward. In [78], the authors sample a million outputs of a 53-qubit circuit in 200 seconds on their Sycamore quantum processor. They argue that the device samples the circuits with a sufficiently low noise of 0.2% (they use the so-called cross entropy benchmarking to quantify this) that classical simulation would exceed 10.000 years.

Original research

The regular brickwork structure shown in Fig. 4.2 is the basis for [1]. We consider a random quantum circuit in a Floquet setup, i.e. periodic in time. Further, each site's dimension is a fixed integer d, for example spins $d = 2$. This is a regime not covered elsewhere in the literature to the best of the author's knowledge. Due to the hardness of analytically tackling this regime, other studies take the limit $d \to \infty$ or use a Brownian non-Floquet setup (which is simpler as each time evolution step can be viewed independently in a Markovian fashion). We choose the constituent unitaries from the Haar measure, or a family of random ensembles parametrised by a coupling strength.

Since the circuit's regime is difficult, we do not study OTOCs. Instead, we concentrate directly on information moving from one site to another by considering single site reduced density matrices. Thanks to the brickwork geometry and the single-site Haar invariance of the random unitary ensembles used, we can show the main result for the reduced state at a single site:

$$\rho_{\text{red}}(t) = \mathbb{1}/d + \alpha(t)\bar{\rho} \tag{4.4}$$

for initial state $\rho_{\text{red}}(0) = \mathbb{1}/d + \bar{\rho}$ at the same site. The constant $\alpha(t)$ can be determined numerically and its behaviour evidences an MBL phase transition (see also section 4.1).

In [2], we study the Brownian SYK model. This can be seen as a Hamiltonian analogue of a Brownian, non-local quantum circuit. Similarly to [76], the motivation to study it stems from the holographic principle (see also

section 5.3).

Our toy model [3] for black hole evaporation is based on a random quantum circuit. Again, it does not display any geometric locality (apart from grouping sites into system and environment). Random unitaries are applied between random sites within the system at a certain rate, such that a continuous limit of a quantum circuit is achieved. The unitaries are either drawn from the Haar distribution, or from the distribution (4.3) conserving a charge. The charge of the system flowing into the environment then mimics the mass of a black hole evaporating. Due to the Brownian nature of the circuit, we can compute Rényi entropies and mutual information to quantify the evaporation process, and information retrieval properties (see section 5.2).

Chapter 5

Black holes from a quantum information perspective

The two fundamental theories in modern physics that shape our understanding of nature are quantum theory and gravity. Both theories are experimentally tested to extraordinary precision. Quantum physics becomes relevant as the de Broglie wavelength $\lambda = h/p$ becomes comparable to relevant length scales of the system in question. Since Planck's constant h is extremely small (compared to scales of everyday objects, such as books), the mass of a particle also has to be extremely small such that the momentum p is of a similar scale and the wavelength λ is appreciable. First and foremost, quantum physics therefore describes the basic interactions of particles, summarised in the standard model. Experimental evidence abounds. As an example, take the dimensionless fine structure constant α, which is related to the strength of the electromagnetic interaction. It is perhaps most readily manifest in the spectrum of atoms, where it leads to splittings of energy levels. The fine structure constant α was measured with an error less than 1 part per billion [79]. This extremely precise measurement result perfectly matches theoretical calculations based on quantum electrodynamics, the quantum field theory describing the electromagnetic interaction; serving as an excellent experimental test.

Gravity may seem easier to grasp than quantum physics, because we experience it directly in everyday life. Nobody is surprised that pens or rain fall down, or that it takes effort to jump or lift a wardrobe. Even mathematically, it first seems deceptively simple: Grade schools teach that all objects fall with the same acceleration 9.81m/s^2. However, this is not the end of the picture. Our best understanding of gravity is Einstein's theory of general relativity, which has many facets escaping our everyday experience of nature. At heart, it is a geometric theory, describing how mass affects the geometry of space-time, and vice-versa. Since larger masses lead to larger effects, gravity can mostly be neglected when studying small systems like atoms, and is very relevant at large, cosmic, length scales. Experimental evidence for various predictions of general relativity were found. For example, the Nobel prize was recently awarded in 2017 for the detection of gravitational waves, caused by two merging black holes [80], and in 2020 for the detection of the black hole in the center of our milky way galaxy [81].

General relativity and quantum physics can work also work in tandem in the same experiment. For example, in the remarkable experiment in [82], the authors built two atomic clocks that operate using techniques based on principles from quantum physics. They were then able to measure a height difference of 33cm by comparing the speeds of the clocks. Due to larger gravity at the clock closer to the earth's core, time passes slower compared to the higher clock.

Yet, at a fundamental level, gravity and quantum theory have escaped unification into one grand physical theory of everything. While high-energy physicists undertook much effort towards unifying the theories, sprouting large fields like string theory or loop quantum gravity, the search for the holy grail of physics is not concluded.

Black holes are an extreme situation. As such, they are a particularly interesting and fruitful setting to study the clash of general relativity and quantum physics. A prominent example for this clash is the black hole information paradox. What happens when quantum information falls into a black hole? In section 5.1 we discuss the paradox, and also cover how its resolution is related to scrambling of quantum information, providing the link to the previous chapters. Next, in section 5.2, we consider more closely information falling into a black hole, and that emitted by Hawking radiation. Hayden and Preskill developed a famous thought experiment to study this setting [27]. Finally, we turn to a different link between black holes and quantum physics in section 5.3. Through the holographic principle, a black hole itself may be described by a dual quantum theory.

Because of the importance of quantum scrambling in high-energy physics, considerable work on quantum chaos and scrambling in many-body systems is published by high-energy physicists and in respective journals. It is exciting that these two fields of physics intersect.

Original research

While the articles [2, 3] are both concerned with chaos, scrambling, and information in many-body quantum systems, motivation stems from the link to black hole physics . In fact, they are published in the Journal of High-Energy Physics. For the former, the link comes from the holographic principle, from which our model is loosely inspired. For the latter, the link is the Hayden-Preskill thought experiment, for which we develop a microscopic random quantum circuit model matching black hole features.

5.1 Black hole information paradox and fast scrambling conjecture

Black holes excite people's imagination since decades. Even the brightest physicists struggle to reconcile black holes with the known theories of gravity and quantum mechanics. Until a satisfactory microscopic quantum gravity description of black holes is found, the two theories remain at clinch. This clinch becomes apparent in the black hole information

paradox.

Black holes are, in fact, not completely black. Instead, they emit Hawking radiation [83, 84], first predicted by Stephen Hawking in 1974. A popular picture for the origin of the radiation is the following. Due to quantum fluctuations in empty space, particle-antiparticle pairs always temporarily pop up randomly everywhere, before annihilating again. When such a pair forms just at the event horizon with one particle on either side, one of them will be sucked further into the black hole, while the other can still escape. The escaping particles make up the Hawking radiation. This picture is still somewhat a toy model. Accurate calculations consist of quantum mechanics in a curved space-time. Since back-reactions to the fixed space-time curvature are excluded, Hawking radiation is sometimes called a semiclassical effect. Hawking radiation is the gravitational analogue to the Unruh effect, in which an accelerated observer in a vacuum does not observe a vacuum, but instead a thermal bath [85].

These calculations of Hawking radiation lead to exact thermal radiation, like any black-body radiation. It has temperature

$$T = \frac{\hbar c^3}{8\pi G k_B} \frac{1}{M}, \tag{5.1}$$

where G is Newton's constant, k_B Boltzmann constant, and M the mass of the black hole. As the black hole emits radiation, it looses mass. In fact, because the radiation's temperature increases as the black hole becomes smaller, it looses mass quicker and quicker, until it has completely evaporated.

During the lifetime of a black hole, it absorbs various quantum information, the infalling objects. According to Hawking's calculations, after the evaporation, the information has been destroyed, as only thermal radiation has been emitted. The black hole thus maps a pure state (the infalling matter) to a mixed density matrix (the Hawking radiation). This is at clinch with the unitarity of quantum mechanics. Time evolution of an entire system (including its environment) in quantum mechanics is always unitary; in fact, the Schrödinger equation is, in principle, reversible. Thermal Hawking radiation breaks unitarity because even mathematically, the mixed thermal state can never be translated back to the initial pure state. This is the basic black hole information paradox.

This basic black hole information paradox puzzled physicists and there was been much debate on its resolution: Stephen Hawking and John Preskill entered into a famous bet on whether black holes destroy information. These "black hole wars" were even covered in a popular science book [86]. To resolve the basic black hole information paradox, strict thermality of the radiation, or unitarity of quantum mechanics must be given up.

The debate was closed when Hawking conceded to losing the bet. Nowadays, the basic paradox is mostly resolved by keeping unitarity, but adding corrections to the thermal Hawking radiation. In fact, tiny corrections cannot be captured by Hawking's calculations [87]. Even if the radiation would be a completely pure state, it could still appear thermal locally. This is the same idea underlying thermalisation of closed quantum systems (see section 3.2): A reduced density matrix of a pure state can resemble a thermal density matrix. For example, in [88] the author's show how all of the information can be encoded

in Hawking radiation that looks completely thermal unless you harness superpolynomial quantum computational power. A powerful set of evidence to resolve the basic black hole information paradox in this fashion and leading to forfeiture of the bet, stems from the AdS-CFT correspondence. As will be explained in section 5.3, it offers a mapping of the gravitational theory with the black hole to a dual quantum theory. This dual quantum theory strictly obeys unitarity, which should be carried over by the duality.

Although the conservation of information was established at the cost of strictly thermal Hawking radiation, more subtle issues in the clinch between gravity and quantum physics remain. In fact, the information paradox persists, but the situation has to be studied more closely. Here we present a few cornerstones and possible resolutions.

As black holes eventually reemit information, one can study the speed of information retrieval. The next section 5.2 studies information retrieval from black holes more closely. The paradox arising is related to the no-cloning theorem in quantum physics. Due to the large space-time curvature, information appears twice within and outside of the black hole in the same spacelike slice, in violation of quantum no-cloning [27]. The reconciliation with quantum physics is further complicated by requiring that an infalling observer does not notice crossing the horizon. The Schwarzschild metric

$$ds^2 = \left(1 - \frac{2MG}{c^2\, r}\right) c^2 dt^2 - \left(1 - \frac{2MG}{c^2\, r}\right)^{-1} dr^2 - r^2 d\Omega^2, \tag{5.2}$$

describes an uncharged non-rotating black hole in general relativity with mass M, Newton's constant G, and coordinates time (t), radius (r) and solid angle (Ω). It is written in such a way that asymptotically, $r \gg 2MG$, a far away observer is manifestly situated in flat Minkowsky space and uses his coordinates t and r. The horizon is situated at $r = 2MG/c^2$, where the Schwarzschild metric becomes singular. However, this does not mean that space-time curvature itself becomes singular! In fact, a coordinate transformation from these Schwarzschild coordinates that removes the singularity at the horizon is possible, for example using Kruskal coordinates. An observer who falls into the black hole does not experience any discontinuity or anything strange when crossing the event horizon. [89]

Black hole complementarity [88, 90] is an important concept used to resolve such issues. Its main postulate is that the inside and outside of a black hole are not two distinct (albeit possibly correlated) quantum systems. Therefore, the overall system is not a tensor product of black hole and environment, $H_{\text{total}} \neq H_{\text{black hole}} \otimes H_{\text{environment}}$. Instead, inside and outside of the black hole are in fact complementary descriptions of the identical quantum system. Any observable $O_{\text{black hole}}$ is related to the observables on the environment in some (non-trivial) fashion, $O_{\text{black hole}} = P(O^1_{\text{environment}}, O^2_{\text{environment}}, \ldots)$. Reference [88] suggests a possible encoding P which is highly non-trivial. The inside operators correspond to logical operators of a quantum error correction code which are very difficult to access. Quantum information appearing twice on the same timelike slice is then no longer a problem; of course it must occur on the inside and outside, as they are just complementary descriptions of the same system. A guiding principle of black hole complementarity is an operational definition of the violation of laws of nature. As long as no observer can operationally confirm that no-cloning has been violated, it needn't bother us. This in fact places an lower bound on the

speed of information scrambling in black holes (see also the next section 5.2), which must not be faster than order $\sim \log N$, where N is the black hole's size. (For the information to be released, it must first become scrambled with the entire black hole.)

The authors AMPS [91] flesh out another aspect of the black hole information paradox. It is a paradox arising when considering entanglement between different regions both close and far from the horizon, violating monogamy of entanglement. Monogamy of entanglement refers to the fact that it is impossible for one qubit to be maximally entangled to two different qubits at the same time. One resolution would be a *firewall* behind the horizon, that breaks entanglement and kills anybody trying to cross it.

We noted above (and see also the next section 5.2 for more details), that an upper speed limit of $\sim \log N$ is imposed on scrambling to avoid the black hole information paradox, at least when operational viewpoints of black hole complementarity are imposed. On the other hand, there is a conjecture concerning the lower speed limit of scrambling: According to the fast scrambling conjecture, no quantum system can scramble faster than $\sim \log N$, and black holes are the fastest scramblers found in nature, saturating this bound [18, 24, 25]. In finite dimensional many-body quantum systems with local interactions, this bound $t_s \sim \log N$ never becomes saturated. Due to the locality of the interactions, it takes longer for information to traverse the system. For example in one dimension with nearest-neighbor interactions, it is clear that it takes at least time $\sim N$ for information from one end to spread to the other end of the system. Section 4.2 gives details of scrambling in various unitary circuit models. In order to achieve the $\log N$ limit, a quantum system must exhibit non-local interactions. Sometimes, such systems are called infinite dimensional, because in local systems, the number of dimensions is related to the connectivity and number of neighbours of each particle (see eg. [24]).

Scrambling at the maximal speed $\sim \log N$ provides a pathway to just barely steer clear of the black hole information paradox, at least when operational viewpoints of black hole complementarity are imposed. Because of this, scrambling in many-body quantum systems is not only of interest to many-body physics (see the previous chapters), but also high-energy physics. In fact, the holographic principle allows to describe a black hole in form of a quantum theory, see section 5.3. Many authors studied scrambling in disordered quantum systems with all-to-all interactions on a quest to learn more about maximal scrambling with $t_s \sim \log N$, see for example [22, 56, 76].

Original research

The articles [2, 3] study scrambling in quantum many-body systems. The systems in question are disordered, time-dependent, and non-local. We find that they, in fact, saturate the bound $t_s \sim \log N$ for maximal scrambling. This gives further credibility to the fast scrambling conjecture.

In both articles, the systems we study are inspired from black hole physics. The time-dependent Hamiltonian dynamics of [2] is motivated by the SYK model, a holographic model frequently used to study the information-theoretic

properties of black holes (see section 5.3). The continuous random circuit model of [3] follows the tradition of studies of random circuits (see section 4.2), and is is set up to allow analysis of information retrieval properties of black holes, see section 5.2.

5.2 Information retrieval from black holes

When quantum information falls into a black hole, it is eventually released with the Hawking radiation - this is the resolution of the black hole information paradox, see above. Astonishingly, this relation can be further analysed quantitatively. Here, we consider two different scenarios from the recent Hayden-Preskill thought experiment [27] from 2007. Some of the ideas go back to the Page curve [92, 93] from 1993. In their landmark article, Hayden and Preskill consider quantum information consumed and emitted by black holes. The protocol they introduced to quantify the quantum information in this process has since been coined the Hayden-Preskill thought experiment.

The microscopic dynamics of a black hole are not yet known. A full theory of quantum gravity would be needed to understand exactly what happens in detail. Instead, to study the information retrieval properties, black holes can be viewed as a black box, and their dynamics modelled as large random unitaries. In information retrieval protocols, Alice throws some information/qubits into the black hole. Together with the other black holes degree of freedoms, these are evolved in time by the black hole's unitary dynamics U. Then, a certain number of qubits are seen as radiation, which is collected by Bob. Bob then tries to infer Alice's original qubits from the collected Hawking radiation. The names Alice and Bob as sender and receiver are standard in classical and quantum information theory alike. Different scenarios exist, depending on Bob's knowledge of the initial black hole. See Fig. 5.1 for an illustration of the information retrieval scenarios. Since we are dealing with quantum information and wish to assess identity of quantum information, Alice's qubit is maximally entangled to an outside reference qubit. If, from the Hawking radiation, Bob can extract qubits maximally entangled to this outside reference qubit, he can fully reconstruct Alice's quantum information.

In the first scenario (see Fig. 5.1 a)), Bob does not have access to the initial black hole state, which is taken to to be a product state. Then, Bob will have to wait until half of the black hole's qubits have been released as radiation (and collected by him). The next radiation quanta will then very quickly reveal Alice's secret [27]. This scenario is related to the Page curve [92, 93]. The Page curve describes the entanglement entropy within a random pure state, such as the evolved state of an initially product state black hole. Consider a bipartition of a state of $N = n + m$ particles into two regions of n and m spin 1/2 systems each (without loss of generality, $m < n$). The maximal possible von Neumann entanglement entropy between the two regions is $S_{m,n} = \log m$. Page calculated [92] that for a random state, this is almost saturated up to order $1/n$ corrections:

$$S_{m,n} \simeq \log m - \frac{m}{2n}. \tag{5.3}$$

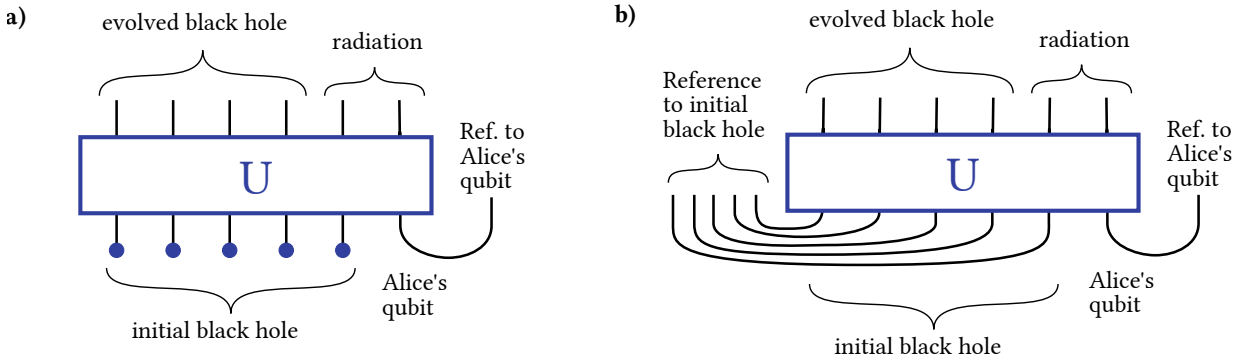

Figure 5.1: Information retrieval from a black hole, whose dynamics are modelled by a black-box random unitary U. Alice injects her qubit into the black hole. Bob has access to the Hawking radiation and tries to recover Alice's qubit. In order to compare his extracted information to Alice's qubit, a maximally entangled reference qubit to her information is kept outside of the black hole. This model has no explicit time dependence, instead, it must be entered by hand, by increasing the dimension of the outgoing radiation and reducing the dimension of the evolved black hole. In scenario **a)**, the black hole is initially in a product state. After the Page time, when a little more than half of the black hole has evaporated, the radiation becomes (almost) maximally entangled with the reference qubit and Bob can recover Alice's information. In scenario **b)**, Bob has access to the initial black hole. This means that in addition to the Hawking radiation, he holds a reference system that is maximally entangled with the initial black hole. Using this further knowledge, he must not wait till more than half of the black hole has evaporated: His joint system of radiation and reference to initial black hole becomes (almost) maximally entangled to Alice's reference qubit very quickly, when only a little more than one qubit is radiated.

A random state is defined by applying a Haar random unitary to an arbitrary state, see also chapter 2. Page's result shows that (large) random pure states are very highly entangled, almost maximally entangled between any choices of subsystems. From this perspective, it is not surprising that Bob has to wait for about half of the black hole to evaporate: After a bit more than half of the black hole has been released as radiation, the radiation is almost maximally entangled to the rest of the evolved black hole as well as the reference qubit. The relevant time scale for information retrieval is the Page time $t_p \sim N$.

In the second scenario (see Fig. 5.1 b)), Bob has access to the initial black hole state. This scenario could arise for a black hole which Bob has studied for its entire lifetime and therefore knows its state. Alternatively, the black hole could be very old, and Bob has collected a huge amount of Hawking radiation, such that he controls a system maximally entangled to the rest of the black hole; this trail of thought corresponds to the Page curve presented in scenario (a). Hayden and Preskill [27] analysed this setting in detail, and found that the information is almost immediately revealed to Bob. Only little more than one qubit has to be released in the Hakwing radiation for Bob to recover Alice's qubit. The relevant time scale for information retrieval is no longer the Page time $t_p \sim N$ as in scenario (a), but the much shorter scrambling time $t_s \sim \log N$. Before information can be released, it must first become scrambled with the entire black hole. This is because the choice of qubits to emit as Hawking radiation is random and does not favor Alice's recently injected information.

In the single random unitary model depicted in Fig. 5.1, scrambling is in fact instantaneous, as the large random unitary couples all spins at once. In more realistic black hole models, and in nature, the scrambling time is not instant but still very fast, much faster than the Page time, where we have to wait for a large amount of radiation to be released. Refering to scenario (b), the authors titled their celebrated article "Black holes as mirrors" that reflect quantum information almost immediately.

Actual black holes are more complex systems than simply a large random unitary U. The previous section 5.1 highlighted some paradoxes that arise when combining quantum and gravitational properties of black holes. Due to the intricate space-time geometry of a black hole, reflection of quantum information may violate the no-cloning theorem. In quantum physics, whenever unitary time evolution is present, quantum information cannot be copied [48]. However, there are spacelike surfaces on which both Alice's infalling qubit and Bob's Hawking radiation are present. A resolution is to use the black hole complementarity viewpoint, and an operational definition of the no-cloning theorem: As long as nobody can operationally verify that cloning has occured, we do not let us be bothered by any cloning. In order to verify the cloning, Bob has to dive into the black hole together with his collected information to compare to Alice's qubit, as the latter can never exit the horizon. In order for it to be impossible to verify the cloning, a lower bound is imposed on the time until reflection. Thus, to save the complementarity solution of the black hole information paradox, it turns out that the reflection of quantum information must not be faster than $\propto \log N$, where N is the size of the black hole [24, 25, 27]. In fact, this bound is saturated, see also section 5.1.

Original research

In [3], we study a random circuit model for the evaporation of a black hole. The exact microscopic dynamics of a black hole dictated by quantum gravity are not known yet. Instead, we propose a microscopic quantum model that can mimic a black hole evaporation. While it is a toy model, it shows that the expected information retrieval properties can arise from a simple microscopic dynamics without any fine tuning, instead of global random unitaries.

The model is based on a continuous version of a random quantum circuit (see also section 4.2). SWAP-gates couple the black hole's degrees of freedom with the environment, and random gates provide the intrinsic dynamics. We can setup exact differential equations, whose solutions tell us about build-up of entanglement entropy, and information retrieval times for both scenarios (a) and (b). The results match the expectations of black holes explained above. In particular, both the $t_p \sim N$ and $t_s \sim \log N$ dependencies of the Page time and scrambling time, governing scenarios (a) and (b) respectively, can be picked up explicitly. This is thanks to the system of differential equations, which can be integrated for a large number of particles N.

To make the model more realistic, we consider a variant where the random gates conserve a $U(1)$ charge. This corresponds to energy conservation. A fully analytical system of differential equations is no longer available, but the exponential Hilbert space can be reduced to calculations in a polynomial Hilbert space size by making use of an emergent permutational symmetry. The results are similar to the case without charge conservation and show the expected properties of black holes.

As quantifiers of interest, we calculate both entanglement entropies, as well as mutual information (see section 3.1). Mutual information between Alice's qubit and the systems accessible by Bob is a direct measure of possible information retrieval.

5.3 Holographic principle and the SYK model

Back in the 1970s, Jacob Bekenstein and Stephen Hawking closely studied the entropy of black holes. Since entropy can only increase across the entire universe, an object falling into a black hole must increase the black hole's entropy [94]. When Hawking discovered Hawking radiation and thereby computed a black hole's temperature, this opened another pathway towards black hole entropy [84]. The entropy of a black hole

$$S_{BH} = \frac{k_B c^3}{4\hbar G} A \tag{5.4}$$

has been named Bekenstein-Hawking entropy. It is proportional to the surface area A of the event horizon. This is surprising, because usually entropy is an extensive quantity, and

proportional to the volume of the system. The microscopic interpretation of the entropy is the logarithm of the number of microstates. For an ideal gas, it is clear that bringing two volumes of equal temperature together, the entropy is additive.

Since the entropy is linked to the surface area of the black hole, it is conceivable that an equivalent description of the black hole exists with all degrees of freedom localized at the surface. This is at heart of the holographic principle. The holographic principle is a general idea, that a d dimensional system may equivalently be described by a corresponding $d-1$ dimensional system [19, 20]. For example, tourist shops frequently sell hologram postcards: The image appears three dimensional, although all of the image is encoded on the two dimensional postcard.

For the study of black holes, the holographic principle was formulated in the form of the AdS-CFT correspondence. The AdS-CFT correspondence encompasses a family of holographic theories that connect a gravitational bulk, an anti-de-Sitter space (AdS), with a conformal field theory (CFT) on the boundary of one dimension less. High energy physics studies several examples, such as the duality between string theory in a 4+1 dimensional $\mathrm{AdS}_5 \times \mathrm{S}^5$ space and 3+1 dimensional supersymmetric Yang-Mills theory, which has been fleshed out in a mathematically rigorous fashion [21].

Anti-de-Sitter space is a space-time geometry with negative curvature, in which space-like slices are hyperbolic. A weak point of research on the AdS-CFT correspondence is, that our actual universe is not anti-de-Sitter, having a positive cosmological constant. As such, the correspondence does not help in the study of actual real-life black holes. Rather, it provides toy models, and some results and intuition may hopefully also be applicable to the real world. Conformal field theories are a certain kind of quantum field theory with strong conformal symmetry constraints.

In holography, the Ryu-Takayanagi conjecture is an important milestone [95]. It directly relates the entanglement within the boundary to the geometry of the bulk. In particular, the von Neumann entanglement entropy S_A of a boundary region in the quantum theory is conjectured to be

$$S_A = \frac{\text{Area of} \gamma_A}{4G}. \tag{5.5}$$

The curve γ_A is that of minimal area through the bulk geometry that can isolate A from the rest of the system. G is simply Newton's constant. As described in section 3.1, entanglement entropy plays a major role in many-body physics. The Ryu-Takayanagi formula manages to bring this important concept across the holographic duality, establishing a strong connection between entanglement and geometry.

Examples of the AdS-CFT correspondence can be exactly constructed with the help of tensor networks [96]. Tensor networks are an important toolbox to deal with and understand entangled many-body systems both analytically and numerically. Above and beyond AdS-CFT and tensor networks, the cited article also connects error correcting codes to these concepts. Quantum error correction is a major branch of quantum information theory. Since any actual physical implementation of a quantum computer will be noisy, a mechanism to correct for errors is necessary. This is much more difficult than classical error correction, as qubits change their value when measured and can further-

more be entangled. Surface codes are one class of quantum error correcting codes. The mapping between bulk and boundary corresponds to mapping between logical (error-free) and physical (noisy) qubits. The article further proves the Ryu-Takayanagi formula for the holographic examples constructed. As a by-product, apart from understanding AdS black holes, study of the holographic principle may prove useful in quantum computation by yielding new forms of error correction. Further, some difficult calculations in CFTs may be carried out more easily in the dual gravitational theory [97].

Before moving to the popular SYK model, let us point out a further connection where the general idea underlying holography manifests itself. Topological quantum systems are many-body systems featuring exotic phases, above and beyond the picture of Landau symmetry breaking [98]. These topological phases are characterised by different patterns of long-range entanglement. A well-known example for a topological quantum system is the topological insulator, and the quantum Hall effect. The general idea underlying holography is present in topological systems in the form of a bulk-boundary correspondence: The bulk physics is reflected in special edge mode excitations occurring only on the boundary.

A popular holographic model that received a lot of attention in the last years is the SYK model, named after its creators Sachdev, Ye, and Kitaev [99, 100]. The SYK model describes a quantum system of N Majorana fermions ψ_i interacting in a disordered q-local all-to-all fashion. Its Hamiltonian is

$$H_{\text{SYK}} = i^{q/2} \sum_{1 \leq i_1 < \ldots < i_q \leq N} J_{i_1,\ldots,i_q} \psi_{i_1} \cdots \psi_{i_q}, \tag{5.6}$$

where the interaction constants $J_{i,\ldots,i_q}$ are random and uncorrelated for different sets of indices. They all have the same mean 0, and the same variance which can be adjusted to tune the energy scale of the system.

Majarona fermions correspond to the the real and imaginary parts of usual complex fermions. Usually, (spinless) fermions in a fermionic Fock space are described by the creation and annihilation operators with anticommutation relations

$$\{a_k, a_l^\dagger\} = \delta_{kl}, \ \{a_k, a_l\} = 0, \ \{a_k^\dagger, a_l^\dagger\} = 0. \tag{5.7}$$

Majarona fermions are then defined as the real and imaginary parts of the these operators

$$\psi_{2k-1} = (a_k + a_k^\dagger), \ \psi_{2k} = (a_k - a_k^\dagger)/i, \ k = 1 \ldots N/2, \tag{5.8}$$

and inherit the following characteristic anticommutation relations:

$$\{\psi_i, \psi_j\} = 2\delta_{ij}, \ \psi_i = \psi_i^\dagger, \ i, j = 1 \ldots N. \tag{5.9}$$

The Hilbert space of N Majorana fermions therefore has dimension $2^{N/2}$ since they correspond to $N/2$ fermions. This can be made explicit by mapping Majorana fermions to spins with the Jordan-Wigner-transformation [101, 102]. A set of N Majorana fermions is mapped to a one-dimensional chain of $N/2$ spin 1/2 particles. Each fermionic operator

then corresponds to a Pauli σ^x or σ^y operator with a tail of σ^z operators:

$$\psi_{2k-1} \to \left(\bigotimes_{i=1}^{k-1} \sigma_i^z\right) \otimes \sigma_k^x \tag{5.10}$$

$$\psi_{2k} \to \left(\bigotimes_{i=1}^{k-1} \sigma_i^z\right) \otimes \sigma_k^y. \tag{5.11}$$

The σ^z tail is necessary for the correct anticommutation relations (5.9). These follow straightforwardly from the usual Pauli anticommutations

$$\sigma_i^\alpha \sigma_i^\beta = \begin{cases} -\sigma_i^\beta \sigma_i^\alpha & \alpha \neq \beta \\ \mathbb{1} & \alpha = \beta. \end{cases} \quad \text{for } \alpha, \beta \in \{x, y, z\} \tag{5.12}$$

The SYK model is of interest for the study of black holes, because it is maximally scrambling (see also section 5.1), as needed for holographic black hole models. Moreover, the large N limit, in which it becomes conformally invariant, is amenable to exact field-theoretic calculations.

Much study was therefore carried out on the chaotic properties of the SYK model. For example, in [103], the authors study the OTOCs and growth of operators. Numerically, they can compute the size distribution of operators for $q = 4$ and $N = 30$. Analytically however, they can make use of the fact that many Feynman diagrams become negligible in the $N \to \infty$ limit, and can give an explicit formula at large N and large q.

In [23], the spectral form factor $\overline{|\operatorname{tr} U(t)|^2}$ (here $U(t)$ is the time evolution operator, and overline indicates the disorder average) is studied. As explained in the context of quantum circuits in section 4.2, it is a diagnostic of scrambling and linked closely to the Haar measure. The spectral form factor for the SYK model is a difficult undertaking, therefore they further introduce and study the SYK model's Brownian companion. In the Brownian SYK model, the disordered coupling constants J in the Hamiltonian (5.6) are not only random and uncorrelated for different subsets of particles, but also random and uncorrelated in time. They therefore acquire a time-dependence; the correlations can be expressed as

$$\overline{J_{i_1 \ldots i_q}(t) J_{i'_1 \ldots i'_q}(t')} = \delta_{i_1 i'_1} \cdots \delta_{i_q i'_q} \delta(t - t') \sigma_J \frac{(q-1)!}{N^{q-1}}. \tag{5.13}$$

The correlations are thus as in Brownian noise, motivating the name. This model is simpler, because each timestep can be disorder averaged independently of the previous, in a Markovian fashion. For the spectral form factor of the Brownian SYK model, the authors [23] are able to give a mapping to a classical Ising model that can be solved exactly. The aim of [76] is also to study the spectral form factor of the SYK model. Instead of the Brownian SYK model, the authors turn to a Brownian qubit model and analogous discrete quantum circuits, see also section 4.2. The Brownian SYK model is the starting point for our work [2].

Original research

In [2], we study chaos and scrambling in the Brownian SYK model. The motivation clearly stems from the fact that SYK plays an important role in the holographic duality. Similarly to discrete quantum circuits, the model becomes simpler to study by considering its time-dependent Brownian version, and it is expected that is still describes well the high-temperature regime.

In order to compute the chaos identifiers tripartite information for information scrambling (section 3.4) and the OTOC for operator spreading (section 3.3), we make use of an emergent permutational symmetry: Individual disorder realisations are not permutationally symmetric, but the chaos identifiers become so after performing the disorder average.

The new numerical method thus developed allows us to consider systems at large finite N, a regime which has previously been very difficult to study. In turn, because we have access to up to a million particles, the $\log N$ behaviour that is expected and necessary for fast scrambling (see section 5.1) can be clearly identified and verified.

Appendix A

Localization with random time-periodic quantum circuits

In this article, we study thermalisation and many-body localisation (see section 4.1) in a one dimensional disordered system, modeled by a random unitary brickwork circuit. Random circuits have ushered in a gold rush in the study of disordered systems (see section 4.2), we consider a new setup: The circuit for a chain of d-dimensional qudits (finite d) is disordered in space, but periodic in time, mimicking Floquet evolution. As this makes calculating disorder averages with respect to the random constituent unitaries difficult, previous studies have shied away from this setup, considering local dimensions $d \to \infty$ or disorder random in time, c.f. section 4.2.

Thermalisation of this circuit bar of conserved quantities would lead to maximally mixed reduced density matrices for each site (see chapter 3.2). By making use of the Haar-invariance of the random unitaries (see section 2), we introduce the twirling technique, allowing us to investigate final reduced density matrices. In particular, we prove the following formula for reduced states at a single site:

$$\rho_{\text{red}}(t) = \mathbb{1}/d + \alpha(t)\bar{\rho}, \tag{A.1}$$

for initial state $\rho_{\text{red}}(0) = \mathbb{1}/d + \bar{\rho}$ at the same site. The constant $\alpha(t)$ can be determined numerically and allows to investigate thermalisation ($\alpha(t) \to 0$) or many-body localisation (finite $\alpha(t)$) for $d = 2$. The numerical computation of $\alpha(t)$ is exponential in t, and we combine a Monte-Carlo method with tensor network tricks to reduce cost.

The behaviour of $\alpha(t)$ shows a phase transition between thermal and MBL phases when tuning the coupling strength defining the ensemble of random unitaries for the circuit. The phase transition can be further pin-pointed in a time-independent manner by studying entanglement entropy (see section 3.1) of the time evolution operator (see section 4.1 for details on this procedure).

Beyond unitary circuits and spin chains, we study the corresponding problem for Gaussian circuits and free fermion chains. Since Gaussian states are fully characterised by the covariance matrix, this setup is simpler and allows stronger arguments both analytically and numerically.

Editors' Suggestion

Localization with random time-periodic quantum circuits

Christoph Sünderhauf,[1] David Pérez-García,[2,3] David A. Huse,[4] Norbert Schuch,[1] and J. Ignacio Cirac[1]

[1]*Max-Planck-Institut für Quantenoptik, Hans-Kopfermann-Str. 1, 85748 Garching, Germany*

[2]*Departamento de Análisis Matemático, Universidad Complutense de Madrid, Plaza de Ciencias 3, 28040 Madrid, Spain*

[3]*ICMAT, Nicolas Cabrera, Campus de Cantoblanco, 28049 Madrid, Spain*

[4]*Physics Department, Princeton University, Princeton, New Jersey 08544, USA*

(Received 22 June 2018; revised manuscript received 2 October 2018; published 30 October 2018)

We consider a random time evolution operator composed of a circuit of random unitaries coupling even and odd neighboring spins on a chain in turn. In spirit of Floquet evolution, the circuit is time-periodic; each time step is repeated with the same random instances. We obtain analytical results for arbitrary local Hilbert space dimension d; on a single site, average time evolution acts as a depolarising channel. In the spin $1/2$ ($d = 2$) case, this is further quantified numerically. For that, we develop a new numerical method that reduces complexity by an exponential factor. Haar-distributed unitaries lead to full depolarization after many time steps, i.e., local thermalization. A unitary probability distribution with tunable coupling strength allows us to observe a many-body localization transition. In addition to a spin chain under a unitary circuit, we consider the analogous problem with Gaussian circuits. We can make stronger statements about the entire covariance matrix instead of single sites only, and find that the dynamics is localizing. For a random time evolution operator homogeneous in space, however, the system delocalizes.

DOI: 10.1103/PhysRevB.98.134204

I. INTRODUCTION

The dynamics of many-body quantum systems has revived the interest in thermalization and localization. In closed systems, there are states that do not thermalize. A simple example is a single particle in a random potential that is Anderson localized [1]. But even if one includes interactions, a new way of many-body localization (MBL) can emerge that also prevents thermalization [2]. Despite great progress in understanding MBL during the last years (see, e.g., Ref. [3] or the review [4]), there are still many open questions.

A typical scenario studied in the context of localization is a system on a one-dimensional lattice, with a short-ranged Hamiltonian containing a kinetic term and a random potential for each site. In the absence of interactions, this single-particle problem displays Anderson localization: starting in one position, the probability of finding the particle at the same position after arbitrary time is lower bounded, and the probability for other positions is exponentially suppressed [5,6]. If one adds interactions, the system can find itself in the thermal or MBL phase, usually dependent on disorder strength. Starting with some information in a specific position, in the thermal phase it will flow away and cannot be recovered locally, and in the MBL phase there will still be traces present at the same position after arbitrarily long times, despite some information slowly flowing away [7–9].

Another scenario is the so-called Floquet evolution. There, one considers not a continuous time evolution generated by time-invariant Hamiltonians, but a discrete-time evolution operator repeated for subsequent time steps. It may arise from a periodic drive or be directly given as a unitary model. Floquet systems are a formidable setting to study localization, because even energy ceases to be a conserved quantity. Anderson localization has been proven for specific Floquet systems [10]. It has been found that Floquet systems are compelling examples for MBL [11,12], which yield sharper transitions between thermal and MBL phases [13].

In addition, circuits of random unitaries have recently been used as a model of chaotic systems [14–22]. In Refs. [14,17], time evolution by a unitary circuit of fixed geometry but independently Haar-distributed random gates at each time step was studied. That model exhibits thermalization to an infinite temperature state, and the authors found ballistic spreading of quantum information by considering the out-of-time-ordered correlator. Subsequently the model was extended to a similar setup [15,18] with a conservation law. In Ref. [16], the authors consider the same unitary circuit in a Floquet setting, where subsequent time steps are repeated with the same random instances. In the limit of infinite local Hilbert space dimension for each qudit, they find thermalization to an infinite temperature state and calculate several values like the spectral form factor or the exponentials of some Renyi-entropies. In other related work [23–25], thermalization of spin chains for certain continuous-time dynamics was found in the context of the average spectral form factor.

Here, we consider several variations of Floquet evolution with a unitary circuit, and analyze if there is localization. We consider as time evolution operator a quantum circuit of depth two, which consists of two alternating layers of random nearest-neighbor unitaries coupling even and odd pairs of sites in turn. The two layers are repeated identically for subsequent time steps such that the total circuit is periodic in time, in the spirit of Floquet evolution. This circuit geometry is the discrete analog of local time-independent Hamiltonian evolution (and could also be obtained by a Trotter decomposition, or the standard form of an index zero matrix product unitary

[48], for example). We perform an average within a (sub)set of unitaries. Typically, we start with a completely mixed state everywhere and a pure state at one site and look at the reduced state of that and other sites at some later time, and determine whether it depends on the initial state, corresponding to localization.

The scenarios we consider are the following: (A) Gaussian circuits, acting on fermionic chains with one mode per site and Gaussian evolution, where the nearest-neighbor unitaries in the circuit are operations that stay within the manifold of fermionic Gaussian states. (B) Spins, with a qudit per site and arbitrary constituent unitaries in the circuit. The first scenario, (A) Gaussian circuits, extends the typical situation in Anderson localization, since the particle number is not conserved. In this scenario, we consider inhomogeneous as well as homogeneous Floquet circuits, where the unitaries coupling sites are independently random for each pair of neighbors or the same along the entire chain. We find that the inhomogeneous setting exhibits localization, whereas the homogeneous Floquet circuit leads to delocalization.

The second scenario, (B) spins, is similar to the models studied in Refs. [14,16,17]. In contrast to Ref. [16], in our work the local Hilbert space dimension of each spin is finite, and in contrast to Refs. [14,17], we work in a Floquet setting. We prove that on a single site, the time evolution acts as a depolarising channel. Further, we find that a chain of qubits can exhibit thermalization or MBL, depending on the probability distribution used to average the unitaries in the circuit; we observe the corresponding phase transition.

Our setup is difficult computationally and analytically, because it requires to study dynamics of many-body systems, averaged over instances of the random Floquet circuit. Methods to exactly calculate averages [26,27] work well when each random matrix appears a small amount of times, or for large dimensions where asymptotic behavior is available. These methods are not useful in our setting, since the same random matrices reappear in each time step (contrary to Refs. [14,17]) and we have a fixed finite dimension of the spins (contrary to Ref. [16]). Instead, we derive analytical results in both cases with a technique we call the twirling technique. It is based on a property of the average, which basically allows us to move arbitrary single-site unitaries through the quantum circuit such that they only appear twice, at the beginning and end, relating initial and final states.

Apart from that, we also perform numerical calculations [47] in both cases. For (A) Gaussian circuits, we can work with the covariance matrix formalism, which is very efficient and allows us to explore very large systems. For (B) spins, the Hilbert space is exponential in chain length. We develop a new numerical method which combines tensor networks and Monte Carlo ideas, drawing from simplifications provided by the analytic results. It reduces the memory and time complexity from 2^{4t} to 2^t for t time steps. This allows us to study relativity long times which, in turn, enables the simulation of up to 39 spins.

This article is organized as follows. First, we introduce the precise models in Sec. II and the quantities we will compute. In Sec. III, we present the main results of this work, and leave the derivations for Sec. IV. There, we also present the twirling technique (Sec. IV A) used throughout the paper, which can also be of interest on its own. Finally, in Sec. V, we present the new numerical method used for spin chains.

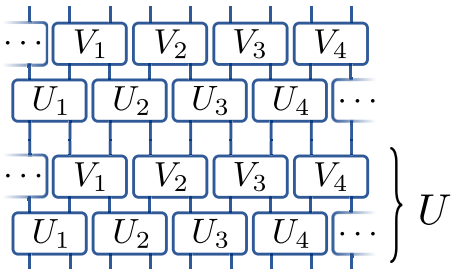

FIG. 1. Random time evolution operator U^2 for two time steps. The vertical lines indicate sites of the chain; each unitary couples two neighboring sites. In the spirit of Floquet evolution, the total evolution operator is time-periodic; the time step is repeated with the same random instances of U_i, V_i.

II. SETTINGS & QUESTIONS

For a one-dimensional chain of N particles, we consider a random unitary time evolution operator U composed of random nearest-neighbor gates according to some probability distribution. The time evolution operator is the unitary circuit with the fixed geometry sketched in Fig. 1 and can be written as

$$U = \left(\bigotimes_i V_i\right)\left(\bigotimes_i U_i\right). \tag{1}$$

The unitary U_i acts on particles $2i-1$ and $2i$ while V_i acts on sites $2i$ and $2i+1$. These two layers are repeated identically (with the same random instances of U_i, V_i) in spirit of Floquet evolution, in contrast to other models [14,17] where each time step is different.

In this article, we study the random circuit as a time evolution operator that is a (A) Gaussian circuit for fermionic chains or (B) Unitary circuit for spin chains. Throughout, the average $\langle\cdots\rangle$ denotes averaging over U_i, V_i. In the next two subsections, we give details of both settings, and define the probability distributions used for the average $\langle\cdots\rangle$ in either setting.

A. Gaussian circuits

First, we consider the problem for a chain of fermionic systems with one fermionic mode per site. Each of the N modes has two Majorana operators

$$c_{2n-1} = a_n^\dagger + a_n, \quad c_{2n} = -i(a_n^\dagger - a_n), \tag{2}$$

with the creation/annihilation operators $a_n^\dagger/a_n$. The two-point correlation functions of Majorana operators for each fermionic state ρ can be gathered in the covariance matrix

$$\Gamma_{kl} := \frac{i}{2}\,\mathrm{Tr}(\rho[c_k, c_l]). \tag{3}$$

Each site of the chain corresponds to a 2×2 block because each site is associated with two Majorana operators. A fermionic Gaussian state (i.e., those that can be generated by the vacuum of a_n by Gaussian functions of the Majorana

operators) is completely and uniquely characterized by its covariance matrix. Here, we consider the covariance matrices of not only Gaussian but arbitrary initial states with vanishing two-point correlators at nonzero distances.

We build the Gaussian circuit of transformations that map Gaussian states to Gaussian states (but can still be applied to general states). The most general such unitary operation acts on the covariance matrix by an orthogonal transformation $O \in \mathrm{O}(2N)$, specifically $\Gamma \to O\Gamma O^{\mathsf{T}}$.

We will consider two classes of these unitary transformations: Gaussian operations generated by Hamiltonians quadratic in the Majorana operators, which correspond to special orthogonal transformations $O \in \mathrm{SO}(2N)$ in the covariance matrix formalism [28,29], and the larger class of all operations $O \in \mathrm{O}(2N)$, which includes local particle-hole transformations [30]. Subsequently, we only consider the covariance matrices of initial and final states.

In this setup, the unitary-circuit time evolution operator (1) is represented as an orthogonal transformation $O \in \mathrm{O}(2N)$ built of random two-site operations $P_i, Q_i \in \mathrm{O}(4)$. With periodic boundary conditions,

$$O = G\left(\bigoplus_{i=1}^{N/2} Q_i\right) G^T \left(\bigoplus_{i=1}^{N/2} P_i\right), \tag{4}$$

where

$$G = \begin{pmatrix} 0 & & & \mathbb{I}_2 \\ \mathbb{I}_2 & 0 & & \\ & \ddots & \ddots & \\ & & \mathbb{I}_2 & 0 \end{pmatrix} \tag{5}$$

takes care of circularly shifting $\bigoplus Q_i$ by one site; i.e., two matrix elements down and right. Thereby P_i couples site $2i-1$ with $2i$ and Q_i couples site $2i$ with $2i+1$.

Our quantity of interest is the average final state $\langle \Gamma_t \rangle$ after t time steps of an initially uncorrelated product state Γ_0, i.e., with a 2×2 block-diagonal covariance matrix. In this formalism, its covariance matrix is

$$\langle \Gamma_t \rangle = \langle O^t \Gamma_0 O^{t\dagger} \rangle. \tag{6}$$

For the expectation value $\langle \cdots \rangle$, we consider two probability measures for the P_i, Q_i: the Haar measure for the orthogonal group $P_i, Q_i \in \mathrm{O}(4)$ and the Haar measure for the special orthogonal group $P_i, Q_i \in \mathrm{SO}(4)$. The Haar distribution (see, e.g., Ref. [31]) for the orthogonal (special orthogonal) group O(4) [SO(4)] is defined as the unique distribution with the property of Haar invariance, which mandates that any transformation

$$P \to APB, \text{ for any } A, B \in \mathrm{O}(4)\ [\mathrm{SO}(4)] \tag{7}$$

does not affect averages $\langle \cdots \rangle$ with respect to $P \in \mathrm{O}(4)$ [SO(4)] [32]. The long-time behavior of an initial covariance matrix is readily accessible to numerical calculations even on long chains, because we need only operate on its covariance matrix, whose dimension grows merely linearly in system size.

We consider two scenarios. In the first scenario, all P_i, Q_i are independently distributed according to one of the Haar measures. This situation is related but not equivalent to that studied in context of Anderson localization. The main reason is that the average over O includes transformations P_i, Q_i that do not conserve particle number. Thus a question to be addressed is whether the well-studied phenomenon of Anderson localization still exists, or if it is modified. To this end we ask, does the average final state $\langle \Gamma_t \rangle$ contain remnant information about the initial state Γ_0? The corresponding results are reported in Sec. III A 1.

Furthermore, we study a second scenario, the homogeneous setting where the time evolution operator O is two-site-translation invariant. In that scenario, randomness is the same for all sites, $P_i = P_j$ and $Q_i = Q_j$, such that there are only two independent transformations; here we consider only the Haar measure over O(4). Again, we ask the same question: Does an impurity in an otherwise translation-invariant state spread all over the chain or stay localized? We present the answer in Sec. III A 2. Occasionally, the time average

$$\langle \Gamma_{t\text{-avg}} \rangle := \lim_{T\to\infty} \frac{1}{T} \sum_{t=0}^{T-1} \langle \Gamma_t \rangle \tag{8}$$

is used to assess the localising or delocalising properties. Physically, it captures the long-time behavior of a typical state. The additional average allows us to make stronger statements.

B. Spins

After studying the evolution of a chain of fermions under Gaussian circuits, we turn to a chain of interacting spins. All particles along the chain have a local Hilbert space dimension d, which may be arbitrary. In that setting, all of the unitaries U_i, V_i composing the circuit U are general unitaries of $U(d^2)$, independently distributed according to some probability distribution for the average $\langle \cdots \rangle$.

We will consider different probability distributions for $U_i, V_i \in U(d^2)$ with the common property of single-site Haar invariance. This means that any transformation of a U_i or V_i of the form

$$U_i \leftrightarrow (w_1 \otimes w_2) U_i (w_3 \otimes w_4) \tag{9}$$

does not affect averages $\langle \cdots \rangle$, for arbitrary choice of $w_j \in U(d)$. For example, the unitary Haar distribution on $U(d^2)$ has this property. It is a distribution uniquely defined by Haar invariance (see, e.g., Ref. [31]), which means that transformations of the form $U \to AUB$, for arbitrary $A, B \in U(d^2)$, do not affect any averages with respect to the Haar distribution of $U \in U(d^2)$ [32].

In this paper, we characterize the average final state $\langle \rho_t \rangle$ obtained from an initial density matrix ρ_0 after t time steps:

$$\langle \rho_t \rangle := \langle U^t \rho_0 U^{t\dagger} \rangle. \tag{10}$$

In particular, for arbitrary initial states ρ_0, we will find a relation between the reduced initial state $\rho_0^{\mathrm{red}} := \mathrm{Tr}_{\{1,\ldots,N\}\setminus\{n\}}\, \rho_0$ on a single site n and the reduced state $\langle \rho_t^{\mathrm{red}} \rangle := \mathrm{Tr}_{\{1,\ldots,N\}\setminus\{n\}} \langle \rho_t \rangle$ of the average final state on the same site. We find that on a single site, average time evolution acts as a depolarising channel. This result is formulated in Sec. III B 1.

With this local characterization of initial and average final states, we assess the long-time behavior of $\langle \rho_t^{\text{red}} \rangle$ numerically. Interacting systems may thermalize, or else display many-body localization. In this context, we ask, does $\langle \rho_t \rangle$ locally remember the initial state (localization) or not (thermalization)? For example, imagine an initial state that is homogeneous except for an impurity at one site. Then we ask, after average time evolution, can we perform local measurements at the same or other sites to recover information about the position and initial state of this impurity? We present our corresponding results in Secs. III B 2 and III B 3.

III. RESULTS

In this section, we present our main results for (A) Gaussian circuits or (B) spins. We leave the details of the derivations, as well as the methods used to obtain them, for the next sections.

A. Gaussian circuits

First, we consider the setting of Gaussian circuits. We will first consider the inhomogeneous case, where orthogonal matrices for different sites are independently random. Then we will give the results for the homogeneous case, where the time evolution operator is invariant under translations by two sites.

1. Inhomogeneous evolution exhibits localization

For uncorrelated initial states Γ_0, i.e., 2×2 block-diagonal Γ_0, we find the following result:

$$\langle \Gamma_t \rangle = c(t, N)\Gamma_0. \tag{11}$$

The constant $c(t, N)$ is independent of the initial state. We obtain this result for both the orthogonal Haar measure, $P_i, Q_i \in \mathrm{O}(4)$, as well as the special orthogonal Haar measure, $P_i, Q_i \in \mathrm{SO}(4)$, with the same constant $c(t, N)$ in both cases. The latter case holds as long as $t < (N-1)/2$, i.e. the system is large enough to accommodate the lightcone without self-intersections. Hence in the thermodynamic limit, O(4) and SO(4) Haar averages are equivalent in this setting. We prove these results in Sec. IV B.

We further study $c(t, N)$ numerically, and plot it in Fig. 2 as a function of time steps t for different system sizes N. We observe that $c(t, N)$ converges to a fixed value $c \approx 0.06$, irrespective of N. After one time step, $c(1, N) = 0$ exactly, which simply is thermalizing evolution with independent Haar distributed orthogonals. Only at longer times does the time-periodic structure of the circuit become manifest and result in appreciably change in measure. Since $c(t, N)$ reaches a nonzero value, we find that Anderson localization still happens in this extended setup; an initially localized impurity stays localized. Each site of the initial state is simply scaled towards the thermal mixture $\Gamma = 0$ by the same factor $c(t, N)$. Nevertheless, after average time evolution, the initial state's covariance matrix can still be fully reconstructed from measured expectation values, albeit their variances increase.

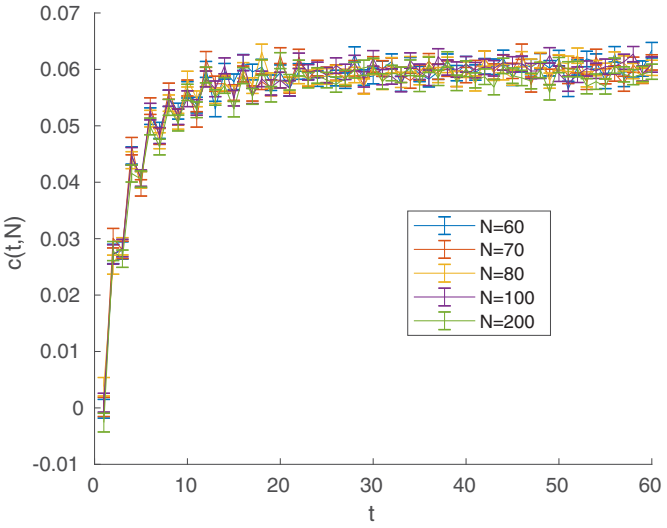

FIG. 2. The constant $c(t, N)$ with which a fermionic covariance matrix is scaled by random time evolution for t time steps, see Eq. (11). We generate 10^4 samples of O(4)-Haar-distributed $P_i, Q_i \in \mathrm{O}(4)$ for each data point. Surprisingly, $c(t, N)$ does not depend on system size N even for t large enough such that the lightcone wraps around the periodic boundaries.

2. Homogeneous evolution delocalizes

Next, let us consider a homogeneous time evolution operator, where $P_i = P_j \in \mathrm{O}(4)$ and $Q_i = Q_j \in \mathrm{O}(4)$ are distributed according to the orthogonal Haar measure. Let Γ_0^n be an initial state with a single site n occupied and all others maximally mixed. This is a zero matrix, except that the 2×2 block for site n is $\gamma := \left(\begin{smallmatrix} 0 & 1 \\ -1 & 0 \end{smallmatrix}\right)$. In Sec. IV C, we show the time-averaged final state of this initially localized state to have the covariance matrix

$$\left\langle \Gamma_{t\text{-avg}}^n \right\rangle := \lim_{T\to\infty} \frac{1}{T} \sum_{t=0}^{T-1} \left\langle \Gamma_t^n \right\rangle = \frac{1}{N/2} \Gamma_\star, \tag{12}$$

under a plausible assumption about disjointness of spectra of matrices that are multiplied by Haar-random orthogonal matrices which we also verified numerically. We characterize $\Gamma_\star$ further in Sec. IV C.

An important part of the result is that the covariance matrix $\Gamma_\star$ depends not on the precise value of n but only on n mod 4. Thus the location n of the impurity cannot be reconstructed from $\langle \Gamma_{t\text{-avg}}^n \rangle$. Moreover, in the thermodynamic limit, the prefactor $1/(N/2)$ causes $\langle \Gamma_{t\text{-avg}}^n \rangle$ to reach the infinite temperature thermal mixture 0. In conclusion, our result implies the absence of localization.

A complementary viewpoint of delocalization is provided by the delocalization of eigenvectors of a single generic random instance of the time evolution operator. In Sec. IV C 1, we prove how this allows us to bound all matrix elements of $\Gamma_{t\text{-avg}}^n$ for a generic evolution operator O with nondegenerate spectrum:

$$\left| \left(\Gamma_{t\text{-avg}}^n \right)_{ij} \right| \leqslant \frac{16}{N} \to 0, \tag{13}$$

in the thermodynamic limit, without resorting to an ensemble average $\langle\cdots\rangle$. On the one hand, this result is stronger than (12) insofar as it shows $\Gamma^n_{t\text{-avg}} \to 0$ in the thermodynamic limit already for single instances of the time evolution operator. On the other hand, it only gives a bound $\leqslant \frac{16}{N}$ and not an explicit form.

B. Spins

We now move from Gaussian circuits to interacting spins. The average $\langle\cdots\rangle$ is now an average over all nearest-neighbor unitaries $U_i, V_i \in U(d^2)$ comprising the time evolution operator, independently distributed according to some probability distribution with single-site Haar invariance (see Sec. II B). Here we will first present the statement that relates the evolution of a single site with a depolarising channel. Then, we show results, which indicate the absence of localization when averaging with the Haar measure on U(4). Finally, we will consider different unitary ensembles, which vary in the degree of entanglement the U_i, V_i generate and present numerical evidence for a thermal-MBL phase transition.

1. Depolarising channel on each site

Our first result is, that on a single site, the average time evolution (10) acts as a depolarising channel. To make this result precise, consider an arbitrary initial state ρ_0. Split its reduced density matrix for one site

$$\rho_0^{\text{red}} = \mathbb{I}_d/d + \bar{\rho}_0^{\text{red}} \tag{14}$$

into traceful and traceless part $\bar{\rho}_0^{\text{red}}$. For the evolved reduced state at the same site, we prove

$$\left\langle \rho_t^{\text{red}} \right\rangle = \mathbb{I}_d/d + \alpha(t)\, \bar{\rho}_0^{\text{red}}. \tag{15}$$

This corresponds to a depolarising channel [33] with depolarization probability $1-\alpha(t)$. The real constant $\alpha(t)$ is independent of the initial state. Provided the lightcone ($2t+1$ sites in width) around the site fits into the system, it is also independent of the position of the site and of system size. Moreover, it is striking that the final state on a single site is affected only by the initial state on the same site, and is independent of the initial state at all other sites. We prove (15) in Sec. IV D where we also derive a similar formula for the two-site reduced density matrix.

If the initial state is free of intersite correlations, with all but one site completely mixed, the final state can be fully characterized. Thereby the initial state $\rho_0 = \mathbb{I}_d/d \otimes \rho_0^{\text{red}} \otimes \mathbb{I}_d/d \otimes \mathbb{I}_d/d \otimes \cdots$ evolves to a final state with the same structure $\langle\rho_t\rangle = \mathbb{I}_d/d \otimes \langle\rho_t^{\text{red}}\rangle \otimes \mathbb{I}_d/d \otimes \mathbb{I}_d/d \otimes \cdots$.

To understand the behavior of the system, it is necessary to determine the behavior of $\alpha(t)$. For this, we will study $\alpha(t)$ numerically for spin 1/2 particles, $d = 2$. In order to access long times, we use a new numerical method (Sec. V). It reduces the complexity for t time steps from $2^{2(2t+1)}$ to 2^t and uses an importance sampling technique to lower the variance. Since the number of spins involved after t time steps is $2t+1$, this in turn has allowed us to reach 39 of them while maintaining an effectively infinite system size.

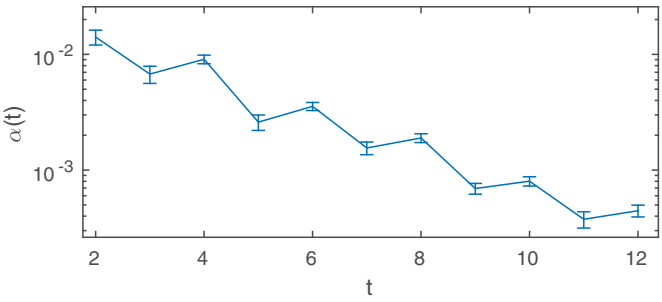

FIG. 3. The constant $\alpha(t)$ relating initial and final states (15) for Haar-distributed unitaries. The figure is indicative of thermalization at long times as α vanishes exponentially in time. For each data point, 10^3 samples of random unitaries were generated.

2. Haar-distributed unitaries thermalize

As a concrete probability distribution for the unitaries U_i, V_i, we first consider the Haar distribution on U(4). In Fig. 3, we present numerical results for this probability distribution. They show that α vanishes exponentially as $t \to \infty$, with a half-life of about 1.8 time steps. Therefore we find thermalization to a locally infinite temperature state: the map (15) describing a single site's evolution becomes completely depolarising in the limit $t \to \infty$ where $\alpha \to 0$. A similar result has been obtained in Ref. [23] in a Hamiltonian (continuous time evolution) setting.

This result is in stark contrast to the analogous setting with Gaussian circuits (Sec. III A 1). A Floquet operator built of unitaries conserving Gaussianity as studied in that setting causes localization, while taking into account all unitaries, it causes thermalization. The reason for this difference can be attributed to the fact that MBL phases are not ubiquitous in parameter space [34], whereas Anderson localization is (in 1D models, as analysed here).

3. Tunable coupling strength and MBL transition

As seen in the previous section, the Haar distribution exhibits thermalizing behavior, since MBL can typically only be found for strong random potentials relative to the coupling [34]. In practice, Haar-distributed U_i and V_i contain many highly entangling operators, which can move information that is initially contained in one site across the chain. This opens up the question of whether MBL can be found by considering less entangling operations. We therefore modify the distribution used for the unitaries composing the time evolution operator.

Every unitary in U(4) can be cast in the form [35]

$$(u_1 \otimes u_2) e^{ia\,\sigma_x\otimes\sigma_x + ib\,\sigma_y\otimes\sigma_y + ic\,\sigma_z\otimes\sigma_z} (u_3 \otimes u_4) \tag{16}$$

with $u_i \in \text{U}(2)$ and coefficients $a, b, c \in \mathbb{R}$. σ_i denote the Pauli matrices. We define a probability distribution for all $U_i, V_i \in \text{U}(4)$ composing the time evolution operator by means of this form, drawing each u_i from the Haar measure for U(2) and a, b, c uniformly from the interval $[-h, h]$. Note that this distribution possesses single-site Haar invariance, so that the results of Sec. III B 1 still apply.

In Fig. 4, we present numerical results for $\alpha(t)$ for distributions with various coupling strengths h. In the figure,

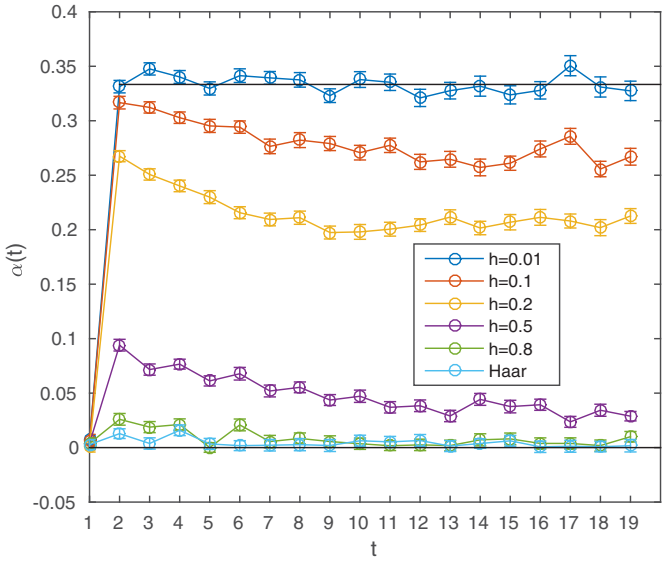

FIG. 4. The constant $\alpha(t)$ relating initial and final states (15) for unitaries distributed according to (16) with random coupling strength h. For strong coupling, $\alpha(t)$ relaxes to zero and the system thermalizes. In contrast, $\alpha(t)$ reaches a finite value at weak couplings and the system displays localization. Horizontal lines indicate $\alpha = 0$ and the exact decoupled value $h = 0$ and $\alpha = 1/3$. See Sec. V for the numerical method used.

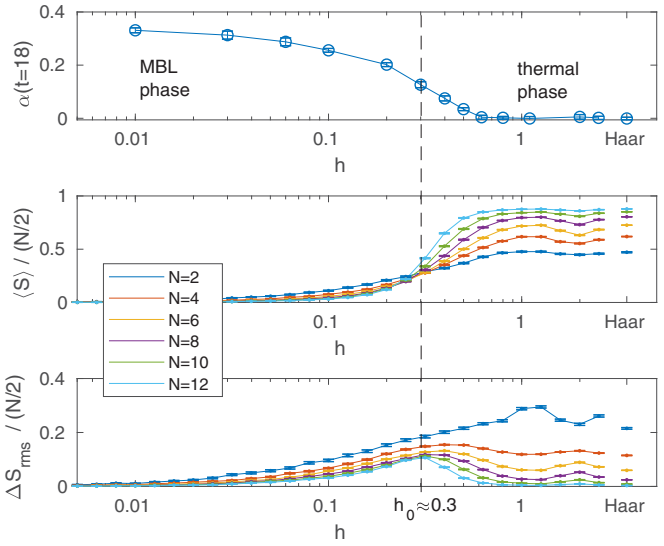

FIG. 5. MBL transition at $h_0 \approx 0.3$. (Top) Late-time value $\alpha(t = 18)$ (as in Fig. 4) as a function of the random coupling strength h, and (rightmost datapoints) for Haar-distributed unitaries. (Middle and bottom) Average bipartite entanglement entropy (base 2) of eigenstates of 10^3 samples of the time evolution operator U, for several system sizes N. In addition to the average entropy of all eigenstates of a random instance U (middle), we calculate the standard deviation of the eigenstates of an instance (bottom). These measures show clear signals of an MBL transition that become more pronounced as the chain length N increases.

we find a crossover from thermalization for large coupling where $\alpha(t) \to 0$ and localization for small coupling where $\alpha(t)$ reaches a finite value and the map (15) keeps information about the initial state. In the completely uncoupled case $h = 0$, $\alpha = 1/3$ is reached exactly (Appendix B), consistent with the behavior for $h \to 0$.

The MBL transition can be extracted from $\alpha(t = \infty)$ as a function of h. Alternatively, it may be pin-pointed by considering the entanglement entropy of the time evolution operator's eigenstates in the limit of an infinite system. In the thermal phase, the eigenstates have volume law entanglement while in the MBL phase they have lower area law entanglement [36,37]. Results obtained from exact diagonalization of small systems are shown in Fig. 5 alongside $\alpha(t = 18)$. It is interesting to consider also the variance of the different eigenstates' entanglement, also plotted in Fig. 5. Because all eigenstates have similar entanglement properties in both thermal and MBL phases, the variance peaks near the phase transition where the entanglement is intermediate between these limits in a way that varies strongly between eigenstates [38]. Those measures all agree and clearly indicate a finite-size or finite-time estimate of the MBL transition at coupling strength near $h_0 \approx 0.3$. Such estimates are known to drift systematically towards the MBL phase as the size of the system is increased [13], as can be seen from the crossings in the middle panel of Fig. 5, so the actual phase transition is most likely at a value of h smaller than this.

IV. PROOFS

In this section, we give detailed proofs for the analytic results reported above. The numerical method is explained in the section after. First, we present a technique used throughout that we call the twirling technique (Sec. IV A). Then we show our results for Gaussian circuits, under inhomogeneous evolution in Sec. IV B and homogeneous evolution in Sec. IV C. In the latter case, we also explain the complementary viewpoint provided by eigenvector delocalization. Finally, we proof the results for spin chains in Sec. IV D.

A. Twirling technique

In this section, we present a technique we call twirling technique, which recurs in the proofs of our results. The idea is to exploit single-site Haar invariance of the probability distribution for the unitaries. Single-site Haar invariance means that any transformation of a U_i or V_i of the form

$$U_i \leftrightarrow (w_1 \otimes w_2) U_i (w_3 \otimes w_4) \tag{17}$$

does not affect averages $\langle \cdots \rangle$, for arbitrary choice of $w_j \in U(d)$.

Our procedure is depicted in Fig. 6. At any site $2n$ (here we demonstrate for even sites), we perform the transformation

$$U_n \to (\mathbb{I}_d \otimes w_{2n}) U_n; V_n \to V_n (w_{2n}^\dagger \otimes \mathbb{I}_d) \tag{18}$$

with arbitrary $w_{2n} \in U(d)$. Then w_{2n} cancels with $w_{2n}^\dagger$ in a repeated application of the time evolution operator U, which transforms as

$$U^t \to w_{2n}^\dagger U^t w_{2n}, \tag{19}$$

w_{2n} only acting on site $2n$.

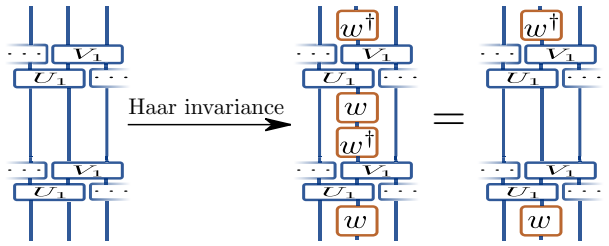

FIG. 6. Illustration of the twirling technique (see Appendix IV A). By single-site Haar invariance, replacing $U_1 \to (\mathbb{I}_d \otimes w)U_1$ and $V_1 \to V_1(w^\dagger \otimes \mathbb{I}_d)$, $w \in U(d)$ does not affect the averaged result. The sketch shows an excerpt of the time evolution operator U. In a repeated application U^t, most w and $w^\dagger$ cancel.

Thus Haar invariance allows us to relate the initial state to the average final state:

$$\langle \rho_t \rangle = \langle U^t \rho_0 U^{t\dagger} \rangle = \langle w_{2n}^\dagger U^t w_{2n} \rho_0 w_{2n}^\dagger U^{t\dagger} w_{2n} \rangle \quad (20)$$

$$= w_{2n}^\dagger \langle \rho_t' \rangle w_{2n} \quad \text{with } \rho_0' = w_{2n} \rho_0 w_{2n}^\dagger. \quad (21)$$

This holds for arbitrary $w_{2n} \in U(d)$ and can be iterated independently at each site. In some cases, it will prove useful to integrate over w_{2n} in (20), which, again, does not alter the result $\langle \cdots \rangle$. An important simplification arises when tracing over sites of the final state, because then in (20) the left- and rightmost $w_{2n}^\dagger$ and w_{2n} cancel. In this paper, we consider only distributions with single-site Haar invariance. Even in its absence, for example, if transformation only with certain w_{2n} are allowed, some results may carry over.

B. Gaussian circuits: Inhomogeneous evolution

In this section, we show the result (11). First, we take $P_i, Q_i \in \mathrm{O}(4)$. Then, we show how to reduce $P_i, Q_i \in \mathrm{SO}(4)$ to the former case.

1. Haar measure on orthogonal group

By linearity of time evolution and Haar-averaging, it suffices to consider only initial states $\Gamma_0^n = \bigoplus_{i=1}^N \delta_{in}\gamma$ having all but site n maximally mixed. The 2×2 covariance matrix for the occupied site is given by $\gamma = \left(\begin{smallmatrix} 0 & 1 \\ -1 & 0 \end{smallmatrix}\right)$.

We adapt the twirling technique (Sec. IV A) to the setting of Gaussian circuits to show that all components of $\langle \Gamma_t^n \rangle$ are zero, except the 2×2 block corresponding to on-site correlations at site n. To this end, consider the transformation

$$\bigoplus P_i \to \Big(\bigoplus P_i\Big)\Sigma; \quad \bigoplus Q_i \to G^\dagger \Sigma G \Big(\bigoplus Q_i\Big) \quad (22)$$

with a diagonal matrix Σ of signs ± 1. Because Σ and $G^\dagger \Sigma G$ have the correct structure to be split among the P_i and Q_i, in spirit of the twirling technique we may perform this transformation using the Haar invariance of the Haar-distributed P_i, Q_i. Specifically, fix $\Sigma_{2n-1,2n-1} = \Sigma_{2n,2n} = +1$ such that $\Sigma \Gamma_0^n \Sigma = \Gamma_0^n$. Then, similarly to (20), single-site Haar invariance implies that

$$\langle \Gamma_t^n \rangle = \langle \Sigma O^t \Sigma \Gamma_0^n \Sigma O^{t\dagger} \Sigma \rangle = \Sigma \langle \Gamma_t^n \rangle \Sigma. \quad (23)$$

For each $i \neq 2n-1, 2n$, we are free to choose $\Sigma_{i,i} = -1$ and all other signs positive. From this we learn that the entire ith row and ith column (except the diagonal entry) of $\langle \Gamma_t^n \rangle$ are zero. The only matrix elements that can be nonzero are the diagonal and the 2×2 block corresponding to site n.

Moreover, the final covariance matrix is real antisymmetric, so the diagonal is also zero and only two entries $\langle \Gamma_t^n \rangle_{2n-1,2n}$, $\langle \Gamma_t^n \rangle_{2n,2n-1}$ remain. These form an antisymmetric 2×2 block at site n. Therefore this block is proportional to the same block of the initial covariance matrix; we can write

$$\langle \Gamma_t^n \rangle = c(t, N, n) \Gamma_0^n. \quad (24)$$

It remains to show that $c(t, N, n)$ are equal for all n. The Haar average treats all unitaries on equal footing, such that within an average O possesses translational invariance by two sites. Therefore $\langle \Gamma_t^{n+2} \rangle = c(t, N, n) \langle \Gamma_0^{n+2} \rangle$, mandating that there can only be two distinct values for n even or odd.

Inversion of the chain corresponds to

$$P_i \to \begin{pmatrix} & \mathbb{I}_2 \\ \mathbb{I}_2 & \end{pmatrix} P_{N/2-i} \begin{pmatrix} & \mathbb{I}_2 \\ \mathbb{I}_2 & \end{pmatrix}, \quad (25)$$

and accordingly for Q_i. It is a symmetry because in the average, $\left(\begin{smallmatrix} & \mathbb{I}_2 \\ \mathbb{I}_2 & \end{smallmatrix}\right)$ can be Haar-absorbed by $P_{N/2-i}$. Inversion invariance implies that there is only one value $c(t, N) = c(t, N, n)$ for both n even and odd, the required form for (11). Any uncorrelated initial state can be decomposed as a linear combination of Γ_0^n's, so by linearity, (11) holds with the same constant $c(t, N)$ for each initial state.

We state a few further conclusions. Note that the particle number of the state changes. Precisely we can formulate

$$c(t, N) = \frac{n(\langle \Gamma_t \rangle)/N - 1/2}{n(\Gamma_0)/N - 1/2} \quad (26)$$

because the particle number $n(\Gamma) = \sum(\lambda_i/2 + 1/2)$ is related to the sum of every second entry λ_i along the state's first offdiagonal. Although we consider Gaussian circuits, transformations beyond those preserving particle number are of paramount importance in this setting (as $c(t, N) \neq 1$) and our results go beyond mere Anderson localization of a single particle.

After one time step, $c(t = 1, N) = 0$ exactly, as direct integration of P_i, Q_i shows [39]. After that, it becomes nonzero. To assess the localising properties of the system, the long-time behavior of $c(t, N)$ is of interest. For this, its time average

$$c(t\text{-avg}, N) := \lim_{T \to \infty} \frac{1}{T} \sum_{t=0}^{T-1} c(t, N) \quad (27)$$

is a useful value. This removes the dependence on the eigenvalues $e^{i\theta_i}$ of O: from (11) we can write

$$c(t, N) = -\tfrac{1}{2} \langle \mathrm{Tr}\, \Gamma_0^n O^t \Gamma_0^n O^{t\dagger} \rangle \quad (28)$$

for any $1 \leqslant n \leqslant N$. Inserting the spectral decomposition $O = \sum_i |v_i\rangle e^{i\theta_i} \langle v_i|$, the generic nondegenerate case $\theta_i \neq \theta_j$ yields

$$c(t\text{-avg}, N) = -\frac{1}{2}\Big\langle \sum_{i,j} \overbrace{\lim_{T\to\infty} \frac{1}{T}\sum_{t=0}^{T-1} e^{i\theta_i t - i\theta_j t}}^{\delta_{ij}} \times \operatorname{Tr} \Gamma_0^n |v_i\rangle\langle v_i| \, \Gamma_0^n |v_j\rangle\langle v_j| \Big\rangle \tag{29}$$

$$= \frac{1}{2}\Big\langle \sum_{i=1}^{2N} \big|\langle v_i|\Gamma_0^n|v_i\rangle\big|^2 \Big\rangle \geqslant 0. \tag{30}$$

While it is expected that this average is strictly positive, its scaling in the thermodynamic limit $N \to \infty$ is unclear. To establish that $c(t, N)$ reaches a finite value and localization holds, we resort to numerical calculations of $c(t, N)$ as shown in Fig. 2.

2. *Haar measure on special orthogonal group*

We will now show that the results for the O(4) Haar measure equally apply when using the SO(4) Haar measure. Let the number of time steps $t < (N-1)/2$, such that the lightcone fits into the periodic system without overlapping. Relate the orthogonal to the special orthogonal group by writing P_i, $Q_i \in \mathrm{O}(4)$ in the form

$$P_i = \begin{pmatrix} 1 & & & \\ & 1 & & \\ & & 1 & \\ & & & -1 \end{pmatrix}^{p_i} \tilde{P}_i, \quad Q_i = \tilde{Q}_i \begin{pmatrix} 1 & & & \\ & -1 & & \\ & & 1 & \\ & & & 1 \end{pmatrix}^{q_i} \tag{31}$$

with $\tilde{P}_i$, $\tilde{Q}_i \in \mathrm{SO}(4)$ and $p_i, q_i \in \mathbb{Z}_2$. Note that the orthogonal Haar distribution for P_i corresponds to the special orthogonal Haar distribution for $\tilde{P}_i$ in combination with the uniform distribution for p_i.

Our strategy will consist in showing that the average

$$\big\langle O^t \Gamma_0^n O^{t\dagger}\big\rangle_{P_i, Q_i \in \mathrm{O}(4)} = \big\langle\big\langle O^t \Gamma_0^n O^{t\dagger}\big\rangle_{\tilde{P}_i, \tilde{Q}_i \in \mathrm{SO}(4)}\big\rangle_{p_i, q_i \in \mathbb{Z}_2} \tag{32}$$

$$= \big\langle O^t \Gamma_0^n O^{t\dagger}\big\rangle_{\substack{\tilde{P}_i,\, \tilde{Q}_i \,\in\, \mathrm{SO}(4) \\ p_i,\, q_i \text{ fixed}}}$$

$$= \big\langle O^t \Gamma_0^n O^{t\dagger}\big\rangle_{P_i, Q_i \in \mathrm{SO}(4)} \tag{33}$$

is independent of how p_i, q_i are fixed, i.e., the equality of (32) and (33). Then the equality of O(4) and SO(4) averages immediately follows for all states; these can can be written as linear combinations of Γ_0^n's. We may absorb all q_i into p_i by the transformation $q_i \to 0$, $p_i \to p_i + q_i$, which uses associativity of matrix multiplication to regroup q_i from $\tilde{Q}_i$ to p_i and $\tilde{P}_i$.

Thanks to SO(4) Haar invariance of $\tilde{Q}_k$ and $\tilde{P}_{k+1}$ (for each index k in turn), whenever $p_k = 1$ we may perform the transformation $p_k \to 0$, $p_{k+1} \to p_{k+1} + 1$. Specifically, this follows from the SO(4)-Haar-invariant transformations

$$\tilde{Q}_k \to \tilde{Q}_k \begin{pmatrix} 1 & & & \\ & -1 & & \\ & & 1 & \\ & & & -1 \end{pmatrix},$$

$$\tilde{P}_{k+1} \to \begin{pmatrix} 1 & & & \\ & -1 & & \\ & & 1 & \\ & & & -1 \end{pmatrix} \tilde{P}_{k+1}. \tag{34}$$

Iterating this transformation for increasing values of k, we may set all $p_i = 0$ except for $p_{N/2}$ which may be 0 or 1. Due to the lightcone size, all occurences of $p_{N/2}$ are multiplied by the zeros in the initial state $\Gamma_0^n = \bigoplus_i \delta_{in}\gamma$ (for $n = N/2$, other initial sites n follow similarly). In conclusion, the average (33) is independent of all p_i, q_i and the main result (11) holds for both the O(4) and SO(4) Haar measures.

C. Gaussian circuits: Homogeneous evolution

In this section, the time evolution operator O is homogeneous, $P = P_i = P_j \in \mathrm{O}(4)$, $Q = Q_i = Q_j \in \mathrm{O}(4)$. We show the result (12) summarized in Sec. III A 2.

a. Fourier transformation of problem. First, let us perform a Fourier transformation of the problem. The periodic structure of O suggests a Fourier transform of two-site blocks with $\mathcal{F} \otimes \mathbb{I}_4$, employing the $N/2 \times N/2$ discrete Fourier matrix

$$\mathcal{F}_{kj} := \frac{1}{\sqrt{N/2}} \exp\left(-2\pi i \frac{(k-1)(j-1)}{N/2}\right), \tag{35}$$

where $k, j = 1, \ldots, N/2$. We will denote Fourier transformed quantities with a hat. The time evolution operator O is block-circulant (4), hence its Fourier transform is block-diagonal and can be written in terms of the diagonal components

$$O \xrightarrow{\mathcal{F}\otimes\mathbb{I}_4} \bigoplus_{k=1}^{N/2} \hat{O}_k, \;\; \hat{O}_k = \hat{G}_k Q \hat{G}_k^\dagger P \in \mathrm{U}(4), \tag{36}$$

with $\hat{G}_k := \left(\begin{smallmatrix} 0 & \exp(2\pi i k/(N/2))\mathbb{I}_2 \\ \mathbb{I}_2 & 0 \end{smallmatrix}\right)$.

b. Localized initial state. Consider now the localized initial state $\Gamma_0^n = \bigoplus_{i=1}^N \delta_{in}\gamma$ with site n occupied (without any loss of generality, we consider n odd) and all other sites maximally mixed. Its Fourier transform is not block-diagonal as for the time evolution operator (36), but also has off-diagonal blocks

$$\Gamma_0^n \xrightarrow{\mathcal{F}\otimes\mathbb{I}_4} \big(\hat{\Gamma}_0^n\big)_{kl} = \frac{1}{N/2} e^{i\phi_{kl}} \begin{pmatrix} \gamma & \\ & 0 \end{pmatrix} \tag{37}$$

with phases $\phi_{kl} = 2\pi(n-1)(k-l)/N$. Accordingly, the final state has off-diagonal blocks, too

$$\langle \Gamma_t^n \rangle \xrightarrow{\mathcal{F}\otimes\mathbb{I}_4} \big\langle \hat{\Gamma}_t^n \big\rangle_{kl} = \frac{1}{N/2} e^{i\phi_{kl}} \Big\langle \hat{O}_k^t \begin{pmatrix} \gamma & \\ & 0 \end{pmatrix} \hat{O}_l^{t\dagger} \Big\rangle. \tag{38}$$

Numerical calculations provide evidence that all blocks $\langle \hat{\Gamma}_t^n \rangle_{kl}$ vanish as $t \to \infty$, except for the diagonal $k = l$, and the pairs $(k, l) = (N/2, N/4)$, $(k, l) = (N/4, N/2)$. These pairs only exist for N divisible by four and correspond to the Fourier phases 0 and π. Only for these two pairs are both $\hat{O}_k$ and $\hat{O}_l$ real.

c. Time-average for localized initial state. As we now argue, in the time average $\langle \Gamma_{t\text{-avg}}^n \rangle$ all Fourier blocks $\langle \hat{\Gamma}_{t\text{-avg}}^n \rangle_{kl}$, $k \neq l$, $(k, l) \neq (N/2, N/4)$, $(k, l) \neq (N/4, N/2)$ are zero. Inserting the spectral decomposition $\hat{O}_k = \sum_{i=1}^4 e^{i\theta_{k,i}} |v_{k,i}\rangle\langle v_{k,i}|$,

the time average is

$$\left\langle \hat{\Gamma}^n_{t\text{-avg}} \right\rangle_{kl} = \frac{e^{i\phi_{kl}}}{N/2} \Bigg\langle \sum_{i,j=1}^{4} \overbrace{\lim_{T\to\infty} \frac{1}{T} \sum_{t=0}^{T-1} e^{i(\theta_{k,i}-\theta_{l,j})t}}^{(*)} \times |v_{k,i}\rangle\langle v_{k,i}| \begin{pmatrix} \gamma & \\ & 0 \end{pmatrix} |v_{l,j}\rangle\langle v_{l,j}| \Bigg\rangle. \quad (39)$$

For each fixed pair (k,l), whenever the sets of eigenvalues $\{e^{i\theta_{k,i}}, i=1,2,3,4\}$ of $\hat{O}_k$ and $\{e^{i\theta_{l,i}}, i=1,2,3,4\}$ of $\hat{O}_l$ are disjoint, $(*)$ is zero. Moreover, for the Haar average $\langle \hat{\Gamma}^n_{t\text{-avg}} \rangle_{kl}$ to vanish for any given pair (k,l), it suffices that the eigenvalue sets are disjoint for all P, Q except a measure zero set. We conjecture that this holds for all pairs (k,l), $k \neq l$ and $(k,l) \neq (N/2, N/4)$, $(k,l) \neq (N/4, N/2)$ [40].

In conclusion, in the time average of (38) of an initially localized state, only Fourier components $k = l$ and $k, l = N/2, N/4$ survive:

$$\left\langle \Gamma^n_{t\text{-avg}} \right\rangle \xrightarrow{\mathcal{F}\otimes\mathbb{I}_4} \left\langle \hat{\Gamma}^n_{t\text{-avg}} \right\rangle_{kl} \quad (40a)$$

$$= \frac{\delta_{k=l}}{N/2} \lim_{T\to\infty} \frac{1}{T} \sum_{t=0}^{T-1} \left\langle \hat{O}_k^t \begin{pmatrix} \gamma & \\ & 0 \end{pmatrix} \hat{O}_k^{t\dagger} \right\rangle \quad (40b)$$

$$+ \frac{\delta_{k=N/2,l=N/4} + \delta_{k=N/4,l=N/2}}{N/2} \quad (40c)$$

$$\times e^{i\phi_{kl}} \lim_{T\to\infty} \frac{1}{T} \sum_{t=0}^{T-1} \left\langle \hat{O}_k^t \begin{pmatrix} \gamma & \\ & 0 \end{pmatrix} \hat{O}_l^{t\dagger} \right\rangle. \quad (40d)$$

Note that the position n of the initial localization is present in (40b) only as n mod 2, determining $\left(\begin{smallmatrix} \gamma & \\ & 0 \end{smallmatrix}\right)$ or $\left(\begin{smallmatrix} 0 & \\ & \gamma \end{smallmatrix}\right)$, and in (40d) only as n mod 4, in the phase $\phi_{kl} = 2\pi(n-1)(k-l)/N = \pm\pi/2\,(n-1)$.

The Fourier back transformation is

$$\left\langle \Gamma^n_{t\text{-avg}} \right\rangle = \frac{1}{N/2} \Gamma_\star := \frac{1}{N/2} (\Gamma'_\star + \Gamma''_\star), \quad (41)$$

where $\Gamma'_\star$ denotes the back transform arising from the diagonal Fourier components (40b) and $\Gamma''_\star$ the back transform arising from the Fourier components $k, l = N/2, N/4$ (40d), each without the prefactor $1/(N/2)$. As discussed in the previous paragraph, $\Gamma_\star$ is only dependent on n mod 4 and, thanks to the prefactor, vanishes in the limit $N \to \infty$. This concludes our result (12).

d. Translation-invariant initial state. On top of the results summarized in Sec. III A 2, we provide a characterization of $\Gamma'_\star$. For this, we need to first consider the translation-invariant initial state $\Gamma_0^{\text{t.i.}}$ with each site occupied. It is invariant under Fourier transformation:

$$\Gamma_0^{\text{t.i.}} = \bigoplus_{i=1}^{N} \gamma \xrightarrow{\mathcal{F}\otimes\mathbb{I}_4} \hat{\Gamma}_0^{\text{t.i.}} = \bigoplus_{k=1}^{N/2} \begin{pmatrix} \gamma & \\ & \gamma \end{pmatrix}. \quad (42)$$

The final state has a block-diagonal Fourier transform and each block has the form

$$\left\langle \Gamma_t^{\text{t.i.}} \right\rangle = \left\langle O^t \Gamma_0^{\text{t.i.}} O^{t\dagger} \right\rangle \xrightarrow{\mathcal{F}\otimes\mathbb{I}_4} \left\langle \hat{\Gamma}_t^{\text{t.i.}} \right\rangle_k = \left\langle \hat{O}_k^t \begin{pmatrix} \gamma & \\ & \gamma \end{pmatrix} \hat{O}_k^{t\dagger} \right\rangle. \quad (43)$$

We will now relate the translation-invariant state's time average $\langle \Gamma^{\text{t.i.}}_{t\text{-avg}} \rangle$ to $\Gamma'_\star$ in the time average of localized initial states.

e. Relating $\Gamma'_\star$ to $\langle \Gamma^{\text{t.i.}}_{t-\text{avg}} \rangle$. We now show that $\Gamma'_\star = \langle \Gamma^{\text{t.i.}}_{t\text{-avg}} \rangle$ except that all rows and columns corresponding to even sites are zero. For this, we exploit Haar invariance, similarly to the twirling technique and the case of inhomogeneous fermionic time evolution. The twirling technique can be used either with the original time evolution operator (4) and (6) or equivalently directly in the Fourier transformed quantities (36) and (43), which in the following is the perspective we take.

First, we show that $\langle \hat{\Gamma}_t^{\text{t.i.}} \rangle_k$ [see (43)] is 2×2 block-diagonal. This follows from the transformation

$$P \to P\Sigma, \quad Q \to \hat{G}_k^\dagger \Sigma^\dagger \hat{G}_k Q \quad (44)$$

with $\Sigma = \left(\begin{smallmatrix} \pm\mathbb{I}_2 & \\ & \pm\mathbb{I}_2 \end{smallmatrix}\right)$. Note that $\hat{G}_k^\dagger \Sigma^\dagger \hat{G}_k$ is real orthogonal as required to apply O(4) Haar invariance. This transformation effects, as in (20),

$$\left\langle \hat{\Gamma}_t^{\text{t.i.}} \right\rangle_k = \langle \Sigma^\dagger \hat{O}_k^t \Sigma \begin{pmatrix} \gamma & \\ & \gamma \end{pmatrix} \Sigma^\dagger \hat{O}_k^{t\dagger} \Sigma \rangle = \Sigma^\dagger \langle \hat{\Gamma}_t^{\text{t.i.}} \rangle_k \Sigma. \quad (45)$$

With appropriate choice of signs in Σ it follows that the off-diagonal blocks of $\langle \hat{\Gamma}_t^{\text{t.i.}} \rangle_k$ vanish.

Now we are in a position to show the relation between $\langle \hat{O}_k^t \left(\begin{smallmatrix} \gamma & \\ & \gamma \end{smallmatrix}\right) \hat{O}_k^{t\dagger} \rangle$ and $\langle \hat{O}_k^t \left(\begin{smallmatrix} \gamma & \\ & 0 \end{smallmatrix}\right) \hat{O}_k^{t\dagger} \rangle$ appearing in the Fourier transformations of $\langle \Gamma^{\text{t.i.}}_{t\text{-avg}} \rangle$ and $\Gamma'_\star$, respectively. For this, use the transformation (44) with

$$\Sigma = \begin{pmatrix} 1 & & & \\ & 1 & & \\ & & 0 & 1 \\ & & 1 & 0 \end{pmatrix}. \quad (46)$$

Again, note $\hat{G}_k^\dagger \Sigma \hat{G}_k$ is real. Then

$$\begin{aligned} &\left\langle \hat{O}_k^t \begin{pmatrix} \gamma & \\ & 0 \end{pmatrix} \hat{O}_k^{t\dagger} \right\rangle \\ &= \frac{1}{2} \left[\left\langle \hat{O}_k^t \begin{pmatrix} \gamma & \\ & \gamma \end{pmatrix} \hat{O}_k^{t\dagger} \right\rangle + \left\langle \hat{O}_k^t \begin{pmatrix} \gamma & \\ & -\gamma \end{pmatrix} \hat{O}_k^{t\dagger} \right\rangle \right] \\ &= \frac{1}{2} \left[\left\langle \hat{O}_k^t \begin{pmatrix} \gamma & \\ & \gamma \end{pmatrix} \hat{O}_k^{t\dagger} \right\rangle + \left\langle \hat{O}_k^t \Sigma \begin{pmatrix} \gamma & \\ & \gamma \end{pmatrix} \Sigma \hat{O}_k^{t\dagger} \right\rangle \right] \\ &= \frac{1}{2} \left[\left\langle \hat{O}_k^t \begin{pmatrix} \gamma & \\ & \gamma \end{pmatrix} \hat{O}_k^{t\dagger} \right\rangle + \Sigma \left\langle \hat{O}_k^t \begin{pmatrix} \gamma & \\ & \gamma \end{pmatrix} \hat{O}_k^{t\dagger} \right\rangle \Sigma \right], \end{aligned} \quad (47)$$

with the last equality due to Haar invariance. Thanks to one term without and one term conjugated by Σ, the first block stays the same and the second block (which corresponds to even sites) cancels. This carries through the Fourier transform $\mathcal{F} \otimes \mathbb{I}_4$, concluding our proof that $\Gamma'_\star = \langle \Gamma^{\text{t.i.}}_{t\text{-avg}} \rangle$ except that all rows and columns corresponding to even sites are zero.

f. Characterization of $\langle \Gamma_t^{t.i.} \rangle$. Now we will further characterize $\langle \Gamma_t^{\text{t.i.}} \rangle$ arising from the translation-invariant initial state. In terms of the Fourier components of $\langle \Gamma_t^{\text{t.i.}} \rangle$, we show below

that

$$\langle \hat{\Gamma}_t^{\text{t.i.}} \rangle_k = c(t,k,N) \begin{pmatrix} \gamma & \\ & \gamma \end{pmatrix}, \tag{48}$$

with a real constant $c(t,k,N)$. This is a similar form as the main result (11) except that there is one constant per Fourier component. The methods in the proof following are also very similar.

We have shown already that $\langle \hat{\Gamma}_t^{\text{t.i.}} \rangle_k$ consists of two 2×2 blocks, in the paragraph of equation (44). $\langle \hat{\Gamma}_t^{\text{t.i.}} \rangle_k$ is evidently anti-Hermitian as a real antisymmetric matrix conjugated with a unitary (43). To prove (48), it remains to show that both blocks are real and identical.

First, we show that both blocks are real. To this end, use the transformation (44) with

$$\Sigma = \begin{pmatrix} 0 & 1 & & \\ -1 & 0 & & \\ & & 0 & 1 \\ & & -1 & 0 \end{pmatrix}. \tag{49}$$

Note that $\hat{G}_k^\dagger \Sigma^\dagger \hat{G}_k$ is real orthogonal, so Haar invariance of P and Q's probability distribution is applicable. For anti-Hermitian 2×2 matrices X,

$$X = \begin{pmatrix} 0 & 1 \\ -1 & 0 \end{pmatrix}^\dagger X \begin{pmatrix} 0 & 1 \\ -1 & 0 \end{pmatrix} \Rightarrow X \text{ real antisymmetric.} \tag{50}$$

Therefore the transformation's effect (45) shows that both blocks are real.

Lastly, we show that both blocks are identical. This is achieved by considering inversion symmetry of the chain. Inversion corresponds to

$$P \to \begin{pmatrix} & \mathbb{I}_2 \\ \mathbb{I}_2 & \end{pmatrix} P \begin{pmatrix} & \mathbb{I}_2 \\ \mathbb{I}_2 & \end{pmatrix} \tag{51}$$

and likewise for Q. This is equivalent to

$$\hat{O}_k \to \begin{pmatrix} & \mathbb{I}_2 \\ \mathbb{I}_2 & \end{pmatrix} \hat{O}_k^* \begin{pmatrix} & \mathbb{I}_2 \\ \mathbb{I}_2 & \end{pmatrix} \tag{52}$$

and

$$\langle \hat{\Gamma}_t^{\text{t.i.}} \rangle_k \to \begin{pmatrix} & \mathbb{I}_2 \\ \mathbb{I}_2 & \end{pmatrix} \langle \hat{\Gamma}_t^{\text{t.i.}} \rangle_k^* \begin{pmatrix} & \mathbb{I}_2 \\ \mathbb{I}_2 & \end{pmatrix}. \tag{53}$$

Thus inversion invariance mandates that both real blocks are the same.

g. Characterization of $c(t,k,N)$. To understand $\langle \Gamma_t^{\text{t.i.}} \rangle$, it remains to characterize $c(t,k,N)$. In Fig. 7, we therefore show numerical calculations of $c(t,k,N)$.

The figure shows that $c(t,k,N)$ converges, except for $\frac{2\pi}{N/2}k = 0, \pi, 2\pi$, where there are oscillations in t. We can calculate the time average of values

$$c(t\text{-avg},k,N) = \frac{1}{4} \quad \text{for } \frac{2\pi}{N/2}k = 0, \pi, 2\pi \tag{54}$$

exactly. In these cases, $\hat{G}_k$ is real orthogonal and can be absorbed by the Haar-invariant transformation $Q \to \hat{G}_k^\dagger Q \hat{G}_k$. In turn, Q can be absorbed by the transformation $P \to Q^\dagger P$. Then we have simply $\hat{O}_k = P$; this corresponds to two sites in the uncoupled case and is explained in Appendix A.

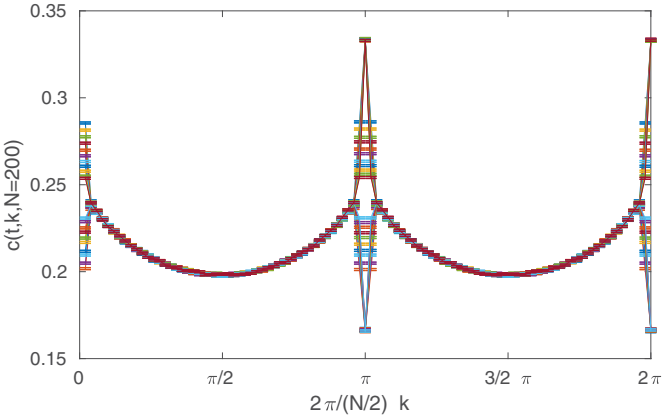

FIG. 7. Constant $c(t,k,N=200)$ for the characterization of $\langle \Gamma_t^{\text{t.i.}} \rangle$ (48) for homogeneous evolution of fermions. Each of the lines shows data for a fixed t from 20 to 50. We perform the orthogonal Haar average by considering 10^6 samples.

The symmetries $k \leftrightarrow -k = N/2 - k$ and "$k \leftrightarrow k + \pi$" of $c(t,k,N)$ are apparent in Fig. 7. The first corresponds to complex conjugation of $\hat{O}_k$, and is a symmetry because $\langle \Gamma_t^{\text{t.i.}} \rangle_k$ is real. The latter symmetry only exists for even $N/2$ and then reads $k \leftrightarrow k + N/4$. It is equivalent to the Haar-invariant transformation

$$Q \to \begin{pmatrix} -\mathbb{I}_2 & \\ & \mathbb{I}_2 \end{pmatrix} Q \begin{pmatrix} \mathbb{I}_2 & \\ & -\mathbb{I}_2 \end{pmatrix}, \tag{55}$$

which effects $e^{\pm 2\pi i k/(N/2)} \to -e^{\pm 2\pi i k/(N/2)}$ in (36).

Homogeneous evolution: Eigenvector delocalization

In this section, we explain in detail a complementary viewpoint to delocalization summarized in Sec. III A 2, eigenvector delocalization. The eigenvectors $\vec{v}_i$ to eigenvalues $e^{i\theta_i}$ of each generic instance of the homogeneous evolution operator O are delocalized. To see this, let $\mathcal{T}$ be the orthogonal operator effecting translation by two sites (four matrix entries). It commutes with O and has $\mathcal{T}^{N/2} = \mathbb{I}_{2N}$. Each $\vec{v}_i$ is therefore eigenvector of $\mathcal{T}$ to a phase ϕ_i and for its components the relation $v_i^{j+4} = e^{\phi_i} v_i^j$ holds circularly. Taking $\vec{v}_i$ normalized,

$$|v_i^j|^2 = \frac{2}{N}\left(\sum_{k=0}^{N/2-1} |v_i^{j+4k}|^2\right) \leqslant \frac{2}{N}|\vec{v}_i|^2 = \frac{2}{N}. \tag{56}$$

In the generic case, where O does not have degenerate eigenvalues, we can give an estimate of the final covariance matrix even without resorting to a Haar average. We expand $\Gamma_{t\text{-avg}}^n$ with the spectral decomposition $O = \sum_k |v_k\rangle e^{i\theta_k} \langle v_k|$ of the specific instance of the time evolution operator:

$$\Gamma_{t\text{-avg}}^n = \lim_{T\to\infty} \frac{1}{T} \sum_{t=0}^{T-1} O^t \Gamma_0^n O^{t\dagger} \tag{57}$$

$$= \sum_{k,l=1}^{2N} \overbrace{\lim_{T\to\infty} \frac{1}{T} \sum_{t=0}^{T-1} e^{i(\theta_k - \theta_l)t}}^{\delta_{\theta_k,\theta_l}} |v_k\rangle\langle v_k| \, \Gamma_0^n \, |v_l\rangle \langle v_l|. \tag{58}$$

Similarly to (29), the time average cancels cross terms.

Let $\vec{e}_j$ be the standard basis. The matrix elements of $\Gamma^n_{t\text{-avg}}$ are then

$$\left\langle e_i|\Gamma^n_{t\text{-avg}}|e_j\right\rangle = \sum_{k=1}^{2N} \langle e_i|v_k\rangle \, \langle v_k|\Gamma^n_0|v_k\rangle \, \langle v_k|e_j\rangle. \tag{59}$$

With the bound (56) for the eigenvector's components, we can show the estimate (13) by expanding $\Gamma^n_0 = |e_{2n-1}\rangle\langle e_{2n}| - |e_{2n}\rangle\langle e_{2n-1}|$:

$$\left|\left(\Gamma^n_{t\text{-avg}}\right)_{ij}\right| = \left|\langle e_i|\Gamma^n_{t\text{-avg}}|e_j\rangle\right| \tag{60}$$

$$\leqslant \underbrace{\sum_{k=1}^{2N}}_{2N} \underbrace{|\langle e_i|v_k\rangle|}_{\leqslant\sqrt{2/N}} \underbrace{|\langle v_k|\Gamma^n_0|v_k\rangle|}_{\leqslant 4/N} \underbrace{|\langle v_k|e_j\rangle|}_{\leqslant\sqrt{2/N}} \leqslant \frac{16}{N}. \tag{61}$$

D. Spins

In this section, we prove our analytic results about spin chains summarized in Sec. III B 1, using the twirling technique from Sec. IV A. We require the probability distribution for the unitaries U_i, V_i comprising the unitary-circuit time evolution operator to possess single-site Haar invariance, as introduced in the settings II B.

The integral over the unitary group

$$\begin{aligned}\int_{U(d)} dw_n \, w_n^\dagger A w_n B_n w_n^\dagger C w_n \\ = \frac{\mathbb{I}_d^n}{d} \operatorname{Tr}_n(B_n) \otimes \frac{d\operatorname{Tr}_n(AC) - \operatorname{Tr}_n(A)\operatorname{Tr}_n(C)}{d^2-1} \\ + B_n \otimes \frac{d\operatorname{Tr}_n(A)\operatorname{Tr}_n(C) - \operatorname{Tr}_n(AC)}{d(d^2-1)}\end{aligned} \tag{62}$$

can be computed exactly [41]. Here, $A, C \in U(d^N)$ are multiqudit operators and $w_n, B_n \in U(d)$ act only on one qudit at site n. The left side of the tensor products is qudit n, while the right side contains all the other sites. The same result is obtained when averaging over a unitary 2-design such as, for qubits, the Clifford group [42] instead of entire $U(d)$.

Similarly, we have the integral

$$\int_{U(d)} dw_i \, w_i D w_i^\dagger = \operatorname{Tr}_i(D) \otimes \mathbb{I}_d^i/d, \tag{63}$$

where $D \in U(d^N)$ is a multiqudit operator and $w_i \in U(d)$ acts only on one qudit at site i. The identity $\mathbb{I}_d^i/d$ is at the qudit site i, which is traced out from D. The integral holds equally for the integrand $w_i^\dagger D w_i$. For this integral, a unitary 1-design is sufficient for w_i, such as for $d = 2$ the Pauli matrices together with the identity.

To show our result (15) for a single-site reduced density matrix at site n, let $I = \{1 \ldots N\}\backslash\{n\}$ be the set of all other sites. Let ρ_0 be the (arbitrary) initial state. With this notation, we will compute the relation between $\operatorname{Tr}_I \rho_0$ and

$$\operatorname{Tr}_I \langle \rho_t\rangle = \operatorname{Tr}_I \langle U^t \rho_0 U^{t\dagger}\rangle. \tag{64}$$

At each site $i \in I$ in turn, the twirling technique (20) results in

$$\operatorname{Tr}_I \langle \rho_t\rangle = \operatorname{Tr}_I \langle w_i^\dagger U^t w_i \rho_0 w_i^\dagger U^{t\dagger} w_i\rangle = \operatorname{Tr}_I \langle U^t w_i \rho_0 w_i^\dagger U^{t\dagger}\rangle. \tag{65}$$

We may integrate over w_i, whose choice is arbitrary, by setting $D = \rho_0$ in formula (63). This gives

$$\operatorname{Tr}_I \langle \rho_t\rangle = \operatorname{Tr}_I \langle U^t [\operatorname{Tr}_i(\rho_0) \otimes \mathbb{I}_d^i/d] U^{t\dagger}\rangle. \tag{66}$$

Iteration of this procedure for each $i \in I$ yields

$$\operatorname{Tr}_I \langle \rho_t\rangle = \operatorname{Tr}_I \langle U^t [\operatorname{Tr}_I(\rho_0) \otimes \mathbb{I}_{d^{N-1}}^I/d^{N-1}] U^{t\dagger}\rangle. \tag{67}$$

The twirling technique at site n allows us to use formula (62) with $A = U^t$, $B_n = \operatorname{Tr}_I(\rho_0)$, $C = U^{t\dagger}$:

$$\operatorname{Tr}_I \langle \rho_t\rangle = \frac{1}{d^{N-1}} \operatorname{Tr}_I \langle w_n^\dagger U^t w_n \operatorname{Tr}_I(\rho_0) w_n^\dagger U^{t\dagger} w_n\rangle \tag{68}$$

$$= \frac{1}{d^{N-1}} \operatorname{Tr}_I \Bigg\langle \frac{\mathbb{I}_d^n}{d} \operatorname{Tr}_n \operatorname{Tr}_I(\rho_0) \tag{69}$$

$$\otimes \frac{d\operatorname{Tr}_n(AC) - \operatorname{Tr}_n A \operatorname{Tr}_n C}{d^2-1} \tag{70}$$

$$+ \operatorname{Tr}_I(\rho_0) \otimes \frac{d\operatorname{Tr}_n A \operatorname{Tr}_n C - \operatorname{Tr}_n(AC)}{d(d^2-1)} \Bigg\rangle \tag{71}$$

$$= \frac{\mathbb{I}_d^n}{d} \frac{d^2 - \lambda(t)}{d^2-1} + \operatorname{Tr}_I(\rho_0) \frac{\lambda(t)-1}{d^2-1} \tag{72}$$

$$= \frac{\mathbb{I}_d^n}{d} + \underbrace{\frac{\lambda(t)-1}{d^2-1}}_{\alpha(t)} \bar{\rho}_0^n. \tag{73}$$

In the third equality, we have used that $\operatorname{Tr}_n \operatorname{Tr}_I(\rho_0) = 1$, $\operatorname{Tr}_I \operatorname{Tr}_n(AC) = d^N$ and defined the constant

$$\lambda(t) = \left\langle \frac{1}{d^{N-1}} \operatorname{Tr}_I(\operatorname{Tr}_n U^t \operatorname{Tr}_n U^{t\dagger})\right\rangle \tag{74}$$

into which we have moved the remaining Haar average. λ is manifestly real and non-negative. In the final equality, we have rewritten the expression in terms of the traceless part $\bar{\rho}_0^n$ of the initial reduced density matrix $\operatorname{Tr}_I \rho_0$. The form (15) of our result can be obtained by setting $\alpha(t) = \frac{\lambda(t)-1}{d^2-1}$.

A lightcone structure emerges in the definition of λ. Only constituent unitaries of U within a lightcone of velocity 2 around site n contribute to λ, all others cancel with their daggered counterpart in consequence of Tr_I. A longer chain will have an additional $\operatorname{Tr}_i(\mathbb{I}_d)$ at each additional site i outside the lightcone, which is precisely canceled by the higher N in the prefactor. (Figure 8 shows a graphical representation of a slightly different quantity but also serves to illustrate this fact.) In combination with Haar invariance of U, within the average $\langle\cdots\rangle$ that treats all constituent unitaries on equal footing, we realize the following. $\lambda(t)$ is independent of site position n or chain length N as long as the lightcone around n does not intersect a boundary, or, in the case of periodic boundary conditions, itself.

After a single time step, $\lambda(1) = 1$ exactly such that the evolution results in a locally maximally mixed site (73). For longer times, we resort to a numerical method for evaluating $\alpha(t) = \frac{\lambda(t)-1}{d^2-1}$, explained in the next Sec. V.

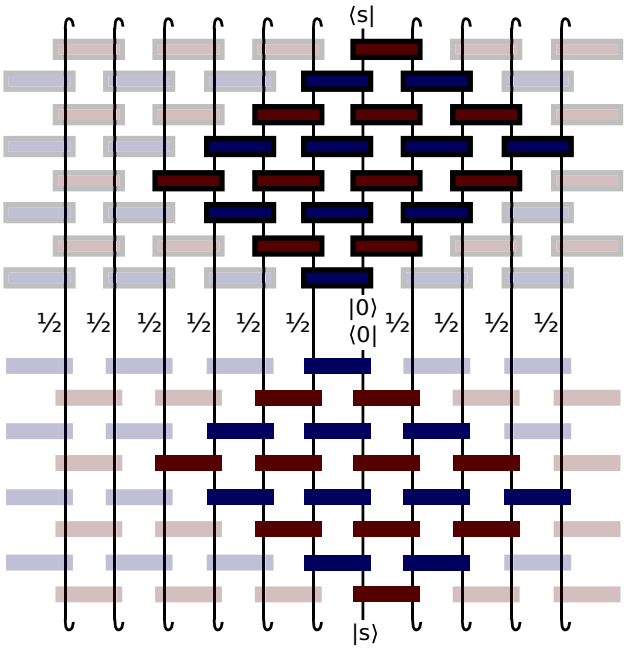

FIG. 8. Diagrammatic representation of (84) for $t = 4$. Unitaries outside of lightcones cancel and two rhomboids remain. A larger system results in more empty traces that do not contribute as they each have a factor $1/2$ attached. Sites are shown in the horizontal direction, unitaries U_i (V_i) are shown as blue (red) boxes. Their daggered counterparts lack a thick border.

Next let us calculate the entire final density matrix $\langle \rho_t \rangle$ for the initial state

$$\rho_0 = \rho_0^n \otimes \mathbb{I}^I_{d^{N-1}}/d^{N-1} \tag{75}$$

that has all sites maximally mixed apart from site n. The twirling technique and formula (63) with $D = U^t \rho_0 U^{t\dagger}$ can be applied at each site $i \in I$ iteratively:

$$\langle \rho_t \rangle = \langle w_i^\dagger U^t w_i \rho_0 w_i^\dagger U^{t\dagger} w_i \rangle = \langle w_i^\dagger U^t \rho_0 U^{t\dagger} w_i \rangle \tag{76}$$

$$= \langle \mathrm{Tr}_i (U^t \rho_0 U^{t\dagger}) \rangle \otimes \mathbb{I}^i_d/d \tag{77}$$

$$= \langle \mathrm{Tr}_I (U^t \rho_0 U^{t\dagger}) \rangle \otimes \mathbb{I}^I_{d^{N-1}}/d^{N-1} \tag{78}$$

$$= \mathrm{Tr}_I \langle \rho_t \rangle \otimes \mathbb{I}^I_{d^{N-1}}/d^{N-1}. \tag{79}$$

All sites of the final state are maximally mixed except for site n, it is related to the initial $\rho_0^n = \mathrm{Tr}_I(\rho_0)$ as per (72).

Let us turn to the behavior of two-site reduced density matrices for the not necessarily adjacent sites n and m, now $I = \{1 \dots N\} \backslash \{n, m\}$. Assume the initial state's reduced density matrix to be a tensor product and split it

$$\mathrm{Tr}_I(\rho_0) = \left(\mathbb{I}^n_d/d + \bar{\rho}_0^n\right) \otimes \left(\mathbb{I}^m_d/d + \bar{\rho}_0^m\right) \tag{80}$$

into traceful and traceless parts.

To determine the final state $\mathrm{Tr}_I \langle \rho_t \rangle$, we employ the same method as before. However we will have to use formula (62) twice, at sites n and m, and the resulting Tr_n and Tr_m terms couple. A calculation yields the compact result

$$\mathrm{Tr}_I \langle \rho_t \rangle = \left(\frac{\mathbb{I}^n_d}{d} + \frac{\lambda - 1}{d^2 - 1}\bar{\rho}_0^n\right) \otimes \left(\frac{\mathbb{I}^m_d}{d} + \frac{\lambda - 1}{d^2 - 1}\bar{\rho}_0^m\right) + \frac{\lambda' - \lambda^2}{(d^2 - 1)^2}\bar{\rho}_0^n \otimes \bar{\rho}_0^m. \tag{81}$$

Here, $\lambda = \lambda(t)$ is the same as before in (74), so the first term is simply an uncorrelated tensor product of the single site result (73). The coefficient

$$\lambda'(t) = \left\langle \frac{1}{d^{N-2}} \mathrm{Tr}_I (\mathrm{Tr}_{n,m}\, U^t\, \mathrm{Tr}_{n,m}\, U^{t\dagger}) \right\rangle \tag{82}$$

appearing in the second term is also real and positive. It depends on $|n - m|$ until the sites are far enough apart such that their lightcones do not intersect. (This requires a sufficient system size.) In that case, $\lambda' = \lambda^2$ and the two-site result (81) reduces to the single-site result (73).

Our method to show that the evolution of a single site is a depolarising channel (73) may readily be generalized to further time evolutions other than the specific quantum circuit considered here. For this, the time-evolution operator must allow for transformations of the form (19), such that the twirling technique can be applied analogously. One such example was studied in Refs. [43,44], which considered a random nonlocal Hamiltonian coupling all N spins, whose diagonalizing matrix is distributed according to the $U(d^N)$ Haar measure. In that case, the expression for $\alpha(t)$ can be simplified in terms of the spectral form factor of the Hamiltonian.

V. NUMERICAL METHOD FOR SPINS

In this section, we present the new numerical method we use for the setting of spin chains. Obtaining numerical values for $\alpha(t)$ of (15) is much more difficult than for $c(t, N)$ in the fermionic case, because the Hilbert space grows exponentially while covariance matrices grow only quadratically in system size N. In the following, we describe a new numerical method that significantly decreases the complexity from 4^{2t+1} to 2^t for t time steps, at effectively infinite system size. For definiteness, we set the local Hilbert space dimension $d = 2$ although our numerical method can be adapted to higher spins.

We determine $\alpha(t)$ by preparing an initial state where one site is spin up $|0\rangle\langle 0|$ and all other sites are maximally mixed. After applying U^t, we project the final reduced density matrix of the one site onto $|0\rangle\langle 0|$. According to (15), this procedure yields

$$(\alpha + 1)/2 = \langle R(U, 0) \rangle_U, \tag{83}$$

$$R(U, s) = \mathrm{Tr}[(\cdots \otimes \mathbb{I}_2 \otimes (|s\rangle\langle s|) \otimes \mathbb{I}_2 \otimes \cdots) \times U^t (\cdots \otimes \mathbb{I}_2/2 \otimes (|0\rangle\langle 0|) \otimes \mathbb{I}_2/2 \otimes \cdots) U^{t\dagger}]. \tag{84}$$

The average $\langle \cdots \rangle_U$ refers to averaging the random U_i, V_i composing U. Leaving the final spin s free allows us to use an importance sampling technique. Before explaining this technique, we will show how to evaluate $R(U, s)$ for a given U, s in a way that is significantly more efficient than the naive procedure.

The evaluation of $R(U, s)$ can be sketched diagrammatically as in Fig. 8. Unitaries outside the light cones cancel in pairs with their daggered counterparts and two rhomboids of width $2t + 1$ sites remain. Considering only this part of the chain, and evaluating the diagram time step by time step, starting from ρ_0 in the middle, we encounter objects of dimension 4^{2t+1}.

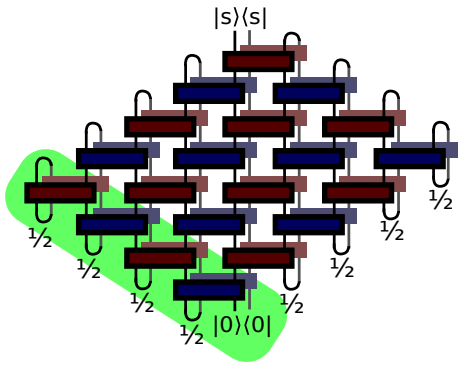

FIG. 9. The rhomboids from Fig. 8 can be folded above each other. The diagram is contracted diagonally, beginning with the shaded green part.

After folding the daggered rhomboid upwards (Fig. 9), we can evaluate the folded rhomboids diagonally. This leads to a square root improvement, we encounter objects of dimension 2^{2t}. Note that this idea may be more generally applicable in tensor network contractions.

Owing to the single-site Haar invariance, the average of (84) remains the same when replacing all of the identities ("U-turns") in the folded rhomboid diagram (Fig. 9) by $|0\rangle\langle 0|$. How this can be achieved is explained in detail in Appendix C. We obtain two (disconnected) rhomboids that correspond to the absolute square of a single rhomboid as illustrated in Fig. 10. Again evaluating diagonally, we gain another square root as the objects only have dimension 2^t.

When sampling $\langle R(U,0)\rangle_U$ according to the single-rhomboid method (Fig. 10), we observe a higher variance than using the folded-rhomboids procedure (Fig. 9). The data in Fig. 3 were compiled with the folded-rhomboids procedure only such that the strongly decreasing variance allows us to resolve the exponential decay of $\alpha(t)$. The exponentially decreasing variance is also indicative of self-averaging of (84). To compile the data in Fig. 4, we want to access longer times and therefore make use of the single-rhomboid optimisation. To counteract the increasing variance, we use an importance sampling technique.

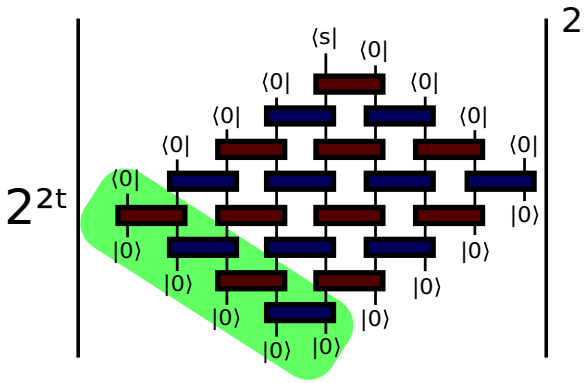

FIG. 10. The absolute value squared of a single rhomboid. The diagram is contracted diagonally starting with the shaded green part. After averaging the unitaries, this diagram has the same value as Fig. 9. See Sec. V and Appendix C for details.

To perform importance sampling, we extend the random variable set to include s alongside $\{U_i\}, \{V_i\}$. Then we generate samples according to the probability distribution $R(U,s)$ with a Metropolis algorithm. Now note that $\langle R(U,0)\rangle_U + \langle R(U,1)\rangle_U = 1$ follows immediately from (84). Thus the normalization of the probability distribution $R(U,s)$ is trivial. The average value of δ_{s0} with respect to this probability distribution therefore results in $\langle R(U,0)\rangle_U = (\alpha+1)/2$.

The method presented here allows us to reduce the complexity of calculating the time evolution of t steps in a system of $2t+1$ sites (size of light cone). Naively, time and space complexity both scale as 4^{2t+1}. Our simplifications give two square roots improvement, yielding a scaling of 2^t. Apart from the average over random unitaries, the numerical procedure is free of approximations.

The Monte Carlo aspect of the method can be generalized to improve the variance of expectation values $R_O = \langle \mathrm{Tr}(O\psi_t)\rangle$ of arbitrary observables O over arbitrary ensembles of initial states or time evolutions determining ψ_t. Towards this end, extend s to a POVM including O instead of just $|0\rangle\langle 0|$ and $|1\rangle\langle 1|$ as for $R(U,s)$ above. Then perform Metropolis sampling of $\langle \mathrm{Tr}(s\psi_t)\rangle$ with respect to the random variables determining ψ_t as well as s, which is taken as an additional random variable. Because of the normalization of the POVM, $\langle \delta_{sO}\rangle_{s,\psi_t} = R_O$.

VI. CONCLUSION AND OUTLOOK

In this paper, we have studied one dimensional particle chains under a random unitary time evolution operator consisting of random nearest-neighbor gates. In spirit of Floquet evolution, the operator is repeated identically for subsequent time steps.

We considered two cases, where the time evolution operator is a Gaussian circuit or consists of general unitaries. First, we were able to show strong results about the average evolution of chains of fermions under the Gaussian circuit time evolution. For Gaussian circuits inhomogeneous in space, we find that any initial state with vanishing two-point correlations at nonzero distances is simply scaled further towards the thermal mixture (11) and the initial two-point correlations can be recovered measuring expectation values; time evolution is localising. If the random time evolution operator is taken homogeneous in space, it delocalizes and leads to thermalization in the thermodynamic limit (12). We expect one can generalize our results to higher order correlation functions than the two-point functions studied in this work.

Next, we also considered spin chains under random unitary nearest-neighbor Floquet dynamics, inhomogeneous in space, with fixed finite local Hilbert space dimension. Our main result is (15); on a single site, the average evolution acts as a depolarising channel, completely independent of any other initial sites.

We employ new numerical methods (Sec. V) to demonstrate that a time evolution composed of Haar distributed unitaries thermalizes. Under a different distribution with tunable random coupling strength, we find two regions of thermalization (strong coupling) and many-body localization (weak coupling), respectively.

As we have studied spins and fermions, it is natural to ask about a bosonic version of the problem. Since, contrary to fermions, each bosonic mode defines an infinite-dimensional Hilbert space, the generalization of Haar unitaries may pose mathematical problems. Nevertheless, for future work it is conceivable to work directly in the symplectic space (that corresponds to the covariance matrices) which is finite.

Both our analytical results as well as the numerical method can readily be generalized to higher dimensions. In the future, they may further also be applied to circuits with different topology and to Hamiltonian Floquet or stroboscopic dynamics with an ensemble of Hamiltonians having single-site Haar invariance.

Note added. During preparation of this manuscript, related work [45] appeared on arXiv that provides evidence for an MBL transition in a different unitary circuit with random coupling strength.

ACKNOWLEDGMENTS

This project has received funding from the European Research Council (ERC) under the European Union's Horizon 2020 research and innovation programme through the ERC Starting Grant WASCOSYS (No. 636201), the ERC Consolidator Grant GAPS (No. 648913), and the ERC Advanced Grant QENOCOBA (No. 742102). D.P.G. acknowledges financial support of Severo Ochoa project SEV-2015-556 funded by MINECO.

APPENDIX A: GAUSSIAN CIRCUITS: UNCOUPLED CASE

In this Appendix, we calculate (54), which we repeat for convenience:

$$c(t\text{-avg}, k, N) = \frac{1}{4} \quad \text{for } \frac{2\pi}{N/2}k = 0, \pi, 2\pi.$$

For these values of k, $\hat{G}_k$ is real and may be absorbed by the Haar-invariant transformation $Q \to \hat{G}_k^\dagger Q \hat{G}_k$ in (36). In turn, Q can be absorbed by the transformation $P \to Q^\dagger P$. Then we have simply $\hat{O}_k = P$.

This corresponds to two sites in the inhomogeneous uncoupled case where $Q_i = \mathbb{I}_4$ in the time evolution operator (4) and only P_i are independently random. We find much stronger localization (intuitively, information cannot spread) where the constant $c(t\text{-avg})$ is one quarter:

$$\langle \Gamma_{t\text{-avg}} \rangle = \tfrac{1}{4}\Gamma_0. \tag{A1}$$

To show this it suffices to consider the first two sites $\Gamma_0^{1,2}$ and $P_1 \in \mathrm{O}(4)$. We introduce an arbitrary $A \in \mathrm{O}(4)$ by $P_1 \to A P_1 A^\dagger$ using Haar invariance

$$\left\langle \Gamma_t^{1,2} \right\rangle = \left\langle A P_1^t A^\dagger \Gamma_0^{1,2} A P_1^{t\dagger} A^\dagger \right\rangle \tag{A2}$$

and are free to integrate A over the orthogonal group. The integral can be evaluated [39] as

$$\left\langle \Gamma_t^{1,2} \right\rangle = \frac{1}{12}\left\langle \left(\operatorname{Tr} P_1^t\right)^2 - \left(\operatorname{Tr} P_1^{2t}\right)\right\rangle \Gamma_0^{1,2} \tag{A3}$$

$$= \frac{1}{12}\left\langle \left(\sum_{i=1}^4 e^{i\beta_i t}\right)^2 - \sum_{i=1}^4 e^{i\beta_i 2t}\right\rangle \Gamma_0^{1,2}, \tag{A4}$$

which is determined by the spectrum $\{e^{i\beta_i}, i = 1, 2, 3, 4\}$ of P_1. We can evaluate this in the time average by observing that almost always

$$\beta_1 = -\beta_2, \quad \beta_3 = -\beta_4 \quad \text{for } \det P_1 = +1 \tag{A5}$$

and

$$\beta_1 = -\beta_2, \quad \beta_3 = 0, \quad \beta_4 = \pi \quad \text{for } \det P_1 = -1. \tag{A6}$$

One can then show that in the time average of (A4), $\langle \cdots \rangle_{\det P_1 = +1} = 4 - 0$ and $\langle \cdots \rangle_{\det P_1 = -1} = 4 - 2$. Altogether the prefactor in (A3) matches the $1/4$ announced in (A1).

APPENDIX B: SPINS: UNCOUPLED CASE

In this Appendix, we find $\alpha(t)$ for the completely uncoupled probability distribution (16), the limit $h = 0$. In that case, $U_i = u_{i,L} \otimes u_{i,R}$ and $V_i = v_{i,L} \otimes v_{i,R}$ are tensor products of single-site unitaries from the U(2) Haar distribution. It then suffices to consider only one site $\rho_0 = \mathbb{I}_2/2 + \bar{\rho}_0$ as all sites are completely independent. Using the transformation $u \to v^\dagger u$, the v can be Haar-absorbed into the u, and we have the time evolution $\langle \rho_t \rangle = \langle u^t \rho_0 u^{t\dagger} \rangle$ which we evaluate for general dimension of ρ_0 and u [43,44].

By Haar invariance the transformation $u \to w^\dagger u w$ shows

$$\langle \rho_t \rangle = \langle w^\dagger u^t w \rho_0 w^\dagger u^{t\dagger} w \rangle. \tag{B1}$$

We can integrate out w with formula (62) and get the result

$$\langle \rho_t \rangle = \frac{\mathbb{I}_d}{d} + \frac{\lambda(t) - 1}{d^2 - 1}\bar{\rho}_0 \tag{B2}$$

with the spectral form factor

$$\lambda(t) = \langle \operatorname{Tr} u^t \operatorname{Tr} u^{t\dagger} \rangle, \tag{B3}$$

which is just (73) and (74) for a one-site chain and empty set I. For Haar-distributed $u \in U(d)$, the spectral form factor saturates at its maximal value $\lambda(t) = d$ for $t \geqslant d$ [46]. In particular, for our $d = 2$ chain and $t > 1$, $\lambda(t) = 2$ and the final state (15) stays constant with $\alpha = 1/3$.

APPENDIX C: SPINS: SIMPLIFICATION FOR NUMERICAL CALCULATIONS

In this section, we show that the computationally more efficient single rhomboid contraction in Fig. 10 is equivalent to the function $R(U, s)$ from equation (84) when taking the average in U_i, V_i. This is needed in Sec. V.

As argued in Sec. V, $R(U, s)$ is equal to the folded rhomboids in Fig. 9. Let us consider each site (i.e., column) of that diagram in turn, apart from the central site containing s. The identities ("U turns") at the top and bottom of the column can be expanded. Linearity gives four new diagrams with all combinations of $|0\rangle\langle 0|$ and $|1\rangle\langle 1|$. Each column has either U_i or V_i both at the top and bottom. In the first case, single-site Haar invariance

$$U_i \to (w \otimes \mathbb{I}_2) U_i, \quad V_i \to (\mathbb{I}_2 \otimes w^\dagger) V_i \tag{C1}$$

allows to insert w and $w^\dagger$ that cancel everywhere except at the very top. By choosing $w = \sigma_x$ the Pauli matrix, $|1\rangle\langle 1|$

at the top can be transformed into $|0\rangle\langle 0|$. This process can be repeated similarly to transform a $|1\rangle\langle 1|$ at the bottom into $|0\rangle\langle 0|$.

In total, applying this procedure at all sites results in 4^{2t} identical diagrams where all top and bottom parts are $|0\rangle\langle 0|$ (except for $|s\rangle\langle s|$). This only partially cancels with 2^{-2t} from the original bottom "U turns," giving the prefactor. The two rhomboids of unitaries and daggered counterparts are then disconnected and can be written as the absolute square of a single rhomboid.

[1] P. W. Anderson, Absence of diffusion in certain random lattices, Phys. Rev. **109**, 1492 (1958).

[2] M. Schreiber, S. S. Hodgman, P. Bordia, H. P. Lüschen, M. H. Fischer, R. Vosk, E. Altman, U. Schneider, and I. Bloch, Observation of many-body localization of interacting fermions in a quasi-random optical lattice, Science **349**, 842 (2015).

[3] D. A. Huse, R. Nandkishore, and V. Oganesyan, Phenomenology of fully many-body-localized systems, Phys. Rev. B **90**, 174202 (2014).

[4] D. A. Abanin and Z. Papić, Recent progress in many-body localization, Ann. Phys. **529**, 1700169 (2017).

[5] G. Stolz, Strategies in localization proofs for one-dimensional random Schrödinger operators, in *Proceedings of the Indian Academy of Sciences-Mathematical Sciences* (Springer, 2002), Vol. 112, pp. 229–243.

[6] M. Aizenman and S. Molchanov, Localization at large disorder and at extreme energies: An elementary derivations, Commun. Math. Phys. **157**, 245 (1993).

[7] J. H. Bardarson, F. Pollmann, and J. E. Moore, Unbounded Growth of Entanglement in Models of Many-Body Localization, Phys. Rev. Lett. **109**, 017202 (2012).

[8] M. C. Bañuls, N. Y. Yao, S. Choi, M. D. Lukin, and J. I. Cirac, Dynamics of quantum information in many-body localized systems, Phys. Rev. B **96**, 174201 (2017).

[9] M. Žnidarič, T. Prosen, and P. Prelovšek, Many-body localization in the Heisenberg XXZ magnet in a random field, Phys. Rev. B **77**, 064426 (2008).

[10] E. Hamza, A. Joye, and G. Stolz, Dynamical localization for unitary Anderson models, Math. Phys. Anal. Geom. **12**, 381 (2009).

[11] P. Ponte, Z. Papić, F. Huveneers, and D. A. Abanin, Many-Body Localization in Periodically Driven Systems, Phys. Rev. Lett. **114**, 140401 (2015).

[12] A. Lazarides, A. Das, and R. Moessner, Fate of Many-Body Localization Under Periodic Driving, Phys. Rev. Lett. **115**, 030402 (2015).

[13] L. Zhang, V. Khemani, and D. A. Huse, A floquet model for the many-body localization transition, Phys. Rev. B **94**, 224202 (2016).

[14] C. W. von Keyserlingk, T. Rakovszky, F. Pollmann, and S. L. Sondhi, Operator Hydrodynamics, Otocs, and Entanglement Growth in Systems Without Conservation Laws, Phys. Rev. X **8**, 021013 (2018).

[15] T. Rakovszky, F. Pollmann, and C. W. von Keyserlingk, Diffusive Hydrodynamics of Out-of-Time-Ordered Correlators with Charge Conservation, Phys. Rev. X **8**, 031058 (2018).

[16] A. Chan, A. De Luca, and J. T. Chalker, Solution of a minimal model for many-body quantum chaos, arXiv:1712.06836.

[17] A. Nahum, S. Vijay, and J. Haah, Operator Spreading in Random Unitary Circuits, Phys. Rev. X **8**, 021014 (2018).

[18] V. Khemani, A. Vishwanath, and D. A. Huse, Operator Spreading and the Emergence of Dissipative Hydrodynamics Under Unitary Evolution with Conservation Laws, Phys. Rev. X **8**, 031057 (2018).

[19] A. Nahum, J. Ruhman, S. Vijay, and J. Haah, Quantum Entanglement Growth Under Random Unitary Dynamics, Phys. Rev. X **7**, 031016 (2017).

[20] M. J. Gullans and D. A. Huse, Entanglement structure of current driven quantum many-body systems, arXiv:1804.00010.

[21] T. Zhou and A. Nahum, Emergent statistical mechanics of entanglement in random unitary circuits, arXiv:1804.09737.

[22] J. Emerson, Y. S. Weinstein, M. Saraceno, S. Lloyd, and D. G. Cory, Pseudo-random unitary operators for quantum information processing, Science **302**, 2098 (2003).

[23] H. Gharibyan, M. Hanada, S. H. Shenker, and M. Tezuka, Onset of random matrix behavior in scrambling systems, J. High Energy Phys. 07 (2018) 124.

[24] P. Kos, M. Ljubotina, and T. Prosen, Many-Body Quantum Chaos: Analytic Connection to Random Matrix Theory, Phys. Rev. X **8**, 021062 (2018).

[25] B. Bertini, P. Kos, and T. Prosen, Exact spectral form factor in a minimal model of many-body quantum chaos, arXiv:1805.00931.

[26] B. Collins and I. Nechita, Random quantum channels I: Graphical calculus and the Bell state phenomenon, Commun. Math. Phys. **297**, 345 (2010).

[27] P. W. Brouwer and C. W. J. Beenakker, Diagrammatic method of integration over the unitary group, with applications to quantum transport in mesoscopic systems, J. Math. Phys. **37**, 4904 (1996).

[28] R. Jozsa and A. Miyake, Matchgates and classical simulation of quantum circuits, Proc. R. Soc. A **464**, 3089 (2008).

[29] S. Bravyi, Lagrangian representation for fermionic linear optics, Quantum Inf. Comput. **5**, 216 (2005).

[30] This class includes (local) particle hole transformations. For example, for a single fermionic mode, particle-hole transformation corresponds to the unitary $U = a + a^\dagger$ ($a^\dagger/a$ creation/annihilation operators) and in the covariance matrix formalism, to $\left(\begin{smallmatrix} 1 & 0 \\ 0 & -1 \end{smallmatrix}\right) \in \mathrm{O}(2)$ with negative determinant. All of the transformations we consider have definite parity as required by superselection rules.

[31] D. L. Cohn, *Measure Theory*, 2nd ed. (Springer, New York, Heidelberg, 2013), Vol. 165.

[32] The Haar distribution will allow us to derive some analytical results. It treats all bases on an equal footing (this means there is no preferred local basis for the evolution), and rotation angles are random. It is also the most depolarising measure and thus one would expect to obtain the most extreme results. Physically, it corresponds to having magnetic fields not only with a random strength, but also a random direction.

[33] M. A. Nielsen and I. L. Chuang, *Quantum Computation and Quantum Information* (Cambridge University Press, Cambridge, 2000).

[34] R. Nandkishore and D. A. Huse, Many-body localization and thermalization in quantum statistical mechanics, Annu. Rev. Condens. Matter Phys. **6**, 15 (2015).

[35] B. Kraus and J. I. Cirac, Optimal creation of entanglement using a two-qubit gate, Phys. Rev. A **63**, 062309 (2001).

[36] D. M. Basko, I. L. Aleiner, and B. L. Altshuler, Metal–insulator transition in a weakly interacting many-electron system with localized single-particle states, Ann. Phys. **321**, 1126 (2006).

[37] B. Bauer and C. Nayak, Area laws in a many-body localized state and its implications for topological order, J. Stat. Mech. (2013) P09005.

[38] J. A. Kjäll, J. H. Bardarson, and F. Pollmann, Many-Body Localization in a Disordered Quantum Ising Chain, Phys. Rev. Lett. **113**, 107204 (2014).

[39] B. Collins and S. Matsumoto, On some properties of orthogonal Weingarten functions, J. Math. Phys. **50**, 113516 (2009).

[40] It is interesting to understand why the statement does not hold for $k = l$ and the two specific pairs. For $k = l$, it is obvious that $\hat{O}_k = \hat{O}_l$ are identical matrices and have identical spectra. The pairs $(k, l) = (N/2, N/4), (N/4, N/2)$ are the only values for which both $\hat{G}_k$ and $\hat{G}_l$ are real. As real orthogonal matrices, the eigenvalues of $\hat{O}_{k/l}$ are real (± 1) or arise as complex-conjugate pairs. In fact, for a quarter of all choices (P, Q), the determinants are $\det \hat{O}_k = \det \hat{O}_l = -1$. These determinants force both matrices to both have an eigenvalue $+1$ and -1.

[41] B. Collins, Moments and cumulants of polynomial random variables on unitary groups, the Itzykson-Zuber integral, and free probability, Int. Math. Res. Not. **2003**, 953 (2003).

[42] Z. Webb, The Clifford group forms a unitary 3-design, Quant. Inform. Comput. **16**, 1379 (2016).

[43] M. Žnidarič, C. Pineda, and I. Garcia-Mata, Non-Markovian Behavior of Small and Large Complex Quantum Systems, Phys. Rev. Lett. **107**, 080404 (2011).

[44] M. Gessner and H.-P. Breuer, Generic features of the dynamics of complex open quantum systems: Statistical approach based on averages over the unitary group, Phys. Rev. E **87**, 042128 (2013).

[45] A. Chan, A. De Luca, and J. T. Chalker, Spectral Statistics in Spatially Extended Chaotic Quantum Many-Body Systems, Phys. Rev. Lett. **121**, 060601 (2018).

[46] M. L. Mehta, *Random Matrices* (Elsevier, San Diego, 2004), Vol. 142.

[47] A. Edelman and N. R. Rao, Random matrix theory, Acta Numerica **14**, 233 (2005).

[48] J. I. Cirac, D. Perez-Garcia, N. Schuch, and F. Verstraete, Matrix product unitaries: Structure, symmetries, and topological invariants, J. Stat. Mech. (2017) 083105.

Appendix B

Quantum chaos in the Brownian SYK model with large finite N: OTOCs and tripartite information

In this article, we study chaos and scrambling in the Brownian SYK model, a time dependent, disordered model with (infinite-range) all-to-all interactions. It was introduced in section 5.3 and is based on the holographic SYK model, which is oftentimes used for its link to black holes.

As explained in section 3.3 and 3.4, OTOCs and the tripartite information are excellent quantifiers of chaos and scrambling. Here, we develop a new method to compute them for finite numbers of particles N. Traditionally, work on the SYK model focuses on the $N \to \infty$ limit, thwarting any attempt to asses finite size scaling of scrambling times.

The new numerical method consists of transforming the disorder-averaged evolution of OTOCs or Rényi entropies into an effective quenched imaginary-time evolution problem void of any disorder. Thanks to an effective permutational symmetry, the dynamics then take place only in a polynomial subspace of the total Hilbert space, which is exponential in N. It admits a description in terms of bosonic modes. By exploiting a further symmetry, the effective dimension can be reduced to N or N^2 for the OTOCs or Rényi entropies. Thus, OTOCs can be computed numerically exactly up to one million ($N = 10^6$) particles. The numerical procedure developed may also be applicable to other observables or other systems with Brownian all-to-all disorder.

The high numerical power allows us to study the OTOCs and tripartite information in detail in their time-dependence and system-size dependence. In particular, we can follow their relaxation to maximal Haar-scrambling at large times. Additionally, a scrambling time $t^* \propto \log N$ proportional to the logarithm of system size can be seen and verified with a scaling collapse. The logarithmic dependence is of great importance to the fast scrambling conjecture for black holes (see section 5.1), and it is remarkable that we can access such a vast scale of N to see a logarithmic dependence as clear as day.

Published for SISSA by Springer

Received: *August 16, 2019*
Accepted: *October 22, 2019*
Published: *November 7, 2019*

Quantum chaos in the Brownian SYK model with large finite N: OTOCs and tripartite information

Christoph Sünderhauf,[a,b] **Lorenzo Piroli,**[a,b] **Xiao-Liang Qi,**[c,d,e] **Norbert Schuch**[a,b] **and J. Ignacio Cirac**[a,b]

[a] *Max-Planck-Institut für Quantenoptik, Hans-Kopfermann-Str. 1, 85748 Garching, Germany*
[b] *Munich Center for Quantum Science and Technology, Schellingstraße 4, 80799 München, Germany*
[c] *Stanford Institute for Theoretical Physics, Stanford University, 382 Via Pueblo Mall, Stanford, CA 94305, U.S.A.*
[d] *Department of Physics, Stanford University, 382 Via Pueblo Mall, Stanford, CA 94305, U.S.A.*
[e] *Google, 100 Mayfield Ave, Mountain View, CA 94043, U.S.A.*
E-mail: christoph.suenderhauf@mpq.mpg.de, lorenzo.piroli@mpq.mpg.de, xlqi@stanford.edu, norbert.schuch@mpq.mpg.de, ignacio.cirac@mpq.mpg.de

Abstract: We consider the Brownian SYK model of N interacting Majorana fermions, with random couplings that are taken to vary independently at each time. We study the out-of-time-ordered correlators (OTOCs) of arbitrary observables and the Rényi-2 tripartite information of the unitary evolution operator, which were proposed as diagnostic tools for quantum chaos and scrambling, respectively. We show that their averaged dynamics can be studied as a quench problem at imaginary times in a model of N qudits, where the Hamiltonian displays site-permutational symmetry. By exploiting a description in terms of bosonic collective modes, we show that for the quantities of interest the dynamics takes place in a subspace of the effective Hilbert space whose dimension grows either linearly or quadratically with N, allowing us to perform numerically exact calculations up to $N = 10^6$. We analyze in detail the interesting features of the OTOCs, including their dependence on the chosen observables, and of the tripartite information. We observe explicitly the emergence of a scrambling time $t^* \sim \ln N$ controlling the onset of both chaotic and scrambling behavior, after which we characterize the exponential decay of the quantities of interest to the corresponding Haar scrambled values.

Keywords: Holography and condensed matter physics (AdS/CMT), Random Systems

ArXiv ePrint: 1908.00775

https://doi.org/10.1007/JHEP11(2019)038

Contents

JHEP11(2019)038

1 Introduction

The study of many body quantum chaos is currently experiencing a golden age, also due to its implications on important aspects in many-body physics such as the thermalization [1, 2] of isolated systems [3–8], or the scrambling of quantum information [9–11]. In fact, the

field has already enjoyed intense research activity more than thirty years ago [12, 13], when the relations between chaotic many-body systems and random matrix theory were first explored. Recently, a renewed interest came from the study of black hole physics and concepts such as scrambling of quantum information, and computational complexity [14–20].

An important milestone in the recent literature is the Sachdev-Ye-Kitaev model [21–23], which was originally proposed by Sachdev and Ye as a model of strongly correlated electron systems, and generalized by Kitaev in 2015 who pointed out its connection to holographic duality. This model describes N Majorana fermions or complex fermions with random all-to-all interactions. In the work we will focus on the Majorana fermion version. The SYK model has already drawn enormous attention from different communities, ranging from quantum gravity [24, 25] to condensed-matter and many-body physics [26–32], due to the concomitance of several unique features. Among these, the model has been shown to be maximally chaotic and yet amenable to exact analysis in the large-N limit [21, 22, 26, 27, 33, 34], making it an ideal playground for the study of chaos and scrambling of quantum information.

In the same years, the effort to better characterize quantum chaos led to the systematic development of reliable indicators for its diagnosis. In particular, out-of-time-ordered correlation (OTOC) functions, historically introduced in the context of disordered superconductors [35], were naturally selected as ideal probes to detect the "scrambling" of local observables [17, 21, 22, 36–38], namely the spreading of their spatial support in the operator basis. It is important to mention that these ideas had far reaching ramifications, motivating the study of OTOCs also in many-body systems with short-range interactions [30, 39–47, 47, 48, 48–53] and in spatially local "quantum unitary circuits" [54–67], which provide minimally structured models for chaotic quantum dynamics. In fact, related studies on information scrambling in a class of random, and in general non-local, circuits (the so-called approximate t-designs) were already carried out within quantum information theory [68–82], where the latter were used to provide rapid approximations to random unitary operators. Finally, we note that OTOCs were also shown to be directly related to the growth of the operator size, i.e. the size of its support [38, 83].

So far, computations of OTOCs in the SYK model have been carried out through field-theoretical approaches in the large-N limit [21, 22, 24, 26]. On the other hand, despite the many works devoted to this topic, results for finite values of N are difficult to obtain, and remain scarce [84–86]. This is also true for numerical computations: the exponential growth of the Hilbert space dimension, and the presence of disorder averages yield strong limitations on the sizes of the systems that can be simulated [38, 87–89]. Still, it would be highly desirable to develop a systematic approach to investigate the properties of the SYK model at finite N, even numerically. Indeed, not only would this allow for inspection of finite-size corrections to the large-N results, but also to compute quantities beyond multi-point correlation functions, for which field-theoretical approaches might be difficult to apply. A notable example is given by the (negative) tripartite information of the evolution operator introduced in ref. [9] in the context of unitary circuits. This was suggested as a valuable tool to quantify the scrambling power of a quantum channel, namely its ability to delocalize information provided as an input. We note that, so far, this quantity has been

JHEP11(2019)038

computed only numerically for small system sizes [9, 90] (see also refs. [91–93], where the tripartite information of given states, and not of the channel, was studied).

Motivated by the above picture, we consider a simpler, but closely related, *Brownian* SYK model, and address the problem of its exact analysis at finite sizes. The model was introduced in ref. [94], and differs from the traditional SYK in that the random couplings are chosen to vary independently at each time. The simplification arising in this case is similar to the one we have in unitary circuits by choosing random gates independently in each layer. Experience from the latter framework suggests that the main features of the chaotic dynamics remain qualitatively unaltered by introducing an additional time-dependence to the spatial disorder, except that random circuits and Brownian models behave like infinite-temperature systems since they do not display energy conservation.

In this work, we focus on the development of a systematic approach to the chaotic dynamics in the Brownian SYK model, which could also be applied, more generally, to other time-dependent, disordered Hamiltonians with infinite-range interactions. In particular, we aim to compute OTOCs of arbitrary local observables, and other dynamical quantities which can be extracted from disordered averages involving up to four unitary evolution operators. These include a Rényi-2 version of the tripartite information introduced in [9], which has been shown to encode information about all possible OTOCs [9].

As a main result of our work, we show that the averaged dynamics of the OTOCs and of the Rényi tripartite information can be studied as a quench problem at imaginary times in a model of N qudits, where the Hamiltonian displays full site-permutational symmetry. We analyze this problem by means of a description in terms of bosonic collective modes, and prove that for the quantities of interest the dynamics takes place in a subspace of the Hilbert space whose dimension grows either linearly or quadratically with N. This allows us to perform numerically exact calculations up to one million particles, and, consequently, analyze in great detail the behavior of OTOCs and of the Rényi tripartite information, highlighting their most interesting features. While some of our results depend on simplifications arising in the special case of the SYK model, we expect that suitable generalizations of our method could be successfully applied also to the study of other disordered time-dependent Hamiltonians with all-to-all interactions.

It is useful to compare our method with that of existing studies, as some of the ideas used in our work are related to other approaches in the literature. First, ref. [94] proposed the Brownian SYK model as a simplified version of the original SYK, and mainly focused on the computation of the spectral form factor [95]. For this specific quantity, it was shown that in the Brownian SYK model an exact solution could be achieved, by means of an elementary mapping to a classical partition function. Our results on OTOCs and tripartite information cannot be obtained using the same approach.

Next, we discuss refs. [73, 74, 77], where a class of random quantum circuits was considered, in which at each layer a single unitary gate is applied to a pair of qudits randomly chosen. There, it was shown that the moments of the evolution operator associated with a time step could be mapped onto a permutational invariant Hamiltonian which generalizes the Lipkin-Meshkov-Glick model [96]. Even though the idea underlying our method is similar, both our mapping and the quantities studied in this paper are different.

JHEP11(2019)038

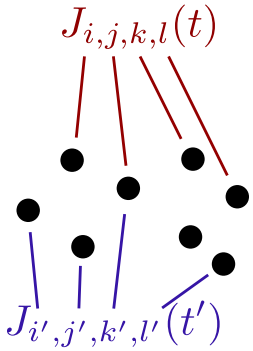

Figure 1. Pictorial representation of the Brownian SYK model described by the Hamiltonian (2.1), for $q = 4$. At each time, all the Majorana fermions are coupled together within clusters of q particles, with time-dependent random interactions.

We also note that the computation of OTOCs in models with a continuous-time evolution in the presence of Brownian disorder and infinite-range interactions have been already addressed in [97, 98] (see also [99, 100]). The system studied in these works, consisting of N qudits driven by an Hamiltonian which is bilinear in the Pauli operators, was introduced as a chaotic toy model in ref. [15], where its scrambling time was first estimated to be logarithmic in N (see also ref. [101], where the spectral form factor was analyzed for the same system). The approach of [97, 98] relies on the derivation, based on an application of Itô calculus [102], of a system of differential equations for the OTOCs of interest. Solving the latter, numerical results were given in ref. [15] for sizes comparable to those that can be reached with our method, while an analytical solution was found in [98] for a particular average of OTOCs. As we will see, our approach differs from that of [97, 98], as we tackle directly the computation of the averaged moments of the evolution operator. This allows us to use the same formalism to also analyze the tripartite information discussed above, which was not addressed in these studies. Finally, we note that rigorous results, relevant to the present paper, for the scrambling properties of continuous-time evolution generated by random Hamiltonians were recently presented in refs. [103, 104].

The organization of the rest of this paper is as follows. In section 2 we introduce the Brownian SYK model and the quantities which will be investigated in this work. We proceed to present the key features of our method in section 3, while our physical results are reported in section 4. The most technical aspects of our study are consigned to section 5 and to a few appendices. Finally, our conclusions are discussed in section 6.

2 The model and the chaos quantifiers

The object of study of this work will be the Brownian SYK model, describing a set of N Majorana fermions with q-local, all-to-all random interactions, cf. figure 1. It is defined on a Hilbert space $\mathcal{H}_N$ of dimension $D = 2^{N/2}$, with N operators ψ_j acting on $\mathcal{H}_N$. They are the representation of standard Majorana fermions, and thus satisfy $\{\psi_j, \psi_k\} = 2\delta_{j,k}$ and $\psi_j^\dagger = \psi_j$ (the quantities of interest in this work will not depend on the representation

JHEP11(2019)038

chosen for the N Majorana fermions). Its time-dependent Hamiltonian reads

$$H_{\rm SYK}(t) = i^{q/2} \sum_{1\leq i_1<i_2<\ldots<i_q\leq N} J_{i_1,\ldots,i_q}(t)\psi_{i_1}\psi_{i_2}\ldots\psi_{i_q}\,. \tag{2.1}$$

Here, the couplings $J_{i_1,\ldots,i_q}(t)$ are random variables, which we assume to be Gaussian distributed with vanishing mean and variance

$$\overline{J_{i_1\ldots i_q}(t)J_{i'_1\ldots i'_q}(t')} = \delta_{i_1 i'_1}\cdots\delta_{i_q i'_q}\,\delta\left(t-t'\right)\sigma_J\frac{(q-1)!}{N^{q-1}}\,, \tag{2.2}$$

where we denoted by $\overline{[\ldots]}$ the average over disorder realizations. While our method could be applied for arbitrary integer values of q, we will focus for concreteness on the case $q=4$. Furthermore, we will choose the constant σ_J in such a way that

$$\overline{J_{i_1\ldots,i_4}(t)J_{i'_1\ldots,i'_4}(t')} = \delta_{i_1 i'_1}\cdots\delta_{i_4 i'_4}\,\delta\left(t-t'\right)\frac{1}{N^3}\,. \tag{2.3}$$

In comparison, the original SYK Hamiltonian shares the same form of (2.1), but with time-independent couplings. In appendix A we additionally discuss the case $q=2$, which lacks chaotic behavior as each disorder realization is non-interacting.

2.1 The OTOCs and the operator spreading

As we have already discussed in section 1, we will be mainly interested in two quantifiers of quantum chaos and scrambling. The first one is given by OTOCs of local observables: explicitly, given two operators $\mathcal{O}$, $\mathcal{O}'$, we define their OTOC on a state ρ as

$$\mathcal{F}_{\mathcal{O},\mathcal{O}'}(t) = \mathrm{tr}\left[\rho\mathcal{O}(t)\mathcal{O}'(0)\mathcal{O}(t)\mathcal{O}'(0)\right]\,, \tag{2.4}$$

where $\mathcal{O}(t) = U^\dagger(t)\mathcal{O}U(t)$, and $U(t)$ is the unitary evolution operator. In this work we will choose the infinite-temperature Gibbs density matrix $\rho = \mathbb{1}/2^{N/2}$, which represents a stationary state for the time-dependent Hamiltonian (2.1).

Importantly, we recall that the OTOC (2.4) can be related to an intuitive notion of the spreading of localized operators under unitary evolution. To this end, we choose for simplicity $\mathcal{O}=\psi_j$, $\mathcal{O}'=\psi_k$ with $j\neq k$, and consider the quantity

$$\mathcal{C}(t) = \frac{1}{2}\mathrm{tr}\left[\rho\left(\{\psi_j(t),\psi_k(0)\}\right)^\dagger\left(\{\psi_j(t),\psi_k(0)\}\right)\right]\,, \tag{2.5}$$

which measures the magnitude of the anticommutator between $\psi_j(t)$ and $\psi_k(0)$. At time $t=0$, one simply has $\mathcal{C}(t)=0$. On the other hand, as time increases, the spacial support of $\psi_j(t)$ will also increase; namely $\psi_j(t)$ will evolve into a complicated sum of strings of Majorana operators. Then, we see that deviations of $\mathcal{C}(t)$ from zero signal that the support of $\psi_j(t)$ has grown to include site k. Accordingly, $\mathcal{C}(t)$ can be understood as a measure of the spatial spreading of the local operator $\psi_j(t)$. The connection between the latter and OTOCs is finally established by the simple relation

$$\mathcal{C}(t) = 1 + \mathrm{Re}\left[\mathrm{tr}\left(\rho\psi_j(t)\psi_k(0)\psi_j(t)\psi_k(0)\right)\right]\,. \tag{2.6}$$

JHEP11(2019)038

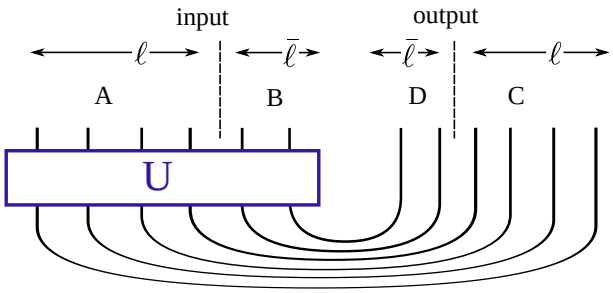

Figure 2. Pictorial representation of the state $|U\rangle\rangle$ defined in eq. (2.8). The operator U is depicted as a box, while its legs correspond to the local Hilbert spaces h_j. The output legs are bent to create a state in a doubled Hilbert space $\mathcal{H}_N \otimes \mathcal{H}'_N$. Each space is partitioned into two regions: A and B for the input space $\mathcal{H}_N$, and C and D for the output space $\mathcal{H}'_N$.

In conclusion, the discussion above allows one to view the OTOCs as a measure of chaos: chaotic dynamics corresponds to OTOCs that vanish sufficiently rapidly with time. On the other hand, for a non-chaotic Hamiltonian one expects information to spread coherently: for large system sizes this results in either a slow decay or a non-vanishing asymptotics of OTOCs [47, 48], while for small ones this causes revivals, consisting in OTOCs frequently returning close to their original value [105].

2.2 Diagnostic of scrambling: the tripartite information in fermionic systems

The OTOCs provide a physically clear definition of quantum chaos in terms of correlation functions between local operators. Other measures probing different features intuitively associated with chaos exist. Among these, the notion of scrambling of information, originally introduced in the study of black hole physics [14, 16], is particularly clear: a quantum system is a good scrambler if a localized perturbation in the initial state spreads over all its degrees of freedom, in such a way that it can no longer be detected by local measurements at large times. In this context, it is useful to think of the unitary evolution as a quantum channel, taking an initial state as the input, and returning the evolved state as the output. In this logic, it was proposed in ref. [9] that the scrambling power of a channel could be conveniently measured by the tripartite information between bipartitions of its input and output, as we review in the following.

For simplicity, let us first consider a system of N qudits, associated with a Hilbert space $\mathcal{H}_N = h_1 \otimes \ldots \otimes h_N$, where $h_j \simeq \mathbb{C}^D$, and a unitary operator $U : \mathcal{H}_N \to \mathcal{H}_N$. In order to study the scrambling properties of U, we wish to interpret it as a state in a suitable space. To this end, we introduce a copy of the original Hilbert space $\mathcal{H}'_N$, and define the maximally entangled state $|I\rangle \in \mathcal{H}_N \otimes \mathcal{H}'_N$ as

$$|I\rangle = \frac{1}{D^{N/2}} \sum_{j=1}^{D^N} |j\rangle \otimes |j'\rangle \ , \tag{2.7}$$

where $\{|j\rangle\}_{j=1}^{D^N}$, $\{|j'\rangle\}_{j'=1}^{D^N}$ are orthonormal bases for $\mathcal{H}_N$ and $\mathcal{H}'_N$, respectively. Note that we choose the basis such that $|I\rangle$ is a direct product of EPR pairs between qudits in the

JHEP11(2019)038

two systems, as is illustrated in figure 2. Then, the operator U can be interpreted as a state in $\mathcal{H}_N \otimes \mathcal{H}'_N$ through the Choi-Jamiolkowski mapping

$$U \mapsto |U\rangle\rangle = (\mathbb{1} \otimes U)\,|I\rangle\ . \tag{2.8}$$

Here the operator U is depicted as a box, whose legs correspond to the local Hilbert spaces h_j; we see that one could intuitively think of the state $|U\rangle\rangle$ as obtained by "bending" the output legs, so as to treat input and output, associated with $\mathcal{H}_N$ and $\mathcal{H}'_N$ respectively, on an equal footing. It should be noted that the mapping from U to $|U\rangle\rangle$ is not unique, as it depends on the choice of state $|I\rangle$. However, different $|I\rangle$ are related by a local unitary transformation, which does not affect the entropy-related quantities we discuss in the following.

Given $|U\rangle\rangle \in \mathcal{H}_N \otimes \mathcal{H}'_N$, one can compute the entanglement entropy between different spatial regions in $\mathcal{H}_N$ and $\mathcal{H}'_N$. We consider in particular bipartitions of $\mathcal{H}_N$ and $\mathcal{H}'_N$ into the complementary subsystems A, B and C,D respectively; in figure 2 a special choice for these regions is shown. Given a pair of bipartitions (A, B) and (C, D), we define the tripartite information as [9]

$$I_3(A:C:D) = I(A:C) + I(A:D) - I(A:CD)\,, \tag{2.9}$$

where CD denotes the union of the regions C and D. Here $I(X:Y)$ is the mutual information between the regions X and Y

$$I(X:Y) = S_X + S_Y - S_{XY}\,, \tag{2.10}$$

where S_X is the von Neumann entropy of the reduced density matrix ρ_X. For instance, we have

$$S_{AC} = -\operatorname{tr}\left[\rho_{AC} \ln \rho_{AC}\right]\,, \tag{2.11}$$

where $\rho_{AC} = \operatorname{tr}_{BD}[\rho]$.

The tripartite information in eq. (2.9) was suggested in ref. [9] as a natural and convenient diagnostic for scrambling. In fact, as in the case of OTOCs, its underlying physical meaning is easy to grasp. From eq. (2.9), we see that $-I_3(A:C:D)$ quantifies the amount of information on the input region A that can be recovered by global measurements in $C \cup D$, but can not be obtained by probing C and D individually. Recalling that $\mathcal{H}'_N = C \cup D$ corresponds to the output, this is exactly a measure of scrambling: if $-I_3(A:C:D)$ is large, it means that the information localized in a subsystem A of the input state can be recovered only by global measurements in the output state, and information has been scrambled. Accordingly, if for any bipartition of $\mathcal{H}_N$ and $\mathcal{H}'_N$, $I_3(A:C:D)$ is negative with an absolute value close to the maximum possible value, the channel U has large scrambling power. Finally, a close connection was established in ref. [9] between the tripartite information (2.9) and the OTOCs, which further corroborated the appeal of the former as a valuable diagnostic of scrambling and, more generally, of chaotic dynamics. This connection is reviewed in appendix B, where we also discuss its generalization to the fermionic setting.

The above discussion is carried out in terms of qudits, whereas in our work we are interested in a fermionic system. At this point, one could employ a Jordan-Wigner representation of the Majorana operators in the Hamiltonian (2.1), interpret the resulting

JHEP11(2019)038

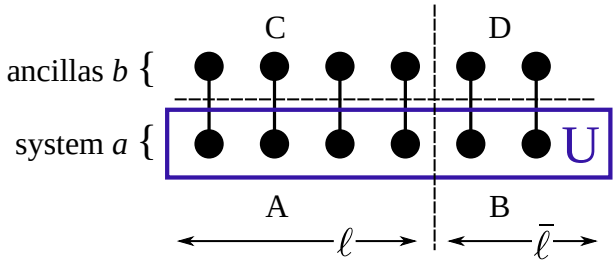

Figure 3. Pictorial representation for the state $|I^{ab}\rangle$ in eq. (2.12). The black bullets in the lower and upper rows represent the original and "replica" fermions ψ_j^a and ψ_j^b, respectively. Each link is a maximally entangled pair, which corresponds to the vacuum for the complex Fermi operators $c_j = \psi_j^a - i\psi_j^b$. The evolution operator U, generated by the Hamiltonian (2.1), is applied only to the original system.

evolution operator as a unitary channel acting on a system of $N/2$ qubits, and define the tripartite information for the latter according to the discussion above. However, given a correspondence between Majorana and Pauli operators via the Jordan-Wigner transformation, it is known that the reduced density matrix of disjoint intervals written in terms of the two is not the same, leading to different results for the corresponding von Neumann entanglement entropy [106, 107]. In our case, we stress that the physical degrees of freedom are represented by the Majorana operators and, accordingly, the tripartite information in eq. (2.9) should be computed in terms of the latter. In this respect, we find it useful to discuss explicitly the generalization of the above construction for Majorana operators, without making direct reference to the tensor-product structure of the doubled Hilbert space associated with the input and output of the channel.

As a first ingredient, we wish to interpret the evolution operator generated by the Hamiltonian (2.1) as a state. To this end, we introduce a system of $2N$ Majorana operators ψ_j^α, where $j = 1, \dots, N$, while α is an index labeling two different species which we denote by a and b. The maximally entangled state $|I^{ab}\rangle$ is then defined as the vacuum state for the complex fermions $c_j = \psi_j^a - i\psi_j^b$ [108], namely

$$\left(\psi_j^a - i\psi_j^b\right) |I^{ab}\rangle = 0\,, \qquad \forall j\,. \tag{2.12}$$

The operator U can now be interpreted as a state in the doubled system through the mapping

$$U(t) \mapsto |U(t)\rangle\rangle = U^a(t)\,|I^{ab}\rangle\,. \tag{2.13}$$

Here the superscript a indicates that the Hamiltonian generating the unitary evolution operator $U^a(t)$ is written in terms of the fermions ψ_j^a. A pictorial representation of this construction is shown in figure 3. One can now proceed to compute the fermionic reduced density matrices for the evolved state $|U(t)\rangle\rangle$, and consequently the corresponding tripartite information as in eq. (2.9). We refer the reader to section 5 for further details.

Unfortunately, despite its great interest, the computation of the tripartite information (2.9) is a very difficult task, which so far has been carried out only numerically for qudit systems of small sizes [6, 90]. For this reason, we study a simpler but closely related

JHEP11(2019)038

quantity, which is obtained from $I_3(A:C:D)$ by considering Rényi, rather than von Neumann, entropies. Specifically, we will compute the following Rényi-2 tripartite information

$$I_3^{(2)}(A:C:D) = I^{(2)}(A:C) + I^{(2)}(A:D) - I^{(2)}(A:CD)\,, \tag{2.14}$$

where

$$I^{(2)}(X:Y) = S_X^{(2)} + S_Y^{(2)} - S_{XY}^{(2)}\,, \tag{2.15}$$

and

$$S_X^{(2)} = -\ln\left[\overline{\mathrm{tr}\left(\rho_X^2\right)}\right]\,. \tag{2.16}$$

We note that, strictly speaking, $S_X^{(2)}$ is not the averaged Rényi entropy of order 2, as the disorder average is taken inside the logarithm. However, ref. [6] showed that the OTOC for a pair of operators in A and C averaged over all operator choices is determined by $\mathrm{tr}\left(\rho_{AD}^2\right)$. Therefore the averaged purity $\overline{\mathrm{tr}\left(\rho_X^2\right)}$ is a meaningful physical quantity to consider. Also, for N not too small, one expects the effect of fluctuations in the disorder to be small, so that $S_X^{(2)}$ remains a good approximation for the Rényi-2 entropy [6, 57].

It is worth to notice that eq. (2.14) can be simplified in general. Indeed, it is easy to show [9]

$$I_3^{(2)}(A:C:D) = \frac{N}{2}\ln(2) - S_{AC}^{(2)} - S_{AD}^{(2)}\,, \tag{2.17}$$

where we used that the dimension of the Hilbert space associated with N Majorana fermions is $D = 2^{N/2}$. Eq. (2.17) tells us that, in order to obtain the tripartite information, it is sufficient to compute the entropies $S_{AC}^{(2)}$ and $S_{AD}^{(2)}$ between different regions of the input and the output.

We conclude this section by stressing that while the Rényi tripartite information (2.14) differs quantitatively from $I_3(A:C:D)$, based on previous studies [108], we can still expect it to display the same qualitative features of the latter, and thus to be a suitable measure for scrambling.

3 Exact approach from emergent permutational symmetry

Having introduced the model and the quantities of interest, we proceed by presenting the general ideas of the method developed in this work. The physical results will be then discussed in section 4, while we postpone the most technical details of our calculations to section 5.

3.1 Decomposing the dynamical problem

We will begin our discussion with the concrete problem of computing the OTOC (2.4), which we rewrite as

$$\mathcal{F}_{\mathcal{O},\mathcal{O}'}(t) = \frac{1}{2^{N/2}}\mathrm{tr}\left\{\mathcal{O}U(t)\mathcal{O}'U^\dagger(t)\mathcal{O}U(t)\mathcal{O}'U^\dagger(t)\right\}\,. \tag{3.1}$$

We recall that the time-dependent, disordered Hamiltonian (2.1) gives rise to a dynamics which can be interpreted as the continuous limit of the discrete process defined by

$$U(t) = e^{-i\Delta t H_{\mathrm{SYK}}(t_n)}e^{-i\Delta t H_{\mathrm{SYK}}(t_{n-1})}\ldots e^{-i\Delta t H_{\mathrm{SYK}}(t_1)}\,, \tag{3.2}$$

JHEP11(2019)038

where $\Delta t = t/n$ and $t_j = j\Delta t$, while the delta function in eq. (2.3) is regularized as

$$\overline{J_{i_1\dots,i_4}(t_r)J_{i'_1\dots,i'_4}(t_s)} = \delta_{i_1 i'_1}\cdots\delta_{i_4 i'_4}\frac{1}{N^3}\frac{\delta_{r,s}}{\Delta t}\,. \tag{3.3}$$

In practice, one can work with the discrete form (3.2) of the evolution operator, and take the continuum limit at the end of the calculations.

In order to compute $\mathcal{F}_{\mathcal{O},\mathcal{O}'}(t)$, we first introduce a resolution of the identity between each pair of operators in (3.1), yielding

$$\begin{aligned}\mathcal{F}_{\mathcal{O},\mathcal{O}'} = \frac{1}{2^{N/2}}\sum_{\substack{i,j,k,l\\ m,n,o,p}} &\langle i|\mathcal{O}|j\rangle\langle j|U|k\rangle\left\langle k\left|\mathcal{O}'\right|l\right\rangle\left\langle l\left|U^\dagger\right|m\right\rangle\\ &\times\langle m|\mathcal{O}|n\rangle\langle n|U|o\rangle\left\langle o\left|\mathcal{O}'\right|p\right\rangle\left\langle p\left|U^\dagger\right|i\right\rangle\,.\end{aligned} \tag{3.4}$$

Here $\{|j\rangle\}$ denotes a basis for the Hilbert space $\mathcal{H}_N$ [introduced before eq. (2.1)] on which the operators ψ_j act. Rearranging the above sum, we obtain

$$\mathcal{F}_{\mathcal{O},\mathcal{O}'} = \langle L|\left(U\otimes U^*\otimes U\otimes U^*\right)|R\rangle\,, \tag{3.5}$$

where

$$|L\rangle = \sum_{i,j,m,n}\langle i|\mathcal{O}|j\rangle\langle m|\mathcal{O}|n\rangle\,|j,m,n,i\rangle\,, \tag{3.6}$$

$$|R\rangle = \sum_{k,lo,p}\left\langle k\left|\mathcal{O}'\right|l\right\rangle\left\langle o\left|\mathcal{O}'\right|p\right\rangle|k,l,o,p\rangle\,. \tag{3.7}$$

Here $U^*(t)$ denotes the complex conjugate of $U(t)$ (which is well defined, once a basis $\{|j\rangle\}$ of $\mathcal{H}_N$ is given) and we introduced the vectors $|i,j,k,l\rangle = |i\rangle\otimes|j\rangle\otimes|k\rangle\otimes|l\rangle \in \mathcal{H}_N^{\otimes 4}$. According to eq. (3.5), the dynamical information about the OTOC is uniquely encoded in the operator $\mathcal{U}(t) \equiv U\otimes U^*\otimes U\otimes U^*$, while $\mathcal{O}$, $\mathcal{O}'$ only affect the "left" and "right" states $|L\rangle$, $|R\rangle$, cf. figure 4 .

From eq. (3.2), we see immediately that $\mathcal{U}(t)$ is written in terms of the operators

$$\chi_j^a := \psi_j\otimes\mathbb{1}\otimes\mathbb{1}\otimes\mathbb{1}\,, \qquad \chi_j^b := \mathbb{1}\otimes\psi_j^*\otimes\mathbb{1}\otimes\mathbb{1}\,, \tag{3.8}$$

$$\chi_j^c := \mathbb{1}\otimes\mathbb{1}\otimes\psi_j\otimes\mathbb{1}\,, \qquad \chi_j^d := \mathbb{1}\otimes\mathbb{1}\otimes\mathbb{1}\otimes\psi_j^*\,, \tag{3.9}$$

which provide a basis for all the operators in $\mathcal{H}_N^{\otimes 4}$. Note that, as we already stressed, ψ_j is the representation of a Majorana fermion, and thus is an operator acting on $\mathcal{H}_N$, for which the tensor product is defined in the usual way. Due to the tensor-product structure of $\mathcal{H}_N^{\otimes 4}$, the operator χ_j^α satisfy mixed commutation and anticommutation relations, namely $\left[\chi_j^\alpha,\chi_k^\beta\right] = 0$ if $\alpha\neq\beta$, while $\left\{\chi_j^\alpha,\chi_k^\alpha\right\} = 2\delta_{j,k}$. On the other hand, it is possible to introduce related operators in $\mathcal{H}_N^{\otimes 4}$ which are all anti-commuting with one another, realizing a truly fermionic algebra. We consider for concreteness the case $N\equiv 0 \pmod 4$ [if $N\equiv 2 \pmod 4$, one has a similar treatment], and introduce

$$\mathcal{Q}^\alpha = \prod_{k=1}^{N}\chi_k^\alpha\,, \quad \alpha = a\,,b\,,c\,,d\,. \tag{3.10}$$

JHEP11(2019)038

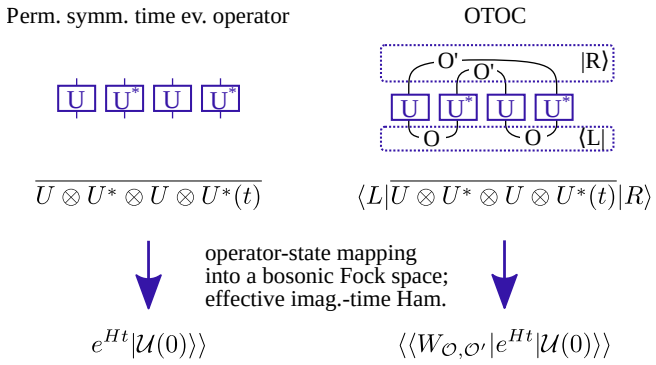

Figure 4. Schematic diagram summarizing our method. The dynamical information about the OTOC is uniquely encoded in the operator $\mathcal{U}(t) \equiv U \otimes U^* \otimes U \otimes U^*(t)$, while the observables $\mathcal{O}, \mathcal{O}'$ define the "right" and "left" states $|L\rangle$, $|R\rangle$ (cf. section 3.1). Exploiting the emergent permutational symmetry, we can map $\overline{U \otimes U^* \otimes U \otimes U^*(t)}$ onto a state $|\overline{\mathcal{U}}(t)\rangle\rangle$ in a bosonic Fock space, in which the dynamics is governed by an effective imaginary-time Hamiltonian evolution (cf. section 3.2). Finally, we express the matrix element of $\overline{\mathcal{U}}(t)$ with respect to $|L\rangle$ and $|R\rangle$ as the overlap between $|\overline{\mathcal{U}}(t)\rangle\rangle$ and an appropriate state $\langle\langle W_{\mathcal{O},\mathcal{O}'}|$ (cf. section 3.3). As a result, the entire computation of the OTOC can be performed very efficiently within a bosonic space, whose dimension grows linearly with N. The Rényi-2 entanglement entropies $S^{(2)}_{AC}$ and $S^{(2)}_{AD}$ are amenable to a similar treatment as the OTOCs.

Then, we can define

$$\psi^a_j = i\mathcal{Q}^a\chi^a_j\,, \qquad \psi^b_j = \mathcal{Q}^a\chi^b_j\,, \tag{3.11}$$

$$\psi^c_j = i\mathcal{Q}^a\mathcal{Q}^b\mathcal{Q}^c\chi^c_j\,, \qquad \psi^d_j = \mathcal{Q}^a\mathcal{Q}^b\mathcal{Q}^c\chi^d_j\,. \tag{3.12}$$

One can easily verify that $\{\psi^\alpha_j\}_{j,\alpha}$ satisfy fermionic anticommutation relations, namely $\{\psi^\alpha_j, \psi^\beta_k\} = 2\delta_{\alpha,\beta}\delta_{j,k}$, and that $\left(\psi^\alpha_j\right)^\dagger = \psi^\alpha_j$. Furthermore, since $(\mathcal{Q}^\alpha)^2 = \mathbb{1}$, we have $\prod_{k=1}^M \chi^\alpha_{j_k} = \prod_{k=1}^M \psi^\alpha_{j_k}$ for any even integer M. Since the Hamiltonian (2.1) contains a sum of products of Majorana operators with an even number of particles, it is then straightforward to show

$$\mathcal{U}(t) = U^a_+(t)U^b_-(t)U^c_+(t)U^d_-(t)\,, \tag{3.13}$$

where

$$U^\alpha_\pm(t) = e^{\mp i\Delta t H^\alpha_{\rm SYK}(t_n)}e^{\mp i\Delta t H^\alpha_{\rm SYK}(t_{n-1})}\ldots e^{\mp i\Delta t H^\alpha_{\rm SYK}(t_1)}\,, \tag{3.14}$$

while $H^\alpha_{\rm SYK}$ is the Hamiltonian (2.1) written in terms of the fermions ψ^α_j. We see that $\mathcal{U}(t)$ can be viewed as an evolution operator on the space of four "replica" Majorana fermions ψ^α_j, labeled by $\alpha = a, b, c, d$. Eq. (3.13) represents the starting point for our subsequent calculations.

The above discussion allows us to decompose the problem of computing the OTOC (3.1) into two logically separated steps:

- compute the disorder average of the generator of the dynamics $\mathcal{U}(t)$, defined in eq. (3.13) (cf. section 3.2);

JHEP11(2019)038

- given the operator $\overline{\mathcal{U}}(t)$, evaluate the matrix element $\langle L|\overline{\mathcal{U}}(t)|R\rangle$, where $|L\rangle$, $|R\rangle$ were introduced in eq. (3.5) and pictorially represented in figure 4 (cf. section 3.3).

Importantly, it is possible to show that the same procedure can be employed for the Rényi-2 tripartite information (2.14): one can express also this quantity in the form of a matrix element $\langle L|\overline{\mathcal{U}}(t)|R\rangle$, for an appropriate choice of the vectors $|L\rangle$ and $|R\rangle$, cf. section 3.3. We will address the two points above separately in the following subsections, for both the OTOCs and the tripartite information, providing a complete overview of the approach developed in this work.

3.2 The generator of the dynamics: mapping to a bosonic system

We start by addressing the computation of the average evolution operator defined in eq. (3.13). Using that even numbers of different Majorana operators commute, and that one can factor disorder averages at different times, we note that eqs. (3.13), (3.14) imply

$$\overline{\mathcal{U}}(t_n) = \overline{e^{-i\Delta t H^a(t_n)} e^{i\Delta t H^b(t_n)} e^{-i\Delta t H^c(t_n)} e^{i\Delta t H^d(t_n)}} \times \overline{\mathcal{U}}(t_{n-1})\,. \tag{3.15}$$

This allows us to write down a linear differential equation for $\overline{\mathcal{U}}(t)$, as follows.

First, from eq. (3.3), we see that, in order to expand the first line at the first order in Δt, each exponential factor has to be expanded up to the *second* order. By doing this, and carefully taking into account the correlations between the couplings, one obtains an equation of the form

$$\overline{\mathcal{U}}(t_n) = \overline{\mathcal{U}}(t_{n-1}) + L\overline{\mathcal{U}}(t_{n-1})\Delta t + O(\Delta t^2)\,, \tag{3.16}$$

namely, taking the limit $\Delta \to 0$

$$\frac{\mathrm{d}}{\mathrm{d}t}\overline{\mathcal{U}}(t) = L\overline{\mathcal{U}}(t)\,, \tag{3.17}$$

where

$$L = \frac{1}{N^3}\Bigg[-2\binom{N}{4} + \sum_{\substack{\alpha,\beta=a,b,c,d \\ \alpha<\beta}} (-1)^{\gamma_{\alpha,\beta}} \times \sum_{i_1<i_2<i_3<i_4} \left(\psi^\alpha_{i_1}\psi^\beta_{i_1}\right)\left(\psi^\alpha_{i_2}\psi^\beta_{i_2}\right)\left(\psi^\alpha_{i_3}\psi^\beta_{i_3}\right)\left(\psi^\alpha_{i_4}\psi^\beta_{i_4}\right)\Bigg]\,. \tag{3.18}$$

Here, the indexes a, b, c, d are ordered as $a < b < c < d$, while we introduced

$$(-1)^{\gamma_{\alpha,\beta}} = \begin{cases} 1 & (\alpha,\beta) = (a,b),(a,d),(b,c),(c,d)\,, \\ -1 & (\alpha,\beta) = (a,c),(b,d)\,. \end{cases} \tag{3.19}$$

We note that, since the disorder average has been already taken, the operator L is time- and disorder-independent. Eq. (3.17) can thus be seen as a Schrodinger equation (at imaginary times) for $\overline{\mathcal{U}}(t)$ in the space $\mathrm{End}(\mathcal{H}_N^{\otimes 4})$ of the linear endomorphisms acting on $\mathcal{H}_N^{\otimes 4}$, where the left matrix multiplication by L is interpreted as a superoperator. In the following, it will be useful to denote by $|\mathcal{O}\rangle\rangle$ the state in $\mathrm{End}(\mathcal{H}_N^{\otimes 4})$ associated with the operator $\mathcal{O}$.

JHEP11(2019)038

In order to proceed, we note that at every time t, the operator $\overline{\mathcal{U}}(t)$ can be written as a linear superposition of operators of the form

$$\mathcal{O}_1^{\alpha_1}\mathcal{O}_2^{\alpha_2}\dots\mathcal{O}_N^{\alpha_N}\,, \tag{3.20}$$

where $\mathcal{O}_j^{\alpha_j}$ is chosen within the set of operators

$$I_j = \{\mathbb{1}, \psi_j^a\psi_j^b, \psi_j^a\psi_j^c, \psi_j^a\psi_j^d, \psi_j^b\psi_j^c, \psi_j^b\psi_j^d, \psi_j^c\psi_j^d, \psi_j^a\psi_j^b\psi_j^c\psi_j^d\}\,. \tag{3.21}$$

Indeed, due to the anticommutation relations of the Majorana operators and the form of the Hamiltonian H, it is easy to see that $\overline{\mathcal{U}}(t)$ can not contain terms with an odd number of fermions at site ψ_j^α. Hence, the dynamics of $|\overline{\mathcal{U}}(t)\rangle\rangle$ takes places in the Hilbert space generated by the vectors

$$|\alpha_1\dots\alpha_N\rangle := |\mathcal{O}_1^{\alpha_1}\mathcal{O}_2^{\alpha_2}\dots\mathcal{O}_N^{\alpha_N}\rangle\rangle\,. \tag{3.22}$$

Here, $\alpha_j \in \{1, ab, ac, ad, bc, bd, cd, abcd\}$, with the convention $\mathcal{O}_j^1 = \mathbb{1}$, $\mathcal{O}_j^{ab} = \psi_j^a\psi_j^b$, …, $\mathcal{O}_j^{abcd} = \psi_j^a\psi_j^b\psi_j^c\psi_j^d$, i.e the ordered set $\{\mathcal{O}_j^\alpha\}_{\alpha=1}^{abcd}$ coincides with I_j in eq. (3.21).

Eq. (3.22) defines the previously announced mapping to a system of N qudits, as one can interpret

$$|\alpha_1\dots\alpha_N\rangle = |\alpha_1\rangle\otimes\dots\otimes|\alpha_N\rangle \in \mathcal{K}_N\,, \tag{3.23}$$

where $\mathcal{K}_N = h_1\otimes\dots\otimes h_N$ and $h_j \simeq \mathbb{C}^8$ is the space generated by $\{|1\rangle\,, |ab\rangle\,, \dots\,, |abcd\rangle\}$. In this picture, the differential equation (3.17) is equivalent to a quench problem in $\mathcal{K}_N$: the system is prepared in the initial product state

$$|\overline{\mathcal{U}}(0)\rangle\rangle = |\mathbb{1}\rangle\rangle = |1\rangle\otimes|1\rangle\otimes\dots\otimes|1\rangle\,, \tag{3.24}$$

and left to evolve according to the differential equation

$$\frac{\mathrm{d}}{\mathrm{d}t}\,|\overline{\mathcal{U}}(t)\rangle\rangle = H\,|\overline{\mathcal{U}}(t)\rangle\rangle\,. \tag{3.25}$$

Here, H [not be confused with H_{SYK} in (2.1)] is an operator acting on $\mathcal{K}_N$ which plays the role of the Hamiltonian driving the imaginary-time dynamics. The precise form H in terms of local operators can be derived by computing the action on the basis operators (3.20) of the left multiplication by L in (3.18); however, even without doing this explicitly, it is easy to show that H is invariant under any permutation of the sites in $\mathcal{K}_N$. This comes from the fact that the operator L in (3.18) is left unchanged under the exchange of the pairs $\psi_i^\alpha\psi_i^\beta$ and $\psi_j^\alpha\psi_j^\beta$ for any choice of i and j. Since the initial state (3.24) also enjoys the same symmetry, we can conclude that the dynamics of $|\overline{\mathcal{U}}(t)\rangle\rangle$ takes place in the subspace $\mathcal{S}_N \subset \mathcal{K}_N$ which is invariant under arbitrary permutations of the sites. This is of course a great simplification for our problem. The permutational symmetry of the Hamiltonian H is "emergent" in the sense that it manifests itself only after taking averages over the Brownian disorder, while the Hamiltonian H_{SYK} in eq. (2.1) does not display this symmetry for individual random realizations.

JHEP11(2019)038

In order to study the dynamics in this subspace, we introduce the basis vectors $|\mathcal{O}_{\vec{n}}\rangle\rangle$ for $\mathcal{S}_N$

$$|\mathcal{O}_{\vec{n}}\rangle\rangle = |n_1, n_{ab}, n_{ac}, n_{ad}, n_{bc}, n_{bd}, n_{cd}, n_{abcd}\rangle = \frac{1}{\sqrt{N! n_1! n_{ab}! n_{ac}! n_{ad}! n_{bc}! n_{bd}! n_{cd}! n_{abcd}!}} \tag{3.26}$$
$$\times \sum_{\pi \in S_N} \pi \underbrace{|1\rangle \otimes \ldots \otimes |1\rangle}_{n_1} \otimes \underbrace{|ab\rangle \otimes \ldots \otimes |ab\rangle}_{n_{ab}} \otimes \underbrace{|ac\rangle \otimes \ldots \otimes |ac\rangle}_{n_{ac}} \otimes \ldots \otimes \underbrace{|abcd\rangle \otimes \ldots \otimes |abcd\rangle}_{n_{abcd}} \pi^{-1},$$

where we used the same notations as in eqs. (3.22), (3.23). Here π is the unitary operator associated with a generic element in the symmetric group S_N, whose action permutes different sites in $\mathcal{K}_N$. Note that, since the sum runs over all the permutations, not all the elements in the sum are linearly independent.

The basis vectors (3.26) of the permutation symmetric space $\mathcal{S}_N$ are labeled by sets of 8 integers $\{n_j\}$, satisfying $\sum_k n_k = N$, where each integer n_k [with $k = 1, ab, \ldots, abcd$] "counts" the number of qudits in the level associated with k. In fact, it is possible to employ a more convenient representation, by viewing the state (3.26) as an 8-mode Fock state generated by bosonic creation operators acting on a vacuum $|\Omega\rangle$. In particular, we have the identification

$$|n_1, \ldots, n_{abcd}\rangle = \frac{1}{\sqrt{n_1! \cdots n_{abcd}!}} (a_1^\dagger)^{n_1} (a_{ab}^\dagger)^{n_{ab}} \cdots (a_{abcd}^\dagger)^{n_{abcd}} |\Omega\rangle \ . \tag{3.27}$$

Here, each operator $a_k^\dagger$ creates a collective mode corresponding to the level associated with k. In this language, the initial state (3.24) is written as $|\overline{\mathcal{U}}(0)\rangle\rangle = \frac{1}{\sqrt{N!}} \left(a_1^\dagger\right)^N |\Omega\rangle$.

This representation is particularly convenient, due to the fact that the Hamiltonian H in eq. (3.25) can be written in terms of the same bosonic operators appearing in eq. (3.27):

$$H = \frac{1}{N^3} \left(-2 \binom{N}{4} + \frac{1}{4!} \sum_{r=1}^{6} (-1)^{\gamma_r} \left[X_r^4 - X_r^2(-6N+8) + 3N(N-2) \right] \right) , \tag{3.28}$$

where X_r is a bilinear operator of bosons. The explicit form of X_r is derived in section 5.1, cf. eqs. (5.7)–(5.12). A formal solution to the problem of computing $\overline{\mathcal{U}}(t)$ is then obtained as

$$|\overline{\mathcal{U}}(t)\rangle\rangle = e^{Ht} |\overline{\mathcal{U}}(0)\rangle\rangle = e^{Ht} \frac{1}{\sqrt{N!}} \left(a_1^\dagger\right)^N |\Omega\rangle \ . \tag{3.29}$$

From its explicit form, one can see that the Hamiltonian H commutes with the operator $\sum_{j=1}^{8} a_j^\dagger a_j$, which "counts" the total number of bosonic modes; accordingly, the evolved state (3.29) always belongs to the finite-dimensional Hilbert space generated by the basis vectors (3.27). However, the dimension of the latter is $D = \binom{N+7}{7}$, which grows as N^7, strongly limiting any numerical computation based on a brute force implementation of eq. (3.29). Luckily, it is possible to show that the Hamiltonian H has additional symmetries, which are unveiled by means of an appropriate Bogoliubov transformation

$$a_n = \frac{1}{\sqrt{8}} C_{n,m} b_m \, , \tag{3.30}$$

JHEP11(2019)038

further reducing the dimension of the effective Hilbert space explored by the dynamics. The matrix element $C_{n,m}$ are reported in section 5.1 [cf. eq. (5.13)]. Then, from the form of the Hamiltonian H in terms of the modes b_j [cf. eqs. (5.14)–(5.19)], one obtains that the number operators

$$n_{1,2} := b_1^\dagger b_1 + b_2^\dagger b_2\,, \qquad n_{3,4} := b_3^\dagger b_3 + b_4^\dagger b_4 \tag{3.31}$$

$$n_{5,6} := b_5^\dagger b_5 + b_6^\dagger b_6\,, \qquad n_{7,8} := b_7^\dagger b_7 + b_8^\dagger b_8 \tag{3.32}$$

are conserved, namely they commute with H. Of course, the initial state can also be expressed in terms of the modes introduced in eq. (3.30). Using the explicit form of $C_{n,m}$, we obtain

$$|\overline{\mathcal{U}}(0)\rangle\rangle = \frac{1}{\sqrt{N!}\sqrt{8}^N}(b_1^\dagger - b_2^\dagger - b_3^\dagger - b_4^\dagger + b_5^\dagger + b_6^\dagger + b_7^\dagger - b_8^\dagger)^N\,|\Omega\rangle \tag{3.33}$$

and find that the total conserved number $n_{1,2} + n_{3,4} + n_{5,6} + n_{7,8}$ is N.

As we will see in the next section, these formulas allow us to work with effective Hilbert spaces whose dimensions grow either linearly or quadratically with N, and hence to provide numerically exact results for very large system sizes.

3.3 The OTOC and the tripartite information

We now discuss the last step of our method, namely the computation of the matrix elements of the form (3.5). Let us consider the most general OTOC

$$\mathcal{F}_{(p,n,m)}(t) = \frac{1}{2^{N/2}}\mathrm{tr}\left\{\Phi^{(p,n)}(t)\Phi^{(p,m)}(0)\Phi^{(p,n)}(t)\Phi^{(p,m)}(0)\right\}\,, \tag{3.34}$$

where we introduced

$$\Phi^{(p,n)} = \psi_{i_1}\cdots\psi_{i_p}\,\psi_{j_1}\cdots\psi_{j_n}\,, \tag{3.35}$$

$$\Phi^{(p,m)} = \psi_{i_1}\cdots\psi_{i_p}\,\psi_{k_1}\cdots\psi_{k_m}\,, \tag{3.36}$$

and where all indices are different, i.e. the operators have only p Majorana fermions in common. Considering eq. (3.5), we can expand $\overline{\mathcal{U}}(t) = \overline{U\otimes U^*\otimes U\otimes U^*}$ into the basis of operators $\mathcal{O}_{\vec{n}}$ corresponding to the vector (3.26) in $\mathrm{End}(\mathcal{H}_N^{\otimes 4})$. We obtain

$$\mathcal{F}_{(p,n,m)}(t) = \sum_{\vec{n}} c_{\vec{n}}(t)\,\langle L|\,(\mathcal{O}_{\vec{n}})\,|R\rangle\,, \tag{3.37}$$

where the sum runs over all the sets $\vec{n} = \{n_j\}$ with $j = 1, ab, \ldots, abcd$ and $\sum_j n_j = N$, while $c_{\vec{n}}(t)$ are the coefficients of $\overline{\mathcal{U}}(t)$ in the basis of the operators $\mathcal{O}_{\vec{n}}$. One can now interpret the sum (3.37) as the scalar product between an appropriate state $|W_{(p,n,m)}\rangle\rangle \in \mathrm{End}(\mathcal{H}_N^{\otimes 4})$ and $|\overline{\mathcal{U}}(t)\rangle\rangle$; namely we can write

$$\mathcal{F}_{(p,n,m)}(t) = \langle\langle W_{(p,n,m)}|\overline{\mathcal{U}}(t)\rangle\rangle\,. \tag{3.38}$$

The whole problem of extracting the numerical value of the OTOC from the knowledge of $\overline{\mathcal{U}}(t)$ then boils down to writing down explicitly $|W_{(p,n,m)}\rangle\rangle$. After this is done, one can straightforwardly compute the overlap (3.38).

JHEP11(2019)038

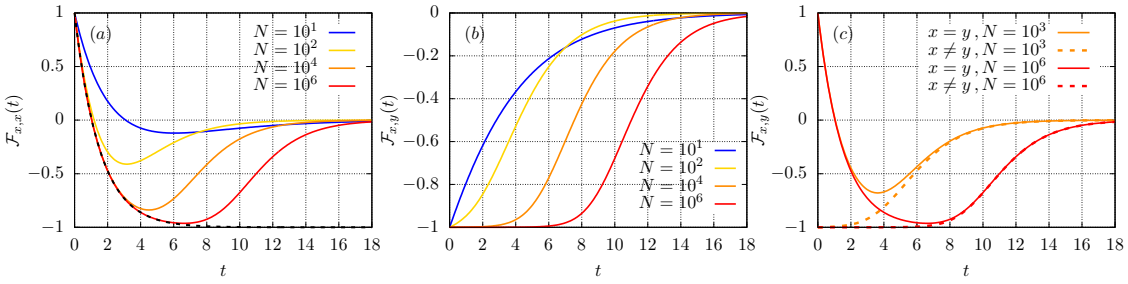

Figure 5. OTOCs $\mathcal{F}_{x,x}(t)$ and $\mathcal{F}_{x,y}(t)$ of single-site Majorana fermions. Subfigures (a) and (b) show our numerical results for increasing system sizes for operators on the same site (from top to bottom) and on different sites (from left to right) respectively. In Subfigure (a) the black dashed line is the analytic prediction (4.2). Subfigure (c): the two different OTOCs are reported in the same plot, where the dynamics after the scrambling time is seen to coincide.

The derivation of the explicit form of $|W_{(p,n,m)}\rangle\rangle$ is however rather technical, and for this reason we postpone it to section 5.2. The final result, instead, is extremely simple, and reads

$$|W_{(p,n,m)}\rangle\rangle = \frac{\sqrt{8}^N}{\sqrt{N!}}(-1)^{m(m-1)/2+n(n-1)/2+nm}(-b_3^\dagger)^p(-b_2^\dagger)^n(-b_4^\dagger)^m(b_1^\dagger)^{N-p-n-m}|\Omega\rangle\,, \tag{3.39}$$

where $|\Omega\rangle$ and b_j were introduced in eqs. (3.27) and (3.30) respectively.

Surprisingly, one can also express the Rényi-2 entropies entering in the definition of the tripartite information (2.14) in the same form. More precisely, choosing the same conventions as figure 2 for the bipartitions of input and output of the evolution operator, one can write

$$\exp\left[-S^{(2)}_{AC}(\bar\ell)\right] = \langle\langle W_{S^{(2)}_{AC}(\bar\ell)}|\overline{\mathcal{U}}(t)\rangle\rangle\,, \tag{3.40}$$

$$\exp\left[-S^{(2)}_{AD}(\bar\ell)\right] = \langle\langle W_{S^{(2)}_{AD}(\bar\ell)}|\overline{\mathcal{U}}(t)\rangle\rangle\,. \tag{3.41}$$

Here $\bar\ell$ is the length of B and D (chosen to be of the same size), while we will use ℓ for the length of the regions A and C.

Once again, we refer the reader to section 5, where this is explicitly shown, while in the following we report the final result of this analysis, which gives

$$|W_{S^{(2)}_{AC}(\bar\ell)}\rangle\rangle = \frac{\sqrt{8}^N}{\sqrt{N!}}\frac{1}{2^N}(b_1^\dagger - b_2^\dagger)^\ell(b_1^\dagger - b_4^\dagger)^{\bar\ell}|\Omega\rangle\,, \tag{3.42}$$

and

$$|W_{S^{(2)}_{AD}(\bar\ell)}\rangle\rangle = \frac{\sqrt{8}^N}{\sqrt{N!}}\frac{1}{2^{N/2+\bar\ell}}(b_1^\dagger)^\ell(b_1^\dagger - b_2^\dagger + b_3^\dagger - b_4^\dagger)^{\bar\ell}|\Omega\rangle\,. \tag{3.43}$$

Similar formulas could be in principle derived also for more general choices of the bipartitions of input and output. This, however, would introduce additional technical difficulties, so we don't derive them here.

JHEP11(2019)038

It is now very important to comment on the form of the formulas presented above, as it allows us to reduce the computational cost required to obtain the physical quantities of interest. Let us first consider the case of the OTOC (3.34), which is conveniently rewritten as

$$\mathcal{F}_{(p,n,m)}(t) = \langle\langle \overline{\mathcal{U}}(0)| \exp(Ht) |W_{(p,n,m)}\rangle\rangle^* . \tag{3.44}$$

Namely, in order to compute $\mathcal{F}_{(p,n,m)}(t)$, one can evolve $|W_{(p,n,m)}\rangle\rangle$ and then take the overlap with the state $|\overline{\mathcal{U}}(0)\rangle$. This is important, as is best appreciated by looking at the simplest instance $p = 0, n = m = 1$. In this case, eq. (3.39) implies that the state $|W_{(0,1,1)}\rangle\rangle$ belongs to the sector of the Hilbert space labeled by the quantum numbers $n_{1,2} = N-1, n_{3,4} = 1, n_{5,6} = n_{7,8} = 0$, where $n_{i,i+1}$ were introduced in eq. (3.31)–(3.32). Since $n_{j,j+1}$ are conserved by the Hamiltonian H, the dynamics takes place in this sector of the Hilbert space, whose dimension can be easily seen to be $D = N$. Accordingly, one can conveniently represent the restricted Hamiltonian in a basis consisting of N elements, and compute $e^{Ht}|W_{(0,1,1)}\rangle\rangle$ in this basis, which allows us to go to system size one million.

Similar considerations hold for the generic OTOC $|W_{(p,n,m)}\rangle\rangle$ (which belongs to the sector $n_{1,2} = N-p-m$, $n_{3,4} = p+m$, $n_{5,6} = n_{7,8} = 0$) and for the Rényi-2 entropies corresponding to (3.42), (3.43). In the latter cases, expanding

$$(b_1^\dagger - b_4^\dagger)^{\bar{\ell}} = \sum_{r=0}^{\bar{\ell}} \binom{\bar{\ell}}{r} \left(b_1^\dagger\right)^r \left(-b_4^\dagger\right)^{\bar{\ell}-r} , \tag{3.45}$$

$$(b_1^\dagger - b_2^\dagger + b_3^\dagger - b_4^\dagger)^{\bar{\ell}} = \sum_{r=0}^{\bar{\ell}} \binom{\bar{\ell}}{r} \left(b_1^\dagger - b_2^\dagger\right)^r \left(b_3^\dagger - b_4^\dagger\right)^{\bar{\ell}-r} , \tag{3.46}$$

one is left with a sum of terms, each of which requires a simulation within Hilbert spaces up to dimensions $N\bar{\ell} \sim N^2$. Putting all together, we see that the computation of the quantities of interest requires us to simulate the dynamics in a Hilbert space whose dimension grows either linearly (for the OTOCs) or quadratically (for the tripartite information) with N.

4 The physical results

In this section we present the main physical results of our work. We begin with the analysis of the OTOCs, and continue with the Rényi-2 tripartite information introduced in eq. (2.14).

4.1 The OTOCs: numerical results

We start by presenting our numerical results for the simplest OTOC

$$\mathcal{F}_{x,y}(t) = \frac{1}{2^{N/2}} \mathrm{tr}\left\{\psi_x(t)\psi_y(0)\psi_x(t)\psi_y(0)\right\} . \tag{4.1}$$

Due to the infinite range of the interactions and the disorder averages, $\mathcal{F}_{x,y}(t)$ does not depend on the precise choice of x and y, but only on whether $x = y$ or $x \neq y$. Both cases are displayed in figure 5, where we report data for increasing values of the system size N. We see that $\mathcal{F}_{x,x}(t)$ and $\mathcal{F}_{x,y}(t)$ (with $x \neq y$) behave qualitatively differently at short

JHEP11(2019)038

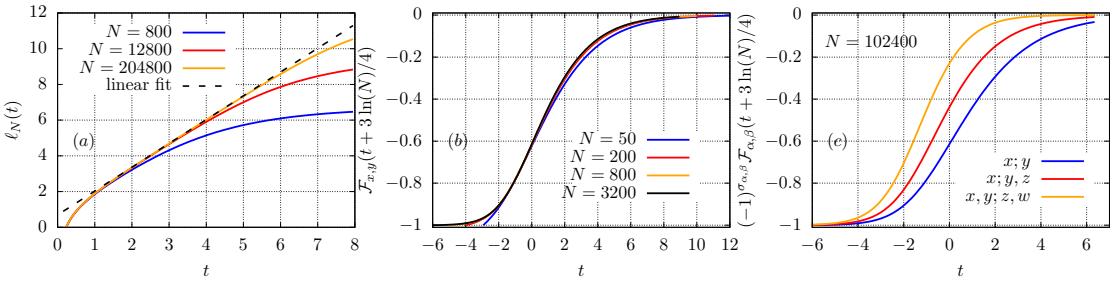

Figure 6. Subfigure (a): rescaled logarithmic OTOC $\ell_N(t)$ [defined in eq. (4.5)]. Solid lines correspond to increasing values of N (from bottom to top), while the dashed black line is the linear ansatz $y(t) = \frac{4}{3}t + \ln(2)$. Subfigure (b): data collapse using the shift (4.7) for the OTOCs $\mathcal{F}_{x,y}(t)$ (with $x \neq y$). Subfigure (c): data collapse for different OTOCs. The curves correspond (from bottom to top) to the OTOCs in eq. (4.1), (4.8) and (4.9) respectively. In order to compare the three curves, we have multiplied $\mathcal{F}_{\alpha,\beta}$ by the global phase $(-1)^{\sigma_{\alpha,\beta}}$, which is -1 for $(\alpha;\beta) = (x, y; z, w)$ and 1 otherwise.

times: the former displays an initial exponential decay, while the latter appears to remain approximately constant. In fact, based on the formulas of the previous section, one can make these statements more precise and show

$$\lim_{N\to\infty} \mathcal{F}_{x,x}(t) = -1 + 2\exp\left(-\frac{2}{3}t\right) , \tag{4.2}$$

$$\lim_{N\to\infty} \mathcal{F}_{x,y}(t) = -1 , \tag{4.3}$$

where the convergence is point-wise in t. This is proven in section (5.3). In both OTOCs $\mathcal{F}_{x,x}(t)$ and $\mathcal{F}_{x,y}(t)$, we see the emergence of a characteristic time $t^*(N)$, increasing with N, which is required before they begin to decay towards zero at large times. One naturally interprets $t^*(N)$ as a scrambling time, which is also consistent with our subsequent analysis of the tripartite information. Finally, in figure 5(c) we plot together the OTOCs for $x = y$ and $x \neq y$, for different systems sizes. We see that after an initial time window, the two OTOCs become indistinguishable, meaning that the information on the initial operators chosen has been completely washed out by the chaotic dynamics.

In order to quantitatively characterize the dependence of the scrambling time $t^*(N)$ on the system size, we test the short-time behavior of $\mathcal{F}_{x,y}(t)$ against the analytical ansatz [33]

$$\mathcal{F}_{x,y}(t) \sim -1 + c_{x,y}\frac{e^{\lambda_{x,y}t}}{N} , \tag{4.4}$$

where $c_{x,y}$ is a constant (independent of N). In particular, we compute

$$\ell_N(t) = \ln\left[1 + \mathcal{F}_{x,y}(t)\right] + \ln N , \tag{4.5}$$

and compare the numerical data against a linear behavior. The results are shown in figure 6(a). We clearly see that as the system size is increased, the curves for $\ell_N(t)$ approach the linear fit $y(t) = \frac{4}{3}t + \ln(2)$, within an initial time interval that is also increasing with N. In turn, this means that the ansatz (4.4) is valid, with the free parameters fixed as

$$\lambda_{x,y} = 4/3 , \qquad c_{x,y} = 2 . \tag{4.6}$$

From this result, we can identify the scrambling time with $t^*(N) = 3\ln(N)/4$.

JHEP11(2019)038

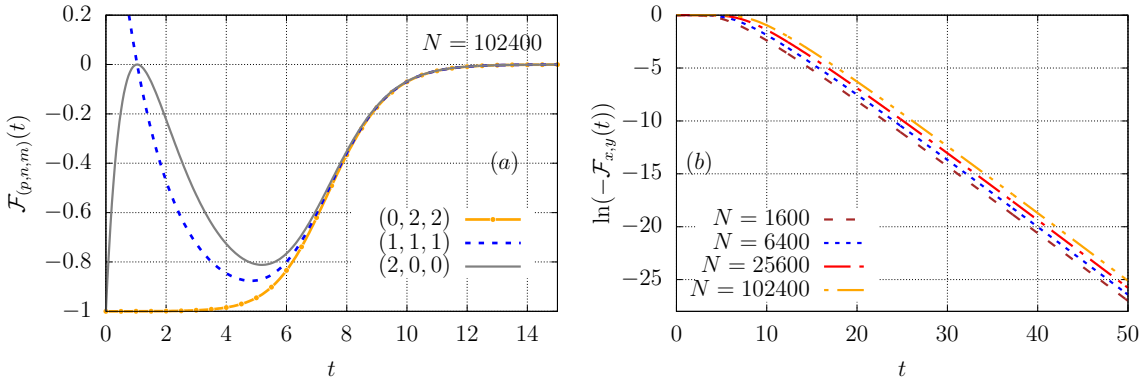

Figure 7. Subfigure (a): time evolution of different OTOCs corresponding to initial strings of Majorana operators with the same length. Each curve is labeled by three integer numbers, according to the convention of eq. (3.34). We see that in this case all the OTOCs quickly approach the same curve. Subfigure (b): large-time behavior of the logarithm of the OTOC $\mathcal{F}_{x,y}(t)$.

The initial behavior in eq. (4.4), together figure 5(b), suggests that a data collapse should take place if we consider the shifted functions

$$\mathcal{F}_{x,y}(t + 3\ln(N)/4)\,, \tag{4.7}$$

where we assumed that the parameters (4.6) are exact. This is plotted in figure 6(b), where we see a remarkable data collapse at all times. In particular, the data appear to be perfectly collapsed already for $N \gtrsim 800$.

Next, we have tested how robust the above predictions are, against different choices of the local observables. We have considered in particular

$$\mathcal{F}_{x;y,z}(t) = \frac{1}{2^{N/2}}\mathrm{tr}\left\{\psi_x(t)\psi_y(0)\psi_z(0)\psi_x(t)\psi_y(0)\psi_z(0)\right\}\,, \tag{4.8}$$

$$\mathcal{F}_{x,y;z,w}(t) = \frac{1}{2^{N/2}}\mathrm{tr}\left\{\psi_x(t)\psi_y(t)\psi_z(0)\psi_w(0)\psi_x(t)\psi_y(t)\psi_z(0)\psi_w(0)\right\}\,. \tag{4.9}$$

We have verified that at short times the ansatz (4.4) is always valid, and that a data collapse always takes place using the shift in eq. (4.7). Furthermore the exponent is universal, namely it is independent of the observables chosen (while the prefactor is not). However, the OTOCs corresponding to distinct choices of local operators are quantitatively different, also after the scrambling time $t^*(N)$, as it can be appreciated from figure 6(c). This can be interpreted by saying that, at finite times, the system retains some information on the initial observable chosen.

In order to investigate this point further, we plot in figure (7)(a) different OTOCs, corresponding to distinct choices of local observables, which are labeled according to the convention of in eq. (3.34). The curves correspond to initial operators that all have the same length, namely that are product of the same number of fermions. In this case, we see that all the OTOCs converge to the same function (up to small corrections) after the scrambling time. Comparing with the results displayed in figure 6(c), we can conclude the

JHEP11(2019)038

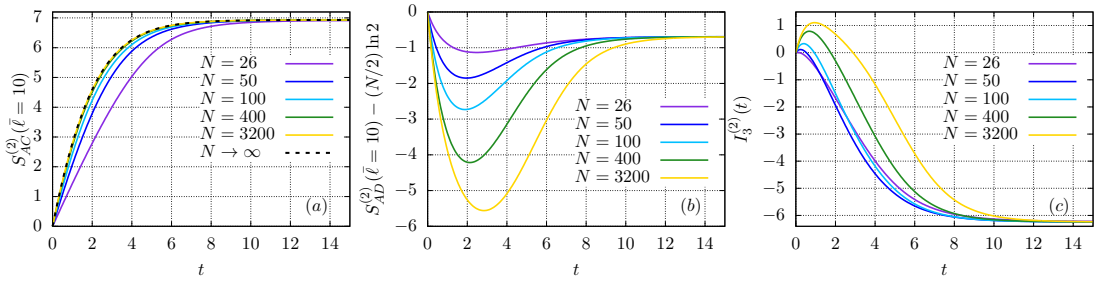

Figure 8. Subfigure (a): time evolution of the Rényi-2 entropies $S^{(2)}_{AC}$ for the subsystem $A\cup C$, as displayed in figure 2, with $\bar{\ell}=10$. Solid lines correspond to increasing values of N (from bottom to top), while the black dashed line is the analytic prediction (4.11). Subfigure (b): time evolution of the Rényi-2 entropy $S^{(2)}_{AD}$ for the subsystem $A\cup D$, with $\bar{\ell}=10$. Note that $S^{(2)}_{AD}$ is shifted by its maximum value $(N/2)\ln 2$. Solid lines correspond to increasing values of N (from top to bottom). Subfigure (c): time evolution of the Rényi-2 tripartite information $I^{(2)}_3(A:C:D)$, for the bipartitions $A\cup B$, $C\cup D$ displayed in figures 2 and 3 , with $\bar{\ell}=10$. Solid lines correspond to increasing values of N (from bottom to top).

following: after the scrambling time, information regarding the specific initial observables is lost, whereas OTOCs corresponding to operators with different initial length can still be distinguished.

Finally, we have investigated the large-time exponential decay of the OTOCs. The data in figure 5 suggest to consider an ansatz of the form

$$\mathcal{F}_{x,y}(t)\sim d_{x,y}\exp\left[-t/\tau_N\right]\,, \tag{4.10}$$

where τ_N should be asymptotically independent of N. In figure 7(b), we plot $\ln(-\mathcal{F}_{x,y}(t))$ for large values of t, and we see that the data are indeed consistent with an exponential decay of $\mathcal{F}_{x,y}(t)$. To be quantitative, we have performed a fit of $\ln(-\mathcal{F}_{x,y}(t))$ using $r_N(t)=a-t/\tau_N-b/t$. For the values of time t available, we have found that the fitted τ_N has a weak dependence on N, with $\tau_N\simeq 1.53\pm 0.04$ for $N\simeq 10^5$. The fitted value appears to be independent of the choice of the local observables, up to the inaccuracy of the extrapolation method.

4.2 The Rényi-2 tripartite information

We finally present our results for the Rényi-2 tripartite information introduced in eq. (2.14). As we discussed in section 3.3, for this quantity the effective dynamics to be computed takes place in a Hilbert space whose dimension grows quadratically with N, so that we are restricted to smaller system sizes than in the case of OTOCs. Furthermore, for large subsystems the value of the entropy becomes very large, so that we also have to deal with issues of numerical precision. Overall, for the computationally worst case of bipartitions of equal size, we are able to provide data up to $N\simeq 400$. More details on the numerical implementations are reported in appendix C.

In figure 8 we present data for the time evolution of the Rényi entropies of the subsystems $A\cup C$ and $A\cup D$, where we used the same partitions as figure 2. The plots correspond to fixed subsystem size and increasing N. Based on the formulas of section 3, in this limit

JHEP11(2019)038

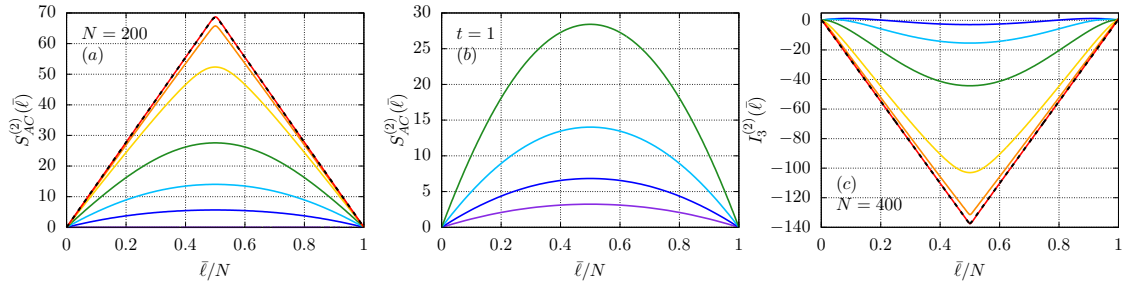

Figure 9. Subfigure (a): Rényi-2 entropies $S^{(2)}_{AC}$ for the subsystem $A\cup C$, as displayed in figure 2, for $N = 200$ and different subsystem sizes $\bar\ell$. Solid lines correspond to the times $t = 0, 0.4, 1, 2, 4, 6, 15$ (from bottom to top). The black dashed line is obtained by Haar average as computed in ref. [9]. Subfigure (b): Rényi-2 entropies $S^{(2)}_{AC}$ computed at $t = 1$, for different subsystem sizes $\bar\ell$. Solid lines correspond to system sizes $N = 50, 100, 200, 400$ (from bottom to top). Subfigure (c): Rényi-2 tripartite information (2.14) for $N = 400$ and different subsystem sizes $\bar\ell$. Solid lines correspond to the times $t = 0, 0.4, 1, 2, 4, 6, 15$ (from top to bottom). The black dashed line is obtained by Haar average as computed in ref. [9].

we are able to compute (cf. section 5.3)

$$\lim_{N\to\infty,\bar\ell,t\ \text{fix}} S^{(2)}_{AC}(\bar\ell, t) = \bar\ell \ln \frac{2}{1 + e^{-2t/3}}\,. \tag{4.11}$$

We see from figure 8(a) that the numerical results are in perfect agreement with this prediction. For finite N, the entropy $S^{(2)}_{AC}(t)$ displays an initial linear increase, eventually reaching a saturation value, as expected from the traditional picture of quantum quenches. The behavior of the Rényi entropy $S^{(2)}_{AD}(t)$ is instead not monotonic, as displayed in figure 8(b). Indeed, one has $S^{(2)}_{AD}(0) = (N/2)\ln 2$, which is the maximum entropy possible, so that at small times $S^{(2)}_{AD}(t)$ has to decrease. Its dynamics is then non-trivial during the initial scrambling time $t^*(N)$, after which it begins an exponential decay towards its large-time stationary value.

Figures 9 and 10 show the same quantities for all the possible values of the subsystems $\bar\ell$, at different times and system sizes. First, we notice that the entropies and the tripartite information are symmetric under exchange $\bar\ell \leftrightarrow \ell = N - \bar\ell$, as they should. Furthermore, we see that for different values of $\bar\ell$ we have the same qualitative behavior, where at large times an asymptotic value is always reached. In fact, it is possible to compute the latter exactly, as it is known that unitary evolutions driven by Brownian Hamiltonians converge in the infinite-time limit to unitary k-designs, for arbitrary positive integers k [103, 104]. As a consequence, the asymptotic properties can be computed using Haar averages. The latter, which were already computed in ref. [9], are reported as dashed lines in figure 9 and 10, towards which convergence is apparent. We note that, while their infinite-time limit could be expected, the entropies undergo non-trivial dynamics at short and intermediate times. This is best appreciated by looking at the entropy $S^{(2)}_{AD}(\bar\ell)$ in figure 10. We see that up to the scrambling time $t^*(N)$ it appears to be decreasing (precisely, its average over $\bar\ell$), while at later times it increases again. This results in the non-trivial dynamics of the tripartite information, which can become positive at short times [cf. figure 8(c)].

JHEP11(2019)038

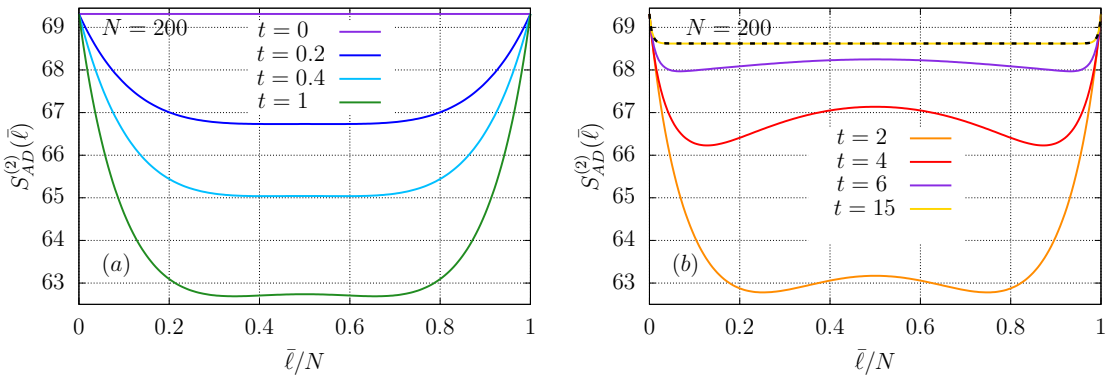

Figure 10. Time evolution of the Rényi-2 entropies $S^{(2)}_{AD}$ for the subsystem $A \cup D$, as displayed in figure 2, for $N = 200$ and different values of $\bar{\ell}$. Solid lines in subfigures (a) and (b) correspond, respectively, to times $t = 0, 0.2, 0.4, 1$ (from top to bottom) and $t = 2, 4, 6, 15$ (from bottom to top). The black dashed line in Subfigure (b) is obtained by Haar average as computed in ref. [9].

5 Deriving the key formulas

In this last section, we finally address the most technical aspects of our calculations, including several details of the method outlined in section 3. We start by presenting the explicit form of the Hamiltonian driving the dynamics in the four-replica space in section 5.1. Next, we derive the key formulas (3.39), (3.42) and (3.43) in section 5.2. Finally, in section 5.3 we report the proof of eqs. (4.2) and (4.11) for the large-N limit of the OTOC $\mathcal{F}_{x,y}(t)$, and of the Rényi entropy $S^{(2)}_{AC}(\bar{\ell})$.

5.1 The Hamiltonian

In this section we show how to derive the explicit form (3.28) of the Hamiltonian driving the imaginary-time evolution in eq. (3.25), from eq. (3.18). We start with the identity

$$4! \sum_{1\le j<k<l<m\le N} x_i x_j x_k x_l = X^4 - X^2(-6N+8) + 3N(N-2)\,, \tag{5.1}$$

with $X = \sum_{i=1}^{N} x_i$, for commuting operators x_i satisfying $x_i^2 = -1$. This can be easily derived as follows (see e.g ref. [94]). First, define

$$f_q = q! \sum_{1\le i_1<\ldots<i_q\le N} x_{i_1} \ldots x_{i_q}\,. \tag{5.2}$$

Then, using $x_j^2 = -1$, it is straightforward to show

$$X f_q = f_{q+1} - q(N+1-q) f_{q-1}\,, \tag{5.3}$$

which immediately yields the desired identity. Eq. (5.1) allows us to write the Hamiltonian in terms of global sums of pairs of single-site Majorana operators.

Next, suppose that for a single-site operator x_i we have

$$x_i \mathcal{O}_i^{\alpha} = c(\alpha) \mathcal{O}_i^{f(\alpha)} \;\; \forall \alpha \in \{1, ab, \ldots, abcd\}\,, \tag{5.4}$$

JHEP11(2019)038

where $\mathcal{O}_j^\alpha$ have been defined after eq. (3.22). Then one can make the following identification

$$X = \sum_{\alpha=1}^{abcd} c(\alpha) a^\dagger_{f(\alpha)} a_\alpha \,, \tag{5.5}$$

namely the action of X on the permutation symmetric basis (3.26) is the same as the r.h.s. of eq. (5.5), as can be checked directly. From this, the final form of the Hamiltonian in terms of bosonic modes a_j is readily obtained, and reads

$$H = \frac{1}{N^3}\left(-2\binom{N}{4} + \frac{1}{4!}\sum_{r=1}^{6}(-1)^{\gamma_r}\left[X_r^4 - X_r^2(-6N+8) + 3N(N-2)\right]\right), \tag{5.6}$$

where $(-1)^{\gamma_r}$ is given in (3.19), while the operators X_r are defined as

$$X_{ab} = a^\dagger_{ab}a_1 - a^\dagger_1 a_{ab} - a^\dagger_{bc}a_{ac} - a^\dagger_{bd}a_{ad} + a^\dagger_{ac}a_{bc} + a^\dagger_{ad}a_{bd} + a^\dagger_{abcd}a_{cd} - a^\dagger_{cd}a_{abcd}\,, \tag{5.7}$$

$$X_{ac} = a^\dagger_{ac}a_1 + a^\dagger_{bc}a_{ab} - a^\dagger_1 a_{ac} - a^\dagger_{cd}a_{ad} - a^\dagger_{ab}a_{bc} - a^\dagger_{abcd}a_{bd} + a^\dagger_{ad}a_{cd} + a^\dagger_{bd}a_{abcd}\,, \tag{5.8}$$

$$X_{ad} = a^\dagger_{ad}a_1 + a^\dagger_{bd}a_{ab} + a^\dagger_{cd}a_{ac} - a^\dagger_1 a_{ad} + a^\dagger_{abcd}a_{bc} - a^\dagger_{ab}a_{bd} - a^\dagger_{ac}a_{cd} - a^\dagger_{bc}a_{abcd}\,, \tag{5.9}$$

$$X_{bc} = a^\dagger_{bc}a_1 - a^\dagger_{ac}a_{ab} + a^\dagger_{ab}a_{ac} + a^\dagger_{abcd}a_{ad} - a^\dagger_1 a_{bc} - a^\dagger_{cd}a_{bd} + a^\dagger_{bd}a_{cd} - a^\dagger_{ad}a_{abcd}\,, \tag{5.10}$$

$$X_{bd} = a^\dagger_{bd}a_1 - a^\dagger_{ad}a_{ab} - a^\dagger_{abcd}a_{ac} + a^\dagger_{ab}a_{ad} + a^\dagger_{cd}a_{bc} - a^\dagger_1 a_{bd} - a^\dagger_{bc}a_{cd} + a^\dagger_{ac}a_{abcd}\,, \tag{5.11}$$

$$X_{cd} = a^\dagger_{cd}a_1 + a^\dagger_{abcd}a_{ab} - a^\dagger_{ad}a_{ac} + a^\dagger_{ac}a_{ad} - a^\dagger_{bd}a_{bc} + a^\dagger_{bc}a_{bd} - a^\dagger_1 a_{cd} - a^\dagger_{ab}a_{abcd}\,. \tag{5.12}$$

Inspection of eq. (5.6) reveals that the Hamiltonian displays several conservation laws. It is natural to look for a Bogoliubov transformation of the modes which makes some of the symmetries apparent. In addition, one would also like this transformation to simplify the convoluted a-mode expression $|\mathcal{W}_{(p,n,m)}\rangle\rangle$ for the OTOCs (5.36). Motivated by this, we look for a transformation where the first boson b_1 is associated with the macroscopically occupied mode in eq. (5.36), and choose the other modes b_j to satisfy canonical commutation relations. While this can be done in different ways, it turns out that a particularly convenient transformation is the one defined by eq. (3.30), where $C_{n,m}$ is the element in the line n and in the column m of the matrix

$$C = \begin{pmatrix} 1 & -1 & -1 & -1 & 1 & 1 & 1 & -1 \\ i & -i & i & i & i & -i & -i & -i \\ 1 & 1 & -1 & 1 & -1 & 1 & -1 & -1 \\ i & i & i & -i & -i & -i & i & -i \\ i & i & i & -i & i & i & -i & i \\ -1 & -1 & 1 & -1 & -1 & 1 & -1 & -1 \\ i & -i & i & i & -i & i & i & i \\ -1 & 1 & 1 & 1 & 1 & 1 & 1 & -1 \end{pmatrix}. \tag{5.13}$$

Indeed, after this Bogoliubov transformation the form of the Hamiltonian immediately reveals the presence of additional symmetries which can be directly exploited for our computations.

JHEP11(2019)038

It is straightforward to rewrite the operators (5.7)–(5.12), and hence the Hamiltonian (5.6), in terms of the new modes b_j. In particular, we have

$$X_{ab} = i(b_1^\dagger b_2 + b_2^\dagger b_1 + b_3^\dagger b_4 + b_4^\dagger b_3 - b_5^\dagger b_5 + b_6^\dagger b_6 + b_7^\dagger b_7 - b_8^\dagger b_8)\,, \tag{5.14}$$

$$X_{ac} = -b_1^\dagger b_2 + b_2^\dagger b_1 + b_3^\dagger b_4 - b_4^\dagger b_3 - b_5^\dagger b_6 + b_6^\dagger b_5 + b_7^\dagger b_8 - b_8^\dagger b_7\,, \tag{5.15}$$

$$X_{ad} = -i(b_1^\dagger b_1 - b_2^\dagger b_2 - b_3^\dagger b_3 + b_4^\dagger b_4 - b_5^\dagger b_6 - b_6^\dagger b_5 - b_7^\dagger b_8 - b_8^\dagger b_7)\,, \tag{5.16}$$

$$X_{bc} = -i(b_1^\dagger b_1 - b_2^\dagger b_2 - b_3^\dagger b_3 + b_4^\dagger b_4 + b_5^\dagger b_6 + b_6^\dagger b_5 + b_7^\dagger b_8 + b_8^\dagger b_7)\,, \tag{5.17}$$

$$X_{bd} = b_1^\dagger b_2 - b_2^\dagger b_1 - b_3^\dagger b_4 + b_4^\dagger b_3 - b_5^\dagger b_6 + b_6^\dagger b_5 + b_7^\dagger b_8 - b_8^\dagger b_7\,, \tag{5.18}$$

$$X_{cd} = i(b_1^\dagger b_2 + b_2^\dagger b_1 + b_3^\dagger b_4 + b_4^\dagger b_3 + b_5^\dagger b_5 - b_6^\dagger b_6 - b_7^\dagger b_7 + b_8^\dagger b_8)\,. \tag{5.19}$$

5.2 Extracting OTOCs and entropies

We now wish to show how to derive an explicit expression for the vectors $|W_{(p,n,m)}\rangle\rangle$, $|W_{S^{(2)}_{AC}(\bar\ell)}\rangle\rangle$ and $|W_{S^{(2)}_{AD}(\bar\ell)}\rangle\rangle$ in eqs. (3.39), (3.42) and (3.43), respectively. In order to simplify this task, we start by proving the following lemma. Let

$$|W_N\rangle\rangle = \sum_{n_1+\cdots+n_{abcd}=N} \frac{1}{\sqrt{N! n_1!\cdots n_{abcd}!}} \sum_{\pi\in S_N} \pi \prod_{x=1}^{N} \alpha_x(z_x)\pi^{-1}|n_1,\ldots,n_{abcd}\rangle, \tag{5.20}$$

where $z_x \in \{1, ab, ac, ad, bc, bd, cd, abcd\}$ is the operator at site x for the permutation π, cf. (3.26) and $\alpha_x(z_x)$ constants. Then

$$|W_N\rangle\rangle = \frac{1}{\sqrt{N!}} \prod_{x=1}^{N} \left(\sum_{z=1}^{abcd} \alpha_x(z) a_z^\dagger\right)|\Omega\rangle\,. \tag{5.21}$$

The equivalence between eqs. (5.20) and (5.21) is best established by directly expanding the product in eq. (5.21), and regrouping the different terms.

Next, we introduce some notations to handle our subsequent calculations in a compact way. In particular, let us rewrite the basis operator $\mathcal{O}_{\vec n}$ in eq. (3.26) as

$$\mathcal{O}_{\vec n} = \frac{1}{\sqrt{N! n_1!\cdots n_{abcd}!}} \times \sum_{\pi\in S_N} \pi\, \Psi^{ab}_{ab}\Psi^{ac}_{ac}\Psi^{ad}_{ad}\Psi^{bc}_{bc}\Psi^{bd}_{bd}\Psi^{cd}_{cd}\Psi^{abcd}_{abcd}\,\pi^{-1}\,. \tag{5.22}$$

Here we introduced the notations $\Psi^{ab}_{ab} = \prod_{p\in I_{ab}} \psi^a_p\psi^b_p$, $\Psi^{ac}_{ac} = \prod_{p\in I_{ac}} \psi^a_p\psi^c_p$, …, $\Psi^{abcd}_{abcd} = \prod_{p\in I_{abcd}} \psi^a_p\psi^b_p\psi^c_p\psi^d_p$, where I_{ab}, I_{ac}, … I_{abcd} are ordered, pairwise disjoint, subsets of $\{1, 2, \ldots N\}$, such that $|I_{ab}| = n_{ab}$, … $|I_{abcd}| = n_{abcd}$. In this notation, upper indexes in Ψ^α_β indicate the type of single-site operators, while lower indices specify which subset of $\{1, 2, \ldots, N\}$ the product of such operators runs over. Consistent with this convention, we also introduce

$$\Psi^a_a = \prod_{p\in I_a} \psi^a_p\,, \tag{5.23}$$

where I_a is the ordered set defined by

$$I_a = I_{ab} \cup I_{ac} \cup I_{ad} \cup I_{abcd}\,, \tag{5.24}$$

JHEP11(2019)038

and whose elements are ordered as they appear in eq. (5.24) (namely, the first n_{ab} elements of I_a are those of I_{ab} with the same order, followed by those of I_{ac}, and so on). Analogously, one can define Ψ^b_b, Ψ^c_c and Ψ^d_d, where

$$I_b = I_{ab} \cup I_{bc} \cup I_{bd} \cup I_{abcd}\,, \tag{5.25}$$

$$I_c = I_{ac} \cup I_{bc} \cup I_{cd} \cup I_{abcd}\,, \tag{5.26}$$

$$I_d = I_{ad} \cup I_{bd} \cup I_{cd} \cup I_{abcd}\,, \tag{5.27}$$

with the elements of I^a, I^b and I^c ordered as they appear in eqs. (5.25), (5.26) and (5.27). Finally, let us consider two disjoint subsets $A \cup B = \{1 \dots N\}$. Then, we define

$$\Psi^{ab}_{abA} = \prod_{p \in I_{ab} \cap A} \psi^a_p \psi^b_p\,, \qquad \Psi^{ab}_{abB} = \prod_{p \in I_{ab} \cap B} \psi^a_p \psi^b_p\,, \tag{5.28}$$

$$\Psi^{a}_{aA} = \prod_{p \in I_{a} \cap A} \psi^a_p\,, \qquad \Psi^{a}_{aB} = \prod_{p \in I_{a} \cap B} \psi^a_p\,, \tag{5.29}$$

and analogously for the other cases. Using these notations, we can rewrite

$$\begin{aligned}
\mathcal{O}_{\vec{n}} =& \mathcal{N} \sum_{\pi \in S_N} \pi\, \Psi^{ab}_{abA} \Psi^{ac}_{acA} \Psi^{ad}_{adA} \Psi^{bc}_{bcA} \Psi^{bd}_{bdA} \Psi^{cd}_{cdA} \Psi^{abcd}_{abcdA} \Psi^{ab}_{abB} \Psi^{ac}_{acB} \Psi^{ad}_{adB} \Psi^{bc}_{bcB} \Psi^{bd}_{bdB} \Psi^{cd}_{cdB} \Psi^{abcd}_{abcdB} \pi^{-1} \\
=& \mathcal{N} \sum_{\pi \in S_N} \pi\, \Psi^{a}_{aB} \Psi^{b}_{bB} \Psi^{c}_{cB} \Psi^{d}_{dB} \Psi^{a}_{aA} \Psi^{b}_{bA} \Psi^{c}_{cA} \Psi^{d}_{dA} (-1)^{\gamma_A + \gamma_B} \pi^{-1} \\
=& \mathcal{N} \sum_{\pi \in S_N} \pi\, \Psi^{a}_{aB} \Psi^{a}_{aA} \Psi^{b}_{bB} \Psi^{b}_{bA} \Psi^{c}_{cB} \Psi^{c}_{cA} \Psi^{d}_{dB} \Psi^{d}_{dA} (-1)^{\gamma_A + \gamma_B + \delta} \pi^{-1}\,,
\end{aligned} \tag{5.30}$$

where $\mathcal{N} = (N! n_1! \cdots n_{abcd}!)^{-1/2}$ is the normalization. In order to write down the first line, we used that even string of different fermions commute, while sorting the Majorana operators in the second line resulted in the phases $(-1)^{\gamma_A}$, $(-1)^{\gamma_B}$. We will not write γ_A, γ_B explicitly, as they will cancel at the end of the calculations. Conversely, one can easily compute the phase $(-1)^\delta$ appearing in the last line of eq. (5.30):

$$\begin{aligned}
(-1)^\delta &= (-1)^{n_{aA}(n_{bB}+n_{cB}+n_{dB}) + n_{bA}(n_{cB}+n_{dB}) + n_{cA} n_{dB}} \\
&= (-1)^{(n^2_{aB}+n^2_{bB}+n^2_{cB}+n^2_{dB})/2}\,.
\end{aligned} \tag{5.31}$$

Here we have used that $n_a = n_{aB} + n_{aA}$ and $n_{aB} + n_{bB} + n_{cB} + n_{dB}$ are even, which can be seen by writing explicitly $n_{aB} = n_{abB} + n_{acB} + n_{adB} + n_{abcdB}$ etc.

Eq. (5.30) is the starting point to derive the explicit form of the vectors $|W_{(p,n,m)}\rangle\rangle$, $|W_{S^{(2)}_{AC}(\bar{\ell})}\rangle\rangle$ and $|W_{S^{(2)}_{AD}(\bar{\ell})}\rangle\rangle$ for OTOCs and Rényi entropies respectively. These are treated in the following, in dedicated subsections.

5.2.1 The OTOCs

We wish to calculate the OTOC (3.34) of the initial operators (3.35), (3.36). Starting from (3.5)–(3.7), we can insert (5.30) for the correlated time evolution operator, where simply $A = \{1 \dots N\}, B = \{\}$ such that there is only one $(-1)^\gamma$ and no $(-1)^\delta$ and we omit the labels A, B. Since this expression involves products of even numbers of Majorana fermions

JHEP11(2019)038

acting on the same "replica" space, we may switch to the operators χ_j^α in eqs. (3.8), (3.9), and perform backwards the steps to derive eq. (3.5) from eq. (3.1). This gives

$$\mathcal{F}_{(p,n,m)} = \sum_{\vec{n}} \mathcal{N} c_{\vec{n}}(t) \sum_{\pi\in S_N} \pi \,\mathrm{tr}\left[\Phi^{(p,n)}\Psi_a\Phi^{(p,m)}\Psi_b^\dagger\Phi^{(p,n)}\Psi_c\Phi^{(p,m)}\Psi_d^\dagger\right](-1)^\gamma \pi^{-1}/2^{N/2}\,, \tag{5.32}$$

where $\Phi^{(p,n)}$, $\Phi^{(p,m)}$ are defined in eqs. (3.35), (3.36). Here, we simply wrote Ψ_a, Ψ_b, Ψ_c and Ψ_d without superscript, as we only have a single copy of the fermionic space. More explicitly, we have, for instance

$$\Psi_a = \prod_{p\in I_a} \psi_p\,, \tag{5.33}$$

where I_a is defined in (5.24).

Next we move the operator pairs $\Phi^{(p,n)}$ and $\Phi^{(p,m)}$ together such that they cancel. Of course, this generates phases through the anti-commutation relations of the fermions; we obtain

$$\begin{aligned}\mathcal{F}_{(p,n,m)} = \sum_{\vec{n}} \mathcal{N} c_{\vec{n}}(t) \sum_{\pi\in S_N} \pi \,\mathrm{tr}\left[\Psi_a\Psi_b^\dagger\Psi_c\Psi_d^\dagger\right](-1)^\gamma (-1)^{n_{a,c}(\{i_\alpha\})+n_{a,b}(\{j_\alpha\})+n_{b,c}(\{k_\alpha\})} \\ \times (-1)^{m(m-1)/2+n(n-1)/2+mn}\pi^{-1}/2^{N/2}\,,\end{aligned} \tag{5.34}$$

where $n_{a,c}(\{i_\alpha\})$ is the number of indeces in $\{i_\alpha\}_{\alpha=1}^p$ which also belong to $I_a \cup I_c$ [as defined in eqs. (5.24), (5.26)]. Analogously, $n_{a,b}(\{j_\alpha\})$ and $n_{b,c}(\{k_\alpha\})$ are, respectively, the numbers of indexes in $\{j_\alpha\}_{\alpha=1}^n$ and in $\{k_\alpha\}_{\alpha=1}^m$ which also belong to $I_a \cup I_b$ and $I_b \cup I_c$. Finally, noticing

$$\mathrm{tr}\left[\Psi_a\Psi_b^\dagger\Psi_c\Psi_d^\dagger\right] = (-1)^{(n_b+n_d)/2}\,\mathrm{tr}\left[\Psi_a\Psi_b\Psi_c\Psi_d\right] = 2^{N/2}(-1)^{(n_b+n_d)/2}(-1)^\gamma, \tag{5.35}$$

we see that the factor $(-1)^\gamma$ in (5.34) is exactly canceled. We are left with an equation of the form (5.20), setting α's appropriately. Thus we may apply the lemma proved before [cf. eq. (5.21)], which directly gives

$$\begin{aligned}|W_{(p,n,m)}\rangle\rangle = \frac{1}{\sqrt{N!}}(-1)^{m(m-1)/2+n(n-1)/2+nm} \\ \times (a_1^\dagger - ia_{ab}^\dagger + a_{ac}^\dagger - ia_{ad}^\dagger - ia_{bc}^\dagger - a_{bd}^\dagger - ia_{cd}^\dagger - a_{abcd}^\dagger)^p \\ \times (a_1^\dagger + ia_{ab}^\dagger - a_{ac}^\dagger - ia_{ad}^\dagger - ia_{bc}^\dagger + a_{bd}^\dagger + ia_{cd}^\dagger - a_{abcd}^\dagger)^n \\ \times (a_1^\dagger - ia_{ab}^\dagger - a_{ac}^\dagger + ia_{ad}^\dagger + ia_{bc}^\dagger + a_{bd}^\dagger - ia_{cd}^\dagger - a_{abcd}^\dagger)^m \\ \times (a_1^\dagger + ia_{ab}^\dagger + a_{ac}^\dagger + ia_{ad}^\dagger + ia_{bc}^\dagger - a_{bd}^\dagger + ia_{cd}^\dagger - a_{abcd}^\dagger)^{N-p-n-m}|\Omega\rangle\,.\end{aligned} \tag{5.36}$$

The result (3.39) is finally obtained after expressing the operators $a_j^\dagger$ in terms of the b-modes, introduced in eq. (3.30).

5.2.2 The Rényi-2 entanglement entropy $S_{AC}^{(2)}(\bar{\ell})$

Next, we turn to the task of deriving the vector $|W_{S_{AC}^{(2)}(\bar{\ell})}\rangle\rangle$ introduced in eq. (3.40), corresponding to the exponential of the second Rényi entropy $S_{AC}^{(2)}(\bar{\ell})$.

JHEP11(2019)038

As we have explained in detail in section 2.2, in order to compute $S^{(2)}_{AC}(\bar{\ell})$, we need to consider the evolved state $U^a\,|I^{ab}\rangle$, where $|I^{ab}\rangle$ was introduced in eq. (2.12), while the time evolution operator U^a acts only on the "replica" space a (cf. figure 3). For our fermionic system, the reduced density matrix of the union of the disjoint sets A and C can then be written as (see e.g. [107])

$$\rho_{AC} = \sum_{F^a_A, F^b_C} \frac{1}{2^\ell} (F^a_A F^b_C)^\dagger \, \langle I^{ab}|U^{a\dagger}(F^a_A F^b_C)U^a|I^{ab}\rangle \ . \tag{5.37}$$

Here we denoted by $\{F^a_A\}$, and $\{F^b_C\}$ a complete basis of operators in A, C respectively; namely F^a_A and F^b_C take value in all the possible strings of Majorana operators supported in A and C. Here, as before, we followed the convention that upper indexes indicate the type of single-site operators, while lower indices specify which subset of $\{1, 2, \ldots, N\}$ the product of such operators runs over. Through simple manipulations, we have

$$\begin{aligned} \mathrm{tr}\left[\overline{\rho^2_{AC}}\right] &= \frac{2^\ell}{2^{2\ell}} \sum_{F_A, F_C} \overline{\underbrace{\langle I^{ab}|\,U^{a\dagger}}_{\langle I^{ab}|U^b_-} F^a_A F^b_C U^a\,|I^{ab}\rangle \underbrace{\langle I^{cd}|\,U^{c\dagger}}_{\langle I^{cd}|U^d_-} \underbrace{F^{d\dagger}_C F^{c\dagger}_A}_{F^c_A F^d_C (-1)^\alpha} U^c\,|I^{cd}\rangle} \\ &= \frac{1}{2^\ell} \sum_{F_A, F_C} (-1)^\alpha \, \langle I^{ab}| \otimes \langle I^{cd}| \ F^a_A \otimes F^c_A \ \overline{U^a_+ U^b_- U^c_+ U^d_-} \ F^b_C \otimes F^d_C \ |I^{ab}\rangle \otimes |I^{cd}\rangle \ , \end{aligned} \tag{5.38}$$

where $U^\alpha_\pm(t)$ are defined in eq. (3.14). From this equation we clearly see that, in complete analogy with the case of the OTOCs, we can write also $\mathrm{tr}\left[\overline{\rho^2_{AC}}\right]$ in the form $\langle L|\overline{\mathcal{U}}(t)\,|R\rangle$. As anticipated, this allows us to apply a procedure similar to the one employed for the OTOCs, and derive the vector $|W_{S^{(2)}_{AC}(\bar{\ell})}\rangle\rangle$. In particular, we can use the notations introduced in section 5.2, and exploit directly eq. (5.30). This yields straightforwardly

$$\begin{aligned} \mathrm{tr}\left[\overline{\rho^2_{AC}}\right] &= \frac{1}{2^\ell \sqrt{N! n_1! \cdots n_{abcd}!}} \sum_{\vec{n}} c_{\vec{n}}(t) \sum_{\pi \in S_N} \pi (-1)^{\gamma_A + \gamma_B + \delta} \\ &\times \underbrace{\sum_{F_A, F_C} (-1)^\alpha \, \langle I^{ab}|F^a_A \Psi^a_{aB} \Psi^a_{aA} \Psi^b_{bB} \Psi^b_{bA} F^b_C |I^{ab}\rangle \, \langle I^{cd}|F^c_A \Psi^c_{cB} \Psi^c_{cA} \Psi^d_{dB} \Psi^d_{dA} F^d_C |I^{cd}\rangle \pi^{-1}}_{(*)} . \end{aligned} \tag{5.39}$$

Next, we compute

$$\begin{aligned} (*) &= \sum_{F_A, F_C} \langle I^{ab}|\Psi^b_{bB}\Psi^b_{bA}F^a_A\Psi^a_{aB}\Psi^a_{aA}F^b_C|I^{ab}\rangle \, \langle I^{cd}|\Psi^d_{dB}\Psi^d_{dA}F^{d\dagger}_C F^{c\dagger}_A \Psi^c_{cB}\Psi^c_{cA}|I^{cd}\rangle \\ &= \sum_{F_A, F_C} \langle I^{ab}|(\Psi^a_{bB}\Psi^a_{bA})^\dagger F^a_A \Psi^a_{aB}\Psi^a_{aA}F^b_C|I^{ab}\rangle \, \langle I^{cd}|F^{d\dagger}_C(\Psi^c_{dB}\Psi^c_{dA})^\dagger F^{c\dagger}_A \Psi^c_{cB}\Psi^c_{cA}|I^{cd}\rangle \\ &= \sum_{F_A, F_C} \langle I^{ab}|\Psi^{a\dagger}_{bA}\Psi^{a\dagger}_{bB}F^a_A\Psi^a_{aB}\Psi^a_{aA}F^{a\dagger}_C|I^{ab}\rangle \, \langle I^{cd}|F^c_C\Psi^{c\dagger}_{dA}\Psi^{c\dagger}_{dB}F^{c\dagger}_A\Psi^c_{cB}\Psi^c_{cA}|I^{cd}\rangle \\ &= \sum_{F_A, F_C} (-1)^{n_{aB}\#F_A + n_{dB}\#F_A} \, \langle I|\Psi^\dagger_{bA} \underbrace{\Psi^\dagger_{bB}\Psi_{aB}}_{2^{-\bar{\ell}/2}\,\mathrm{tr}\,\Psi^\dagger_{bB}\Psi_{aB}} F_A \Psi_{aA} F^\dagger_C |I\rangle \\ &\qquad \times \langle I|F_C \Psi^\dagger_{dA} F^\dagger_A \underbrace{\Psi^\dagger_{dB}\Psi_{cB}}_{2^{-\bar{\ell}/2}\,\mathrm{tr}\,\Psi^\dagger_{dB}\Psi_{cB}} \Psi_{cA}|I\rangle \end{aligned} \tag{5.40}$$

JHEP11(2019)038

In (5.40), all Majorana operators are in the same system, so we leave away the doubled system label. To extract the traces, note that those are the only operators acting on the region B of the system. Thus the Majorana fermions on those sites B already have to cancel in pairs, or the expectation value $\langle I|\cdot|I\rangle$ will be zero. Similarly, the only value of F_C with non-zero contribution has

$$\Psi^\dagger_{bA} F_A \Psi_{aA} F^\dagger_C = \pm 1 \Rightarrow F_C = \pm \Psi^\dagger_{bA} F_A \Psi_{aA}\,, \tag{5.41}$$

which can be inserted into the second expectation value, canceling the ± 1 and giving

$$\begin{aligned}(*) &= \frac{1}{2^{\bar\ell/2}} \operatorname{tr}\left[\Psi^\dagger_{bB}\Psi_{aB}\right] \frac{1}{2^{\bar\ell/2}} \operatorname{tr}\left[\Psi^\dagger_{dB}\Psi_{cB}\right] \langle I|I\rangle \\ &\quad \times \langle I|\Psi^\dagger_{bA} \sum_{F_A} (-1)^{\#(\Psi_{aA}\Psi^\dagger_{dA})\#F_A} F_A \Psi_{aA}\Psi^\dagger_{dA} F^\dagger_A \Psi_{cA}|I\rangle \\ &= 2^{-\bar\ell} \operatorname{tr}\left[\Psi^\dagger_{bB}\Psi_{aB}\right] \operatorname{tr}\left[\Psi^\dagger_{dB}\Psi_{cB}\right] \operatorname{tr}\left[\Psi_{aA}\Psi^\dagger_{dA}\right] \operatorname{tr}\left[\Psi^\dagger_{bA}\Psi_{cA}\right] \\ &= 2^{-\bar\ell}(-1)^{\frac{n_b+n_d}{2}+n_{bB}+n_{dB}} \operatorname{tr}\left[\Psi_{aB}\Psi_{bB}\right] \operatorname{tr}\left[\Psi_{cB}\Psi_{dB}\right] \operatorname{tr}\left[\Psi_{aA}\Psi_{dA}\right] \operatorname{tr}\left[\Psi_{bA}\Psi_{cA}\right]\,. \end{aligned} \tag{5.42}$$

Here, in order to go from the first to the second line, we made use of the identity (B.8) in appendix B.2. The last line of (5.42) is non-zero only for

$$\begin{aligned} &n_1 = n_{1B} + n_{1A}\,, && n_{ab} = n_{abB}\,, && n_{ac} = 0\,, \\ &n_{ad} = n_{adA}\,, && n_{bc} = n_{bcA}\,, && n_{bd} = 0\,, \\ &n_{cd} = n_{cdB}\,, && n_{abcd} = n_{abcdB} + n_{abcdA}\,. \end{aligned} \tag{5.43}$$

With this we see that the traces evaluate as $(-1)^{\gamma_B+\gamma_A}$. Also, it shows that $n_{aB} \equiv n_{bB} \equiv n_{bA} \equiv n_{cA} \equiv n_{cB} \equiv n_{dB} \pmod 2$, such that $(-1)^\delta = +1$. Putting all together, we get

$$\operatorname{tr}\overline{\rho^2_{AC}} = \sum_{\vec n} \frac{c_{\vec n}(t)}{\sqrt{N! n_1! \cdots n_{abcd}!}} \times \sum_{\pi\in S_N} \pi\, (-1)^{(n_b+n_d)/2} \delta(\pi) \pi^{-1} \tag{5.44}$$

where the Kronecker delta $\delta(\pi)$ enforces the constraints (5.43). This expression can also be cast into the form (5.20) by setting some α's to zero. Then eq. (5.21) gives us

$$|W_{S^{(2)}_{AD}(\bar\ell)}\rangle\rangle = \frac{1}{\sqrt{N!}} \left[i a^\dagger_{ab} + i a^\dagger_{cd} + (a^\dagger_1 - a^\dagger_{abcd})\right]^\ell \left[i a^\dagger_{ad} + i a^\dagger_{bc} + (a^\dagger_1 - a^\dagger_{abcd})\right]^{\bar\ell} |\Omega\rangle\,. \tag{5.45}$$

Transformation to b-modes (3.30) finally yields the result anticipated in eq. (3.42).

An analogous treatment can be carried out for the case of the entropy $S^{(2)}_{AD}$. Since the technical steps are very similar, we report them in appendix D.

5.3 Some large-N limits

In this section, we finally show how one can compute the limit $N \to \infty$, while keeping time t fixed, for the OTOCs and the Rényi-2 entropies, and derive in particular eqs. (4.2) and (4.11).

We start with the case of OTOCs, and consider eq. (3.44). As a first simplification, we only need to keep modes b_1 through b_4 in the Hamiltonian and initial state $\langle\langle\overline{\mathcal{U}}(0)|$ as the

JHEP11(2019)038

others are not present in $|W_{(p,n,m)}\rangle\rangle$. Next, we switch to ladder operators with an unusual normalization, specifically

$$\tilde{b}_i^\dagger |n_i\rangle_{\tilde{b}} = |n_i+1\rangle_{\tilde{b}}\,,\ \tilde{b}_i |n_i\rangle_{\tilde{b}} = n_i |n_i-1\rangle_{\tilde{b}}\,. \tag{5.46}$$

This now allows us to take the leading order in N for each term of the exponential e^{Ht}, using that $\tilde{b}_1 \sim N$ as $p, n, m \ll N$. We obtain

$$\lim_{N\to\infty} \langle\langle \overline{\mathcal{U}}(0)|e^{Ht}|W_{(p,n,m)}\rangle\rangle = \sum_{m=0}^{\infty} \langle\langle \overline{\mathcal{U}}(0)| \left(\lim_{N\to\infty} H\right)^m |W_{(p,n,m)}\rangle\rangle t^m/m!\,, \tag{5.47}$$

with

$$\lim_{N\to\infty} H = H_A + H_B + H_C, \tag{5.48}$$

$$H_A = \frac{2}{3}(\tilde{b}_2^{\dagger 2}\tilde{b}_1^2/N^2 - 1)\tilde{b}_2^\dagger \tilde{b}_2, \tag{5.49}$$

$$H_B = \frac{2}{3N^3}\tilde{b}_2^{\dagger 3}\tilde{b}_1^3\tilde{b}_4^\dagger \tilde{b}_3, \tag{5.50}$$

$$H_C = -\frac{2}{3}\tilde{b}_3^\dagger \tilde{b}_3\,. \tag{5.51}$$

As $\langle\langle \overline{\mathcal{U}}(0)|\,(\tilde{b}_2^{\dagger 2}\tilde{b}_1^2/N^2 - 1) = 0$ at the highest order in N, terms with H_A do not contribute at the leading order. For the OTOC $\mathcal{F}_{x,y}(t)$, also H_B and H_C cannot occur, because $|W_{x,y}\rangle\rangle$ (3.39) does not contain any b_3-modes. The asymptotic result is then the constant $\mathcal{F}_{x,y}(t) \to \langle\langle \overline{\mathcal{U}}(0)|1|W_{x,y}\rangle\rangle = -1$, as reported in (4.3). In contrast, for the OTOC $\mathcal{F}_{x,x}(t)$, the state $|W_{x,x}\rangle\rangle$ does contain one b_3-mode such that H_B can appear at most once. The remaining Hamiltonian is still simple enough to finally derive the exponential decay (4.2). We stress that we can only expect these limits to be point-wise in t due to the exchange of limits in (5.47); in fact, convergence is clearly not uniform, as can be seen from the exact numerical results.

The case of the entropy $S_{AC}^{(2)}(t)$ is treated along similar lines. We first perform a further mode transformation

$$\begin{aligned} c_1 &= (b_1 - b_2)/\sqrt{2}\,, & c_2 &= (b_1 + b_2)/\sqrt{2}\,, \\ c_3 &= (b_3 + b_4)/\sqrt{2}\,, & c_4 &= (b_4 - b_3)/\sqrt{2}\,, \end{aligned} \tag{5.52}$$

such that

$$|W_{S^{(2)}_{AC(\bar{\ell})}}\rangle\rangle = \frac{2^N}{\sqrt{N!}}\frac{1}{2^{\bar{\ell}}}(c_1^\dagger)^\ell (c_1^\dagger + c_2^\dagger - c_3^\dagger - c_4^\dagger)^{\bar{\ell}}\,|\Omega\rangle\ . \tag{5.53}$$

We may now follow the same procedure as for the OTOCs. In fact, the Hamiltonian has the exact same form in terms of the modes b_j and c_j. Taking $\bar{\ell} \ll N$, eq. (5.48) is therefore valid, after substituting the modes $\tilde{b}_j$ with $\tilde{c}_j$. Now, the initial state

$$\langle\langle \overline{\mathcal{U}}(0)| = \langle\Omega|\,(c_1 - c_3)^N \frac{1}{\sqrt{N!}2^N} \tag{5.54}$$

annihilates both H_A and H_B ensuing in a very simple (quadratic) asymptotic Hamiltonian H_C. From this, eq. (4.11) follows straightforwardly.

JHEP11(2019)038

6 Conclusions

In this work, we have developed an approach to analyze the chaotic dynamics in the Brownian SYK model, a system of N Majorana fermions coupled together via random, time-dependent interactions. We have shown that the OTOCs and the tripartite information of the unitary evolution can be studied as a quench problem (at imaginary times) in a system of N qudits, which can be conveniently investigated in terms of bosonic modes, due to an emergent permutational symmetry. Exploiting the latter, we were able to produce numerically exact results up to $N = 10^6$, and to study several features of the chaotic dynamics at finite size.

We have analyzed in detail the dependence of the OTOCs on the observables chosen, highlighting the pieces of information on the initial operators which are not washed out by the chaotic dynamics. In particular, after the scrambling time $t^*(N) \sim \ln N$, the OTOCs of distinct operators converge to the same curve if they have the same length, namely if they are written as products of the same number of Majorana fermions, whereas the curves of different OTOCs can be distinguished after the scrambling time $t^*(N)$ if the length is different. Furthermore, we have verified that the exponent of the initial exponential growth of the OTOCs is universal and performed a data collapse for increasing system sizes. Regarding the tripartite information, we have shown that its evolution is non-trivial during the initial scrambling time, while at large times it always decays exponentially to the corresponding Haar-scrambled value; this result is consistent with the rigorous recent findings of refs. [103, 104]

The approach developed in this paper can be generalized to other models where the Hamiltonian displays all-to-all random interactions, with time-dependent Brownian disorder. Indeed, one can straightforwardly follow the steps outlined in section 3, and study the dynamics of OTOCs and tripartite information as a quench problem in a qudit system with site permutational symmetry. In turn, this implies that the effective imaginary-time dynamics takes place in a Hilbert space whose dimension grows as a polynomial in N. Of course, one would need to investigate for each case whether a further reduction of the effective dimension takes place, as for the Brownian SYK model studied in this paper.

It is possible that the final formulas obtained with our method (which have been used in this work mainly for efficient numerical computations) could be simplified further and evaluated to exact analytic expressions in the large-N limit. In fact, by means of a different approach, an exact result for a suitable average of OTOCs was found in ref. [98] for the Brownian dynamics generated by a disordered Hamiltonian in a qudit system. It would be interesting to see whether ideas related to the work [98] could be used here, to obtain analytic expressions for the OTOCs of arbitrary observables and for the tripartite information, in the large-N limit.

Finally, the approach presented in this paper could also be applied to compute quantities involving higher moments of the evolution operator $U(t)$, such as Rényi entropies of higher order, or the Rényi-2 operator entanglement entropy of local observables [109, 110]. In these cases, however, the application of our method would be inevitably more complicated. More importantly, it is not granted that a reduction of the Hilbert-space dimension

JHEP11(2019)038

could be achieved by means of a transformation analogous to (3.30). In any case, it would be certainly interesting to investigate these points further.

Acknowledgments

LP thanks Bruno Bertini and Tomaz Prosen for discussions related to this work. XLQ thanks the helpful discussions with David Huse and Alex Streicher. LP acknowledges support from the Alexander von Humboldt foundation. JIC and NS acknowledge support by the EU Horizon 2020 program through the ERC Advanced Grant QENOCOBA (No. 742102, JIC) and the ERC Starting Grant WASCOSYS (No. 636201, NS), and from the DFG (German Research Foundation) under Germany's Excellence Strategy — EXC-2111 — 390814868. XLQ is supported by the National Science Foundation under grant No. 1720504, and in part by the Department of Energy under grant No. DE-SC0019380.

A Non-interacting case: $q = 2$

In this section, we study the Brownian SYK model (2.1) for $q = 2$. We choose the constant σ_J in (2.2) such that the disorder's correlations are given by

$$\overline{J_{ij}(t)J_{i'j'}(t')} = \delta_{ii'}\delta_{jj'}\delta(t-t')\frac{1}{N}\,. \tag{A.1}$$

Each disorder realization is governed by a free Hamiltonian, therefore we do not expect any scrambling of operators or decay of OTOCs.

The method developed in this article can be applied to arbitrary q and we may study the non-interacting case within its framework. The states

$$|W_{(p,n,m)}\rangle\rangle,\ |W_{S^{(2)}_{AC}(\bar{\ell})}\rangle\rangle,\ |W_{S^{(2)}_{AD}(\bar{\ell})}\rangle\rangle,\ \text{and}\ |\overline{\mathcal{U}}(0)\rangle\rangle \tag{A.2}$$

representing the OTOC (3.39), Rényi-2 entanglement entropies (3.40) and (3.41), and initial time evolution operator (3.33) are independent of q as long as q is even. However, the effective Hamiltonian reflects the change of q and is simpler. Along the same lines as for $q = 4$ (see section 3.2), we can compute

$$\frac{\mathrm{d}}{\mathrm{d}t}\overline{\mathcal{U}(t)} = L\overline{\mathcal{U}(t)}, \tag{A.3}$$

$$L = \frac{1}{N}\left[-2\binom{N}{2} - \sum_{\substack{\alpha,\beta=a,b,c,d\\ \alpha<\beta}}\sum_{i<j}(\psi_i^\alpha\psi_i^\beta)(\psi_j^\alpha\psi_j^\beta)\right]. \tag{A.4}$$

The corresponding representation of the effective Hamiltonian after operator-state mapping in bosonic modes is

$$|\overline{\mathcal{U}}(t)\rangle\rangle = e^{Ht}\,|\overline{U}(0)\rangle\rangle, \tag{A.5}$$

$$H = \frac{1}{N}\left[-2\binom{N}{2} - 3N - \frac{1}{2}\sum_{r=ab}^{cd}X_r^2\right] \tag{A.6}$$

$$= -\frac{4}{N}(b_1^\dagger b_3^\dagger - b_2^\dagger b_4^\dagger)(b_1 b_3 - b_2 b_4), \tag{A.7}$$

JHEP11(2019)038

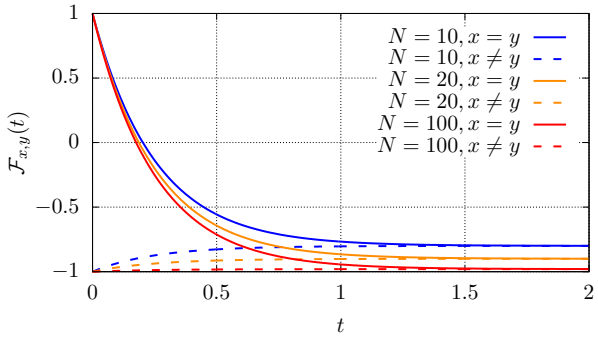

Figure 11. OTOCs $\mathcal{F}_{x,x}(t)$ (solid lines) and $\mathcal{F}_{x,y}(t)$ (dashed lines) for single site Majorana fermions. We show the analytical results (A.9) and (A.8) for various system sizes N. At long times, they decay to the same value $-1 + \frac{2}{N} \neq 0$, indicating the absence of scrambling.

where the six X_r operators are the same as in the corresponding expression (3.28) for $q = 4$.

For the two simple OTOCs $\mathcal{F}_{x,y}(t)$ and $\mathcal{F}_{x,x}(t)$ the dynamics only explores the two-level subspace spanned by $|N-1,0,1,0\rangle$ and $|N-2,1,0,1\rangle$. Therefore we can compute these OTOCs analytically and obtain

$$\mathcal{F}_{x,y}(t) = -1 + \frac{2}{N} - \frac{2}{N} e^{-4t}\,, \tag{A.8}$$

$$\mathcal{F}_{x,x}(t) = -1 + \frac{2}{N} + \frac{2}{N} e^{-4t}(N-1)\,. \tag{A.9}$$

The curves are plotted in figure 11. As expected, the OTOCs do not decay to zero at long times, as the non-interacting model is not chaotic. Since the tripartite information can be written as an average of OTOCs [9], it too will lack the characteristics of scrambling.

We now make a comment on the so-called "length" of the operator $\psi_j(t)$, see e.g. [38]. At any time t, we can always write

$$\psi_j(t) = \sum_s \sum_{\{k_j\}} \underbrace{\psi_{k_1} \cdots \psi_{k_s}}_{\text{length } s} c_{s,\{k_j\}}(t)\,, \tag{A.10}$$

and define the average length $L(t)$ as

$$L(t) = \sum_s s \sum_{\{k_j\}} |c_{s,\{k_j\}}|^2\,. \tag{A.11}$$

It can be shown that the average length is related to an appropriate average over OTOCs, namely [38]

$$L(t) = \frac{N + \mathcal{F}_{x,x}(t) + (N-1)\mathcal{F}_{x,y}(t)}{2}. \tag{A.12}$$

Using this relation, if follows from our results (A.8)–(A.9) that the length is constant 1. This is expected because the Gaussian dynamics preserves the length of products of Majorana operators.

JHEP11(2019)038

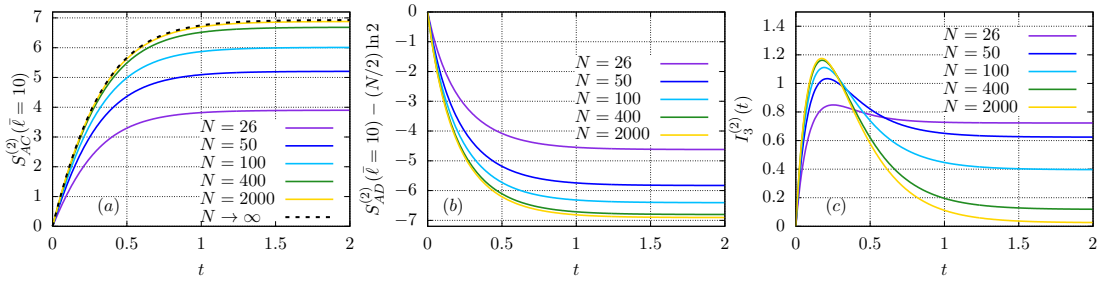

Figure 12. For the free case ($q = 2$), we show the time behavior of the entanglement entropies $S^{(2)}_{AC}$ (a), $S^{(2)}_{AD}$ (b) and tripartite information $I^{(2)}_3$ (c) for several system sizes N and fixed subsystem size $\bar{\ell} = 10$. In (a), we also indicate the limit (A.13). The tripartite information is always positive, which means that the non-interacting system does not scramble quantum information.

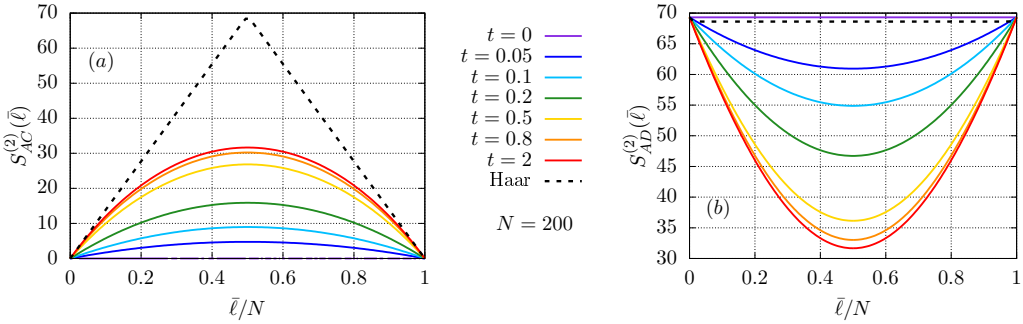

Figure 13. The entanglement entropies $S^{(2)}_{AC}$ (a) and $S^{(2)}_{AD}$ (b) for various subsystem sizes $\bar{\ell}$ and several times t in the free case. The black dotted lines show the values reached with Haar-scrambling.

Next, we can calculate the entanglement entropies numerically, just like in the interacting case. We present the results in figure 12. In the limit $N \to \infty, \bar{\ell}, t$ fixed, we can derive

$$\lim_{N\to\infty,\bar{\ell},t \text{ fix}} S^{(2)}_{AC}(\bar{\ell},t) = \bar{\ell}\ln\frac{2}{1+e^{-4t}}, \tag{A.13}$$

along the same lines as in section 5.3. While the entropy $S^{(2)}_{AC}(\bar{\ell})$ saturates to its maximal Haar value at large N and t, the behavior of $S^{(2)}_{AD}(\bar{\ell})$ is qualitatively different from the interacting case (figure 8). This leads to the tripartite information being positive at all times and system sizes, indicating the absence of scrambling.

As for the interacting case, we can also study the entanglement entropies' dependence on the subsystem size, see figure 13. Comparing against figures 9 and 10, we see that in the free case, the entanglement entropies do not reach the maximal Haar scrambled values at finite ratios $\bar{\ell}/N$.

B Relation between OTOCs and Rényi-2 entropies

In this appendix we review the relation between OTOCs and Rényi-2 entropies in the case of unitary evolution operators defined on qubit systems, and generalize the latter for

JHEP11(2019)038

fermionic (Majorana) systems. We focus on the configuration displayed in figure 2, taking the regions A and C of the same size and position (and analogously for B and D).

B.1 The case of Pauli matrices

We start by giving a derivation of the aforementioned relation for a system of qubits, along the lines of the one in ref. [9]. First, we can write the reduced density matrix ρ_{AC} as

$$\rho_{AC} = \frac{1}{2^{a+c}} \sum_{j,k} \left(O_j^A O_k^C\right)^\dagger \langle I | U_{AB}^\dagger O_j^A O_k^C U_{AB} | I \rangle \ , \tag{B.1}$$

where the sum is over the complete bases $\{O_j^A\}$ and $\{O_k^C\}$ of strings of Pauli operators in A and C, while a and c are equal to the number of sites in A and C. The state $|I\rangle$ is the maximally entangled state connecting $A \cup B$ and $C \cup D$, satisfying

$$O_j^C \, |I\rangle = \left(O_j^A\right)^T |I\rangle \ , \tag{B.2}$$

while U_{AB} is the evolution operator acting non-trivially only on the system $A \cup B$. Then, using the orthogonality of the Pauli operators, and after simple simplifications, we have

$$\mathrm{tr}\left[\rho_{AC}^2\right] = 2^{-a-c-2N} \sum_{j,k} \mathrm{tr}\left[U_{AB}^\dagger O_j^A U_{AB} O_k^A\right] \times \mathrm{tr}\left[O_k^A U_{AB}^\dagger O_j^A U_{AB}\right] . \tag{B.3}$$

Consider now the sum

$$2^{-a-c-3N} \sum_{j,k,\tilde{j},\tilde{k}} \mathrm{tr}\left[O_{\tilde{j}}^A O_{\tilde{k}}^B \left(U_{AB}^\dagger O_j^A U_{AB} O_k^A\right) O_{\tilde{j}}^A O_{\tilde{k}}^B \left(O_k^A U_{AB}^\dagger O_j^A U_{AB}\right)\right] . \tag{B.4}$$

Using the identity [9]

$$\sum_j A_j \mathcal{O} A_j = |A| \, \mathrm{tr}_A\{\mathcal{O}\} \, , \tag{B.5}$$

(here A_j are a complete basis of operators for the Hilbert space associated with A, while $|A|$ is its dimension), one immediately obtains that the r.h.s. of eq. (B.3) is equal to (B.4). Therefore

$$\begin{aligned} \mathrm{tr}\left[\rho_{AC}^2\right] &= 2^{-a-c-3N} \sum_{j,k,\tilde{j},\tilde{k}} \mathrm{tr}\left[O_{\tilde{j}}^A O_{\tilde{k}}^B \left(U_{AB}^\dagger O_j^A U_{AB} O_k^A\right) O_{\tilde{j}}^A O_{\tilde{k}}^B \left(O_k^A U_{AB}^\dagger O_j^A U_{AB}\right)\right] \\ &= \frac{1}{2^{3N-a+c}} \sum_{j,l} \mathrm{tr}\left[O_l^B O_j^A(t) O_l^B O_j^A(t)\right] \end{aligned} \tag{B.6}$$

In the last step, we summed over k, used once again the identity (B.5), and finally renamed the indexes $\tilde{k} = l$. Putting all together, we find

$$\frac{1}{4^{a+d}} \frac{1}{2^N} \sum_{j,k} \mathrm{tr}\left[O_j^A(t) O_k^D(0) O_j^A(t) O_k^D(0)\right] = 2^{N-a-d-S_{AC}^{(2)}} . \tag{B.7}$$

This is exactly the same result as in [9]. An analogous derivation holds for the case of $S_{AD}^{(2)}$. This equation encodes a close connection between the tripartite information and the OTOCs, and allows one to establish that chaos, as measure by small values of all OTOCs, implies scrambling [9]. In the next section we show that a similar relation, with the addition of proper signs, holds in the case of fermionic systems.

JHEP11(2019)038

B.2 The case of Majorana operators

For Majorana operators one needs a different treatment. Indeed, the identity (B.5) is no longer valid, but should be modified as follows. Let $\mathcal{O}$ be an operator with a well defined parity of Majorana operators, i.e. $\mathcal{O}$ is the sum of strings of operators that are either all even or all odd. Then, by expanding in the operator basis of Majorana operators, one can prove

$$\sum_j (-1)^{\ell_j \ell_{\mathcal{O}}} A_j \mathcal{O} A_j^\dagger = |A| \operatorname{tr}_A\{\mathcal{O}\}. \tag{B.8}$$

Here ℓ_j is the length of the operator A_j. For example, if $A_j = \psi_1\psi_4$ then $\ell_j = 2$. Analogously, $\ell_{\mathcal{O}}$ is the length of one of the terms in $\mathcal{O}$. Since all these terms have the same parity, it does not matter which one we choose. We can then proceed as in the previous sections, now paying attention to the order of the operators involved in the calculations. First, we have

$$\rho_{AC} = \frac{1}{2^{a+c}} \sum_{j,k} \left(O_j^A O_k^C\right)^\dagger \langle I | U_{AB}^\dagger O_j^A O_k^C U_{AB} | I \rangle \ , \tag{B.9}$$

where now a and c are *half* the number of sites in A and C. Proceeding as before, we have

$$\operatorname{tr}\left[\rho_{AC}^2\right] = 2^{-a-c-2n} \sum_{j,k} \operatorname{tr}\left[U_{AB}^\dagger O_j^A U_{AB} \left(O_k^A\right)^\dagger\right] \times \operatorname{tr}\left[O_k^A U_{AB}^\dagger \left(O_j^A\right)^\dagger U_{AB}\right] , \tag{B.10}$$

where $n = N/2$. Consider now the sum

$$\begin{aligned} &2^{-a-c-3n} \sum_{j,k,\tilde{j},\tilde{k}} (-1)^{\ell_{\tilde{j}}(\ell_j+\ell_k)+\ell_{\tilde{k}}(\ell_j+\ell_k)} \\ &\quad \times \operatorname{tr}\left[O_{\tilde{j}}^A O_{\tilde{k}}^B \left(U_{AB}^\dagger O_j^A U_{AB} \left(O_k^A\right)^\dagger\right) \left(O_{\tilde{k}}^B\right)^\dagger \left(O_{\tilde{j}}^A\right)^\dagger \left(O_k^A U_{AB}^\dagger \left(O_j^A\right)^\dagger U_{AB}\right)\right] . \end{aligned} \tag{B.11}$$

Noticing now that the evolution operator can always be written as sum of even strings of Majorana operators, one can directly apply the identity (B.8) to prove that the r.h.s. of (B.10) is equal to (B.11). On the other hand, using

$$\ell_{\tilde{j}}(\ell_j + \ell_k) + \ell_{\tilde{k}}(\ell_j + \ell_k) = \ell_j(\ell_{\tilde{j}} + \ell_{\tilde{k}}) + \ell_k(\ell_{\tilde{j}} + \ell_{\tilde{k}}) \, , \tag{B.12}$$

we can sum over k by employing once again the identity (B.8), and finally rename $\tilde{k} = r$. Putting all together, we obtain

$$\operatorname{tr}\left[\rho_{AC}^2\right] = \frac{1}{2^{3n-a+c}} \sum_{j,r} (-1)^{\ell_j \ell_r} \operatorname{tr}\left[O_r^B O_j^A(t) \left(O_r^B\right)^\dagger \left(O_j^A(t)\right)^\dagger\right] . \tag{B.13}$$

We see that additional signs appear in the sum over the OTOCs with respect to the case of Pauli matrices. However, the Rényi-2 entropy still encodes global information about the sum of the OTOCs over extended regions of the system.

JHEP11(2019)038

C Details on the numerical implementation

In this section, we explain a few details for the numerical computation. For the OTOCs, we implement (3.44) in terms of the modes b_1, b_2, b_3, b_4, as explained in the main text. For the entropies however, we use different modes. While we could likewise implement (3.40) and (3.41) in b-modes, this introduces large numerical error as N increases, due to cancellations of large numbers. Instead we have found that for the entropy $S^{(2)}_{AC}$, a numerical calculation in terms of modes c_1, c_2, c_3, c_4 (5.52) is most stable. For the entropy $S^{(2)}_{AD}$, we found that using the modes b_1, b_2, c_3, c_4 gives the most stable results. For our numerical calculation we have therefore transformed initial state $|\overline{\mathcal{U}}(0)\rangle\rangle$ (3.33), effective Hamiltonian H (5.6) and $|W_{S^{(2)}_{AC,BD}(\bar{\ell})}\rangle\rangle$ (3.42)–(3.43) into these modes.

D The Rényi-2 entanglement entropy $S^{(2)}_{AD}(\bar{\ell})$

In this appendix, we turn to the task of deriving the vector $|W_{S^{(2)}_{AD}(\bar{\ell})}\rangle\rangle$ introduced in eq. (3.41), corresponding to the exponential of the second Rényi entropy $S^{(2)}_{AD}(\bar{\ell})$. The discussion goes along the same lines of the one presented in section 5.2.2 for the entropy $S^{(2)}_{AC}(\bar{\ell})$. Writing out the partial trace as done for the other entropy, we get

$$\rho_{AD} = \sum_{F^a_A, F^b_D} \frac{1}{2^{N/2}} (F^a_A F^b_D)^\dagger \, \langle I^{ab}|U^{a\dagger}(F^a_A F^b_D)U^a|I^{ab}\rangle \,, \tag{D.1}$$

where we denoted by $\{F^a_A\}$ and $\{F^b_D\}$ a complete basis for the operators in A, D respectively; namely F^a_A and F^b_D take value in all the possible strings of Majorana operators supported in A and D. We can continue along the same lines as for the other entropy, giving

$$\mathrm{tr}\left[\overline{\rho^2_{AD}}\right] = \frac{1}{2^{N/2}\sqrt{N! n_1! \cdots n_{abcd}!}} \sum_{\vec{n}} c_{\vec{n}}(t) \sum_{\pi \in S_N} \pi (-1)^{\gamma_A + \gamma_B + \delta} \, (*) \pi^{-1} \,. \tag{D.2}$$

Here the term $(*)$ can be evaluated as for the other entropy up until (5.40). Then, however, $\Psi^{a\dagger}_{bB}$ and Ψ^a_{aB} are not the only parts in the first expression acting on this subspace, now F^a_D also does. So, continuing from $(*)$ and dropping the doubled system label as all operators are in the same system, we have

$$\begin{aligned}(*) &= \sum_{F_A, F_D} \langle I^{ab}|\Psi^{a\dagger}_{bA}\Psi^{a\dagger}_{bB}F^a_A\Psi^a_{aB}\Psi^a_{aA}F^{a\dagger}_D|I^{ab}\rangle \, \langle I^{cd}|F^c_D\Psi^{c\dagger}_{dA}\Psi^{c\dagger}_{dB}F^{c\dagger}_A\Psi^c_{cB}\Psi^c_{cA}|I^{cd}\rangle \\ &= \sum_{F_A, F_D} \langle I|\Psi^\dagger_{bA}F_A\Psi_{aA}\Psi^\dagger_{bB}\Psi_{aB}F^\dagger_D|I\rangle \, \langle I|F_D\Psi^\dagger_{dB}\Psi_{cB}\Psi^\dagger_{dA}F^\dagger_A\Psi_{cA}|I\rangle \,. \end{aligned} \tag{D.3}$$

The left side is only non-zero for

$$\Psi^\dagger_{bA}F_A\Psi_{aA} = \pm 1 \Rightarrow F^\dagger_A = \pm\Psi_{aA}\Psi^\dagger_{bA} \tag{D.4}$$

$$\Psi^\dagger_{bB}\Psi_{aB}F^\dagger_D = \pm 1 \Rightarrow F_D = \pm\Psi^\dagger_{bB}\Psi_{aB} \tag{D.5}$$

JHEP11(2019)038

such that we can evaluate the sum $\sum_{F_A,F_D}$, inserting these in the right side. We get

$$\begin{aligned}
(*) &= \langle I|I\rangle \, \langle I|\Psi^\dagger_{bB}\Psi_{aB}\Psi^\dagger_{dB}\Psi_{cB}\,\Psi^\dagger_{dA}\Psi_{aA}\Psi^\dagger_{bA}\Psi_{cA}|I\rangle \\
&= \mathrm{tr}\,\Psi^\dagger_{bB}\Psi_{aB}\Psi^\dagger_{dB}\Psi_{cB}/2^{\bar\ell/2}\ \mathrm{tr}\,\Psi^\dagger_{dA}\Psi_{aA}\Psi^\dagger_{bA}\Psi_{cA}/2^{\bar\ell/2} \\
&= \mathrm{tr}\,\Psi_{dB}\Psi_{cB}\Psi_{bB}\Psi_{aB}/2^{\bar\ell/2}\ \mathrm{tr}\,\Psi_{aA}\Psi_{bA}\Psi_{cA}\Psi_{dA}/2^{\bar\ell/2}(-1)^{\frac{n_b+n_d}{2}+n_{bB}+n_{dB}} \\
&= \mathrm{tr}(\Psi_{aB}\Psi_{bB}\Psi_{cB}\Psi_{dB})^\dagger/2^{\bar\ell/2}\ \mathrm{tr}\,\Psi_{aA}\Psi_{bA}\Psi_{cA}\Psi_{dA}/2^{\bar\ell/2}(-1)^{\frac{n_b+n_d}{2}+n_{bB}+n_{dB}} \\
&\quad \times (-1)^{(n_{aB}(n_{aB}-1)+n_{bB}(n_{bB}-1)+n_{cB}(n_{cB}-1)+n_{dB}(n_{dB}-1))/2} \\
&= (-1)^{\gamma_A+\gamma_B}(-1)^{(n_b+n_d)/2}(-1)^{(n_{aB}(n_{aB}-1)+n_{bB}(n_{bB}+1)+n_{cB}(n_{cB}-1)+n_{dB}(n_{dB}+1))/2}\,.
\end{aligned} \tag{D.6}$$

The traces now give $(-1)^{\gamma_A}$ and $(-1)^{\gamma_B}$, respectively. Inserted back into (5.40), these cancel, and the δ partially cancels the other phases,

$$\mathrm{tr}\left[\overline{\rho^2_{AD}}\right] = \frac{1}{2^{N/2}\sqrt{N!n_1!\cdots n_{abcd}!}}\sum_{\vec n} c_{\vec n}(t)\sum_{\pi\in S_N}\pi(-1)^{(n_b+n_d)/2}(-1)^{(-n_{aB}+n_{bB}-n_{cB}+n_{dB})/2}\pi^{-1}. \tag{D.7}$$

Again, this has the form (5.20) with suitable choices of α's. Then, according to eq. (5.21) we obtain

$$\begin{aligned}
|W_{S^{(2)}_{AC}(\bar\ell)}\rangle\rangle \;=\; &\frac{1}{2^{N/2}\sqrt{N!}}\left[a^\dagger_1 + ia^\dagger_{ab} + ia^\dagger_{ad} + ia^\dagger_{bc} + ia^\dagger_{cd} - a^\dagger_{abcd} + a^\dagger_{ac} - a^\dagger_{bd}\right]^\ell \\
&\times \left[a^\dagger_1 + ia^\dagger_{ab} + ia^\dagger_{ad} + ia^\dagger_{bc} + ia^\dagger_{cd} - a^\dagger_{abcd} - a^\dagger_{ac} + a^\dagger_{bd}\right]^{\bar\ell}|\Omega\rangle\,.
\end{aligned} \tag{D.8}$$

Finally, the transformation to b-modes in (3.30) results in eq. (3.43).

References

[1] J.M. Deutsch, *Quantum statistical mechanics in a closed system*, *Phys. Rev.* **A 43** (1991) 2046.

[2] M. Srednicki, *Chaos and quantum thermalization*, *Phys. Rev.* **E 50** (1994) 888.

[3] M. Rigol, V. Dunjko and M. Olshanii, *Thermalization and its mechanism for generic isolated quantum systems*, *Nature* **452** (2008) 854.

[4] L. D'Alessio, Y. Kafri, A. Polkovnikov and M. Rigol, *From quantum chaos and eigenstate thermalization to statistical mechanics and thermodynamics*, *Adv. Phys.* **65** (2016) 239.

[5] Y.D. Lensky and X.-L. Qi, *Chaos and high temperature pure state thermalization*, *JHEP* **06** (2019) 025 [arXiv:1805.03675] [INSPIRE].

[6] P. Hosur and X.-L. Qi, *Characterizing eigenstate thermalization via measures in the Fock space of operators*, *Phys. Rev.* **E 93** (2016) 042138.

[7] T. Hartman and J. Maldacena, *Time evolution of entanglement entropy from black hole interiors*, *JHEP* **05** (2013) 014 [arXiv:1303.1080] [INSPIRE].

JHEP11(2019)038

[8] H. Liu and S.J. Suh, *Entanglement tsunami: universal scaling in holographic thermalization*, *Phys. Rev. Lett.* **112** (2014) 011601 [arXiv:1305.7244] [INSPIRE].

[9] P. Hosur, X.-L. Qi, D.A. Roberts and B. Yoshida, *Chaos in quantum channels*, *JHEP* **02** (2016) 004 [arXiv:1511.04021] [INSPIRE].

[10] K.A. Landsman et al., *Verified quantum information scrambling*, *Nature* **567** (2019) 61 [arXiv:1806.02807] [INSPIRE].

[11] G. Bentsen, Y. Gu and A. Lucas, *Fast scrambling on sparse graphs*, *Proc. Nat. Acad. Sci.* **116** (2019) 6689 [arXiv:1805.08215] [INSPIRE].

[12] M.C. Gutzwiller, *Chaos in classical and quantum mechanics*, Springer, New York, NY, U.S.A. (1990).

[13] H.-J. Stoöckmann, *Quantum chaos: an introduction*, Cambridge University Press, Cambridge, U.K. (2007).

[14] Y. Sekino and L. Susskind, *Fast scramblers*, *JHEP* **10** (2008) 065 [arXiv:0808.2096] [INSPIRE].

[15] N. Lashkari, D. Stanford, M. Hastings, T. Osborne and P. Hayden, *Towards the fast scrambling conjecture*, *JHEP* **04** (2013) 022 [arXiv:1111.6580] [INSPIRE].

[16] P. Hayden and J. Preskill, *Black holes as mirrors: quantum information in random subsystems*, *JHEP* **09** (2007) 120 [arXiv:0708.4025] [INSPIRE].

[17] S.H. Shenker and D. Stanford, *Multiple shocks*, *JHEP* **12** (2014) 046 [arXiv:1312.3296] [INSPIRE].

[18] A. Kitaev, *Hidden correlations in the Hawking radiation and thermal noise*, talk at *Fundamental Physics Prize Symposium*, University of California, Santa Barbara, CA, U.S.A., 12 February 2014.

[19] L. Susskind, *Computational complexity and black hole horizons*, *Fortsch. Phys.* **64** (2016) 44 [arXiv:1403.5695] [INSPIRE].

[20] A.R. Brown, D.A. Roberts, L. Susskind, B. Swingle and Y. Zhao, *Complexity, action and black holes*, *Phys. Rev.* **D 93** (2016) 086006 [arXiv:1512.04993] [INSPIRE].

[21] A. Kitaev, *A simple model of quantum holography (part 1)*, talk at *KITP strings seminar and Entanglement* 2015 *program*, University of California, Santa Barbara, CA, U.S.A., 7 April 2015.

[22] A. Kitaev, *A simple model of quantum holography (part 2)*, talk at *KITP strings seminar and Entanglement* 2015 *program*, University of California, Santa Barbara, CA, U.S.A., 27 May 2015.

[23] S. Sachdev and J. Ye, *Gapless spin fluid ground state in a random, quantum Heisenberg magnet*, *Phys. Rev. Lett.* **70** (1993) 3339 [cond-mat/9212030] [INSPIRE].

[24] J. Maldacena and D. Stanford, *Remarks on the Sachdev-Ye-Kitaev model*, *Phys. Rev.* **D 94** (2016) 106002 [arXiv:1604.07818] [INSPIRE].

[25] J. Maldacena, D. Stanford and Z. Yang, *Conformal symmetry and its breaking in two dimensional nearly anti-de-Sitter space*, *PTEP* **2016** (2016) 12C104 [arXiv:1606.01857] [INSPIRE].

[26] J. Polchinski and V. Rosenhaus, *The spectrum in the Sachdev-Ye-Kitaev model*, *JHEP* **04** (2016) 001 [arXiv:1601.06768] [INSPIRE].

JHEP11(2019)038

[27] D. Bagrets, A. Altland and A. Kamenev, *Sachdev-Ye-Kitaev model as Liouville quantum mechanics*, *Nucl. Phys.* **B 911** (2016) 191 [arXiv:1607.00694] [INSPIRE].

[28] R.A. Davison, W. Fu, A. Georges, Y. Gu, K. Jensen and S. Sachdev, *Thermoelectric transport in disordered metals without quasiparticles: the Sachdev-Ye-Kitaev models and holography*, *Phys. Rev.* **B 95** (2017) 155131 [arXiv:1612.00849] [INSPIRE].

[29] I.R. Klebanov and G. Tarnopolsky, *Uncolored random tensors, melon diagrams and the Sachdev-Ye-Kitaev models*, *Phys. Rev.* **D 95** (2017) 046004 [arXiv:1611.08915] [INSPIRE].

[30] Y. Gu, X.-L. Qi and D. Stanford, *Local criticality, diffusion and chaos in generalized Sachdev-Ye-Kitaev models*, *JHEP* **05** (2017) 125 [arXiv:1609.07832] [INSPIRE].

[31] X.-Y. Song, C.-M. Jian and L. Balents, *Strongly correlated metal built from Sachdev-Ye-Kitaev models*, *Phys. Rev. Lett.* **119** (2017) 216601 [arXiv:1705.00117] [INSPIRE].

[32] D. Chowdhury, Y. Werman, E. Berg and T. Senthil, *Translationally invariant non-Fermi liquid metals with critical Fermi-surfaces: solvable models*, *Phys. Rev.* **X 8** (2018) 031024 [arXiv:1801.06178] [INSPIRE].

[33] J. Maldacena, S.H. Shenker and D. Stanford, *A bound on chaos*, *JHEP* **08** (2016) 106 [arXiv:1503.01409] [INSPIRE].

[34] D. Bagrets, A. Altland and A. Kamenev, *Power-law out of time order correlation functions in the SYK model*, *Nucl. Phys.* **B 921** (2017) 727 [arXiv:1702.08902] [INSPIRE].

[35] A. Larkin and Y.N. Ovchinnikov, *Quasiclassical method in the theory of superconductivity*, *Sov. Phys. JETP* **28** (1969) 1200 [*Zh. Eksp. Teor. Fiz.* **55** (1969) 2262].

[36] S.H. Shenker and D. Stanford, *Black holes and the butterfly effect*, *JHEP* **03** (2014) 067 [arXiv:1306.0622] [INSPIRE].

[37] D.A. Roberts, D. Stanford and L. Susskind, *Localized shocks*, *JHEP* **03** (2015) 051 [arXiv:1409.8180] [INSPIRE].

[38] D.A. Roberts, D. Stanford and A. Streicher, *Operator growth in the SYK model*, *JHEP* **06** (2018) 122 [arXiv:1802.02633] [INSPIRE].

[39] D.A. Roberts and B. Swingle, *Lieb-Robinson bound and the butterfly effect in quantum field theories*, *Phys. Rev. Lett.* **117** (2016) 091602 [arXiv:1603.09298] [INSPIRE].

[40] I.L. Aleiner, L. Faoro and L.B. Ioffe, *Microscopic model of quantum butterfly effect: out-of-time-order correlators and traveling combustion waves*, *Annals Phys.* **375** (2016) 378 [arXiv:1609.01251] [INSPIRE].

[41] B. Swingle and D. Chowdhury, *Slow scrambling in disordered quantum systems*, *Phys. Rev.* **B 95** (2017) 060201 [arXiv:1608.03280] [INSPIRE].

[42] N. Yunger Halpern, *Jarzynski-like equality for the out-of-time-ordered correlator*, *Phys. Rev.* **A 95** (2017) 012120 [arXiv:1609.00015] [INSPIRE].

[43] A.A. Patel and S. Sachdev, *Quantum chaos on a critical Fermi surface*, *Proc. Nat. Acad. Sci.* **114** (2017) 1844 [arXiv:1611.00003] [INSPIRE].

[44] I. Kukuljan, S. Grozdanov and T. Prosen, *Weak quantum chaos*, *Phys. Rev.* **B 96** (2017) 060301 [arXiv:1701.09147] [INSPIRE].

[45] B. Dóra and R. Moessner, *Out-of-time-ordered density correlators in Luttinger liquids*, *Phys. Rev. Lett.* **119** (2017) 026802 [arXiv:1612.00614] [INSPIRE].

JHEP11(2019)038

[46] N. Tsuji, P. Werner and M. Ueda, *Exact out-of-time-ordered correlation functions for an interacting lattice fermion model*, *Phys. Rev.* **A 95** (2017) 011601 [arXiv:1610.01251] [INSPIRE].

[47] C.-J. Lin and O.I. Motrunich, *Out-of-time-ordered correlators in a quantum Ising chain*, *Phys. Rev.* **B 97** (2018) 144304 [arXiv:1801.01636] [INSPIRE].

[48] C.-J. Lin and O.I. Motrunich, *Out-of-time-ordered correlators in short-range and long-range hard-core boson models and in the Luttinger-liquid model*, *Phys. Rev.* **B 98** (2018) 134305 [arXiv:1807.08826] [INSPIRE].

[49] A. Smith, J. Knolle, R. Moessner and D.L. Kovrizhin, *Logarithmic spreading of out-of-time-ordered correlators without many-body localization*, *Phys. Rev. Lett.* **123** (2019) 086602 [arXiv:1812.07981] [INSPIRE].

[50] S. Nakamura, E. Iyoda, T. Deguchi and T. Sagawa, *Universal scrambling in gapless quantum spin chains*, *Phys. Rev.* **B 99** (2019) 224305 [arXiv:1904.09778] [INSPIRE].

[51] M. McGinley, A. Nunnenkamp and J. Knolle, *Slow growth of out-of-time-order correlators and entanglement entropy in integrable disordered systems*, *Phys. Rev. Lett.* **122** (2019) 020603 [arXiv:1807.06039] [INSPIRE].

[52] Y. Huang, F.G. S.L. Brandão and Y.-L. Zhang, *Finite-size scaling of out-of-time-ordered correlators at late times*, *Phys. Rev. Lett.* **123** (2019) 010601 [arXiv:1705.07597] [INSPIRE].

[53] J. Chávez-Carlos et al., *Quantum and classical Lyapunov exponents in atom-field interaction systems*, *Phys. Rev. Lett.* **122** (2019) 024101 [arXiv:1807.10292] [INSPIRE].

[54] A. Nahum, J. Ruhman, S. Vijay and J. Haah, *Quantum entanglement growth under random unitary dynamics*, *Phys. Rev.* **X 7** (2017) 031016 [arXiv:1608.06950] [INSPIRE].

[55] C. Sünderhauf, D. Pérez-García, D.A. Huse, N. Schuch and J.I. Cirac, *Localization with random time-periodic quantum circuits*, *Phys. Rev.* **B 98** (2018) 134204 [arXiv:1805.08487] [INSPIRE].

[56] A. Nahum, S. Vijay and J. Haah, *Operator spreading in random unitary circuits*, *Phys. Rev.* **X 8** (2018) 021014 [arXiv:1705.08975] [INSPIRE].

[57] C. von Keyserlingk, T. Rakovszky, F. Pollmann and S. Sondhi, *Operator hydrodynamics, OTOCs and entanglement growth in systems without conservation laws*, *Phys. Rev.* **X 8** (2018) 021013 [arXiv:1705.08910] [INSPIRE].

[58] A. Chan, A. De Luca and J.T. Chalker, *Solution of a minimal model for many-body quantum chaos*, *Phys. Rev.* **X 8** (2018) 041019 [arXiv:1712.06836] [INSPIRE].

[59] A. Chan, A. De Luca and J.T. Chalker, *Spectral statistics in spatially extended chaotic quantum many-body systems*, *Phys. Rev. Lett.* **121** (2018) 060601 [arXiv:1803.03841] [INSPIRE].

[60] T. Rakovszky, F. Pollmann and C.W. von Keyserlingk, *Diffusive hydrodynamics of out-of-time-ordered correlators with charge conservation*, *Phys. Rev.* **X 8** (2018) 031058 [arXiv:1710.09827] [INSPIRE].

[61] V. Khemani, A. Vishwanath and D.A. Huse, *Operator spreading and the emergence of dissipation in unitary dynamics with conservation laws*, *Phys. Rev.* **X 8** (2018) 031057 [arXiv:1710.09835] [INSPIRE].

JHEP11(2019)038

[62] P. Kos, M. Ljubotina and T. Prosen, *Many-body quantum chaos: analytic connection to random matrix theory*, *Phys. Rev.* **X 8** (2018) 021062 [arXiv:1712.02665] [INSPIRE].

[63] B. Bertini, P. Kos and T. Prosen, *Exact spectral form factor in a minimal model of many-body quantum chaos*, *Phys. Rev. Lett.* **121** (2018) 264101 [arXiv:1805.00931] [INSPIRE].

[64] N. Hunter-Jones, *Unitary designs from statistical mechanics in random quantum circuits*, arXiv:1905.12053 [INSPIRE].

[65] M.J. Gullans and D.A. Huse, *Entanglement structure of current-driven diffusive fermion systems*, *Phys. Rev.* **X 9** (2019) 021007 [arXiv:1804.00010] [INSPIRE].

[66] T. Zhou and A. Nahum, *Emergent statistical mechanics of entanglement in random unitary circuits*, *Phys. Rev.* **B 99** (2019) 174205 [arXiv:1804.09737] [INSPIRE].

[67] A.J. Friedman, A. Chan, A. De Luca and J.T. Chalker, *Spectral statistics and many-body quantum chaos with conserved charge*, arXiv:1906.07736 [INSPIRE].

[68] J. Emerson, E. Livine and S. Lloyd, *Convergence conditions for random quantum circuits*, *Phys. Rev.* **A 72** (2005) 060302.

[69] J. Emerson, *Pseudo-random unitary operators for quantum information processing*, *Science* **302** (2003) 2098.

[70] O.C.O. Dahlsten, R. Oliveira and M.B. Plenio, *The emergence of typical entanglement in two-party random processes*, *J. Phys.* **A 40** (2007) 8081.

[71] D. Gross, K. Audenaert and J. Eisert, *Evenly distributed unitaries: on the structure of unitary designs*, *J. Math. Phys.* **48** (2007) 052104.

[72] R. Oliveira, O.C.O. Dahlsten and M.B. Plenio, *Generic entanglement can be generated efficiently*, *Phys. Rev. Lett.* **98** (2007) 130502.

[73] M. Žnidarič, *Optimal two-qubit gate for generation of random bipartite entanglement*, *Phys. Rev.* **A 76** (2007) 012318.

[74] M. Žnidarič, *Exact convergence times for generation of random bipartite entanglement*, *Phys. Rev.* **A 78** (2008) 032324.

[75] L. Arnaud and D. Braun, *Efficiency of producing random unitary matrices with quantum circuits*, *Phys. Rev.* **A 78** (2008) 062329.

[76] A.W. Harrow and R.A. Low, *Random quantum circuits are approximate* 2*-designs*, *Commun. Math. Phys.* **291** (2009) 257.

[77] W.G. Brown and L. Viola, *Convergence rates for arbitrary statistical moments of random quantum circuits*, *Phys. Rev. Lett.* **104** (2010) 250501.

[78] I.T. Diniz and D. Jonathan, *Comment on "random quantum circuits are approximate* 2*-designs"*, *Commun. Math. Phys.* **304** (2011) 281.

[79] W. Brown and O. Fawzi, *Scrambling speed of random quantum circuits*, arXiv:1210.6644 [INSPIRE].

[80] F.G. S.L. Brandão, A.W. Harrow and M. Horodecki, *Local random quantum circuits are approximate polynomial-designs*, *Commun. Math. Phys.* **346** (2016) 397 [arXiv:1208.0692] [INSPIRE].

JHEP11(2019)038

[81] Y. Nakata, C. Hirche, M. Koashi and A. Winter, *Efficient quantum pseudorandomness with nearly time-independent Hamiltonian dynamics*, *Phys. Rev.* **X 7** (2017) 021006 [arXiv:1609.07021] [INSPIRE].

[82] S. Choi, Y. Bao, X.-L. Qi and E. Altman, *Quantum error correction in scrambling dynamics and measurement induced phase transition*, arXiv:1903.05124 [INSPIRE].

[83] X.-L. Qi and A. Streicher, *Quantum epidemiology: operator growth, thermal effects and SYK*, *JHEP* **08** (2019) 012 [arXiv:1810.11958] [INSPIRE].

[84] A.M. García-García and J.J.M. Verbaarschot, *Spectral and thermodynamic properties of the Sachdev-Ye-Kitaev model*, *Phys. Rev.* **D 94** (2016) 126010 [arXiv:1610.03816] [INSPIRE].

[85] A.M. García-García and J.J.M. Verbaarschot, *Analytical spectral density of the Sachdev-Ye-Kitaev model at finite N*, *Phys. Rev.* **D 96** (2017) 066012 [arXiv:1701.06593] [INSPIRE].

[86] A.M. García-García, Y. Jia and J.J.M. Verbaarschot, *Exact moments of the Sachdev-Ye-Kitaev model up to order* $1/N^2$, *JHEP* **04** (2018) 146 [arXiv:1801.02696] [INSPIRE].

[87] W. Fu and S. Sachdev, *Numerical study of fermion and boson models with infinite-range random interactions*, *Phys. Rev.* **B 94** (2016) 035135 [arXiv:1603.05246] [INSPIRE].

[88] J.S. Cotler et al., *Black holes and random matrices*, *JHEP* **05** (2017) 118 [*Erratum ibid.* **09** (2018) 002] [arXiv:1611.04650] [INSPIRE].

[89] G. Gur-Ari, R. Mahajan and A. Vaezi, *Does the SYK model have a spin glass phase?*, *JHEP* **11** (2018) 070 [arXiv:1806.10145] [INSPIRE].

[90] O. Schnaack, N. Bölter, S. Paeckel, S.R. Manmana, S. Kehrein and M. Schmitt, *Tripartite information, scrambling and the role of Hilbert space partitioning in quantum lattice models*, arXiv:1808.05646 [INSPIRE].

[91] E. Iyoda and T. Sagawa, *Scrambling of quantum information in quantum many-body systems*, *Phys. Rev.* **A 97** (2018) 042330 [arXiv:1704.04850] [INSPIRE].

[92] S. Pappalardi, A. Russomanno, B. Žunkovič, F. Iemini, A. Silva and R. Fazio, *Scrambling and entanglement spreading in long-range spin chains*, *Phys. Rev.* **B 98** (2018) 134303 [arXiv:1806.00022] [INSPIRE].

[93] A. Seshadri, V. Madhok and A. Lakshminarayan, *Tripartite mutual information, entanglement and scrambling in permutation symmetric systems with an application to quantum chaos*, *Phys. Rev.* **E 98** (2018) 052205 [arXiv:1806.00113] [INSPIRE].

[94] P. Saad, S.H. Shenker and D. Stanford, *A semiclassical ramp in SYK and in gravity*, arXiv:1806.06840 [INSPIRE].

[95] F. Haake, *Quantum signatures of chaos*, Springer, Berlin, Heidelberg, Germany (2010).

[96] P. Ribeiro, J. Vidal and R. Mosseri, *Exact spectrum of the Lipkin-Meshkov-Glick model in the thermodynamic limit and finite-size corrections*, *Phys. Rev.* **E 78** (2008) 021106.

[97] S.H. Shenker and D. Stanford, *Stringy effects in scrambling*, *JHEP* **05** (2015) 132 [arXiv:1412.6087] [INSPIRE].

[98] T. Zhou and X. Chen, *Operator dynamics in a Brownian quantum circuit*, *Phys. Rev.* **E 99** (2019) 052212 [arXiv:1805.09307] [INSPIRE].

JHEP11(2019)038

[99] S. Xu and B. Swingle, *Locality, quantum fluctuations and scrambling*, *Phys. Rev.* **X 9** (2019) 031048 [arXiv:1805.05376] [INSPIRE].

[100] X. Chen and T. Zhou, *Quantum chaos dynamics in long-range power law interaction systems*, *Phys. Rev.* **B 100** (2019) 064305 [arXiv:1808.09812] [INSPIRE].

[101] H. Gharibyan, M. Hanada, S.H. Shenker and M. Tezuka, *Onset of random matrix behavior in scrambling systems*, *JHEP* **07** (2018) 124 [*Erratum ibid.* **02** (2019) 197] [arXiv:1803.08050] [INSPIRE].

[102] K. Parthasarathy, *An introduction to quantum stochastic calculus*, *Monogr. Math.* **85**, Birkhäuser, Basel, Switzerland (1992)

[103] L. Banchi, D. Burgarth and M.J. Kastoryano, *Driven quantum dynamics: will it blend?*, *Phys. Rev.* **X 7** (2017) 041015 [arXiv:1704.03041] [INSPIRE].

[104] E. Onorati, O. Buerschaper, M. Kliesch, W. Brown, A.H. Werner and J. Eisert, *Mixing properties of stochastic quantum Hamiltonians*, *Commun. Math. Phys.* **355** (2017) 905 [arXiv:1606.01914] [INSPIRE].

[105] J.R. González Alonso, N. Yunger Halpern and J. Dressel, *Out-of-time-ordered-correlator quasiprobabilities robustly witness scrambling*, *Phys. Rev. Lett.* **122** (2019) 040404 [arXiv:1806.09637] [INSPIRE].

[106] F. Iglói and I. Peschel, *On reduced density matrices for disjoint subsystems*, *Europhys. Lett.* **89** (2010) 40001.

[107] M. Fagotti and P. Calabrese, *Entanglement entropy of two disjoint blocks in XY chains*, *J. Statist. Mech.* **2010** (2010) P04016.

[108] Y. Gu, A. Lucas and X.-L. Qi, *Spread of entanglement in a Sachdev-Ye-Kitaev chain*, *JHEP* **09** (2017) 120 [arXiv:1708.00871] [INSPIRE].

[109] T. Prosen and I. Pižorn, *Operator space entanglement entropy in a transverse Ising chain*, *Phys. Rev.* **A 76** (2007) 032316.

[110] J. Dubail, *Entanglement scaling of operators: a conformal field theory approach, with a glimpse of simulability of long-time dynamics in* $1+1d$, *J. Phys.* **A 50** (2017) 234001 [arXiv:1612.08630] [INSPIRE].

JHEP11(2019)038

Appendix C

A random unitary circuit model for black hole evaporation

In this article, we propose and study the continuum limit of a random unitary circuit (see section 4.2) as a model for black hole evaporation. The intrinsic dynamics within the system (corresponding to the black hole) are non-local 2-body random unitaries, while the coupling with an environment is provided by SWAP operations at random (non-local) positions. While it is a toy model, our work shows that the information-retrieval properties of a black hole can stem from a quantum model without any fine tuning, as expected from the holographic principle (c.f. chapter 5).

For random unitaries in the circuit drawn from the Haar measure, we can set up a linear system of $N + 1$ differential equations that can be easily numerically integrated (system size N). However, we also turn to a more realistic model, where the random unitaries conserve a $U(1)$ charge, mimicking energy conservation. Then, the system does not reach a maximally mixed state at late times, but leaks charge to the environment until it reaches the zero-charge fixed point. In this setup, we can use a similar numerical method to the one developed in our work on the Brownian SYK model (see appendix B), based on an effective permutational symmetry after performing the disorder average. Numerically exact calculations then allow us to study the information-theoretic properties in detail for various system sizes N.

The build-up (and decay) of entanglement entropy allows the identification of two distinct timescales: The scrambling time $t_s \propto \log N$ due to the intrinsic dynamics of the system, and the Page time $t_p \propto N$ due to the coupling with the environment. Further, we directly study the information retrieval properties of the evaporating black hole. In line with the Hayden-Preskill protocol explained in section 5.2, we compute mutual information between Alice's qubit injected into the black hole, and Hawking radiation collected from the evaporating black hole by Bob. Depending on Bob's access to the black hole's initial configuration, we clearly see that the relevant timescale is either the Page time or the much lower scrambling time, in line with the theory presented in section 5.2.

JHEP

Published for SISSA by Springer

Received: March 2, 2020
Accepted: March 20, 2020
Published: April 9, 2020

A random unitary circuit model for black hole evaporation

Lorenzo Piroli,[a,b,1] **Christoph Sünderhauf**[a,b,1] **and Xiao-Liang Qi**[c,d]

[a] *Max-Planck-Institut für Quantenoptik, Hans-Kopfermann-Str. 1, 85748 Garching, Germany*

[b] *Munich Center for Quantum Science and Technology, Schellingstraße 4, 80799 München, Germany*

[c] *Stanford Institute for Theoretical Physics, Stanford University, Stanford, California 94305, U.S.A.*

[d] *Department of Physics, Stanford University, Stanford, California 94305, U.S.A.*

E-mail: lpiroli@mpq.mpg.de, christoph.suenderhauf@mpq.mpg.de, xlqi@stanford.edu

Abstract: Inspired by the Hayden-Preskill protocol for black hole evaporation, we consider the dynamics of a quantum many-body qudit system coupled to an external environment, where the time evolution is driven by the continuous limit of certain 2-local random unitary circuits. We study both cases where the unitaries are chosen with and without a conserved U(1) charge and focus on two aspects of the dynamics. First, we study analytically and numerically the growth of the entanglement entropy of the system, showing that two different time scales appear: one is intrinsic to the internal dynamics (the scrambling time), while the other depends on the system-environment coupling. In the presence of a U(1) conserved charge, we show that the entanglement follows a Page-like behavior in time: it begins to decrease in the middle stage of the "evaporation", and decreases monotonically afterwards. Second, we study the time needed to retrieve information initially injected in the system from measurements on the environment qudits. Based on explicit numerical computations, we characterize such time both when the retriever has control over the initial configuration or not, showing that different scales appear in the two cases.

Keywords: Quantum Dissipative Systems, Random Systems

ArXiv ePrint: 2002.09236

[1] These authors contributed equally to this work.

https://doi.org/10.1007/JHEP04(2020)063

JHEP04(2020)063

Contents

JHEP04(2020)063

1 Introduction

In the past decade, quantum information ideas have become increasingly relevant in high energy physics, especially in connection to the black hole information paradox [1–5]. In this context, a particularly fruitful line of research was initiated by the seminal work by Hayden and Preskill [6], where the authors studied how quantum information is released from a black hole, under the assumption that it is not destroyed during the evaporation process. Their study suggested that information could be released in a time which is much shorter than the black hole lifetime, and related to the time needed for localized information to spread, or *scramble*, over all the degrees of freedom.

These considerations provided an obvious motivation for a systematic study of information scrambling and the related concept of many-body quantum chaos, also due to the subsequent conjecture by Sekino and Susskind that black holes are the fastest scramblers in nature [7, 8]. In turn, this led to the development of several measures of information spreading and chaos, including out-of-time-ordered correlation (OTOC) functions [9–14]

(historically introduced in the context of disordered superconductors [15]), and the tripartite mutual information defined in ref. [16].

Due to the intrinsic complexity of generic many-body quantum systems, several works on the topic relied on the study of a class of simplified dynamical models given by random unitary circuits (RUCs), originally introduced within quantum information theory [17–27], and continuous Brownian dynamics [28–30]. These models are generally defined in terms of a set of d-level systems (qudits), sequentially updated by randomly chosen unitary gates (RUCs) or time-dependent random Hamiltonians (continuous Brownian dynamics). It turns out that these systems are typically fast scramblers [28], and their study allowed us to investigate quantitatively several interesting features that are expected in more realistic chaotic systems [28, 31–34]. As a parallel development, these ideas also had important ramifications in condensed matter and many-body physics, where local RUCs have been extensively studied in the past few years [35–47], for instance in connection with aspects of entanglement spreading and thermalization in isolated systems [48, 49].

In this work, motivated by the recent technical advances in the study of RUCs, and inspired by the Hayden-Preskill evaporation protocol, we consider the dynamics of a quantum many-body qudit system coupled to an external environment, where the time evolution is driven by the continuous limit of certain 2-local RUCs. These consist of qudits nonlocally coupled, but with only two of them interacting at a time. This setting allows us to study quantitatively the contribution of the environment and internal dynamics on the scrambling of information. Furthermore, we consider a modified tensor network model with U(1) charge conservation, which evaporates to a unique vacuum state, instead of reaching the maximally entangled state. This provides a more realistic toy model of evaporating black hole in flat space, for which the entropy after the Page time eventually decreases to zero [50, 51]. The U(1) charge conservation is an analog of the energy conservation.

In the rest of this paper, we focus on two aspects of the dynamics. First, we study analytically and numerically the growth of the second Rényi entropy of the system, highlighting the implications of conservation laws and the emergence of two different time scales: one is intrinsic to the internal dynamics (the scrambling time), while the other depends on the system-environment coupling. Second, following Hayden and Preskill [6], we study the time needed to retrieve information initially injected in the system from measurements on the environment qudits, and how this depends on the knowledge of the initial configuration of the system.

In the past years, several works have appeared discussing ideas and techniques related to those of the present paper. First, we note that our setting differs from those studied in refs. [52–60] in the context of measurement-induced phase transitions. Indeed, in our model no projective measurement is taken, and we consider instead an environment which is eventually traced over in our calculations. A similar setting was studied in ref. [61], but there the authors considered random global Hamiltonians, with no notion of local interactions. Next, quantum mechanical evaporation protocols displaying some analogy with our setting were investigated in refs. [62, 63] for an SYK model [11, 64] coupled to an external environment (see also [65]). However, the dynamics studied in these works is not Brownian, and is analyzed by means of the Keldysh formalism.

JHEP04(2020)063

It is also worth to stress that over the years many qudit models have been introduced to capture aspects of the black hole evaporation process [66–82]. In particular, a Page-like behavior in time for the entanglement entropy has already been observed in some of these [67, 68, 79, 81]. However, in most of these examples the evolution is very carefully engineered and allows one to only study numerically small system sizes.

We also mention that very recently the effects of decoherence on information scrambling has been analyzed in ref. [83] within a quantum teleportation protocol related to the setting of this paper, see also ref. [84] for an experimental implementation. Furthermore, we note that the Hayden-Preskill protocol with a U(1) conserved charge has been studied before in ref. [85], where global random unitary transformations (instead of k-local circuits) were considered. Finally, two papers closely related to the present article appeared very recently. First, a random quantum circuit model for black hole evaporation was studied in ref. [86], but there the authors focused on a different setup and quantities. Second, analogously to our work, the emergence of a Page curve in a unitary toy model for a black hole has also been shown in ref. [87], based on recently-developed concepts of many-body quantum chaos. However, in this work we focus on a specific microscopic model which is different from the one studied in ref. [87], and employ different techniques in our calculations.

The rest of this manuscript is organized as follows. In section 2 we introduce our model, while in section 3 we analyze the growth of the entanglement both in the case of Haar-scrambled local unitary evolution (section 3.1) and in the presence of a U(1) conserved charge (section 3.2). The retrieval of quantum information initially injected in the system is studied in section 4, while we report our conclusions in section 5. Finally, the most technical aspects of our work are consigned to a few appendices.

2 The model

We start by introducing the model studied in the rest of this work, which is pictorially depicted in figure 1. We consider two sets of N and M d-level systems (qudits), denoted respectively by $\mathcal{S}$ (the system) and $\mathcal{E}$ (the environment). The Hilbert spaces associated with $\mathcal{S}$ and $\mathcal{E}$ are then $\mathcal{H}_{\mathcal{S}} = \bigotimes_{j=1}^{N} h_{\mathcal{S}}^{(j)}$ and $\mathcal{H}_{\mathcal{E}} = \bigotimes_{j=1}^{M} h_{\mathcal{E}}^{(j)}$, with $h_{\mathcal{S}}^{(j)}, h_{\mathcal{E}}^{(j)} \simeq \mathbb{C}^d$. We anticipate that in our calculations we will always take the limit $M \to \infty$, corresponding to the physical situation where the number of degrees of freedom in the environment is much larger than in the system.

Motivated by the Hayden-Preskill evaporation protocol [6], we would like to construct a quantum circuit which implements a fast-scrambling dynamics for $\mathcal{S}$ and with a tunable coupling between $\mathcal{S}$ and $\mathcal{E}$. Let us begin by considering a discrete process, and divide the time interval $[0, t]$ into n steps $t_j = (j/n)t$, so that $t_j - t_{j-1} = \Delta t = t/n$. At each time step, the system evolves according to the following rules:

1. with probability p_1, two qudits in $\mathcal{S}$, placed at random positions i and j, interact. We model this process by the action on $h_{\mathcal{S}}^{(i)} \otimes h_{\mathcal{S}}^{(j)}$ of a unitary operator $U_{i,j}$, chosen out of a suitable random ensemble;

JHEP04(2020)063

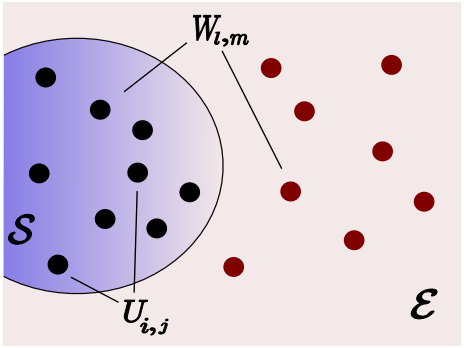

Figure 1. Pictorial representation of the model introduced in section 2. We consider a system $\mathcal{S}$ and an environment $\mathcal{E}$ consisting of N and M qudits respectively. The evolution is driven by the continuous limit of a random quantum circuit which implements a fast-scrambling dynamics for $\mathcal{S}$ with a tunable coupling between $\mathcal{S}$ and $\mathcal{E}$. At each infinitesimal time step Δt a random unitary operator $U_{i,j}$ is applied to randomly chosen qudits in $\mathcal{S}$ with probability $p_1 = N\lambda_1\Delta t$, while a swap $W_{l,m}$ between a qudit in the system and one in the environment (randomly chosen) is applied with probability $p_2 = \lambda_2\Delta t$.

2. with probability $p_2 \leq 1 - p_1$, one qudit in $\mathcal{S}$ and one qubit in $\mathcal{E}$ at random positions are swapped. This models the simplest possible interaction between $\mathcal{S}$ and $\mathcal{E}$.

Note that at each time step the system is not evolved with probability $1 - p_1 - p_2$. The random choice of interacting qudits should be considered as "fixed once chosen": as we will see later, this means that when multiple replicas of the system are considered, the circuit is always identical in each copy.

The above rule defines a quantum circuit with discrete time steps. It is convenient to take a continuous limit of the former, which allows us to simplify some aspects of the computations. In order to do so, we choose the probability p_1 and p_2 to scale with the time interval Δt as

$$p_1 = N\lambda_1\Delta t\,, \tag{2.1}$$

$$p_2 = \lambda_2\Delta t\,, \tag{2.2}$$

where λ_1, and λ_2 are two positive real numbers. Note that while both p_1 and p_2 are proportional to Δt, they have a different dependence on N. As we will comment on again later, this ensures that the internal time scales are much shorter that those related to the interaction with the environment, as it is assumed within the Hayden-Preskill protocol [6]. With the above choices, expectation values of observables computed at time t display a well defined limit for $\Delta t \to 0$ (namely $n \to \infty$), yielding a continuous dynamics for $\mathcal{S} \cup \mathcal{E}$. Importantly, we will be interested in the limit of an infinitely large environment, which will then play the role of a "qudit" reservoir. In the discrete dynamics, it is enough to choose the number M of environment qudits to be $M \gg Nt/\Delta t$, so that $M \to \infty$ in the continuous limit.

In the rest of this work, we will focus on the computation of *averaged* physical quantities: at each time step this amounts to averaging over all the possible choices of pairs

JHEP04(2020)063

of qudits and of gates $U_{i,j}$, with the proper probability distribution. For a given fixed time t, this is equivalent to averaging over all the realizations of allowed quantum circuits. A crucial point is that each individual realization corresponds to a unitary evolution. In particular, if the initial state of $\mathcal{S} \cup \mathcal{E}$ is pure, it will remain so for any realization, and its von Neumann entanglement entropy will remain zero for all times (and so will its average over realizations).

Finally, regarding the ensemble of two-qudit gates $U_{i,j}$, we will consider two distinct physical situations. In the first one, the internal dynamics is "maximally chaotic", namely each gate $U_{i,j}$ is drawn out of a Haar distribution. In the second situation, we assume a locally conserved U(1) charge, namely we choose each gate $U_{i,j}$ to preserve the U(1) sectors in the product $h_{\mathcal{S}}^{(i)} \otimes h_{\mathcal{S}}^{(j)}$, as it was done in refs. [39, 42] for the case of spatially local RUCs.

3 The entanglement growth

In this section we study the entanglement growth for a subsystem $K \subset \mathcal{S}$, which is naturally quantified by means of the von Neumann entanglement entropy

$$S_K(t) = -\mathrm{tr}_K \left[\rho_K(t) \log_2 \rho_K(t)\right] , \tag{3.1}$$

where $\rho_K(t)$ is the density matrix reduced to the subsystem K. Denoting by $\{|j\rangle\}_{j=0}^{d-1}$, a basis for the local Hilbert spaces $h_{\mathcal{S}}$,$h_{\mathcal{E}}$, we will assume that both the system and the environment are initialized in product states, denoted by $|\Psi_0^{\mathcal{S}}\rangle$ and $|\Psi_0^{\mathcal{E}}\rangle$ respectively. In particular we set, for finite M,

$$|\Psi_0^{\mathcal{E}}\rangle = |0\rangle^{\otimes M} , \tag{3.2}$$

while we will consider different initial product states for $\mathcal{S}$. Note that by construction there is no entanglement between $\mathcal{S}$ and $\mathcal{E}$ at time $t = 0$.

Despite the importance of the von Neumann entanglement entropy, it is known that the latter is difficult to obtain in the setting of RUCs [35]. For this reason, in the following we focus on the related Rényi-2 entropy; more precisely, we will compute

$$S_K^{(2)}(t) = -\log_2 \left\{\mathrm{tr}_K \left\{\mathbb{E}\left[\rho_K^2(t)\right]\right\}\right\} . \tag{3.3}$$

We note that $S_K^{(2)}(t)$ is not the averaged second Rényi entropy, as the disorder average is taken inside the logarithm. In fact, eq. (3.3) is proportional to the logarithm of the averaged purity $\mathcal{P}_K$, which is defined as

$$\mathcal{P}_K(t) = \mathrm{tr}_K \left\{\mathbb{E}\left[\rho_K^2(t)\right]\right\} . \tag{3.4}$$

However, for large N one expects the effect of fluctuations in the disorder to be small, so that the behavior of $S_K^{(2)}(t)$ should be qualitatively the same as the averaged Rényi-2 entropy [38].

Let us now define $\overline{K} = \mathcal{S} \setminus K$ and rewrite

$$\begin{aligned} \mathrm{tr}_K \left\{\mathbb{E}\left[\rho_K^2(t)\right]\right\} &= \mathrm{tr}_K \left\{\mathbb{E}\left[\mathrm{tr}_{\overline{K}}\left[\rho_{\mathcal{S}}(t)\right] \mathrm{tr}_{\overline{K}}\left[\rho_{\mathcal{S}}(t)\right]\right]\right\} \\ &= \mathrm{tr}_{K\otimes K}\left\{X_K \, \mathrm{tr}_{\overline{K}\otimes\overline{K}}\left\{\mathbb{E}\left[\rho_{\mathcal{S}}(t) \otimes \rho_{\mathcal{S}}(t)\right]\right\}\right\} \\ &= \mathrm{tr}\left\{X_K \mathbb{E}\left[\rho_{\mathcal{S}}(t) \otimes \rho_{\mathcal{S}}(t)\right]\right\} \end{aligned} \tag{3.5}$$

JHEP04(2020)063

where X_K is a swap operator exchanging the two copies of K, while in the last line, "tr" represents the trace over the entire Hilbert space. From this expression it is clear that $S_K^{(2)}(t)$ is completely determined by the knowledge of $\mathbb{E}\left[\rho_{\mathcal{S}}(t)\otimes\rho_{\mathcal{S}}(t)\right]$. In order to compute the latter, it is convenient to recall the Choi-Jamiolkowski mapping which allows us to interpret the operator $\rho_{\mathcal{S}}(t)\otimes\rho_{\mathcal{S}}(t)$ (defined on the tensor product of two "replicas" $\mathcal{H}_{\mathcal{S}}\otimes\mathcal{H}_{\mathcal{S}}$) as a state in $\mathcal{H}_{\mathcal{S}}^{\otimes 4}$. In particular, we define

$$|\rho_{\mathcal{S}}(t)\otimes\rho_{\mathcal{S}}(t)\rangle\rangle = \left(\mathbb{1}_{\mathcal{H}_S}\otimes\rho_{\mathcal{S}}(t)\otimes\mathbb{1}_{\mathcal{H}_S}\otimes\rho_{\mathcal{S}}(t)\right)|I^+\rangle_{1,\dots,N}\,, \tag{3.6}$$

where we introduced the maximally entangled state

$$|I^+\rangle_{1,\dots,N} = \bigotimes_{k=1}^{N}|I^+\rangle_k\,, \tag{3.7}$$

with

$$|I^+\rangle_k = \sum_{a,b=0}^{d-1}\left(|a\rangle_k\otimes|a\rangle_k\right)\otimes\left(|b\rangle_k\otimes|b\rangle_k\right)\,. \tag{3.8}$$

In the following, we label with 1 and 2 the Hilbert spaces of the two replicas associated with $\rho_S(t)$ in eq. (3.6), and with $\bar{1}$ and $\bar{2}$ the other two. Accordingly, the Hilbert space corresponding to the four replicas is

$$\widetilde{\mathcal{H}}_{\mathcal{S}} = \mathcal{H}_{\mathcal{S}}^{(\bar{1})}\otimes\mathcal{H}_{\mathcal{S}}^{(1)}\otimes\mathcal{H}_{\mathcal{S}}^{(\bar{2})}\otimes\mathcal{H}_{\mathcal{S}}^{(2)}\,. \tag{3.9}$$

Finally, we also define

$$|I^-\rangle_k = \sum_{a,b=0}^{d-1}\left(|a\rangle_k\otimes|b\rangle_k\right)\otimes\left(|b\rangle_k\otimes|a\rangle_k\right). \tag{3.10}$$

Within this formalism one can recover the value of the purity using

$$\mathcal{P}_K(t)\equiv\mathrm{tr}_K\left\{\mathbb{E}\left[\rho_K^2(t)\right]\right\} = \langle\langle W_K|\mathbb{E}\left[\rho_{\mathcal{S}}(t)\otimes\rho_{\mathcal{S}}(t)\right]\rangle\rangle\,, \tag{3.11}$$

where

$$|W_K\rangle\rangle = \bigotimes_{k\in K}|I^-\rangle_k\bigotimes_{k\in\overline{K}}|I^+\rangle_k\,. \tag{3.12}$$

Eq. (3.11) can be verified straightforwardly by expanding the scalar product. We note that when the initial state $|\Psi_0^{\mathcal{S}}\rangle$ is a product state and invariant under arbitrary permutations of qudits in $\mathcal{H}_{\mathcal{S}}$, then the initial state $|\rho_{\mathcal{S}}(0)\otimes\rho_{\mathcal{S}}(0)\rangle\rangle$, is invariant under permutation of qudits in $\widetilde{H}_{\mathcal{S}}$. As it will be clear from the subsequent discussion, this is also true for the evolved state $|\rho_{\mathcal{S}}(t)\otimes\rho_{\mathcal{S}}(t)\rangle\rangle$: accordingly, the value of the purity $\mathcal{P}_K(t)$ only depends on the cardinality of K, $k=|K|$, and not on which sites belong to K and we may write $\mathcal{P}_k(t)=\mathcal{P}_K(t)$.

The formalism above allows us to write an equation describing the evolution of the state $\mathbb{E}\left[|\rho_{\mathcal{S}}(t)\otimes\rho_{\mathcal{S}}(t)\rangle\rangle\right]$ under the continuous RUC introduced in section 2. In particular, in the limit $M\to\infty$, we derive in appendix A

$$\frac{\mathrm{d}}{\mathrm{d}t}\mathbb{E}\left[|\rho_{\mathcal{S}}(t)\otimes\rho_{\mathcal{S}}(t)\rangle\rangle\right] = -\mathcal{L}\mathbb{E}\left[|\rho_{\mathcal{S}}(t)\otimes\rho_{\mathcal{S}}(t)\rangle\rangle\right]\,, \tag{3.13}$$

JHEP04(2020)063

where $\mathcal{L}$ is a super operator (the *Lindbladian*) acting on $\widetilde{\mathcal{H}}_{\mathcal{S}}$, which reads

$$\mathcal{L} = \frac{2\lambda_1}{N-1} \sum_{1\leq j<k\leq N} (1-\mathcal{U}_{j,k}) + \frac{\lambda_2}{N} \sum_{j=1}^{N} \left(1 - |0,0,0,0\rangle_j \langle I^+|_j\right) , \tag{3.14}$$

with

$$\mathcal{U}_{j,k} = \mathbb{E}\left[U^*_{j,k} \otimes U_{j,k} \otimes U^*_{j,k} \otimes U_{j,k}\right] . \tag{3.15}$$

In order to proceed further, we need to specify the probability distribution for the two-qudit unitary gates $U_{i,j}$, which in turn determines the average in eq. (3.15). As we already anticipated, we focus on two different physical situations. First we consider the case where $U_{i,j}$ are Haar-distributed over the group $\mathrm{U}(d^2)$, which corresponds to a maximally chaotic evolution. Second, we consider random gates $U_{i,j}$ with a block structure determined by the presence of a U(1) charge, as done for local RUCs in refs. [39, 42]. The two cases are treated separately in the next subsections.

3.1 Random Brownian circuit without conservation law

As we have anticipated, we start by choosing the unitary gates $U_{i,j}$ to be Haar distributed over $\mathrm{U}(d^2)$. In this case, the average in eq. (3.15) can be computed easily, and we have (see for instance refs. [37, 38])

$$\mathcal{U}_{j,k} = \frac{1}{d^4-1}\left[|\mathcal{I}^+_{j,k}\rangle\langle\mathcal{I}^+_{j,k}| + |\mathcal{I}^-_{j,k}\rangle\langle\mathcal{I}^-_{j,k}| - \frac{1}{d^2}\left(|\mathcal{I}^+_{j,k}\rangle\langle\mathcal{I}^-_{j,k}| + |\mathcal{I}^-_{j,k}\rangle\langle\mathcal{I}^+_{j,k}|\right)\right] , \tag{3.16}$$

where

$$|\mathcal{I}^\pm_{j,k}\rangle = |I^\pm\rangle_j \otimes |I^\pm\rangle_k . \tag{3.17}$$

Furthermore, throughout this section we initialize the system in the product state

$$|\Psi^{\mathcal{S}}_0\rangle = |1\rangle^{\otimes N} , \tag{3.18}$$

With the above choices, one can now plug the explicit expression (3.16) into (3.14) and solve, at least numerically, eq. (3.13).

Unfortunately, the exact numerical solution to eq. (3.13) is difficult to obtain for large values of N, as the dimension of $\widetilde{H}_{\mathcal{S}}$ grows exponentially with the system size. Luckily, in the present case the problem can be considerably simplified due to permutation symmetry between different qubits, and one does not need to solve eq. (3.13) directly. Instead, based on eq. (3.11), it is possible to derive the following system of differential equations

$$\frac{\mathrm{d}\mathcal{P}_n(t)}{\mathrm{d}t} = \frac{2\lambda_1 n(N-n)}{N-1}\frac{d}{(d^2+1)}\left[-\left(d+\frac{1}{d}\right)\mathcal{P}_n(t) + \mathcal{P}_{n-1}(t) + \mathcal{P}_{n+1}(t)\right] - \frac{\lambda_2 n}{N}(\mathcal{P}_n - \mathcal{P}_{n-1}) , \tag{3.19}$$

for $n = 0,\ldots,N$ and with the convention $\mathcal{P}_{-1}(t) = \mathcal{P}_{N+1}(t) \equiv 0$. Here $\mathcal{P}_n(t)$ is the purity for a subsystem with n qudits, while the initial conditions [corresponding to the state (3.18)] are

$$\mathcal{P}_n(0) = 1 , \qquad n = 0,\ldots,N . \tag{3.20}$$

JHEP04(2020)063

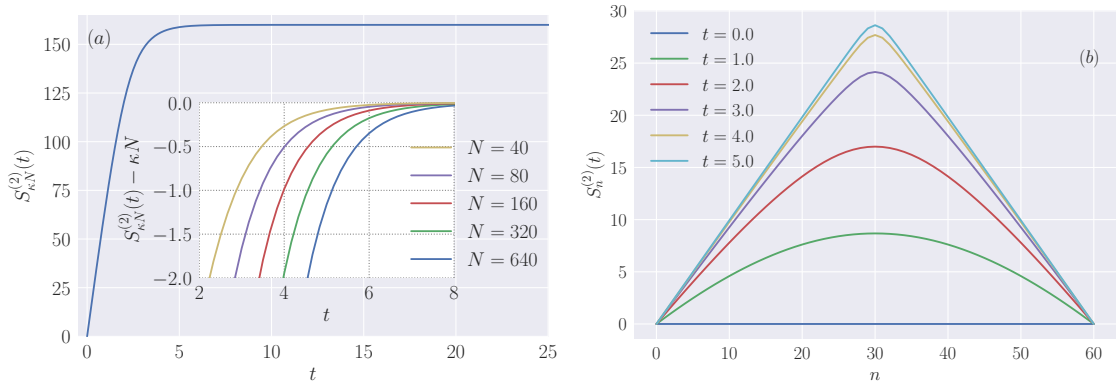

Figure 2. Rényi entropy dynamics for different subsystems, obtained by solving eq. (3.19) with $\lambda_2 = 0$ (no coupling with the environment), $\lambda_1 = 1$ and local dimension $d = 2$. Subfigure (a), main panel: Rényi-2 entropy $S^{(2)}_{\kappa N}(t)$ as a function of time, for $N = 640$ and $\kappa = 1/4$. Inset: the plot shows the difference between $S^{(2)}_{\kappa N}(t)$ and its maximum possible value κN as a function of time and for increasing system sizes N. Denoting by $t^*_{(\kappa N)}$ the amount of time needed before $\mathcal{S}^{(2)}_{\kappa N}(t) - \kappa N$ becomes larger than a small negative constant ε (cf. the main text), it is clear from the plot that $t^*_{(\kappa N)} \sim \ln(N)$. Subfigure (b): Rényi-2 entropy $S^{(2)}_n(t)$ as a function of the subsystem size n, for different times.

We note that eq. (3.19) represents a rare example where an explicit result for the dynamics of the Rényi entropy can be obtained for open systems [88]. Since its derivation is rather technical, we reported it in appendix B.

It is important to comment on this result. First, we note that setting $\lambda_2 = 0$ in eq. (3.19), we recover the same set of equations (up to prefactors) that was derived in ref. [28] for a Brownian Hamiltonian evolution. Thus, the internal dynamics driven by the RUC defined in section 2 is qualitatively equivalent to a continuous Brownian Hamiltonian evolution. This observation allows us to apply directly some of the results of ref. [28] to our model.

In particular, it was shown in ref. [28] that the system (3.19) leads (for $\lambda_2 = 0$) to the emergence of a time scale which is logarithmic in N. More precisely, let us call $t^*_{(k)}$ the amount of time needed before the purity of a subsystem of size k becomes less than $(1 + \delta)2^{-k}$, where δ is a small positive real number, and 2^{-k} is the purity of a maximally mixed state. Then, for $0 < \kappa < 1$ fixed, it was shown that $t^*_{(\kappa N)} \sim \ln(N) t^*_{(1)}$. In our case, due to the choice made in eq. (2.1), we have that $t^*_{(1)}$ has a constant limit for $N \to \infty$, so that $t^*_{(\kappa N)} \sim \ln(N)$ for large N. In ref. [28] this was defined as the *scrambling time* of the system. Note that, following later developments, the scrambling time is now usually defined as the time needed for OTOCs to decay to zero. However, the latter was shown to be also logarithmic in the system size N for the Brownian Hamiltonian evolution of ref. [28], see ref. [33], so that, up to prefactors, they can be identified in our model.

The features of the entanglement dynamics for $\lambda_2 = 0$ discussed above are illustrated in figure 2, from which the emergence of a time scale logarithmic in N is manifest.

JHEP04(2020)063

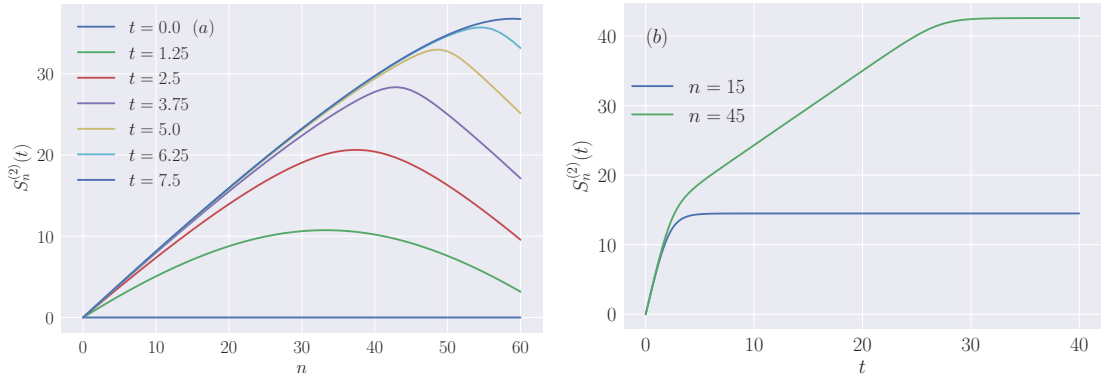

Figure 3. Rényi entropy dynamics for different subsystems, obtained by solving eq. (3.19), for local dimension $d = 2$ and $N = 60$. Subfigure (a): Rényi-2 entropy $S_n^{(2)}(t)$ as a function of the subsystem size n, for different times, with $\lambda_1 = 1$ and $\lambda_2 = 10$. Subfigure (b): $S_n^{(2)}(t)$ as a function of time for subsystems containing 15 and $N - 15 = 45$ qudits. The parameters are chosen as $\lambda_1 = 1$, $\lambda_2 = 1.5$.

Next, note that for $\lambda_1 = 0$ eq. (3.19) predicts the purity of any subsystem to remain constant, namely $\mathcal{P}_n(t) \equiv 1$ for all values of n. This is due to the fact that, in each realization of the quantum circuit, $\mathcal{S}$ remains a pure state, since the evolution only amounts to an exchange of qudits $|1\rangle$ and $|0\rangle$ between $\mathcal{S}$ and $\mathcal{E}$. On the other hand, when both $\lambda_1, \lambda_2 \neq 0$, the entanglement growth is non-trivial. In the following, we present our results based on the numerical solution of eq. (3.19).

In figure 3(a) we report the numerical values of $S_n^{(2)}(t)$ as a function of the subsystem size n, for different times t and $\lambda_2 \neq 0$. We can immediately appreciate that the effect of the environment is to increase the entanglement of $\mathcal{S}$, even though the environment itself consists of a product state. This is due to following mechanism: if j is a qudit in $\mathcal{S}$, the internal dynamics will generate entanglement between j and $\mathcal{S} \setminus j$. When j is swapped with a qudit in $\mathcal{E}$, the latter becomes entanglement between $\mathcal{S} \setminus j$ and $\mathcal{E}$. As a consequence, $\mathcal{S}$ does not remain in a pure state, and its entanglement grows in time. We also see that the Rényi entropy of K and $\mathcal{S} \setminus K$ is not equal anymore, since the larger of the two can accommodate more entanglement with $\mathcal{E}$.

It is particularly interesting to follow the time evolution of a subsystem K larger than half of the system size, as displayed in figure 3(b). We see that there are two relevant time scales that characterize its qualitative behavior: for short times, the Rényi entropy $S_K^{(2)}(t)$ is essentially on top of $S_{N\setminus K}^{(2)}(t)$. After a time t_s, $S_K^{(2)}(t)$ starts to increase with a constant slope up to a time t_p, at which saturation occurs (the indices s and p stand for "scrambling" and "Page" respectively: the use of these names will be justified in the next section). We can interpret the increase of $S_K^{(2)}(t)$ for $t < t_s$ as mainly due to the internal scrambling dynamics. Based on this picture, we expect $t_s \sim \ln(N)$, while, due to the normalization choice in eqs. (2.1) and (2.2), $t_p \gg t_s$ for large N.

To verify this, we have computed numerically the time derivative of $S_K^{(2)}(t)$, from which the emergence of different regimes is manifest, cf. figure 4. We see that for $t < t_s$

JHEP04(2020)063

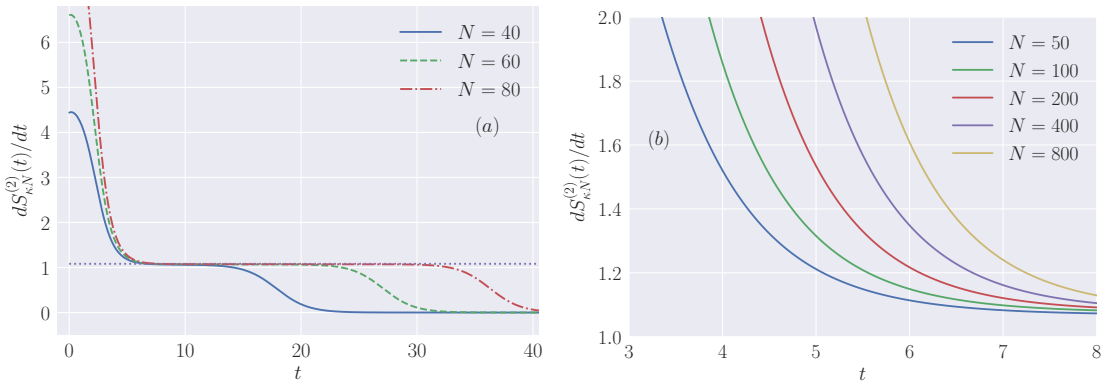

Figure 4. Subfigure (a): time derivative of the Rényi-2 entropy $S^{(2)}_{\kappa N}(t)$ as a function of time, for different values of the system size N. The constant dotted line corresponds the value s_λ defined in eq. (3.21). Subfigure (b): same data shown in the region close to t_s (cf. the main text). In both figures we chose $\kappa = 3/4$, local dimension $d = 2$ and $\lambda_1 = 1$, $\lambda_2 = 1.5$.

the derivative is large and increases with N, while for $t_s < t < t_p$ it approaches a constant s_{λ_2} as $N \to \infty$. It is not straightforward to compute s_{λ_2} directly from eq. (3.19): indeed, while at short times the r.h.s. of eq. (3.19) is dominated by the term proportional to λ_1, for $t \sim t_s$ the absolute value of the latter becomes comparable to the term proportional to λ_2 and both contribute in a non-negligible way to s_{λ_2}. Nevertheless, we can make the conjecture

$$s_{\lambda_2} = \frac{(d-1)}{d}\frac{\lambda_2}{\ln(2)}\,. \tag{3.21}$$

In order to motivate eq. (3.21), we consider the case $K = \mathcal{S}$, so that only the term proportional to λ_2 in eq. (3.19) is non-vanishing. In the limit $\lambda_2 \to 0$, one can make the assumption that that after a time $t > t_s \sim \ln(N)$ the system is almost maximally scrambled. Then, for large n one would get $\mathcal{P}_n(t) \simeq d^{-N+n}$, so that

$$\frac{\mathrm{d}\mathcal{P}_N(t)}{\mathrm{d}t} \simeq -\frac{\lambda_2(d-1)}{d}\mathcal{P}_N(t)\,, \tag{3.22}$$

and so

$$\frac{\mathrm{d}}{\mathrm{d}t}S^{(2)}_N(t) = -\frac{\mathrm{d}}{\mathrm{d}t}\log_2\mathcal{P}_N(t) = -\frac{1}{\mathcal{P}_N(t)\ln 2}\frac{\mathrm{d}}{\mathrm{d}t}\mathcal{P}_N(t) = \frac{(d-1)}{d}\frac{\lambda_2}{\ln 2}\,. \tag{3.23}$$

Remarkably, we found that eq. (3.21) is in perfect agreement with the numerical solution to eq. (3.19) for arbitrary values of λ_1 and λ_2, and also for general $K \subset \mathcal{S}$ (with $|K| > N/2$), suggesting that it should be possible to derive it rigorously from eq. (3.19).

We can estimate t_s precisely, by defining it as the amount of time needed in order for $dS^{(2)}_K(t)/dt$ to become smaller than $s_{\lambda_2} + \varepsilon$, where ε is a positive small number. We see clearly from figure 4(b) that $t_s \sim \ln(N)$, as we also verified with a quantitative fit. On the other hand, one can define analogously t_p to be the amount of time needed in order for $dS^{(2)}_K(t)/dt$ to be smaller than a small positive constant, and as it is clear from figure 4(a), one has $t_p \sim N$, so that indeed $t_p \gg t_s$.

JHEP04(2020)063

In summary, the above analysis shows that in the presence of both internal dynamics and system-environment interaction, two distinct time scales emerge: one can be associated with the internal scrambling time t_s, with $t_s \sim \ln(N)$, while the other, t_p, depends on the interaction with $\mathcal{E}$, and for the RUC constructed in section 2 we have $t_p \sim N$.

3.2 Random dynamics with a conserved U(1) charge

In the previous subsection we have seen that the second Rényi entropy for a subsystem $K \subset \mathcal{S}$ grows always monotonically with time, even if $\mathcal{E}$ is initialized in the product state $|0\rangle^{\otimes M}$. On the other hand, in a unitary black hole evaporation process, one expects that the entanglement follows a "Page-like" behavior in time [51]: namely it initially grows but starts to decrease in the middle stage of the evaporation, and eventually vanishes when the black hole evaporates completely.[1] This difference between a black hole and random tensor networks originates from the absence of energy conservation in the latter. In the long-time limit, the black hole returns to a vacuum state since its energy leaves with the radiation, while the random tensor network model approaches a random state with large entanglement entropy between the system and the bath.

It is difficult to introduce energy conservation in tensor network models, but it is possible to introduce a U(1) charge conservation, which plays a similar role. When the bath is infinitely large and initialized in the zero (i.e. lowest) charge "vacuum" state, the black hole charge will gradually decrease and approach zero in the final state. As long as the zero-charge state is unique, the black hole entropy will eventually vanish in the long-time limit (for a very different approach that achieves similar phenomena, see ref. [67]).

We implement a dynamics with a U(1) conserved charge by imposing that the two-qudit unitary gates $U_{i,j}$ have some special structure, as done in refs. [39, 42] for the case of spatially local circuits. For the rest of this section, we will focus on the case of qubits, namely $d = 2$. Then, following [39, 42] we consider gates of the form

$$U_{i,j} = \begin{pmatrix} U_{Q=0} & & \\ & U_{Q=1} & \\ & & U_{Q=2} \end{pmatrix} , \tag{3.24}$$

where the first and last blocks are 1×1 and the second block is a 2×2 Haar-random unitary matrix. Since the interaction with the environment is driven by swap gates, eq. (3.24) defines a dynamics conserving the charge

$$Q_{\mathcal{S}\cup\mathcal{E}} = \sum_{j \in \mathcal{S}\cup\mathcal{E}} q_j \, , \tag{3.25}$$

where the charge operator is

$$q_j = \begin{pmatrix} 0 & 0 \\ 0 & 1 \end{pmatrix} . \tag{3.26}$$

on each site.

[1] In some toy models such as ref. [86], this was introduced by hand, moving qubits from black hole to the bath at each time step.

JHEP04(2020)063

Averaging over unitary gates of the form (3.24) introduces additional computational difficulties with respect to the case of Haar-distributed operators. In particular, by exploiting the results derived in ref. [39], eq. (3.16) has to be replaced by

$$\begin{aligned}\mathcal{U}_{j,k} = &\sum_{s=\pm}\sum_{Q_j\neq Q_k}\frac{1}{d_{Q_j}d_{Q_k}}\left|\mathcal{I}^s_{Q_jQ_k}\right\rangle\left\langle\mathcal{I}^s_{Q_jQ_k}\right| \\ &+\sum_{s=\pm}\sum_{\mathcal{Q}}\frac{1}{d_Q^2-1}\left[\left|\mathcal{I}^s_{QQ}\right\rangle\left\langle\mathcal{I}^s_{QQ}\right| - \frac{1}{d_Q}\left|\mathcal{I}^s_{QQ}\right\rangle\left\langle\mathcal{I}^{-s}_{QQ}\right|\right] .\end{aligned} \tag{3.27}$$

Here $|\mathcal{I}^{\pm}_{Q_jQ_k}\rangle$ are states living in the tensor-product of two local sites of the four replica space. In terms of single-site states, they can be written as

$$\left|\mathcal{I}^{+}_{Q_jQ_k}\right\rangle = \sum_{\alpha\beta\gamma\delta}|\alpha\alpha\beta\beta\rangle_j|\gamma\gamma\delta\delta\rangle_k\delta_{\alpha+\gamma=Q_j}\delta_{\beta+\delta=Q_k} , \tag{3.28}$$

$$\left|\mathcal{I}^{-}_{Q_jQ_k}\right\rangle = \sum_{\alpha\beta\gamma\delta}|\alpha\beta\beta\alpha\rangle_j|\gamma\delta\delta\gamma\rangle_k\delta_{\alpha+\gamma=Q_1}\delta_{\beta+\delta=Q_k} , \tag{3.29}$$

where, for the case of qubits, the Greek indices take value in $\{0,1\}$, while $d_0 = d_2 = 1$ and $d_1 = 2$.

The form of eq. (3.27) makes the computations considerably more involved. In particular, one can not derive a set of N differential equations for the purity, and a different strategy is needed to obtain $S^{(2)}_K(t)$ efficiently. Luckily, one can exploit an observation of ref. [39]. Namely, the states $|\mathcal{I}^{\pm}_{Q_jQ_k}\rangle$ can be written in terms of the following 6 states [39]

$$|\mathbf{0}\rangle \equiv |0000\rangle , \qquad |\mathbf{1}\rangle \equiv |1111\rangle , \tag{3.30}$$

$$|A\rangle \equiv |1100\rangle , \qquad |B\rangle \equiv |0011\rangle , \tag{3.31}$$

$$|C\rangle \equiv |1001\rangle , \qquad |D\rangle \equiv |0110\rangle . \tag{3.32}$$

Once again, we stress that the states $|\mathbf{0}\rangle$, $|\mathbf{1}\rangle$, $|A\rangle$, $|B\rangle$, $|C\rangle$ and $|D\rangle$ live in a single local space of the four replicas. This means that the evolution dictated by the averaged gates $\mathcal{U}_{j,k}$ effectively takes place in a Hilbert space $\widetilde{\mathcal{H}}^{\text{eff}}_{\mathcal{S}} = h^{\text{eff}}_1 \otimes \cdots \otimes h^{\text{eff}}_N$, where $h^{\text{eff}}_j \simeq \mathbb{C}^6$ so that $\mathcal{U}_{i,j}$ is a matrix acting on the space $\mathbb{C}^6 \otimes \mathbb{C}^6$.

The above consideration becomes particularly powerful when combined with the underlying permutational symmetry of the operator $\mathcal{L}$ and of the initial state $|\rho_{\mathcal{S}}(0)\otimes\rho_{\mathcal{S}}(0)\rangle\rangle$. Indeed, this allows us to exploit a logic which is similar to the one developed in ref. [34], and obtain an efficient scheme to compute the evolution of the system in a numerically exact fashion.

We start by introducing the following class of permutationally invariant states on the space $\widetilde{\mathcal{H}}^{\text{eff}}_{\mathcal{S}}$

$$\begin{aligned}&|n_{\mathbf{0}}, n_{\mathbf{1}}, n_A, n_B, n_C, n_D\rangle \\ &= \frac{1}{\sqrt{N! n_{\mathbf{0}}! n_{\mathbf{1}}! n_A! n_B! n_C! n_D!}}\sum_{\pi\in S_N}\pi\,\underbrace{|\mathbf{0}\rangle\otimes\cdots\otimes|\mathbf{0}\rangle}_{n_{\mathbf{0}}}\otimes\cdots\otimes\underbrace{|D\rangle\otimes\cdots\otimes|D\rangle}_{n_D}\pi^{-1} .\end{aligned} \tag{3.33}$$

JHEP04(2020)063

Importantly, we can rewrite these states by introducing a set of bosonic creation operators as [34]

$$|n_{\mathbf{0}}, n_{\mathbf{1}}, n_A, n_B, n_C, n_D\rangle = \frac{1}{\sqrt{n_{\mathbf{0}}! n_{\mathbf{1}}! n_A! n_B! n_C! n_D!}} \left(a_{\mathbf{0}}^\dagger\right)^{n_{\mathbf{0}}} \left(a_{\mathbf{1}}^\dagger\right)^{n_{\mathbf{1}}} \left(a_A^\dagger\right)^{n_A} \left(a_B^\dagger\right)^{n_B} \left(a_C^\dagger\right)^{n_C} \left(a_D^\dagger\right)^{n_D} |\Omega\rangle \,, \tag{3.34}$$

where $[a_j, a_k] = \left[a_j^\dagger, a_k^\dagger\right] = 0$ and $\left[a_j, a_k^\dagger\right] = \delta_{j,k}$, while $|\Omega\rangle$ is a vacuum state. One of the advantages of the bosonic representation is that the operator $\mathcal{L}$, the initial state $|\rho_{\mathcal{S}}(0) \otimes \rho_{\mathcal{S}}(0)\rangle\rangle$ and the vector $|W_K\rangle\rangle$ defined in eq. (3.12) admit a simple expression in terms of the a-operators. Since we won't make use of them in the following, we report them in appendix C, to which we refer the interested reader.

Since both the initial state and the Lindbladian $\mathcal{L}$ are invariant under arbitrary permutation of qubits, the states (3.34) form a basis of the Hilbert space in which the dynamics takes place. Crucially, the corresponding dimension is

$$D_{\text{perm}} = \binom{N+5}{5} = N^5 + O(N^4) \,, \tag{3.35}$$

and thus grows only polynomially (rather than exponentially) with N. In practice D_{perm} is still very large for the values of N considered in the previous subsection. Nevertheless, we were able to perform numerically exact calculations up to $N = 80$. This was done by implementing the matrix corresponding to $\mathcal{L}$ in the vector basis (3.34), and then computing the evolved state $|\rho_{\mathcal{S}}(t) \otimes \rho_{\mathcal{S}}(t)\rangle\rangle$ solving the system of differential equations encoded in eq. (3.13). Note that in this way we did not need to diagonalize exactly the matrix associated with $\mathcal{L}$, which would be unfeasible for $N = 80$. In rest of this section, we report the numerical results obtained by following the above procedure.

We first consider the case where the system is initialized in the product state (3.18), and study the time evolution of the Rényi entropy $S_K^{(2)}(t)$ for different subsystems $K \subset \mathcal{S}$, as reported in figure 5. We immediately see that the qualitative behavior is different from the Haar-scrambled case, since $S_K^{(2)}(t)$ is a non-monotonic function. For a given subsystem K, with $|K| = \kappa N$ and $\kappa \in [0, 1]$, we have verified that the time t_p at which $S_{\kappa N}^{(2)}(t)$ reaches its maximum grows linearly with N/λ_2. We call t_p the Page-time [51]. After t_p, we see from figure 5 that $S_{\kappa N}^{(2)}(t)$ decreases and approaches zero exponentially fast, with an exponent that does not appear to depend on κ.

Besides its non-monotonic behavior, $S_K^{(2)}(t)$ displays another qualitative difference. Indeed, the initial state of $\mathcal{S}$, defined in eq. (3.18), is a fixed point for the internal dynamics. Hence, at short times, one can not distinguish clearly the contribution of the internal scrambling, since the initial growth of $S_K^{(2)}(t)$ is only due to system-environment coupling (there is no evolution if $\lambda_2 = 0$). For this reason, we consider in figure 6 the Rényi entropy $S_K^{(2)}(t)$, for the initial state

$$|\Psi_0^{\mathcal{S}}\rangle = \bigotimes_{j=1}^{N/2} |0\rangle_j \bigotimes_{j=N/2+1}^{N} |1\rangle_j \,. \tag{3.36}$$

JHEP04(2020)063

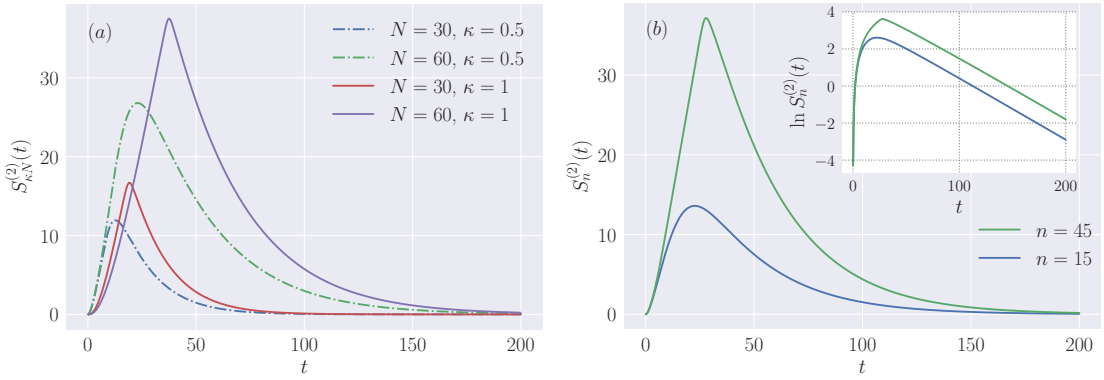

Figure 5. Rényi entropy $S_n^{(2)}(t)$ as a function of time for $\lambda_1 = 1$ and $\lambda_2 = 2$. The plots correspond to a random evolution in the presence of a global U(1) conserved charge, while the system is initialized as in eq. (3.18). Subfigures (a): $S^{(2)}_{\kappa N}(t)$ for different values of the system size N and $\kappa = 0.5, 1$. Subfigure (b): $S_n^{(2)}(t)$ for $N = 60$ and subsystems containing 15 and $N - 15 = 45$ qubits. Inset: $\ln S_n^{(2)}(t)$ for the same values of n.

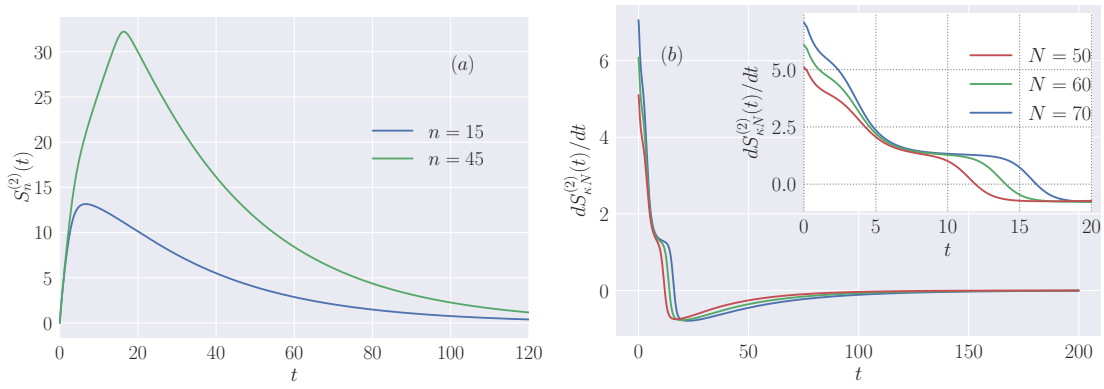

Figure 6. Subfigure (a): Rényi entropy $S_n^{(2)}(t)$ as a function of time for $N = 60$ and subsystems containing 15 and $N - 15 = 45$ qubits. The plot corresponds to a random evolution in the presence of a global U(1) conserved charge, while the system is initialized as in eq. (3.36). The evolution parameters are set to $\lambda_1 = 1$ and $\lambda_2 = 2$. Subfigure (b): time derivative of the Rényi-2 entropy $S^{(2)}_{\kappa N}(t)$ as a function of time, for $\kappa = 7/10$ and increasing values of N. The evolution parameters are set to $\lambda_1 = 1$ and $\lambda_2 = 2$. The inset shows the same plot in the time region close to t_s (cf. the main text).

Note that this state is not invariant under permutation of qubits. Accordingly, we consider a protocol where not only we sample over different realizations of the RUC, but we also take an average over all the initial product states obtained by permuting the qubits in (3.36): namely, we average over all product states where half of the qubits are initialized to $|0\rangle$, and the rest are set to $|1\rangle$. It is straightforward to see that in the four replica space $\widetilde{H}_{\mathcal{S}}$ the state $|\rho_{\mathcal{S}}(0) \otimes \rho_{\mathcal{S}}(0)\rangle\rangle$ (obtained after averaging over the initial configurations) is indeed permutationally invariant, and we can employ the approach explained above.

JHEP04(2020)063

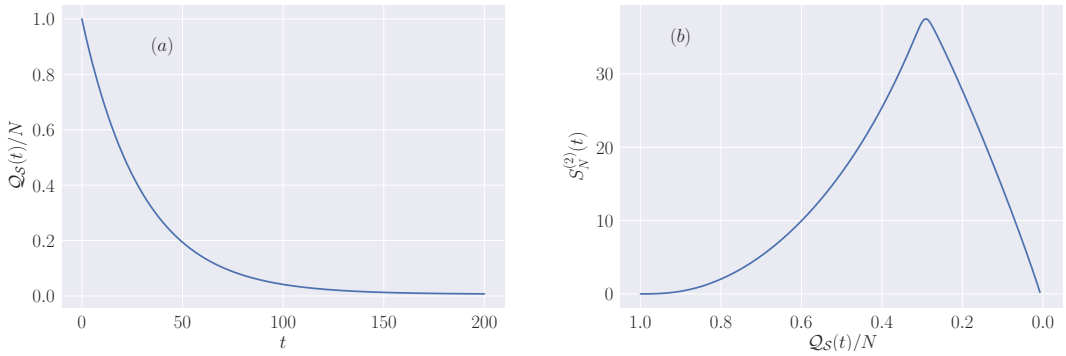

Figure 7. Subfigure (a): time evolution of the system charge $\mathcal{Q}_S(t)$ defined in eq. (3.37). Subfigure (b): Rényi entropy $S_N^{(2)}(t)$ as a function of the charge $\mathcal{Q}_S(t)$ (note the inverted scale on the x-axis). The plots correspond to a random evolution in the presence of a global U(1) conserved charge, while the system is initialized as in eq. (3.18). The evolution parameters are set to $\lambda_1 = 1$ and $\lambda_2 = 2$, and the system size is $N = 60$.

As expected, we see from figure 6(a) a separation of time scales for the initial state (3.36). In order to make this more transparent, and following the previous section, we report in figure 6(b) the time derivative of the Rényi-2 entropy $S_{\kappa N}^{(2)}(t)$. Although the results are now plagued by larger finite-N effects, we can see the same qualitative behavior displayed in figure 4 for the Haar-scrambled dynamics. In particular, after a time $t_s \sim \ln N$ the derivatives appear to approach a plateau, and it remains approximately constant for $t_s < t < t_p$, where $t_p \sim N$ is the Page time.

Finally, in order to push further the analogy between our model and a unitary black hole evaporation process, it is interesting to study the time evolution of the system charge

$$\mathcal{Q}_S(t) = \mathrm{tr}_S\left\{\mathbb{E}\left[\rho_S(t)\right]\sum_{j\in S} q_j\right\}. \tag{3.37}$$

The computation of $\mathcal{Q}_S(t)$ can be carried out using the very same techniques outlined above for the second Rényi entropy. In fact, we note that the calculations are simpler, since they only involve two replicas, instead of four. In particular, it turns out that the average charge can be obtained as the solution to a system of $(N+1)^2$ coupled linear differential equations, which can be easily treated numerically. Since no additional complication arises, we omit the details of the computation here, and only report our final numerical results. These are displayed in figure 7, where we also show $S_N^{(2)}(t)$ as a function of $\mathcal{Q}_S(t)$.

We note that the dimension of the Hilbert space associated with a given integer value Q of the charge is $\binom{N}{Q}$. Of course, the evolved system state will have nonzero projection onto different sectors of the charge at a given time. Nevertheless, we can define an effective "black hole" Hilbert space dimension associated with the averaged charge as

$$D_{BH}(t) = \binom{N}{\mathcal{Q}_S(t)}. \tag{3.38}$$

We see that the behavior of $D_{BH}(t)$ depends on the initial state chosen for $\mathcal{S}$. If the system is initialized as in eq. (3.18), then the effective Hilbert space dimension will first increase,

JHEP04(2020)063

and then decrease after $\mathcal{Q}_{\mathcal{S}}(t)$ reaches the value $N/2$. On the other hand, if the system is initialized in the state (3.36), the effective Hilbert space decreases monotonically, as one would expect in a more realistic unitary black hole evaporation process.

Before leaving this section, we comment on the choice (3.2) for the initial state of the environment. As we have mentioned, this is motivated by an analogy with the black hole evaporation process, where (3.2) plays the role of the "global" vacuum state. However, it is natural to wonder what would happen if $\mathcal{E}$ is initialized, instead, in a random product state. In this case, a non-vanishing charge would be pumped into the system at each time interval, so one would expect that the qualitative behavior of the Rényi entropy would be similar as in the evolution without the U(1) conserved charge. We have verified by explicit numerical calculations that this is indeed the case. In particular, if $\mathcal{E}$ is initialized in a random product state we observe no monotonic decrease of the Rényi entropy after the Page time.

4 Retrieval of quantum information

In this section we finally discuss how the RUC introduced in section 2 provides a microscopic model for the information-retrieval protocol studied by Hayden and Preskill [6], and allows us to investigate quantitatively several aspects of the latter. We start by briefly reviewing the setting of ref. [6], and then proceed to present our results.

We recall that the information stored in a black hole is emitted in the form of Hawking radiation [2], so that one can ask what is the minimum amount of time that is needed before such information can be recollected from measurements performed outside of the black hole. In order to make contact with our model, we interpret $\mathcal{S}$ as the black hole, while $\mathcal{E}$ consists of all its exterior degrees of freedom (hence including Hawking radiation). Following ref. [6], we then imagine that Alice injects a qudit A into the system at time $t = 0$, and that a third party $\mathcal{C}$ (Charlie), holds a reference qudit which is maximally entangled with the former. The system is in contact with $\mathcal{E}$ and evolved by the RUC introduced in section 2. Finally, we imagine that Bob wants to recover information on the injected qudit by only performing measurements outside of $\mathcal{S}$. Depending on the initial configuration of the system, the ability to faithfully do so after a given time t is captured quantitatively by the mutual information between different sets of qudits, as we now explain.

First, let us consider the setting pictorially depicted in figure 8(a): in this case, Bob has no control over the initial configuration of the system $\mathcal{S}$, which is initialized in a given product state at time $t = 0$. The capability of recovering information on the injected qudit by measurements on $\mathcal{E}$ is quantified by the mutual information

$$I_{(a),[\mathcal{C},\mathcal{E}]}(t) = S_{\mathcal{C}}(t) + S_{\mathcal{E}}(t) - S_{\mathcal{C}\cup\mathcal{E}}(t)\,, \tag{4.1}$$

which tells us how much information can be extracted from the reference qudit $\mathcal{C}$ by accessing those in $\mathcal{E}$. In particular, if $I_{(a),[\mathcal{C},\mathcal{E}]}(t)$ is close to its maximal value, then Bob can faithfully recover the information initially injected into $\mathcal{S}$. Note that in eq. (4.1) we used an index (a) to distinguish the two settings in figure 8. As usual, due to computational

JHEP04(2020)063

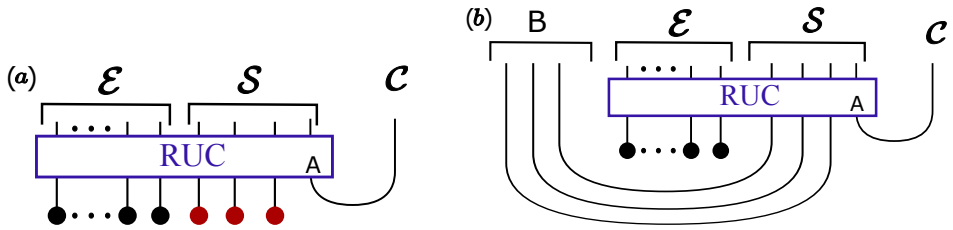

Figure 8. Pictorial representation of the two settings considered in section 4. In the first case [subfigure (a)], we initialize the system $\mathcal{S}$ (the "black hole") in a product state. A qudit A is initially injected into the black hole, and a third party ($\mathcal{C}$) holds a reference system, namely an ancilla which is maximally entangled with the former at time $t = 0$. The system is in contact with $\mathcal{E}$ (representing the exterior of the black hole, including Hawking radiation) and evolved by the RUC introduced in section 2. In the second setting [subfigure (b)], the retriever (B) initially holds a copy of the black hole, namely $\mathcal{S}$ is initialized in a maximally entangled state with a set of ancillary qudits.

limitations, in the following we will not compute the quantity in eq. (4.1), but rather its Rényi-2 version, namely

$$I^{(2)}_{(a),[\mathcal{C},\mathcal{E}]}(t) = S^{(2)}_{\mathcal{C}}(t) + S^{(2)}_{\mathcal{E}}(t) - S^{(2)}_{\mathcal{C}\cup\mathcal{E}}(t)\,, \tag{4.2}$$

where $\mathcal{S}^{(2)}_K(t)$, for a given system K, is defined in eq. (3.3).

In the second setting, displayed in figure 8(b), we imagine instead that the black hole formed long ago, and that Bob has been collecting its emitted Hawking radiation ever since. Accordingly, by the time the qudit A is injected, the black hole $\mathcal{S}$ is in a maximally entangled state with the previously emitted radiation system, which is under Bob's control [region B in figure 8(b)]. In this case, Bob can also access these qudits, together with those in the environment $\mathcal{E}$, and his capability to recover the initially injected information is quantified by $I_{(b),[\mathcal{C},\mathcal{E}\cup B]}(t)$. Accordingly, analogously to the previous case, in the following we will compute its Rényi-2 counterpart

$$I^{(2)}_{(b),[\mathcal{C},\mathcal{E}\cup B]}(t) = S^{(2)}_{\mathcal{C}}(t) + S^{(2)}_{\mathcal{E}\cup B}(t) - S^{(2)}_{\mathcal{C}\cup\mathcal{E}\cup B}(t)\,. \tag{4.3}$$

It turns out that the formalism introduced in the previous section is adequate to compute numerically the mutual information in eqs. (4.2) and (4.3), for both RUCs without and with a conserved U(1) charge. To see this, we can exploit the fact that the Rényi entropy of a subsystem K is equal to that of its complementary one (with respect to the whole space), and rewrite

$$I^{(2)}_{(a),[\mathcal{C},\mathcal{E}]}(t) = S^{(2)}_{\mathcal{C}}(t) + S^{(2)}_{\mathcal{S}\cup\mathcal{C}}(t) - S^{(2)}_{\mathcal{S}}(t)\,, \tag{4.4}$$

$$I^{(2)}_{(b),[\mathcal{C},\mathcal{E}\cup B]}(t) = S^{(2)}_{\mathcal{C}}(t) + S^{(2)}_{\mathcal{S}\cup\mathcal{C}}(t) - S^{(2)}_{\mathcal{S}}(t)\,. \tag{4.5}$$

Each individual entropy in the r.h.s. of the above equations can be computed by exploiting the approach in section 3.1 (for the maximally chaotic RUC) and in section 3.2 (in the presence of a conserved U(1) charge). In particular, in each case we can map the problem onto the computation of the time evolution in a four replica space $\widetilde{H}_{\mathcal{S}}$, where the dynamics

JHEP04(2020)063

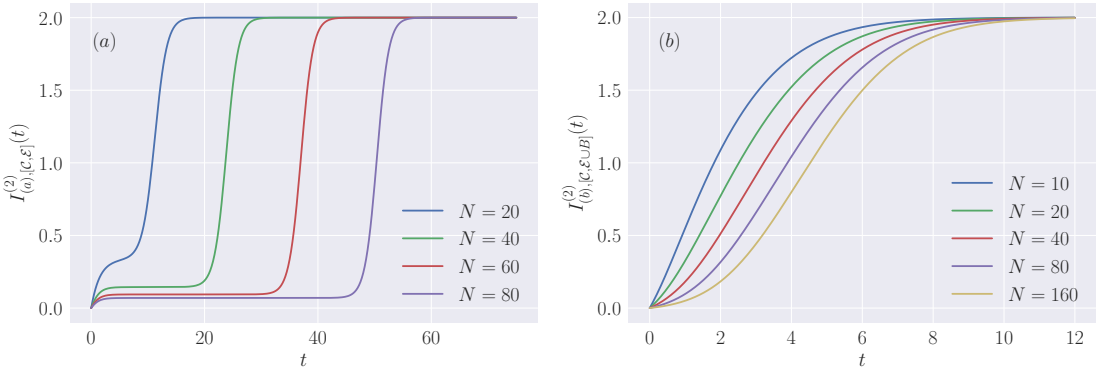

Figure 9. Subfigure (a): mutual information $I^{(2)}_{(a),[\mathcal{C},\mathcal{E}]}(t)$ [defined in eq. (4.2)] for the setting displayed in figure 8(a), and increasing values of N. Subfigure (b): mutual information $I^{(2)}_{(b),[\mathcal{C},\mathcal{E}\cup\mathcal{B}]}(t)$ [defined in eq. (4.3)] for the setting displayed in figure 8(b), and increasing values of N. For both plots, the evolution is driven by the maximally chaotic RUC of section 2 (without conserved charges), where we set $\lambda_1 = 1$, $\lambda_2 = 2$ and chose $d = 2$.

is driven by the Lindbladian operator (3.14). The only difference with respect to the steps presented in the previous section is in the initial state and purity vector $\langle\langle W_K|$, which have to be modified for each individual term in the r.h.s. of eqs. (4.4) and (4.5). Since these calculations do not present additional difficulties, we report them in appendix D, and in the rest of this section we present our final results.

We begin by discussing figure 9, where we report data for the maximally chaotic RUC (no conserved charge). Subfigures (a) and (b) correspond to the two different settings discussed above, and display respectively $I^{(2)}_{(a),[\mathcal{C},\mathcal{E}]}(t)$ and $I^{(2)}_{(b),[\mathcal{C},\mathcal{E}\cup B]}(t)$ for increasing values of N. In both cases, the mutual information has a monotonic behavior, although with qualitative differences. In the first case, it reaches its maximum value in a time which is clearly proportional to the system size N. Interestingly, we see that after a time scale of the order of the scrambling time $t_s \sim \ln N$, the mutual information reaches a small non-zero value, which, however, is seen to decrease with the system size N. We can interpret this as follows: after the scrambling time, Bob is able to only reconstruct a small amount of the initially injected information, and needs to wait for a time proportional to the black hole size in order to retrieve all of it.

Conversely, we see from figure 9(b) that the information retrieval is much faster in the case Bob holds a copy of the black hole [cf. figure 8(b)]. In particular, from the plot we clearly see that the mutual information reaches its maximum value after a time which is logarithmic with the system size N, namely the scrambling time.

We have repeated the same calculations for a RUC with a conserved U(1) charge, and reported our results in figure 10. We see that the functions $I^{(2)}_{(a),[\mathcal{C},\mathcal{E}]}(t)$ and $I^{(2)}_{(b),[\mathcal{C},\mathcal{E}\cup B]}(t)$ display the same qualitative features. It is interesting to note that, in the setting corresponding to subfigure (a) of figure 8, the value of the mutual information after the scrambling time is larger than that in the maximally chaotic case, although still vanishing for $N \to \infty$. This is intuitive: the presence of conservation laws constrains the Hilbert space that can be explored by the system, hence generally increasing the knowledge on its state.

JHEP04(2020)063

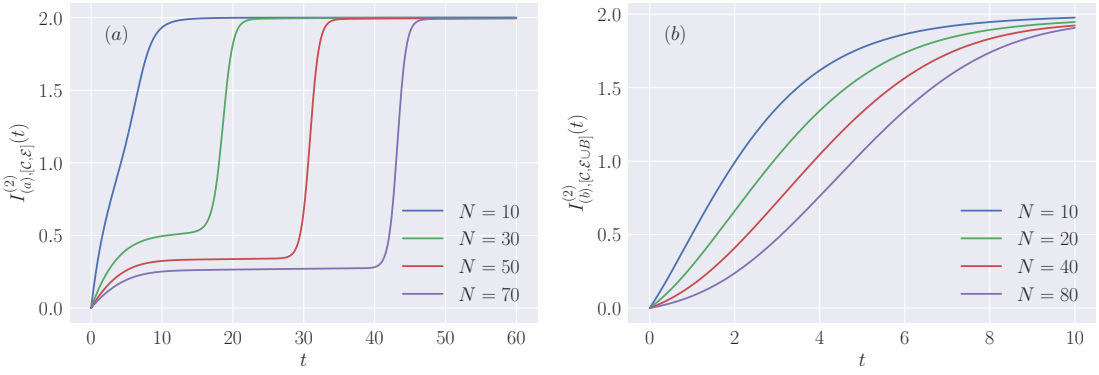

Figure 10. Same plots as in figure 9. The evolution is now driven by the RUC with a conserved U(1) charge defined in section 3.2, where we set $\lambda_1 = 1$, $\lambda_2 = 2$ (and $d = 2$).

In energy conserved systems, the Lyapunov exponent measured by OTOC growth generically depends on temperature. Usually a slower scrambling occurs at lower temperature T, and an upper bound of $2\pi T$ has been proven for a particular regularized version of the OTOC [13]. The analog of temperature dependence in our model is the charge dependence of the information retrieval time. We expect that when the charge is closer to 0 or 1, the Hilbert space size is smaller, leading to a similar effect as reducing temperature in energy conserved system. For this purpose, we study the mutual information growth for states with different charge. To this end, we first consider the protocol depicted in figure 8(a), but we initialize the system $\mathcal{S}$ in the product state

$$|\Psi_0^{\mathcal{S}}\rangle = \bigotimes_{j=1}^{n} |0\rangle_j \bigotimes_{j=n+1}^{N-1} |1\rangle_j \ . \tag{4.6}$$

As we have clarified after eq. (3.36), we actually consider averages over all the initial states obtained by permuting different qubits in eq. (4.6), namely over all the product states with n qubits initialized to $|0\rangle$ and $(N-1-n)$ to $|1\rangle$ (where the last qubit N corresponds to A, and is entangled to the ancilla $\mathcal{C}$). This allows us to exploit the permutational symmetry in the four-replica space, and proceed following the very same steps outlined above to obtain numerically exact data for the mutual information $I^{(2)}_{(a),[\mathcal{C},\mathcal{E}]}(t)$.

We report our results in figure 11, for different values of n, and a fixed system size $N = 60$. In subfigures (a) and (b) we report data for decreasing values of the initial charge $Q = N-1-n$, respectively larger or smaller than $N/2$. As we have already pointed out, in the former case the effective Hilbert space dimension (3.38) has a non-monotonic behavior, whereas in the latter case it is monotonically decreasing, as one would expect in a more realistic unitary evaporation protocol. This is reflected in the fact that, at short times, the two plots display a different qualitative behavior as n increases: in subfigure (a), $I^{(2)}_{(a),[\mathcal{C},\mathcal{E}]}(t)$ decreases as n increases, while the opposite happens in subfigure (b).

In subfigure (c) we report instead the logarithm of the difference between the maximum value 2 of the mutual information and $I^{(2)}_{(a),[\mathcal{C},\mathcal{E}]}(t)$ at late times. The plot shows the

JHEP04(2020)063

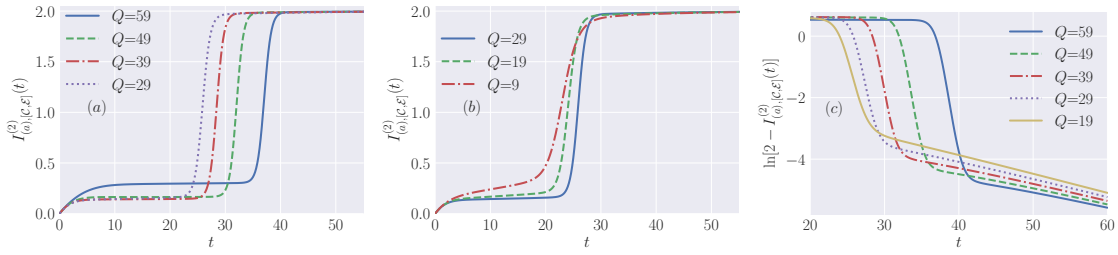

Figure 11. Mutual information $I^{(2)}_{(a),[\mathcal{C},\mathcal{E}]}(t)$ [defined in eq. (4.2)] for the setting displayed in figure 8(a). Subfigures (a) and (b) correspond to the initial state (4.6) for different values of the initial charge $Q = N - 1 - n$, respectively larger and smaller than $N/2$. Subfigure (c) shows $\ln\left[2 - I^{(2)}_{(a),[\mathcal{C},\mathcal{E}]}(t)\right]$ for the same state (and different values of Q) at late times. For all plots, the evolution is driven by the RUC with a conserved U(1) charge defined in section 3.2, where we set $\lambda_1 = 1$, $\lambda_2 = 2$ and $N = 60$ (while we chose $d = 2$).

emergence of an exponential decay, which starts first for smaller initial charge (a larger initial charge takes longer to evaporate).

Next, we consider the protocol reported in figure 8(b). In this case, the initial state is given by a maximally entangled state between $\mathcal{S}$ and B. This has a non-vanishing projection over all the charge sectors, so we can not vary arbitrarily its charge, as for figure 8(a). For this reason, we consider a different setting, which maintains some of its features, but allows us to tune the initial charge of $\mathcal{S}$. This is depicted in figure 12. The idea is to initialize the system in a product state, and let the RUC generate an entangled state between $\mathcal{S}$ and $\mathcal{E}$. After the Page time, $\mathcal{S}$ is approximately a maximally mixed state in a certain charge sector (with charge decreasing in time), as we discussed earlier. At time $t = t_1$, we introduce a new qubit which is maximally entangled with an ancillary one, denoted by $\mathcal{C}$. After that, the dynamics of $\mathcal{E} \cup \mathcal{S}$ is dictated by the same RUC for a time t_2. We are interested in the retrieval of this qubit in $\mathcal{E}$. Thus we study the mutual information

$$I^{(2)}_{(c),[\mathcal{C},\mathcal{E}]}(t_2) = S^{(2)}_{\mathcal{C}}(t_1 + t_2) + S^{(2)}_{\mathcal{E}}(t_1 + t_2) - S^{(2)}_{\mathcal{C}\cup\mathcal{E}}(t_1 + t_2)\,, \tag{4.7}$$

where the index (c) here is used to distinguish this protocol from those in figure 8. As usual, we average over the choice of the qudit A: this allows us, once again, to rely on the permutational symmetry in the four-replica space, and exploit the exact same techniques developed so far to efficiently simulate the dynamics (cf. appendix D.3). We report our numerical results in figures 13 and 14, which we now discuss.

First, figure 13(a) displays the mutual information $I^{(2)}_{(c),[\mathcal{C},\mathcal{E}]}(t_2)$ for increasing values of t_1. The plot corresponds to $N = 40$ and initial charge $Q = N - 1 = 39$, while $\lambda_1 = 1$, $\lambda_2 = 2$. For this choice of the parameters, the Page time is $t_p \sim 25$ [cf. figure 10(a)], so that $t_1 < t_p$ for the data reported in figure 13(a). In this case, we see that $I_{(c),[\mathcal{C},\mathcal{E}]}(t_2)$ saturates faster as time increases, which is what we expect. Indeed, for t_1 smaller than the Page time t_p, the RUC increases the entanglement between $\mathcal{S}$ and $\mathcal{E}$, so a retriever accessing $\mathcal{E}$ at time $t = t_1$ has more control over the configuration of the "black hole" when the extra qubit is injected.

JHEP04(2020)063

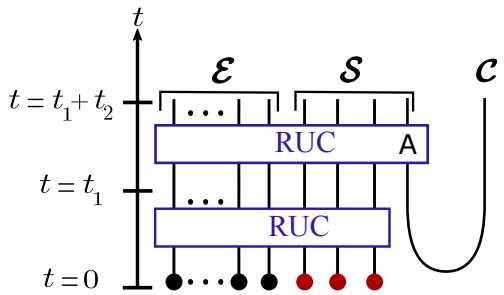

Figure 12. Pictorial representation of the third settings considered in section 4. We initialize the system $\mathcal{S}$ (the "black hole") in a product state, except for a qubit A, randomly chosen, which is maximally entangled with an ancillary one, denoted by $\mathcal{C}$. The system $\mathcal{E} \cup \mathcal{S} \setminus A$ is evolved with the RUC with a U(1) conserved charge for a time t_1. After that, $\mathcal{E} \cup \mathcal{S}$ is evolved with the same RUC, for a time t_2.

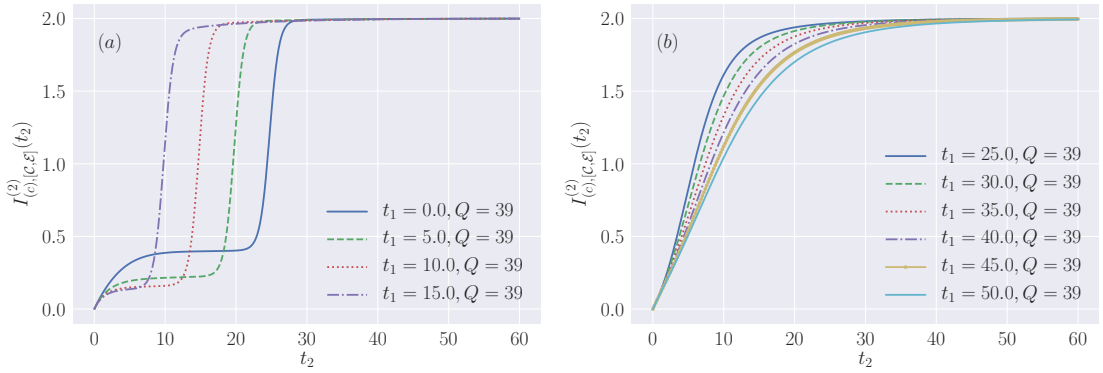

Figure 13. Mutual information $I^{(2)}_{(c),[\mathcal{C},\mathcal{E}]}(t_2)$ [defined in eq. (4.7)] for the setting displayed in figure 12. Subfigures (a) and (b) show the mutual information for initial charge $Q = 39$ and increasing values of t_1, respectively smaller and larger than the Page time t_p. For all plots, the evolution is driven by the RUC with a conserved U(1) charge defined in section 3.2, where we set $\lambda_1 = 1$, $\lambda_2 = 2$ and $N = 40$ (while we chose $d = 2$).

At $t_1 \sim t_p$, $\mathcal{S}$ and $\mathcal{E}$ will be maximally entangled within a given charge sector. Thus, the retriever should be able to faithfully recollect information on the injected qubit after the scrambling time t_s. However, since the charge is conserved, the portion of the Hilbert space that can be explored during the dynamics is smaller that 2^N. For this reason, we expect $t_s \propto \log S$, where $S = \ln D_{BH}(t_p)$ and $D_{BH}(t_p)$ is the effective dimension defined in eq. (3.38). Unfortunately, we can not reach large enough system sizes to test this statement quantitatively.

Next, we report in figure 13(b) the mutual information $I^{(2)}_{(c),[\mathcal{C},\mathcal{E}]}(t_2)$ for $t_1 > t_p$ and fixed initial charge Q. The plot shows that as t_1 increases the mutual information saturates more slowly, which is due to the fact that the entanglement between $\mathcal{S}$ and $\mathcal{E}$ decreases for $t_1 > t_p$. In this respect, it is particularly simple to understand the limit $t_1 \to \infty$: in this case the configuration of $\mathcal{S}$ at time $t = t_1$ will be extremely close to the vacuum, and there will be essentially no scrambling of information in $\mathcal{S}$, leading to an extremely slow saturation of $I^{(2)}_{(c),[\mathcal{C},\mathcal{E}]}(t_2)$.

JHEP04(2020)063

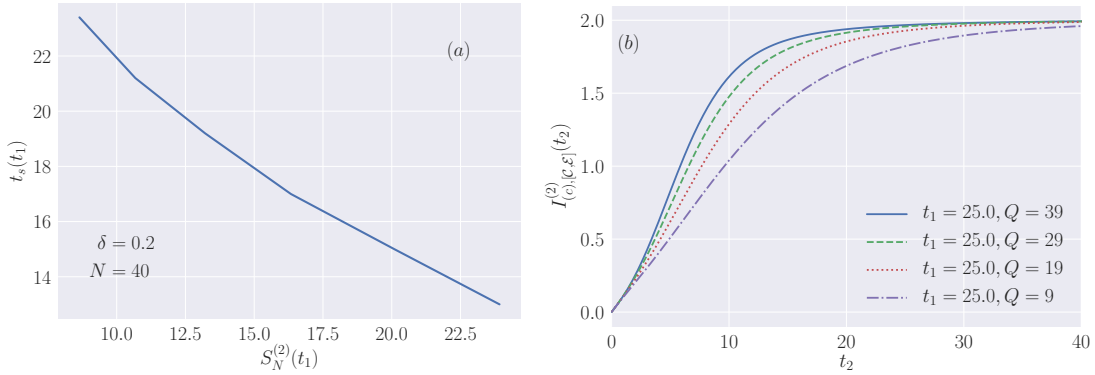

Figure 14. Subfigure (a): scrambling time $t_s(t_1)$ as a function of $S_N^{(2)}(t_1)$. Here $t_s(t_1)$ is defined as the value of t_2 at which $I^{(2)}_{(c),[\mathcal{C},\mathcal{E}]}(t_2)$ reaches the value $2-\delta$. In the plot, we chose $\delta = 0.2$. Subfigure (b): mutual information $I^{(2)}_{(c),[\mathcal{C},\mathcal{E}]}(t_2)$ for various initial charges Q and fixed t_1. For all plots, the evolution is driven by the RUC with a conserved U(1) charge defined in section 3.2, where we set $\lambda_1 = 1$, $\lambda_2 = 2$ and $N = 40$ (while we chose $d = 2$).

From figure 13(b) we can also extract the dependence of the scrambling time for information injected at time t_1 on the system Rényi-2 entropy at time t_1, namely $S_N^{(2)}(t_1)$. Here the scrambling time $t_s(t_1)$ is defined as the value of t_2 at which the mutual information reaches the value $2-\delta$, where δ is some small positive number. This is reported in figure 14(a), where we chose $\delta = 0.2$. From the plot it is clear that $t_s(t_1)$ is a monotonically decreasing function of $S_N^{(2)}(t_1)$ for $t_1 > t_p$, as we already discussed above.

Finally, figure 14(b) shows $I^{(2)}_{(c),[\mathcal{C},\mathcal{E}]}(t_2)$ for different values of the initial charge Q, for fixed $t_1 \sim t_p(Q = 39)$ (the Page time depends on the initial charge). In this case, we see that $I^{(2)}_{(c),[\mathcal{C},\mathcal{E}]}(t_2)$ is decreasing with Q, which is what we expect: if the initial charge is small, then the corresponding Page time is short. So, for $Q < 39$ and a given time $t_1 > t_p(Q = 39)$, the entanglement between $\mathcal{S}$ and $\mathcal{E}$ will be small, leaving the retriever with little control over the configuration of $\mathcal{S}$ when the extra qubit is injected.

5 Conclusions

In this work, we have considered the dynamics of a quantum many-body qudit system coupled to an external environment, where the time evolution is driven by the continuous limit of certain 2-local random unitary circuits. We have shown that the growth of the second Rényi entropy displays two different time scales that are related to the internal information scrambling and the interaction with the environment. Furthermore, we have characterized the qualitative differences that emerge choosing the unitaries to be Haar-distributed or with a conserved U(1) charge. In the latter case, we have shown that the entanglement displays a Page-like behavior in time, where it begins to decrease in the middle stage of the "evaporation". Finally, we have shown that our model provides a microscopic realization of the Hayden-Preskill protocol for information retrieval, studying quantitatively the time evolution of the mutual information between different subsystems.

JHEP04(2020)063

The conserved U(1) charge provides a tunable effective Hilbert space size, and allow us to study the charge dependence of scrambling dynamics.

The RUC considered in this work can be enriched in a number of ways. For instance, we have always considered the limit where the environment has an infinite number of qudits, that are non-interacting with one another. One could wonder whether the qualitative features described in this work are modified by considering an environment with a finite number of qudits, possibly with a non-trivial internal dynamics.

Next, it would be extremely interesting to consider the growth of local operators [9–14] in our setting. While the effect of decoherence on the latter has been already considered in the literature [83], our model provides an ideal playground where numerical and analytic results can be derived for large values of N, and the implications of conservation laws explored in detail. We plan to go back to these questions in future investigations.

Finally, when compared to holographic duality, our model gives us a toy model for the boundary dynamics. It would be interesting to use a tensor network approach to describe bulk degrees of freedom, and study the entanglement wedge structure.

Acknowledgments

We are very grateful to Ignacio Cirac, Vedika Khemani, Norbert Schuch, for early collaboration on this project and valuable comments on this manuscript. We thank Masamichi Miyaji, Zhenbin Yang, Shunyu Yao, Shangnan Zhou for helpful discussions. LP acknowledges support from the Alexander von Humboldt foundation. XLQ is supported by the National Science Foundation under grant No. 1720504, the Simons Foundation, and in part by the Department of Energy under grant No. DE-SC0019380.

A Derivation of the Lindbladian for the Rényi entropies

We wish to write down an evolution equation for the state $|\rho_{\mathcal{S}}(t)\otimes\rho_{\mathcal{S}}(t)\rangle\rangle$. To this end, we start with the discrete version of the quantum circuit introduced in section 2. Choosing a time t_j fixed, we focus on an individual realization of the circuit. This defines a global unitary transformation on $\mathcal{S}\cup\mathcal{E}$ which we denote by $U(t_j)$. Then, we have

$$\begin{aligned}|\rho_{\mathcal{S}}(t_j+\Delta t)\otimes\rho_{\mathcal{S}}(t_j+\Delta t)\rangle\rangle = \mathbb{1}_{\mathcal{H}_{\mathcal{S}}}\otimes\mathrm{tr}_{\mathcal{E}}\left\{U(t_j+\Delta t)\rho U^{\dagger}(t_j+\Delta t)\right\}\otimes\\ \mathbb{1}_{\mathcal{H}_{\mathcal{S}}}\otimes\mathrm{tr}_{\mathcal{E}}\left\{U(t_j+\Delta t)\rho U^{\dagger}(t_j+\Delta t)\right\}|I^{+}\rangle_{1,\ldots,N}\ .\end{aligned}\tag{A.1}$$

The operator $U(t_j+\Delta t)$ is obtained from $U(t_j)$ by applying a suitable unitary operator. In particular, according to the evolution described in section 2, we have three possibilities:

- with probability $1-p_1-p_2$ no unitary is applied at time t_j, so that $U(t_j+\Delta t)=U(t_j)$;
- with probability p_1 a unitary between j and k is applied, so that $U(t_j+\Delta t)=U_{j,k}U(t)$
- with probability p_2 a swap exchanges one qudit in $\mathcal{S}$ and one qudit in $\mathcal{E}$.

We can now take the average over all possible realizations. We note that the average can be taken independently at each time step, so that, due to the above considerations, the r. h. s. of eq. (A.1) splits into the sum of three contributions

$$\mathbb{E}\left[|\rho_{\mathcal{S}}(t_j+\Delta t)\otimes\rho_{\mathcal{S}}(t_j+\Delta t)\rangle\rangle\right] = (1-p_1-p_2)C_1 + p_1 C_2 + p_2 C_3\,. \tag{A.2}$$

The first, corresponding to no unitary applied, is trivial

$$C_1 = \mathbb{E}\left[|\rho_{\mathcal{S}}(t_j)\otimes\rho_{\mathcal{S}}(t_j)\rangle\rangle\right]\,. \tag{A.3}$$

Next, C_2 can be easily determined, since the action of $U_{j,k}$, for $j,k\in\mathcal{S}$, commutes with tracing over $\mathcal{E}$. We obtain

$$C_2 = \frac{2}{N(N-1)}\sum_{j<k}\mathbb{E}\left[U^*_{j,k}\otimes U_{j,k}\otimes U^*_{j,k}\otimes U_{j,k}\right]\mathbb{E}\left[|\rho_{\mathcal{S}}(t_j)\otimes\rho_{\mathcal{S}}(t_j)\rangle\rangle\right]\,. \tag{A.4}$$

The term C_3 is more complicated, because it couples the system $\mathcal{S}$ and the environment $\mathcal{E}$. However, it can be computed explicitly in the limit $M\to\infty$. Indeed, let us denote by j and k the qudits in $\mathcal{S}$ and $\mathcal{E}$ respectively that are swapped at time t_j. Assuming $M\gg Nt_j/\Delta t$, we have a negligible probability that qudit k in the environment has interacted before with $\mathcal{S}$. Hence, we can assume k to be in its initial configuration $|0\rangle_k$, and hence having no entanglement with the rest of the qudits in $\mathcal{E}$. Under this assumption (which becomes exact in the limit $M\to\infty$), it is straightforward to compute

$$C_3 = \frac{1}{N}\sum_{j=1}^{N}|0,0,0,0\rangle_j\,\langle I^+|_j\,\mathbb{E}\left[|\rho_{\mathcal{S}}(t_j)\otimes\rho_{\mathcal{S}}(t_j)\rangle\rangle\right]\,, \tag{A.5}$$

where $|I^+\rangle_j$ was introduced in (3.8). Putting all together and scaling the probabilities p_1 and p_2 with Δt and N as defined in (2.1) and (2.2) results in

$$\mathbb{E}\left[|\rho_{\mathcal{S}}(t_j+\Delta t)\otimes\rho_{\mathcal{S}}(t_j+\Delta t)\rangle\rangle\right] = (1-\Delta t\mathcal{L})\mathbb{E}\left[|\rho_{\mathcal{S}}(t_j)\otimes\rho_{\mathcal{S}}(t_j)\rangle\rangle\right] \tag{A.6}$$

with the final Lindbladian (3.14) as $\mathcal{L}$. In the limit $\Delta t\to 0$ we recover the differential equation (3.13).

B Derivation of the system of differential equations for the purity in the Haar-scrambled case

In the maximally chaotic case, we do not need to evaluate directly (3.13) to obtain $|\rho_{\mathcal{S}}(t)\otimes\rho_{\mathcal{S}}(t)\rangle\rangle$. Instead, we can derive the system (3.19) of $N+1$ coupled differential equations for the purities $\mathcal{P}_n = \langle\langle W_n|\rho_{\mathcal{S}}\otimes\rho_{\mathcal{S}}\rangle\rangle$ (see (3.11)) for subsystems of size n.

To this end, we insert the Lindbladian (3.14) into the equation (3.11) defining the purity,

$$\frac{d\mathcal{P}_n(t)}{dt} = \langle\langle W_n|(-\mathcal{L})|\rho_{\mathcal{S}}(t)\otimes\rho_{\mathcal{S}}(t)\rangle\rangle. \tag{B.1}$$

JHEP04(2020)063

Next, the action of $\langle\langle W_n|$ from (3.12) onto the Lindbladian $\mathcal{L}$ from (3.14) with $\mathcal{U}_{i,j}$ from (3.16) can be computed. Using the identities

$$\langle I_j^{\pm}|I_k^{\pm}\rangle = d^2\delta_{jk},\ \langle I_j^{\pm}|I_k^{\mp}\rangle = d\delta_{jk},\ \text{and}\ \langle I_j^{\pm}|0,0,0,0_k\rangle = \delta_{jk}\,, \tag{B.2}$$

and keeping in mind that for $\langle\langle W_n| = \langle\langle W_K|$ only the size $|K| = n$ of the region matters, this results in

$$\begin{aligned}
&\langle\langle W_n|(-\mathcal{L}) = \\
&\quad -\frac{2\lambda_1}{N-1}\Bigg(\frac{N(N-1)}{2}\langle\langle W_n| - \frac{n(n-1)}{2}\frac{1}{d^4-1}\Big[d^2\langle\langle W_{n-2}| + d^4\langle\langle W_n| \\
&\quad -\frac{1}{d^2}\left(d^2\langle\langle W_n| + d^4\langle\langle W_{n-2}|\right)\Big] \\
&\quad -\frac{(N-n)(N-n-1)}{2}\frac{1}{d^4-1}\left[d^4\langle\langle W_n| + d^2\langle\langle W_{n+2}| - \frac{1}{d^2}\left(d^4\langle\langle W_{n+2}| + d^2\langle\langle W_n|\right)\right] \\
&\quad -n(N-n)\frac{1}{d^4-1}\left[d^3\langle\langle W_{n-1}| + d^3\langle\langle W_{n+1}| - \frac{1}{d^2}\left(d^3\langle\langle W_{n+1}| + d^3\langle\langle W_{n-1}|\right)\right]\Bigg) \\
&\quad -\frac{\lambda_2}{N}\left(N\langle\langle W_n| - n\langle\langle W_{n-1}| - (N-n)\langle\langle W_n|\right) \\
&= -\frac{2\lambda_1}{N-1}\left(n(N-n)\langle\langle W_n| - \frac{n(N-n)d}{d^2+1}\left[\langle\langle W_{n-1}| + \langle\langle W_{n+1}|\right]\right) \\
&\quad -\frac{\lambda_2 n}{N}\left(\langle\langle W_n| - \langle\langle W_{n-1}|\right)
\end{aligned} \tag{B.3}$$

by considering separately the three sets of terms in the sum $\sum_{1\le j<k\le N}$ where the j'th and k'th site of $\langle\langle W_n|$ consist of $\langle I^{\pm}|_j, \langle I^{\pm}|_k$ with the signs $+,+$ or $-,-$ or opposite, respectively. The differential equation (3.19) for the purities $\mathcal{P}_n(t)$ then easily follows.

C Derivation of the relevant formulas in the bosonic formalism

In this section we discuss in more detail the formalism introduced in section 3.2, and derive a set of formulas that are needed for numerical implementations. We start by showing how to write operators in terms of the bosonic a-operators. First, we notice that one simply has

$$\sum_{j=1}^{N}\left(|x\rangle\langle y|\right)_j = a_x^\dagger a_y\,, \tag{C.1}$$

as can be explicitly checked by comparing the action of the two sides on any state. From this, is follows

$$\begin{aligned}
&\sum_{j<k}^{N}\Big[\left(|x\rangle\langle z|\right)_j\otimes\left(|y\rangle\langle t|\right)_k + \left(|y\rangle\langle t|\right)_j\otimes\left(|x\rangle\langle z|\right)_k\Big] \\
&= \left(\sum_{j=1}^{N}\left(|x\rangle\langle z|\right)_j\right)\left(\sum_{j=1}^{N}\left(|y\rangle\langle t|\right)_j\right) - \delta_{y,z}\sum_{j=1}^{N}|x\rangle\langle t| \\
&= a_x^\dagger a_z a_y^\dagger a_t - \delta_{y,z}a_x^\dagger a_t \\
&= a_x^\dagger a_y^\dagger a_z a_t\,.
\end{aligned} \tag{C.2}$$

JHEP04(2020)063

for $x, y, z, t = \mathbf{0}, \mathbf{1}, A, B, C, D$. One can now prove a general formula, which can be directly applied for implementing the effective Hamiltonians appearing in the main text. Let us consider

$$\sum_{j<k} \sum_{x,y,z,t} \left(\Gamma_{x,y} \left| x \right\rangle_j \otimes \left| y \right\rangle_k \right) \left(\Lambda_{z,t} \left\langle z \right|_j \otimes \left\langle t \right|_k \right) =: (*) \,, \tag{C.3}$$

where $\Gamma_{x,y} = \Gamma_{y,x}$ and $\Lambda_{z,t} = \Lambda_{t,z}$ are symmetric matrices. We can rewrite

$$\begin{aligned} (*) &= \sum_{j<k} \sum_{x,y,z,t} \Gamma_{x,y} \Lambda_{z,t} \left(\left| x \right\rangle \left\langle z \right| \right)_j \otimes \left(\left| y \right\rangle \left\langle t \right| \right)_k \,, \\ &= \frac{1}{2} \sum_{j<k} \sum_{x,y,z,t} \Gamma_{x,y} \Lambda_{z,t} \left[\left(\left| x \right\rangle \left\langle z \right| \right)_j \otimes \left(\left| y \right\rangle \left\langle t \right| \right)_k + \left(\left| y \right\rangle \left\langle t \right| \right)_j \otimes \left(\left| x \right\rangle \left\langle z \right| \right)_k \right] \\ &\quad + \frac{1}{2} \sum_{j<k} \sum_{x,y,z,t} \Gamma_{x,y} \Lambda_{z,t} \left[\left(\left| x \right\rangle \left\langle z \right| \right)_j \otimes \left(\left| y \right\rangle \left\langle t \right| \right)_k - \left(\left| y \right\rangle \left\langle t \right| \right)_j \otimes \left(\left| x \right\rangle \left\langle z \right| \right)_k \right] . \end{aligned} \tag{C.4}$$

In the second term, the parenthesis that multiplies $\Gamma_{x,y}\Lambda_{z,t}$ is antisymmetric under simultaneous exchange $x \leftrightarrow y$, $z \leftrightarrow t$. Since $\Gamma_{x,y}\Lambda_{z,t}$ is instead symmetric, the sum is zero. Accordingly, we have

$$\begin{aligned} (*) &= \frac{1}{2} \sum_{j<k} \sum_{x,y,z,t} \Gamma_{x,y} \Lambda_{z,t} \left[\left(\left| x \right\rangle \left\langle z \right| \right)_j \otimes \left(\left| y \right\rangle \left\langle t \right| \right)_k + \left(\left| y \right\rangle \left\langle t \right| \right)_j \otimes \left(\left| x \right\rangle \left\langle z \right| \right)_k \right] \\ &= \frac{1}{2} \sum_{x,y,z,t} \Gamma_{x,y} \Lambda_{z,t} \left[a_x^\dagger a_y^\dagger a_z a_t \right] . \end{aligned} \tag{C.5}$$

where we used eq. (C.2).

Finally, we show how to write symmetrized states in terms of bosonic a-operators. For this we consider a general state described by coefficients $c_{i,z}$, $i \in \{1, \dots, N\}, z \in \{\mathbf{0}, \mathbf{1}, A, B, C, D\}$, which we symmetrize:

$$\begin{aligned} &\frac{1}{N!} \sum_{\pi \in S_N} \pi \bigotimes_{i=1}^{N} \left(c_{i,\mathbf{0}} \left| \mathbf{0} \right\rangle_i + c_{i,\mathbf{1}} \left| \mathbf{1} \right\rangle_i + c_{i,A} \left| A \right\rangle_i + \cdots \right) \pi^{-1} \\ &= \frac{1}{N!} \sum_{\pi \in S_N} \pi \sum_{I_\mathbf{0} \cup I_\mathbf{1} \cup I_A \cup \cdots = \{1 \dots N\}} c_{I_\mathbf{0},\mathbf{0}} \left| \mathbf{0} \right\rangle^{\otimes I_\mathbf{0}} c_{I_\mathbf{1},\mathbf{1}} \left| \mathbf{1} \right\rangle^{\otimes I_\mathbf{1}} c_{I_A,A} \left| A \right\rangle^{\otimes I_A} \cdots \pi^{-1} \\ &= \frac{1}{N!} \sum_{I_\mathbf{0} \cup I_\mathbf{1} \cup I_A \cup \cdots = \{1 \dots N\}} \sqrt{N! \# I_\mathbf{0}! \# I_\mathbf{1}! \# I_A! \cdots} c_{I_\mathbf{0},\mathbf{0}} c_{I_\mathbf{1},\mathbf{1}} c_{I_A,A} \cdots \left| \# I_\mathbf{0}, \# I_\mathbf{1}, \# I_A, \dots \right\rangle \\ &= \frac{\sqrt{N!}}{N!} \sum_{I_\mathbf{0} \cup I_\mathbf{1} \cup I_A \cup \cdots = \{1 \dots N\}} c_{I_\mathbf{0},\mathbf{0}} (a_\mathbf{0}^\dagger)^{\# I_\mathbf{0}} c_{I_\mathbf{1},\mathbf{1}} (a_\mathbf{1}^\dagger)^{\# I_\mathbf{1}} c_{I_A,A} (a_A^\dagger)^{\# I_A} \left| \Omega \right\rangle \\ &= \frac{1}{\sqrt{N!}} \prod_{i=1}^{N} (c_{i,\mathbf{0}} a_\mathbf{0}^\dagger + c_{i,\mathbf{1}} a_\mathbf{1}^\dagger + c_{i,A} a_A^\dagger + \cdots) \left| \Omega \right\rangle \end{aligned} \tag{C.6}$$

where $c_{I,z} = \prod_{i \in I} c_{i,z}$.

From the above general formulas, it is now straightforward to rewrite the Lindbladian (3.14), with the choice (3.27), in terms of bosonic operators, together with the states

JHEP04(2020)063

relevant for our computations. In particular, we derived

$$\begin{aligned}\sum_{j<k}\mathcal{U}_{j,k} = \frac{1}{2}\left(\sum_{\alpha=\mathbf{0},\mathbf{1},A,B,C,D} a^\dagger_\alpha a^\dagger_\alpha a_\alpha a_\alpha\right) + \sum_{\alpha=A,B,C,D}\left(a^\dagger_{\mathbf{0}}a^\dagger_\alpha a_{\mathbf{0}}a_\alpha + a^\dagger_{\mathbf{1}}a^\dagger_\alpha a_{\mathbf{1}}a_\alpha\right)\\ +\frac{1}{3}\left(a^\dagger_{\mathbf{0}}a^\dagger_{\mathbf{1}}a_A a_B + a^\dagger_A a^\dagger_B a_{\mathbf{0}}a_{\mathbf{1}} + a^\dagger_{\mathbf{0}}a^\dagger_{\mathbf{1}}a_C a_D + a^\dagger_C a^\dagger_D a_{\mathbf{0}}a_{\mathbf{1}}\right)\\ +\frac{1}{3}\left(2a^\dagger_{\mathbf{0}}a^\dagger_{\mathbf{1}}a_{\mathbf{0}}a_{\mathbf{1}} + 2a^\dagger_A a^\dagger_B a_A a_B + 2a^\dagger_C a^\dagger_D a_C a_D - a^\dagger_C a^\dagger_D a_A a_B - a^\dagger_A a^\dagger_B a_C a_D\right),\end{aligned} \tag{C.7}$$

and

$$\sum_{j=1}^{N}|0,0,0,0\rangle_j\langle I^+|_j = \sum_{j=1}^{N}|\mathbf{0}\rangle_j\left(\langle\mathbf{0}|_j + \langle\mathbf{1}|_j + \langle A|_j + \langle B|_j\right) = a^\dagger_{\mathbf{0}}(a_{\mathbf{0}} + a_{\mathbf{1}} + a_A + a_B)\,. \tag{C.8}$$

Furthermore, it follows from eq. (C.6) that eq. (3.12) can be rewritten in terms of bosonic modes as

$$|W_K\rangle\rangle = \frac{1}{\sqrt{N!}}(a^\dagger_{\mathbf{0}} + a^\dagger_{\mathbf{1}} + a^\dagger_A + a^\dagger_B)^{N-k}(a^\dagger_{\mathbf{0}} + a^\dagger_{\mathbf{1}} + a^\dagger_C + a^\dagger_D)^k\cdots|\Omega\rangle\,, \tag{C.9}$$

where $k = |K|$. Note that eq. (C.9) actually corresponds to symmetrizing over all possible sets K of k elements. This is correct, since we are interested in the overlap (3.11), and the state $|\rho_{\mathcal{S}}(t)\otimes\rho_{\mathcal{S}}(t)\rangle\rangle$ is invariant under arbitrary permutations.

Finally, let us consider the initial state (3.18). It is immediate to see that this corresponds to the state

$$|\rho_{\mathcal{S}}(0)\otimes\rho_{\mathcal{S}}(0)\rangle\rangle = |n_{\mathbf{0}} = 0, n_{\mathbf{1}} = N, n_A = 0, n_B = 0, n_C = 0, n_D = 0\rangle\rangle\,. \tag{C.10}$$

Similarly, averaging the initial state (3.36) over all the possible permutations of qubits, we obtain the initial state

$$|\rho_{\mathcal{S}}(0)\otimes\rho_{\mathcal{S}}(0)\rangle\rangle = \frac{(N/2)!}{\sqrt{N!}}|n_{\mathbf{0}} = N/2, n_{\mathbf{1}} = N/2, n_A = 0, n_B = 0, n_C = 0, n_D = 0\rangle\rangle\,. \tag{C.11}$$

D Details on the computation of the mutual information

In this section we provide all the necessary details to obtain the results on information retrieval presented in section 4. For ease of presentation and numerical efficiency, we restrict to qubits.

D.1 Scenario (a)

Let us begin with scenario (a), in which the black hole is in an initial product state except for one qubit A [cf. figure 8(a)]. Rather than the initial product state (3.18) for the system $\mathcal{S}$, the initial state is now an entangled state

$$|\Psi_0^{\mathcal{S}\cup\mathcal{C}}\rangle = \frac{1}{\sqrt{2}}\sum_{s=0,1}\bigotimes_{j=1}^{N-1}|1\rangle_j\otimes|s\rangle_A\otimes|s\rangle_{\mathcal{C}}\,, \tag{D.1}$$

JHEP04(2020)063

with the two-replica Jamiolkowski representation

$$|\rho_{\mathcal{S}\cup\mathcal{C}}(0)\otimes\rho_{\mathcal{S}\cup\mathcal{C}}(0)\rangle\rangle = \frac{1}{4}\sum_{s\in\{0,1\}^4}\bigotimes_{j=1}^{N-1}|\mathbf{1}\rangle_j\otimes|s\rangle_A\otimes|s\rangle_{\mathcal{C}}\,. \tag{D.2}$$

After time evolution, we may extract the purities necessary for the mutual information (4.4) similarly to (3.11), but the vector $|W\rangle\rangle$ is now defined on systems $\mathcal{S}$ and $\mathcal{C}$. In particular, for the various Rényi entropies needed, we have

$$|W_{\mathcal{C}}\rangle\rangle = \bigotimes_{j\in\mathcal{S}}|I^+\rangle_j\otimes|I^-\rangle_{\mathcal{C}} \tag{D.3}$$

$$|W_{\mathcal{S}\cup\mathcal{C}}\rangle\rangle = \bigotimes_{j\in\mathcal{S}}|I^-\rangle_j\otimes|I^-\rangle_{\mathcal{C}}\,, \tag{D.4}$$

$$|W_{\mathcal{S}}\rangle\rangle = \bigotimes_{j\in\mathcal{S}}|I^-\rangle_j\otimes|I^+\rangle_{\mathcal{C}}\,. \tag{D.5}$$

In order to perform the calculation of the purities

$$\mathcal{P}_X(t) = \langle\langle W_X|e^{-\mathcal{L}t}|\rho_{\mathcal{S}\cup\mathcal{C}}(0)\otimes\rho_{\mathcal{S}\cup\mathcal{C}}(0)\rangle\rangle, \tag{D.6}$$

we symmetrize over system $\mathcal{S}$, including the location choice of qubit A entangled to $\mathcal{C}$. Due to the projection onto $\langle I^\pm|_{\mathcal{C}}$, the sum over s may be restricted to $s\in\{\mathbf{0},\mathbf{1},A,B,C,D\}$.

In the maximally chaotic case, we can derive and use the differential equation (3.19) as in section 3.1, with initial conditions

$$\mathcal{P}_{K\cup\mathcal{C}} = \frac{k}{N}+\frac{1}{2}\frac{N-k}{N}\,, \tag{D.7}$$

$$\mathcal{P}_K = \frac{1}{2}\frac{k}{N}+\frac{N-k}{N}\,, \tag{D.8}$$

where $K\subset\mathcal{S}$, $k=|K|$ as usual.

For the case with conservation laws, the symmetrization allows us to express all the states in the four replica space in the bosonic formalism as in section 3.2, within which we can numerically compute the purities. For this, one needs to write down explicitly an expression for $|\rho_{\mathcal{S}\cup\mathcal{C}}(0)\otimes\rho_{\mathcal{S}\cup\mathcal{C}}(0)\rangle\rangle$. To this end, let us generalize the case considered in eq. (D.1), by considering instead the case corresponding to the initial state (4.6), where we sum over all the possible permutations of qubits. Then, following the technical derivations in the previous section, it is possible to derive

$$|\rho_{\mathcal{S}\cup\mathcal{C}}(0)\otimes\rho_{\mathcal{S}\cup\mathcal{C}}(0)\rangle\rangle = \frac{1}{4}\sum_{s\in\{\mathbf{0},\mathbf{1},A,B,C,D\}}\frac{1}{\sqrt{N!}}a_s^\dagger(a_{\mathbf{1}}^\dagger)^{N-1-n}(a_{\mathbf{0}}^\dagger)^n\,|\Omega\rangle_{\mathcal{S}}\otimes|s\rangle_{\mathcal{C}}\,. \tag{D.9}$$

Note that here we have $N-1$, and not N, appearing in the second exponent, because one qubit is maximally entangled with $\mathcal{C}$, so only $N-1$ qubits in $\mathcal{S}$ are in a product state.

JHEP04(2020)063

D.2 Scenario (*b*)

Now let us move to scenario (b), in which the black hole is maximally entangled to a retriever B, except for one qubit A, that is maximally entangled to $\mathcal{C}$ [cf. figure 8(*b*)]. Here, the initial state is an entangled state which reads

$$|\rho_{\mathcal{S}\cup\mathcal{C}\cup B}(0)\otimes\rho_{\mathcal{S}\cup\mathcal{C}\cup B}(0)\rangle\rangle = \frac{1}{4^N}\bigotimes_{j=1}^{N-1}\sum_{s_j\in\{0,1\}^4}(|s_j\rangle_{\mathcal{S},j}\otimes|s_j\rangle_{B,j})\otimes\sum_{s\in\{0,1\}^4}|s\rangle_A\otimes|s\rangle_{\mathcal{C}}\,. \tag{D.10}$$

The $|W\rangle\rangle$ vectors for the purities involved in the mutual information (4.3) are as in (D.5) with an additional $|I^+\rangle_{B,j}$ for each $j\in B$, since B is never within a region we compute the purity of. Therefore we may directly evaluate $\sum_{s_j\in\{0,1\}^N}|s_j\rangle_{\mathcal{S},j}\langle I^+|s_j\rangle_{B,j} = |\mathbf{0}\rangle+|\mathbf{1}\rangle+|A\rangle+|B\rangle$ and use the simplified initial state

$$|\rho_{\mathcal{S}\cup\mathcal{C}}(0)\otimes\rho_{\mathcal{S}\cup\mathcal{C}}(0)\rangle\rangle = \frac{1}{4^N}\sum_{s\in\{0,1\}^4}\bigotimes_{j=1}^{N-1}(|\mathbf{0}\rangle_j+|\mathbf{1}\rangle_j+|A\rangle_j+|B\rangle_j)\otimes|s\rangle_A\otimes|s\rangle_{\mathcal{C}} \tag{D.11}$$

$$= \frac{1}{4^N}\sum_{s\in\{\mathbf{0},\mathbf{1},A,B,C,D\}}\frac{1}{\sqrt{N!}}a_s^\dagger(a_{\mathbf{0}}^\dagger+a_{\mathbf{1}}^\dagger+a_A^\dagger+a_B^\dagger)^{N-1}|\Omega\rangle_{\mathcal{S}}\otimes|s\rangle_{\mathcal{C}} \tag{D.12}$$

after restriction of s and symmetrization of $\mathcal{S}$ as above. For the evolution with charge conservation, this bosonic formalism is again the basis for our numerical calculations.

Note, finally, that in the case of Haar-scrambled evolution, we can again use the differential equation (3.19), where the initial conditions are now

$$\mathcal{P}_{K\cup\mathcal{C}} = \frac{k}{N}\frac{1}{2^{k-1}}+\frac{N-k}{N}\frac{1}{2^{k+1}}\,, \tag{D.13}$$

$$\mathcal{P}_K = \frac{1}{2^k}\,. \tag{D.14}$$

D.3 Scenario (*c*)

In order to implement the two-step protocol depicted in figure 12, it is crucial to remember that the interaction with the bath is Markovian. First, we simply evolve for time t_1 the initial pure (and symmetrized) state (4.6) of $N-1$ qubits in a given charge sector. Then, we add a qubit s maximally entangled to the ancilla. Symmetrizing its position, this amounts to the following change of basis vectors of the system state:

$$|n_{\mathbf{0}},n_{\mathbf{1}},\ldots,n_D\rangle_{\mathcal{S}}\to\frac{1}{4}\sum_{s\in\{\mathbf{0},\mathbf{1},A,B,C,D\}}\sqrt{\frac{n_s+1}{N}}\,|n_{\mathbf{0}}+\delta_{s\mathbf{0}},n_{\mathbf{1}}+\delta_{s\mathbf{1}},\ldots,n_D+\delta_{sD}\rangle_{\mathcal{S}}\otimes|s\rangle_{\mathcal{C}}\,. \tag{D.15}$$

The rest of the protocol is then analogous to scenario (a) for time t_2 and the initial mixed state above.

JHEP04(2020)063

References

[1] S.W. Hawking, *Particle Creation by Black Holes*, *Commun. Math. Phys.* **43** (1975) 199 [*Erratum ibid.* **46** (1976) 206] [INSPIRE].

[2] S.W. Hawking, *Breakdown of Predictability in Gravitational Collapse*, *Phys. Rev.* **D 14** (1976) 2460 [INSPIRE].

[3] A. Almheiri, D. Marolf, J. Polchinski and J. Sully, *Black Holes: Complementarity or Firewalls?*, *JHEP* **02** (2013) 062 [arXiv:1207.3123] [INSPIRE].

[4] G. Penington, *Entanglement Wedge Reconstruction and the Information Paradox*, arXiv:1905.08255 [INSPIRE].

[5] A. Almheiri, N. Engelhardt, D. Marolf and H. Maxfield, *The entropy of bulk quantum fields and the entanglement wedge of an evaporating black hole*, *JHEP* **12** (2019) 063 [arXiv:1905.08762] [INSPIRE].

[6] P. Hayden and J. Preskill, *Black holes as mirrors: Quantum information in random subsystems*, *JHEP* **09** (2007) 120 [arXiv:0708.4025] [INSPIRE].

[7] Y. Sekino and L. Susskind, *Fast scramblers*, *JHEP* **10** (2008) 065 [arXiv:0808.2096] [INSPIRE].

[8] L. Susskind, *Addendum to Fast Scramblers*, arXiv:1101.6048 [INSPIRE].

[9] S.H. Shenker and D. Stanford, *Black holes and the butterfly effect*, *JHEP* **03** (2014) 067 [arXiv:1306.0622] [INSPIRE].

[10] S.H. Shenker and D. Stanford, *Multiple Shocks*, *JHEP* **12** (2014) 046 [arXiv:1312.3296] [INSPIRE].

[11] A. Kitaev, *A simple model of quantum holography*, KITP strings seminar and Entanglement 2015 program, http://online.kitp.ucsb.edu/online/entangled15/kitaev/ (2015).

[12] D.A. Roberts, D. Stanford and L. Susskind, *Localized shocks*, *JHEP* **03** (2015) 051 [arXiv:1409.8180] [INSPIRE].

[13] J. Maldacena, S.H. Shenker and D. Stanford, *A bound on chaos*, *JHEP* **08** (2016) 106 [arXiv:1503.01409] [INSPIRE].

[14] D.A. Roberts, D. Stanford and A. Streicher, *Operator growth in the SYK model*, *JHEP* **06** (2018) 122 [arXiv:1802.02633] [INSPIRE].

[15] A. Larkin and Y.N. Ovchinnikov, *Quasiclassical method in the theory of superconductivity*, *Sov. Phys. JETP* **28** (1969) 1200, http://www.jetp.ac.ru/cgi-bin/dn/e_028_06_1200.pdf.

[16] P. Hosur, X.-L. Qi, D.A. Roberts and B. Yoshida, *Chaos in quantum channels*, *JHEP* **02** (2016) 004 [arXiv:1511.04021] [INSPIRE].

[17] J. Emerson, E. Livine and S. Lloyd, *Convergence conditions for random quantum circuits*, *Phys. Rev.* **A 72** (2005) 060302 [quant-ph/0503210].

[18] O.C. Dahlsten, R. Oliveira and M.B. Plenio, *The emergence of typical entanglement in two-party random processes*, *Phys. Rev.* **A 40** (2007) 8081.

[19] D. Gross, K. Audenaert and J. Eisert, *Evenly distributed unitaries: On the structure of unitary designs*, *J. Math. Phys.* **48** (2007) 052104 [quant-ph/0611002].

[20] M. Žnidarič, *Optimal two-qubit gate for generation of random bipartite entanglement*, *Phys. Rev.* **A 76** (2007) 012318 [quant-ph/0702240].

JHEP04(2020)063

[21] M. Žnidarič, *Exact convergence times for generation of random bipartite entanglement*, *Phys. Rev.* **A 78** (2008) 032324 [arXiv:0809.0554] [INSPIRE].

[22] L. Arnaud and D. Braun, *Efficiency of producing random unitary matrices with quantum circuits*, *Phys. Rev.* **A 78** (2008) 062329 [arXiv:0807.0775] [INSPIRE].

[23] A.W. Harrow and R.A. Low, *Random Quantum Circuits are Approximate 2-designs*, *Commun. Math. Phys.* **291** (2009) 257 [arXiv:0802.1919].

[24] W.G. Brown and L. Viola, *Convergence Rates for Arbitrary Statistical Moments of Random Quantum Circuits*, *Phys. Rev. Lett.* **104** (2010) 250501 [arXiv:0910.0913].

[25] I.T. Diniz and D. Jonathan, *Comment on "Random Quantum Circuits are Approximate 2-designs" by A.W. Harrow and R.A. Low (Commun. Math. Phys. 291, 257-302 (2009))*, *Commun. Math. Phys.* **304** (2011) 281 [arXiv:1006.4202].

[26] F.G. S.L. Brandão, A.W. Harrow and M. Horodecki, *Local Random Quantum Circuits are Approximate Polynomial-Designs*, *Commun. Math. Phys.* **346** (2016) 397 [arXiv:1208.0692] [INSPIRE].

[27] Y. Nakata, C. Hirche, M. Koashi and A. Winter, *Efficient Quantum Pseudorandomness with Nearly Time-Independent Hamiltonian Dynamics*, *Phys. Rev.* **X 7** (2017) 021006 [arXiv:1609.07021] [INSPIRE].

[28] N. Lashkari, D. Stanford, M. Hastings, T. Osborne and P. Hayden, *Towards the Fast Scrambling Conjecture*, *JHEP* **04** (2013) 022 [arXiv:1111.6580] [INSPIRE].

[29] E. Onorati, O. Buerschaper, M. Kliesch, W. Brown, A.H. Werner and J. Eisert, *Mixing properties of stochastic quantum Hamiltonians*, *Commun. Math. Phys.* **355** (2017) 905 [arXiv:1606.01914] [INSPIRE].

[30] L. Banchi, D. Burgarth and M.J. Kastoryano, *Driven Quantum Dynamics: Will It Blend?*, *Phys. Rev.* **X 7** (2017) 041015 [arXiv:1704.03041] [INSPIRE].

[31] H. Gharibyan, M. Hanada, S.H. Shenker and M. Tezuka, *Onset of Random Matrix Behavior in Scrambling Systems*, *JHEP* **07** (2018) 124 [*Erratum ibid.* **1902** (2019) 197] [arXiv:1803.08050] [INSPIRE].

[32] P. Saad, S.H. Shenker and D. Stanford, *A semiclassical ramp in SYK and in gravity*, arXiv:1806.06840 [INSPIRE].

[33] T. Zhou and X. Chen, *Operator dynamics in a Brownian quantum circuit*, *Phys. Rev.* **E 99** (2019) 052212 [arXiv:1805.09307] [INSPIRE].

[34] C. Sünderhauf, L. Piroli, X.-L. Qi, N. Schuch and J.I. Cirac, *Quantum chaos in the Brownian SYK model with large finite N: OTOCs and tripartite information*, *JHEP* **11** (2019) 038 [arXiv:1908.00775] [INSPIRE].

[35] A. Nahum, J. Ruhman, S. Vijay and J. Haah, *Quantum Entanglement Growth Under Random Unitary Dynamics*, *Phys. Rev.* **X 7** (2017) 031016 [arXiv:1608.06950] [INSPIRE].

[36] C. Sünderhauf, D. Pérez-García, D.A. Huse, N. Schuch and J.I. Cirac, *Localization with random time-periodic quantum circuits*, *Phys. Rev.* **B 98** (2018) 134204 [arXiv:1805.08487] [INSPIRE].

[37] A. Nahum, S. Vijay and J. Haah, *Operator Spreading in Random Unitary Circuits*, *Phys. Rev.* **X 8** (2018) 021014 [arXiv:1705.08975] [INSPIRE].

JHEP04(2020)063

[38] C. von Keyserlingk, T. Rakovszky, F. Pollmann and S. Sondhi, *Operator hydrodynamics, OTOCs and entanglement growth in systems without conservation laws*, *Phys. Rev.* **X 8** (2018) 021013 [arXiv:1705.08910] [INSPIRE].

[39] T. Rakovszky, F. Pollmann and C.W. von Keyserlingk, *Diffusive hydrodynamics of out-of-time-ordered correlators with charge conservation*, *Phys. Rev.* **X 8** (2018) 031058 [arXiv:1710.09827] [INSPIRE].

[40] A. Chan, A. De Luca and J.T. Chalker, *Solution of a minimal model for many-body quantum chaos*, *Phys. Rev.* **X 8** (2018) 041019 [arXiv:1712.06836] [INSPIRE].

[41] A. Chan, A. De Luca and J.T. Chalker, *Spectral statistics in spatially extended chaotic quantum many-body systems*, *Phys. Rev. Lett.* **121** (2018) 060601 [arXiv:1803.03841] [INSPIRE].

[42] V. Khemani, A. Vishwanath and D.A. Huse, *Operator spreading and the emergence of dissipation in unitary dynamics with conservation laws*, *Phys. Rev.* **X 8** (2018) 031057 [arXiv:1710.09835] [INSPIRE].

[43] P. Kos, M. Ljubotina and T. Prosen, *Many-body quantum chaos: Analytic connection to random matrix theory*, *Phys. Rev.* **X 8** (2018) 021062 [arXiv:1712.02665] [INSPIRE].

[44] B. Bertini, P. Kos and T. Prosen, *Exact Spectral Form Factor in a Minimal Model of Many-Body Quantum Chaos*, *Phys. Rev. Lett.* **121** (2018) 264101 [arXiv:1805.00931] [INSPIRE].

[45] N. Hunter-Jones, *Unitary designs from statistical mechanics in random quantum circuits*, arXiv:1905.12053 [INSPIRE].

[46] M.J. Gullans and D.A. Huse, *Entanglement structure of current-driven diffusive fermion systems*, *Phys. Rev.* **X 9** (2019) 021007 [arXiv:1804.00010] [INSPIRE].

[47] Q. Zhuang, T. Schuster, B. Yoshida and N.Y. Yao, *Scrambling and Complexity in Phase Space*, *Phys. Rev.* **A 99** (2019) 062334 [arXiv:1902.04076] [INSPIRE].

[48] L. D'Alessio, Y. Kafri, A. Polkovnikov and M. Rigol, *From quantum chaos and eigenstate thermalization to statistical mechanics and thermodynamics*, *Adv. Phys.* **65** (2016) 239 [arXiv:1509.06411] [INSPIRE].

[49] M. Rigol, V. Dunjko and M. Olshanii, *Thermalization and its mechanism for generic isolated quantum systems*, *Nature* **452** (2008) 854 [arXiv:0708.1324] [INSPIRE].

[50] D.N. Page, *Information in black hole radiation*, *Phys. Rev. Lett.* **71** (1993) 3743 [hep-th/9306083] [INSPIRE].

[51] D.N. Page, *Hawking radiation and black hole thermodynamics*, *New J. Phys.* **7** (2005) 203 [hep-th/0409024] [INSPIRE].

[52] Y. Li, X. Chen and M.P.A. Fisher, *Quantum Zeno effect and the many-body entanglement transition*, *Phys. Rev.* **B 98** (2018) 205136 [arXiv:1808.06134] [INSPIRE].

[53] Y. Li, X. Chen and M.P.A. Fisher, *Measurement-driven entanglement transition in hybrid quantum circuits*, *Phys. Rev.* **B 100** (2019) 134306 [arXiv:1901.08092] [INSPIRE].

[54] B. Skinner, J. Ruhman and A. Nahum, *Measurement-Induced Phase Transitions in the Dynamics of Entanglement*, *Phys. Rev.* **X 9** (2019) 031009 [arXiv:1808.05953] [INSPIRE].

[55] M.J. Gullans and D.A. Huse, *Dynamical purification phase transition induced by quantum measurements*, arXiv:1905.05195 [INSPIRE].

JHEP04(2020)063

[56] A. Zabalo, M.J. Gullans, J.H. Wilson, S. Gopalakrishnan, D.A. Huse and J.H. Pixley, *Critical properties of the measurement-induced transition in random quantum circuits*, *Phys. Rev.* **B 101** (2020) 060301 [arXiv:1911.00008] [INSPIRE].

[57] Y. Bao, S. Choi and E. Altman, *Theory of the phase transition in random unitary circuits with measurements*, *Phys. Rev.* **B 101** (2020) 104301 [arXiv:1908.04305] [INSPIRE].

[58] S. Choi, Y. Bao, X.-L. Qi and E. Altman, *Quantum Error Correction in Scrambling Dynamics and Measurement Induced Phase Transition*, arXiv:1903.05124 [INSPIRE].

[59] R. Vasseur, A.C. Potter, Y.-Z. You and A.W.W. Ludwig, *Entanglement Transitions from Holographic Random Tensor Networks*, *Phys. Rev.* **B 100** (2019) 134203 [arXiv:1807.07082] [INSPIRE].

[60] M.J. Gullans and D.A. Huse, *Scalable probes of measurement-induced criticality*, arXiv:1910.00020 [INSPIRE].

[61] D. Chernowitz and V. Gritsev, *Entanglement Dynamics of Random GUE Hamiltonians*, arXiv:2001.00140 [INSPIRE].

[62] A. Almheiri, A. Milekhin and B. Swingle, *Universal Constraints on Energy Flow and SYK Thermalization*, arXiv:1912.04912 [INSPIRE].

[63] P. Zhang, *Evaporation dynamics of the Sachdev-Ye-Kitaev model*, *Phys. Rev.* **B 100** (2019) 245104 [arXiv:1909.10637] [INSPIRE].

[64] S. Sachdev and J. Ye, *Gapless spin fluid ground state in a random, quantum Heisenberg magnet*, *Phys. Rev. Lett.* **70** (1993) 3339 [cond-mat/9212030] [INSPIRE].

[65] Y. Chen, H. Zhai and P. Zhang, *Tunable Quantum Chaos in the Sachdev-Ye-Kitaev Model Coupled to a Thermal Bath*, *JHEP* **07** (2017) 150 [arXiv:1705.09818] [INSPIRE].

[66] S.D. Mathur, *The Information paradox: A Pedagogical introduction*, *Class. Quant. Grav.* **26** (2009) 224001 [arXiv:0909.1038] [INSPIRE].

[67] B. Czech, K. Larjo and M. Rozali, *Black Holes as Rubik's Cubes*, *JHEP* **08** (2011) 143 [arXiv:1106.5229] [INSPIRE].

[68] S.D. Mathur and C.J. Plumberg, *Correlations in Hawking radiation and the infall problem*, *JHEP* **09** (2011) 093 [arXiv:1101.4899] [INSPIRE].

[69] S.D. Mathur, *The Information paradox and the infall problem*, *Class. Quant. Grav.* **28** (2011) 125010 [arXiv:1012.2101] [INSPIRE].

[70] Q.-y. Cai, B. Zhang, M.-s. Zhan and L. You, *Comment on 'What the information loss is not'*, arXiv:1210.2048 [INSPIRE].

[71] L. Brady and V. Sahakian, *Scrambling with Matrix Black Holes*, *Phys. Rev.* **D 88** (2013) 046003 [arXiv:1306.5200] [INSPIRE].

[72] S.B. Giddings, *Models for unitary black hole disintegration*, *Phys. Rev.* **D 85** (2012) 044038 [arXiv:1108.2015] [INSPIRE].

[73] S.G. Avery, B.D. Chowdhury and A. Puhm, *Unitarity and fuzzball complementarity: 'Alice fuzzes but may not even know it!'*, *JHEP* **09** (2013) 012 [arXiv:1210.6996] [INSPIRE].

[74] S.B. Giddings and Y. Shi, *Quantum information transfer and models for black hole mechanics*, *Phys. Rev.* **D 87** (2013) 064031 [arXiv:1205.4732] [INSPIRE].

JHEP04(2020)063

[75] S.G. Avery, *Qubit Models of Black Hole Evaporation*, *JHEP* **01** (2013) 176 [arXiv:1109.2911] [INSPIRE].

[76] E. Verlinde and H. Verlinde, *Passing through the Firewall*, arXiv:1306.0515 [INSPIRE].

[77] A. Roy, M.H. Rahat, M. Al Alvi and M.A. Matin, *Does Considering Quantum Correlations Resolve the Information Paradox?*, arXiv:1312.2176 [INSPIRE].

[78] R. Hübener, Y. Sekino and J. Eisert, *Equilibration in low-dimensional quantum matrix models*, *JHEP* **04** (2015) 166 [arXiv:1403.1392] [INSPIRE].

[79] K. Brádler and C. Adami, *One-shot decoupling and Page curves from a dynamical model for black hole evaporation*, *Phys. Rev. Lett.* **116** (2016) 101301 [arXiv:1505.02840] [INSPIRE].

[80] S. Leutheusser and M. Van Raamsdonk, *Tensor Network Models of Unitary Black Hole Evaporation*, *JHEP* **08** (2017) 141 [arXiv:1611.08613] [INSPIRE].

[81] T. Tokusumi, A. Matsumura and Y. Nambu, *Quantum Circuit Model of Black Hole Evaporation*, *Class. Quant. Grav.* **35** (2018) 235013 [arXiv:1807.07672] [INSPIRE].

[82] M.A. Alvi, M. Majumdar, M.A. Matin, M.H. Rahat and A. Roy, *Modifications of the Page Curve from correlations within Hawking radiation*, *Phys. Lett.* **B 797** (2019) 134881.

[83] B. Yoshida and N.Y. Yao, *Disentangling Scrambling and Decoherence via Quantum Teleportation*, *Phys. Rev.* **X 9** (2019) 011006 [arXiv:1803.10772] [INSPIRE].

[84] K.A. Landsman et al., *Verified Quantum Information Scrambling*, *Nature* **567** (2019) 61 [arXiv:1806.02807] [INSPIRE].

[85] B. Yoshida, *Soft mode and interior operator in the Hayden-Preskill thought experiment*, *Phys. Rev.* **D 100** (2019) 086001 [arXiv:1812.07353] [INSPIRE].

[86] K. Agarwal and N. Bao, *A toy model for decoherence in the black hole information problem*, arXiv:1912.09491 [INSPIRE].

[87] H. Liu and S. Vardhan, *A dynamical mechanism for the Page curve from quantum chaos*, arXiv:2002.05734 [INSPIRE].

[88] V. Alba and F. Carollo, *Spreading of correlations in Markovian open quantum systems*, arXiv:2002.09527 [INSPIRE].

JHEP04(2020)063

Bibliography

[1] Christoph Sünderhauf, David Pérez-García, David A. Huse, Norbert Schuch, and J. Ignacio Cirac. "Localization with random time-periodic quantum circuits". In: *Physical Review B* 98.13 (2018). arXiv: 1805.08487.

[2] Christoph Sünderhauf, Lorenzo Piroli, Xiao-Liang Qi, Norbert Schuch, and J. Ignacio Cirac. "Quantum chaos in the Brownian SYK model with large finite N: OTOCs and tripartite information". In: *Journal of High Energy Physics* 2019.11 (2019). arXiv: 1908.00775.

[3] Lorenzo Piroli, Christoph Sünderhauf, and Xiao-Liang Qi. "A random unitary circuit model for black hole evaporation". In: *Journal of High Energy Physics* 2020.4 (2020). arXiv: 2002.09236.

[4] Zongping Gong, Christoph Sünderhauf, Norbert Schuch, and J. Ignacio Cirac. "Classification of Matrix-Product Unitaries with Symmetries". In: *Physical Review Letters* 124.10 (2020). arXiv: 1812.09183.

[5] Emanuele Galiffi, Christoph Sünderhauf, Maarten DeKieviet, and Sandro Wimberger. "Two-dimensional simulation of quantum reflection". In: *Journal of Physics B Atomic Molecular Physics* 50.9, 095001 (2017), p. 095001. arXiv: 1712.09874.

[6] Carl M. Bender, Nima Hassanpour, Daniel W. Hook, S. P. Klevansky, Christoph Sünderhauf, and Zichao Wen. "Behavior of eigenvalues in a region of broken PT symmetry". In: *Physical Review A* 95.5, 052113 (2017), p. 052113. arXiv: 1702.03811.

[7] Michael Schreiber, Sean S. Hodgman, Pranjal Bordia, Henrik P. Lüschen, Mark H. Fischer, Ronen Vosk, Ehud Altman, Ulrich Schneider, and Immanuel Bloch. "Observation of many-body localization of interacting fermions in a quasirandom optical lattice". In: *Science* 349.6250 (2015), pp. 842–845. arXiv: 1501.05661.

[8] Jae-yoon Choi, Sebastian Hild, Johannes Zeiher, Peter Schauß, Antonio Rubio-Abadal, Tarik Yefsah, Vedika Khemani, David A. Huse, Immanuel Bloch, and Christian Gross. "Exploring the many-body localization transition in two dimensions". In: *Science* 352.6293 (2016), pp. 1547–1552. arXiv: 1604.04178.

[9] Dmitry A Abanin and Zlatko Papić. "Recent progress in many-body localization". In: *Annalen der Physik* 529.7 (2017). arXiv: 1705.09103.

[10] Marcos Rigol, Vanja Dunjko, Vladimir Yurovsky, and Maxim Olshanii. "Relaxation in a Completely Integrable Many-Body Quantum System: An AbInitio Study of the Dynamics of the Highly Excited States of 1D Lattice Hard-Core Bosons". In: *Physical Review Letters* 98.5, 050405 (2007), p. 050405. arXiv: cond-mat/0604476.

[11] Marcos Rigol, Vanja Dunjko, and Maxim Olshanii. "Thermalization and its mechanism for generic isolated quantum systems". In: *Nature* 452.7189 (2008), pp. 854–858. arXiv: 0708.1324.

[12] J. Eisert, M. Friesdorf, and C. Gogolin. "Quantum many-body systems out of equilibrium". In: *Nature Physics* 11.2 (2015), pp. 124–130. arXiv: 1408.5148.

[13] Christian Gogolin and Jens Eisert. "Equilibration, thermalisation, and the emergence of statistical mechanics in closed quantum systems". In: *Reports on Progress in Physics* 79.5, 056001 (2016), p. 056001. arXiv: 1503.07538.

[14] Arijeet Pal and David A. Huse. "Many-body localization phase transition". In: *Physical Review B* 82.17, 174411 (2010), p. 174411. arXiv: 1010.1992.

[15] David A. Huse, Rahul Nandkishore, and Vadim Oganesyan. "Phenomenology of fully many-body-localized systems". In: *Physical Review B* 90.17 (2014). arXiv: 1408.4297.

[16] C. W. von Keyserlingk, Tibor Rakovszky, Frank Pollmann, and S. L. Sondhi. "Operator Hydrodynamics, OTOCs, and Entanglement Growth in Systems without Conservation Laws". In: *Physical Review X* 8.2, 021013 (2018), p. 021013. arXiv: 1705.08910.

[17] Adam Nahum, Sagar Vijay, and Jeongwan Haah. "Operator Spreading in Random Unitary Circuits". In: *Physical Review X* 8.2, 021014 (2018), p. 021014. arXiv: 1705.08975.

[18] Juan Maldacena, Stephen H. Shenker, and Douglas Stanford. "A bound on chaos". In: *Journal of High Energy Physics* 2016.8 (2016). arXiv: 1503.01409.

[19] G. 't Hooft. "Dimensional Reduction in Quantum Gravity". In: *arXiv e-prints*, gr-qc/9310026 (1993), gr–qc/9310026. arXiv: gr-qc/9310026.

[20] Leonard Susskind. "The world as a hologram". In: *Journal of Mathematical Physics* 36.11 (1995), pp. 6377–6396. arXiv: hep-th/9409089.

[21] Juan Martin Maldacena. "The Large N limit of superconformal field theories and supergravity". In: *Int. J. Theor. Phys.* 38 (1999). [Adv. Theor. Math. Phys.2,231(1998)], pp. 1113–1133. arXiv: hep-th/9711200.

[22] Nima Lashkari, Douglas Stanford, Matthew Hastings, Tobias Osborne, and Patrick Hayden. "Towards the fast scrambling conjecture". In: *Journal of High Energy Physics* 2013, 22 (2013), p. 22. arXiv: 1111.6580.

[23] Phil Saad, Stephen H. Shenker, and Douglas Stanford. "A semiclassical ramp in SYK and in gravity". In: *arXiv e-prints*, arXiv:1806.06840 (2018), arXiv:1806.06840. arXiv: 1806.06840.

[24] Yasuhiro Sekino and L. Susskind. "Fast scramblers". In: *Journal of High Energy Physics* 2008.10, 065 (2008), p. 065. arXiv: 0808.2096.

[25] Leonard Susskind. "Addendum to Fast Scramblers". In: *arXiv e-prints*, arXiv:1101.6048 (2011), arXiv:1101.6048. arXiv: 1101.6048.

[26] Madan Lal Mehta. *Random matrices*. Vol. 142. San Diego: Elsevier, 2004. ISBN: 0-12-088409-7.

[27] Patrick Hayden and John Preskill. "Black holes as mirrors: quantum information in random subsystems". In: *Journal of High Energy Physics* 2007.9, 120 (2007), p. 120. arXiv: 0708.4025.

[28] Adam Nahum, Jonathan Ruhman, Sagar Vijay, and Jeongwan Haah. "Quantum Entanglement Growth under Random Unitary Dynamics". In: *Physical Review X* 7.3, 031016 (2017), p. 031016. arXiv: 1608.06950.

[29] Donald L Cohn. *Measure theory*. 2nd ed. Vol. 165. New York, Heidelberg: Springer, 2003. ISBN: 978-1-4614-6956-8.

[30] Alfred Haar. "Der Massbegriff in der Theorie der Kontinuierlichen Gruppen". In: *Annals of Mathematics* 34.1 (1933), pp. 147–169.

[31] A. Hurwitz. "über die Erzeugung der Invarianten durch Integration". In: *Nachrichten von der Gesellschaft der Wissenschaften zu Göttingen, Mathematisch-Physikalische Klasse* 1 (1897), pp. 71–90.

[32] Christoph Spengler, Marcus Huber, and Beatrix C. Hiesmayr. "Composite parameterization and Haar measure for all unitary and special unitary groups". In: *Journal of Mathematical Physics* 53.1 (2012), p. 013501. arXiv: 1103.3408.

[33] K Zyczkowski and M Kus. "Random unitary matrices". In: *Journal of Physics A: Mathematical and General* 27.12 (1994), pp. 4235–4245.

[34] Benoît Collins. "Moments and cumulants of polynomial random variables on unitarygroups, the Itzykson-Zuber integral, and free probability". In: *International Mathematics Research Notices* 2003.17 (2003), pp. 953–982. arXiv: math-ph/0205010.

[35] Benoît Collins and Piotr Śniady. "Integration with Respect to the Haar Measure on Unitary, Orthogonal and Symplectic Group". In: *Communications in Mathematical Physics* 264.3 (2006), pp. 773–795. arXiv: math-ph/0402073.

[36] Benoît Collins and Sho Matsumoto. "On some properties of orthogonal Weingarten functions". In: *Journal of Mathematical Physics* 50.11 (2009), p. 113516. arXiv: 0903.5143.

[37] Benoît Collins and Ion Nechita. "Random Quantum Channels I: Graphical Calculus and the Bell State Phenomenon". In: *Communications in Mathematical Physics* 297.2 (2010), pp. 345–370. arXiv: 0905.2313.

[38] P. W. Brouwer and C. W. J. Beenakker. "Diagrammatic method of integration over the unitary group, with applications to quantum transport in mesoscopic systems". In: *Journal of Mathematical Physics* 37.10 (1996), pp. 4904–4934. arXiv: cond-mat/9604059.

[39] Benoît Collins and Sho Matsumoto. "Weingarten calculus via orthogonality relations: new applications". In: *ALEA* 14 (2017), pp. 631–656. arXiv: 1701.04493.

[40] Francesco Mezzadri. "How to generate random matrices from the classical compact groups". In: (2006). arXiv: math-ph/0609050.

[41] Alan Edelman and N. Raj Rao. "Random matrix theory". In: *Acta Numerica* 14 (2005), pp. 233–297.

[42] William H Press, Saul A Teukolsky, William T Vetterling, and Brian P Flannery. *Numerical recipes 3rd edition: The art of scientific computing*. Cambridge university press, 2007.

[43] Karol Zyczkowski and Hans-Jürgen Sommers. "Induced measures in the space of mixed quantum states". In: *Journal of Physics A Mathematical General* 34.35 (2001), pp. 7111–7125. arXiv: quant-ph/0012101.

[44] A. Einstein, B. Podolsky, and N. Rosen. "Can Quantum-Mechanical Description of Physical Reality Be Considered Complete?" In: *Phys. Rev.* 47 (10 1935), pp. 777–780.

[45] Max Born. *Physik im Wandel meiner Zeit*. 1st ed. 1983. Facetten der Physik. Wiesbaden: Vieweg+Teubner Verlag, 1983. ISBN: 9783322887948.

[46] J. S. Bell. "On the Einstein Podolsky Rosen paradox". In: *Physics Physique Fizika* 1 (3 1964), pp. 195–200.

[47] BIG Bell Test Collaboration. "Challenging local realism with human choices". In: *Nature* 557.7704 (2018), pp. 212–216. arXiv: 1805.04431.

[48] Michael A. Nielsen and Isaac J. Chuang. *Quantum Computation and Quantum Information*. Cambridge: Cambridge University Press, 2000. ISBN: 0-521-63503-9.

[49] James D. Patterson and Bernard C. Bailey. *Solid-State Physics : Introduction to the Theory*. 1st ed. 2007. Berlin, Heidelberg: Springer-Verlag, 2007, p. 717. ISBN: 978-3-540-24115-7.

[50] Román Orús. "Tensor networks for complex quantum systems". In: *Nature Reviews Physics* 1.9 (2019), pp. 538–550. arXiv: 1812.04011.

[51] Berry Groisman, Sandu Popescu, and Andreas Winter. "Quantum, classical, and total amount of correlations in a quantum state". In: *Physical Review A* 72.3, 032317 (2005), p. 032317. arXiv: quant-ph/0410091.

[52] J. M. Deutsch. "Quantum statistical mechanics in a closed system". In: *Physical Review A* 43.4 (1991), pp. 2046–2049.

[53] Mark Srednicki. "Chaos and quantum thermalization". In: *Physical Review E* 50.2 (1994), pp. 888–901. arXiv: cond-mat/9403051.

[54] AI Larkin and Yu N Ovchinnikov. "Quasiclassical method in the theory of superconductivity". In: *Sov Phys JETP* 28.6 (1969), pp. 1200–1205.

[55] Brian Swingle. "Unscrambling the physics of out-of-time-order correlators". In: *Nature Physics* 14.10 (2018), pp. 988–990.

[56] Tianci Zhou and Xiao Chen. "Operator dynamics in a Brownian quantum circuit". In: *Physical Review E* 99.5 (2019). arXiv: 1805.09307.

[57] Bryce Kobrin, Zhenbin Yang, Gregory D. Kahanamoku-Meyer, Christopher T. Olund, Joel E. Moore, Douglas Stanford, and Norman Y. Yao. *Many-Body Chaos in the Sachdev-Ye-Kitaev Model*. 2020. arXiv: 2002.05725.

[58] Pavan Hosur, Xiao-Liang Qi, Daniel A. Roberts, and Beni Yoshida. "Chaos in quantum channels". In: *Journal of High Energy Physics* 2016.2 (2016). arXiv: 1511.04021.

[59] Pasquale Calabrese and John Cardy. "Evolution of entanglement entropy in one-dimensional systems". In: *Journal of Statistical Mechanics: Theory and Experiment* 2005.4 (2005), p. 04010. arXiv: cond-mat/0503393.

[60] Vincenzo Alba and Pasquale Calabrese. "Entanglement and thermodynamics after a quantum quench in integrable systems". In: *Proceedings of the National Academy of Science* 114.30 (2017), pp. 7947–7951. arXiv: 1608.00614.

[61] P. W. Anderson. "Absence of Diffusion in Certain Random Lattices". In: *Phys. Rev.* 109 (5 1958), pp. 1492–1505.

[62] Aart Lagendijk, Bart Van Tiggelen, and Diederik S Wiersma. "Fifty years of Anderson localization". In: *Phys. Today* 62.8 (2009), pp. 24–29.

[63] Michael Aizenman and Stanislav Molchanov. "Localization at large disorder and at extreme energies: An elementary derivations". In: *Communications in Mathematical Physics* 157.2 (1993), pp. 245–278.

[64] Günter Stolz. "Strategies in localization proofs for one-dimensional random Schrödinger operators". In: *Proceedings of the Indian Academy of Sciences-Mathematical Sciences*. Vol. 112. 1. Springer. 2002, pp. 229–243.

[65] Jonas A. Kjäll, Jens H. Bardarson, and Frank Pollmann. "Many-Body Localization in a Disordered Quantum Ising Chain". In: *Physical Review Letters* 113.10, 107204 (2014), p. 107204. arXiv: 1403.1568.

[66] Pedro Ponte, Z. Papić, François Huveneers, and Dmitry A. Abanin. "Many-Body Localization in Periodically Driven Systems". In: *Physical Review Letters* 114.14, 140401 (2015), p. 140401. arXiv: 1410.8518.

[67] Achilleas Lazarides, Arnab Das, and Roderich Moessner. "Fate of Many-Body Localization Under Periodic Driving". In: *Physical Review Letters* 115.3, 030402 (2015), p. 030402. arXiv: 1410.3455.

[68] Liangsheng Zhang, Vedika Khemani, and David A. Huse. "A Floquet model for the many-body localization transition". In: *Physical Review B* 94.22, 224202 (2016), p. 224202. arXiv: 1609.00390.

[69] Fernando G. S. L. Brandão, Aram W. Harrow, and Michał Horodecki. "Local Random Quantum Circuits are Approximate Polynomial-Designs". In: *Communications in Mathematical Physics* 346.2 (2016), pp. 397–434. arXiv: 1208.0692.

[70] Jonas Haferkamp, Felipe Montealegre-Mora, Markus Heinrich, Jens Eisert, David Gross, and Ingo Roth. "Quantum homeopathy works: Efficient unitary designs with a system-size independent number of non-Clifford gates". In: *arXiv e-prints*, arXiv:2002.09524 (2020), arXiv:2002.09524. arXiv: 2002.09524.

[71] Tibor Rakovszky, Frank Pollmann, and C. W. von Keyserlingk. "Diffusive Hydrodynamics of Out-of-Time-Ordered Correlators with Charge Conservation". In: *Physical Review X* 8.3, 031058 (2018), p. 031058. arXiv: 1710.09827.

[72] Vedika Khemani, Ashvin Vishwanath, and David A. Huse. "Operator Spreading and the Emergence of Dissipative Hydrodynamics under Unitary Evolution with Conservation Laws". In: *Physical Review X* 8.3, 031057 (2018), p. 031057. arXiv: 1710.09835.

[73] Amos Chan, Andrea De Luca, and J. T. Chalker. "Solution of a Minimal Model for Many-Body Quantum Chaos". In: *Physical Review X* 8.4, 041019 (2018), p. 041019. arXiv: 1712.06836.

[74] Aaron J. Friedman, Amos Chan, Andrea De Luca, and J. T. Chalker. "Spectral Statistics and Many-Body Quantum Chaos with Conserved Charge". In: *Physical Review Letters* 123.21, 210603 (2019), p. 210603. arXiv: 1906.07736.

[75] Amos Chan, Andrea De Luca, and J. T. Chalker. "Spectral Statistics in Spatially Extended Chaotic Quantum Many-Body Systems". In: *Physical Review Letters* 121.6, 060601 (2018), p. 060601. arXiv: 1803.03841.

[76] Hrant Gharibyan, Masanori Hanada, Stephen H. Shenker, and Masaki Tezuka. "Onset of random matrix behavior in scrambling systems". In: *Journal of High Energy Physics* 2018.7, 124 (2018), p. 124. arXiv: 1803.08050.

[77] Bruno Bertini and Lorenzo Piroli. "Scrambling in Random Unitary Circuits: Exact Results". In: *arXiv e-prints*, arXiv:2004.13697 (2020), arXiv:2004.13697. arXiv: 2004.13697.

[78] Frank Arute, Kunal Arya, Ryan Babbush, Dave Bacon, Joseph C Bardin, Rami Barends, Rupak Biswas, Sergio Boixo, Fernando GSL Brandao, David A Buell, et al. "Quantum supremacy using a programmable superconducting processor". In: *Nature* 574.7779 (2019), pp. 505–510.

[79] Richard H. Parker, Chenghui Yu, Weicheng Zhong, Brian Estey, and Holger Müller. "Measurement of the fine-structure constant as a test of the Standard Model". In: *Science* 360.6385 (2018), pp. 191–195. arXiv: 1812.04130.

[80] LIGO Scientific Collaboration and Virgo Collaboration. "Observation of Gravitational Waves from a Binary Black Hole Merger". In: *Physical Review Letters* 116.6, 061102 (2016), p. 061102. arXiv: 1602.03837.

[81] The Nobel Committee for Physics. *Theoretical Foundation for Black Holes and the Supermassive Compact Object at the Galactic Centre*. Nobel Media AB 2021. 2021. URL: https://www.nobelprize.org/prizes/physics/2020/advanced-information/.

[82] C. W. Chou, D. B. Hume, T. Rosenband, and D. J. Wineland. "Optical Clocks and Relativity". In: *Science* 329.5999 (2010), p. 1630.

[83] S. W. Hawking. "Black hole explosions?" In: *Nature* 248.5443 (1974), pp. 30–31.

[84] S. W. Hawking. "Particle creation by black holes". In: *Communications in Mathematical Physics* 43.3 (1975), pp. 199–220.

[85] W. G. Unruh. "Notes on black-hole evaporation". In: *Physical Review D* 14.4 (1976), pp. 870–892.

[86] Leonard Susskind. *The Black Hole War: My Battle with Stephen Hawking to Make the World Safe for Quantum Mechanics*. New York: Little, Brown and Company, 2008. ISBN: 978-0-316-03269-8.

[87] Vijay Balasubramanian and Bartłomiej Czech. "Quantitative approaches to information recovery from black holes". In: *Classical and Quantum Gravity* 28.16, 163001 (2011), p. 163001. arXiv: 1102.3566.

[88] Isaac Kim, Eugene Tang, and John Preskill. "The ghost in the radiation: robust encodings of the black hole interior". In: *Journal of High Energy Physics* 2020.6, 31 (2020), p. 31. arXiv: 2003.05451.

[89] James Lindesay Leonard Susskind. *Introduction to Black Holes, Information, and the String Theory Revolution*. Singapore: World Scientific Publishing Company, 2004. ISBN: 981-256-083-1.

[90] Leonard Susskind, Lárus Thorlacius, and John Uglum. "The stretched horizon and black hole complementarity". In: *Physical Review D* 48.8 (1993), pp. 3743–3761. arXiv: hep-th/9306069.

[91] Ahmed Almheiri, Donald Marolf, Joseph Polchinski, and James Sully. "Black holes: complementarity or firewalls?" In: *Journal of High Energy Physics* 2013, 62 (2013), p. 62. arXiv: 1207.3123.

[92] Don N. Page. "Average entropy of a subsystem". In: *Physical Review Letters* 71.9 (1993), pp. 1291–1294. arXiv: gr-qc/9305007.

[93] Don N. Page. "Information in black hole radiation". In: *Physical Review Letters* 71.23 (1993), pp. 3743–3746. arXiv: hep-th/9306083.

[94] Jacob D. Bekenstein. "Black Holes and Entropy". In: *Physical Review D* 7.8 (1973), pp. 2333–2346.

[95] Shinsei Ryu and Tadashi Takayanagi. "Holographic Derivation of Entanglement Entropy from the anti de Sitter Space/Conformal Field Theory Correspondence". In: *Physical Review Letters* 96.18, 181602 (2006), p. 181602. arXiv: hep-th/0603001.

[96] Fernando Pastawski, Beni Yoshida, Daniel Harlow, and John Preskill. "Holographic quantum error-correcting codes: toy models for the bulk/boundary correspondence". In: *Journal of High Energy Physics* 2015, 149 (2015), p. 149. arXiv: 1503.06237.

[97] Igor R. Klebanov and Juan M. Maldacena. "Solving quantum field theories via curved spacetimes". In: *Physics Today* 62.1 (2009), p. 28.

[98] Xiao-Gang Wen. *Quantum Field Theory of Many-Body Systems*. Oxford, New York: Oxford University Press, 2004. ISBN: 0-19-853094-3.

[99] Subir Sachdev and Jinwu Ye. "Gapless spin-fluid ground state in a random quantum Heisenberg magnet". In: *Physical Review Letters* 70.21 (1993), pp. 3339–3342. arXiv: cond-mat/9212030.

[100] A. Kitaev. "*A simple model of quantum holography*". KITP strings seminar and Entanglement 2015 program; http://online.kitp.ucsb.edu/online/entangled15/kitaev/. 2015.

[101] P. Jordan and E. Wigner. "Über das Paulische Äquivalenzverbot". In: *Zeitschrift fur Physik* 47.9-10 (1928), pp. 631–651.

[102] Richard Jozsa and Akimasa Miyake. "Matchgates and classical simulation of quantum circuits". In: *Proceedings of the Royal Society of London Series A* 464.2100 (2008), pp. 3089–3106. arXiv: 0804.4050.

[103] Daniel A. Roberts, Douglas Stanford, and Alexandre Streicher. "Operator growth in the SYK model". In: *Journal of High Energy Physics* 2018.6, 122 (2018), p. 122. arXiv: 1802.02633.

Acknowledgements

First and foremost, I would like to thank Ignacio Cirac. I feel very lucky and equally thankful that I had the opportunity to be his PhD student at the Max Planck Institute of Quantum Optics.

Next, I would like to thank all of my collaborators throughout my PhD with whom I've coauthored articles[1]: Lorenzo Piroli, Norbert Schuch, Ignacio Cirac, Xiao-Liang Qi, David Pérez-García, David Huse and Zongping Gong. I worked especially closely with Lorenzo, Norbert and Ignacio. They always had an open ear, and I learned a lot from them. A special thank you goes to Lorenzo for kindly offering to read a draft of this thesis.

MPQ is a wonderful place to do research, the entire theory division is to thank. I would like to explicitly name Andrea Kluth and Regina Jasny, without who's dedication nothing at all would work. Over the years, I had the pleasure to share an office with Jordi Tura, Johannes Knörzer, Anna Hackenbroich, Ilya Kull, Miguel Bello, Tommaso Guaita, Stavros Efthymiou, and Arthur Christianen. The submission of my thesis at LMU was made possible by Christian Schilling as well as Matthias Punk.

I am grateful to my parents, who always helped me and my siblings along our paths and supported us in our endeavors.

Finally, I would like to thank millions of people, contemporary and historic. By creating and participating in a society that enabled me to focus on theoretical quantum physics, they were of fundamental importance for the present thesis.

[1] While research is a joint effort thriving from close collaboration, a few individual contributions can be pointed out: [1] C.S. prepared the manuscript, implemented and performed the numerical computations, and fleshed out proofs. D.P., D.H., N.S., and I.C. provided valuable discussions throughout. [2] C.S. implemented and performed the numerical computations and derived the quantifiers' expressions in the effective Hilbert space. C.S. and L.P. wrote the manuscript and researched jointly. X.Q., N.S., and I.C. provided valuable discussions throughout. [3] C.S. implemented and performed the numerical computations. L.P. prepared the manuscript with some help by C.S. X.Q. provided valuable guidance in direction and interpretation, and L.P. and C.S. researched jointly.